PALEOCEANOGRAPHY OF THE INDONESIAN SEAS OVER THE PAST 25,000 YEARS

by

Deborah Khider

A Dissertation Presented to the
FACULTY OF THE USC GRADUATE SCHOOL
UNIVERSITY OF SOUTHERN CALIFORNIA
In Partial Fulfillment of the
Requirements for the Degree
DOCTOR OF PHILOSOPHY
(OCEAN SCIENCES)

August 2011

Acknowledgements

The work presented in this dissertation would not have been possible without the guidance and help of several individuals. First and foremost, I would like to thank my advisor Dr. Lowell Stott, with whom it has been an honor to work with over the past 5 years. I appreciate all his contributions of time, ideas, and funding which made the studies presented in this dissertation possible. I am thankful for the joy and enthusiasm he showed over the years as I slowly learned to become a scientist, for his support through the hardships of the PhD as well as his advice for the development of my own academic career. I would also like to thank Dr. Julien Emile-Geay for his patience in teaching me the value of a good statistical analysis in paleoceanographic research as well as his personal guidance and support, and Dr. Douglas Hammond for his excellent courses and help in battling the inconsistencies of dating inherent to marine sediment cores. I would also like to thank my outside committee member, Dr. Ronald Henry (Civil and Environmental Engineering), for his support since my undergraduate days at USC and for helpful feedbacks.

I am also thankful to Miguel Rincon, for his patience in teaching me all the analytical techniques and to my various labmates over the years, namely, Dr. Reetta Saikku, who will stay a life-long friend, Dr. Max Berkelhammer, Dr. Nikolaus Buenning, Andres Martinez, Patrick Horan, and Mengfan Zhu.

I would like to acknowledge the contribution of Dr. Reetta Saikku and Dr. Robert Thunell (University of South Carolina), who provided some of the data and samples shown in the various studies. I also gratefully acknowledge the funding sources that made my PhD work possible, and in particular the National Science Foundation and the USC Department of Earth Sciences.

My time at USC was made enjoyable in large part due to the many friends and groups that became part of my life. It has been a pleasure to work (and live) in the Earth Sciences department for 5 years. Specifically, I would like to thank the staff for their help; Cindy Waite, John Yu, John McRaney and Vardui Ter-Simonian.

Finally, I would like to thank my family for all their love and encouragement. I would like to thank my parents who raised me with a passion for scientific knowledge and who supported me in all my pursuits, including the desire to study in the United States.

Table of Contents

List of Tables

List of Figures

Abstract

The work presented in this dissertation focuses on the paleoceanography of the Indonesian Seas over the past 25,000 years; a region that plays a critical role in the global atmospheric and oceanic circulation. The modern oceanography of the Indonesian Seas is very complex due to the combined impact of the East Asian Monsoon, the Australian Monsoon, the migration of the Inter-Tropical Convergence Zone (ITCZ) and the El Niño Southern Oscillation, which is reflected in sea surface temperature (SST) and salinity (SSS) changes in this region on both intra- and interannual timescales.

Therefore, in order to explore the impacts of these various climate systems on the paleoceanography of the Indonesian Seas, unbiased estimates of past SST/SSS are needed. One of the most common technique to infer past changes in SST is the measurement of Mg/Ca in the planktonic foraminifer *Globigeriniodes ruber* (white). When combined with the stable oxygen isotope ($\delta^{18}O$) measurements on the same foraminiferal sample, this technique allows to reconstruct past changes in $\delta^{18}O_{sw}$, which varies linearly with SSS. This method assumes that the primary control on foraminiferal Mg/Ca is temperature, although several studies have shown that salinity can play an important role in the assimilation of Mg into biogenic calcite. Here I use foraminiferal Mg/Ca measurements from 165 core-top and sediment trap data with a global geographic distribution to show (1) that the

Mg/Ca sensitivity to temperature is less than previously estimated (6%/°C vs 9%/°C) and (2) that although the effect of salinity on foraminiferal Mg/Ca is small between 32psu and 37psu (6%/psu), it needs to be taken into consideration to derive unbiased sea surface temperature and salinity estimates, especially on glacial/interglacial timescale. I propose a new set of calibration equations for estimating sea surface temperature and salinity in the 15-30°C/32-37psu range based on the paired measurements of Mg/Ca and $\delta^{18}O_c$ on the same foraminiferal sample, which apply to the Indonesian Seas on glacial/interglacial timescales.

These equations are then applied to eight published records from this region spanning the past 25,000 years. The unbiased estimates suggest a 4-4.5°C cooling in this region at the Last Glacial Maximum (LGM) as opposed to 2.5-3°C inferred from traditional Mg/Ca calibration equations. This cooling was accompanied by a region-wide local freshening, consistent with a more southerly position of the ITCZ and enhanced transport of ^{18}O-depleted moisture from the Atlantic at the LGM. The record also suggests the presence of a temperature oscillation of ~0.3-0.5°C during the deglaciation, coincident with the Northern Hemisphere Bølling-Allerød/Younger Dryas. This millennial temperature oscillation is accompanied by salinity changes, coincident with a change in the intensity of the summer East Asian Monsoon. SSSs reached a maximum in the early Holocene, supporting the hypothesis of a westward repositioning/expansion

of the Western Pacific Warm Pool. SSSs then decreased over the Holocene, an observation consistent with a southerly displacement of the ITCZ. The flooding of the Sunda Shelf and the re-establishment of the “freshwater plug” in the southern Makassar Strait at 9.5ky B.P. is apparent in the SSS record, although there is no definite evidence for associated changes in heat transport from the Pacific to the Indian Ocean from the SST records.

The Holocene has experienced several episodes of warming, culminating to the present warming trend. The last climate oscillation is the so-called Medieval Climate Anomaly/Little Ice Age (MCA/LIA). In order to investigate the hydrographic variability associated with the East Asian Monsoon, the relative mean position of the ITCZ and ENSO over this time interval, five high-resolution SST/SSS records from different locations within the Indonesian Seas are compared. The results suggest that hydrographic variability in this region was strongly associated with the MCA/LIA climate oscillation. Taken together, the records indicate a ~0.5-1°C temperature change between the MCA and LIA. One of the records also indicates that, on average, the MCA was cooler than the 20th century, although several decades during the MCA show a warming comparable to that of the 20th century. The results also indicate a strengthening (weakening) of the East Asian Monsoon over the MCA (LIA), coincident with a northward (southward) migration of the ITCZ. However, the results do not indicate a

preponderant role for ENSO in controlling the surface hydrographic variability found in this region over the past 2,000 years.

In order to investigate the behavior of ENSO over the MCA/LIA, I used the stable isotope values of individual specimens of the thermocline-dwelling planktonic foraminifer *Pulleniatina obliquiloculata* from a sediment core collected from the Northern Makassar Strait. At this location, the $\delta^{18}O_c$ produced by this foraminifer reflect the temperature and salinity variability that accompanies both eastern as well as central Pacific types of ENSO. Changes in ENSO strength/ frequency were estimated by comparing the spread and symmetry of $\delta^{18}O_{calcite}$ values extracted from discrete time horizons in this sediment core. The spread of individual $\delta^{18}O_{calcite}$ values is interpreted to be a measure of the strength of both phases of ENSO while the symmetry of the $\delta^{18}O_{calcite}$ distributions is used to evaluate the relative strength/frequency of El Niño and La Niña events. In contrast to previous studies, robust and resistant statistics were used to quantify the spread and symmetry of the $\delta^{18}O_{calcite}$ distributions; an approach motivated by the relatively small sample size and the presence of outliers. The results indicate that ENSO has remained remarkably constant over the past millennium, with no systematic difference between the relatively warm conditions of the MCA and the cool conditions of the LIA. However, the MCA was characterized by stronger/more frequent La Niña than El Niño; an observation consistent with the medieval megadroughts documented from sites in western North America.

Chapter 1:

Introduction

1.1. Why study paleoceanography?

Over the past 150 years, temperatures in the lower atmosphere have risen by ~0.6°C (Manning et al., 2007). Most of this change in temperature has been attributed to the rise of anthropogenic CO_2 (Crowley, 2000). However, in order to put this temperature rise in the proper context, long records of past temperature variability are needed. Specifically, high-resolution temperature records spanning periods of rapid atmospheric CO_2 rise such as the last deglaciation as well as period of stable atmospheric CO_2 concentration such as the last 2000 years (a period referred to as the Common Era) should provide a basis to assess the role of natural climate variability in the current warming trend.

The ocean covers about 70% of the Earth's surface and plays a dominant role in controlling our climate on a variety of timescales. For instance, the ocean helps moderate diurnal as well as seasonal temperature swings. The high heat capacity of the ocean is also partly responsible for the development of the monsoon systems, which provides the much needed water for agriculture in some regions of the world. The Asian monsoon alone affects more than half of humanity worldwide. Failure of the Asian Monsoon and the consequent droughts (Cook et al., 2010) that occurred in the late 1630's and early 1640's contributed to the fall of the Chinese Ming Dynasty (Shen et al., 2007). The overturning of surface waters in the North Atlantic to produce North Atlantic Deep Water (NADW) helps regulate the climate of Europe. In the absence of NADW production, temperatures in the North Atlantic drops sharply (Broecker, 1997; Broecker, 1998; Broecker and Hemming, 2001; Denton et al., 2010; Ganopolski and Rahmstorf, 2001). In the tropics, the El Niño Southern Oscillation (ENSO) is the dominant role of interannual climate variability, and has the potential of affecting climate worldwide. In the United States alone, the floods, droughts and other disturbances caused by the 1997-98 El Niño cost an estimated $25billion (Chagnon, 2000). Finally, the ocean represents the largest reservoir of carbon in the short-term carbon cycle, having the potential to sequester/release several gigatons of carbon away from/to the atmosphere on millennial timescales. Considering the fundamental role of the oceans in the Earth's climate system, quantifying past oceanographic changes (paleoceanography) is an important step toward understanding past climate changes, and specifically the role of CO_2 in these changes.

1.2. Why the Indonesian Seas?

The tropics represent ~50% of the Earth's surface and receive most of the Sun's energy. This energy is then released as latent heat that drives the global atmospheric circulation (Peixoto and Oort, 1992). Therefore, any discussion about climate variability should include an assessment of tropical variability, including the Indo-Pacific Warm Pool. The Indonesian Seas, located at the edge of the western Pacific warm pool, represent the warmest reservoir of surface waters on Earth and, as such, act as a source of convective energy for the global atmospheric circulation (Qu et al., 2005). The Indonesian Maritime Continent is also located at the confluence of two major climatic systems: the East Asian Monsoon and ENSO, which influence the modern-day oceanography. The Indonesian Seaway also represents the only low-latitude conduit for inter-basin exchange of surface waters, and, as such, plays a vital role in the global thermohaline circulation (Bray et al., 1996; Gordon, 1986). The transfer of tropical waters from the Pacific Ocean into the Indian Ocean through the so-called Indonesian Throughflow (ITF), amid a narrow labyrinth of deep and shallow seas, is of primary importance for the freshwater and heat budget of these oceans (Gordon, 2005). A growing interest in the paleoceanography of this region over the past two decades have increased our understanding of the dynamics of this region over timescales ranging from the past few centuries to several million years ago. However, important questions still remain unanswered:

1. *How have topographic changes affected the ITF?* And how crucial were these changes to the heat budget of the Pacific and Indian Ocean?

2. What is the hydrographic variability associated with the East Asian Monsoon and ENSO?

3. *What was the behavior of ENSO in the past?*

1.3. Why the past 25,000 years?

The last 25,000 years of Earth's history are marked by both one of the most dramatic and abrupt climate shift, the last deglaciation (~20-10ka) as well as one of the most stable period, the Holocene. Therefore, quantifying the behavior of the tropics, and in particular the Indo-Pacific warm pool over the past 25,000 years provide the best benchmark we have to assess natural tropical variability.

How the Earth has emerged from fully glacial conditions at ~100ky intervals over the past 0.5 million years is still a paleoclimatology enigma. By the 1980's, proxy data gathered by the CLIMAP group provided compelling evidence that the glacial cycles were paced by changes in Northern Hemisphere summer insolation (CLIMAP Project Members, 1976). The question then became: how can small changes in insolation produce the most profound climate swings of the Quaternary? The answer lies in amplifying feedbacks within the climate system, with changes in the strength of the Atlantic Meridional Circulation (AMOC) and atmospheric CO_2 as primary candidates. However, this AMOC-centric view of climate change fails to account for tropical dynamics and its potential role in abrupt climate change through ENSO-like teleconnections as first pointed out by

Cane (1998). In contrast to the major reorganization that took place during the last deglaciation, the Holocene has long been regarded as a period in Earth's history characterized by a relatively stable climate. This view has been challenged by the recognition that the past 10,000 years of our planet's history was marked by abrupt climate events, albeit of smaller amplitudes than their glacial counterparts. Examples of such events include the 8.2kyr event, and more recently the Medieval Climate Anomaly/Little Ice Age of the past 1,000 years. Therefore, quantifying oceanographic changes that took place within the Indonesian Seas during these periods of radically different background climate conditions should provide a basis to (1) quantify the role of natural climate variability in the current warming trend and (2) assess, through the help of climate models, the role of the tropical Pacific in abrupt climate change. Specifically, studying the paleoceanography of the Indonesian Seas over the past 25,000 years should help answer the following questions:

4. *What is the range of sea surface temperature variability that can be expected in the Indonesian Seas?* And how does the rate of modern sea surface temperature rise compare to that of the last deglaciation and of the past 2,000 years?

5. Were changes in the Indonesian Seas generally coincident with North Atlantic climate change?

1.4. Outline

Chapter 1 focuses on the modern oceanography of the ~10% of the equatorial circumference associated with the Indonesian Seas. I will discuss the role of the East Asian and Australian Monsoon in shaping the observed seasonal cycle in combination with the migration of the Inter-Tropical Convergence Zone (ITCZ) as well as the role of the ITF in the heat and freshwater budget of the Pacific and Indian Ocean.

Chapter 2 focuses on the development of a temperature/salinity proxy, which can then be applied to marine cores over the timescales of interest. Specifically, I will propose a new calibration for the Mg/Ca of the planktonic foraminifer *Globigerinoides ruber* that takes into account the influence of salinity on the Mg incorporation into the calcite lattice. In combination with the stable oxygen isotopic composition ($\delta^{18}O_c$) of the same foraminiferal sample, *G. ruber* Mg/Ca can be used to deconvolve changes in sea surface temperature and salinity in the Indo-Pacific Warm Pool over the past 25,000 years.

This new calibration is then applied to eight existing sedimentary records from this region. A full reevaluation of the deglacial and Holocene history of the Indonesian Seas "through the eyes" of these records is provided in Chapter 4. Specifically, I will discuss the sea surface temperature/salinity changes occurring during the last deglaciation and their connection with changes in the strength of the East Asian Monsoon and the mean position of the ITCZ. I will also evaluate the relative timing of these changes with those occurring in the North Atlantic. Finally, the last 25,000 years offer a unique opportunity to study how topographic changes affected the ITF strength and the heat and freshwater fluxes from the Pacific to the Indian Ocean.

Chapter 4 and 5 deal with hydrographic variability in the Indo-Pacific warm pool over the past 2,000 years. Specifically, Chapter 4 focuses on the heterogeneity among the various SST and SSS records and how these differences can be used to distinguish among the various factors that affect hydrographic variability in this region; namely, ENSO, the East Asian monsoon, and the mean position of the Inter-Tropical Convergence Zone. Chapter 5 attempts to assess past changes in ENSO variability through the statistical treatment of $\delta^{18}O_c$ distributions obtained from the measurements of hundreds of individual specimens of the thermocline-dweller *Pulleniatina obliquiloculata*, a technique which can prove valuable to extract additional paleoceanographic information from planktonic foraminifera.

Chapter 2:

Regional Oceanography

2.1. The El Niño Southern Oscillation

The term El Niño (Spanish for the "Christ Child") was originally coined by fishermen off the coast of South America to describe the appearance of unusually warm water in the Pacific Ocean in association with less abundant fisheries and heavy rain (Babkina, 2003). The name was used for the tendency of the phenomenon to arrive around Christmas. This term is now used to describe the anomalous patterns of sea surface temperatures (SST) that develop every 2-7 years across the tropical Pacific Ocean.

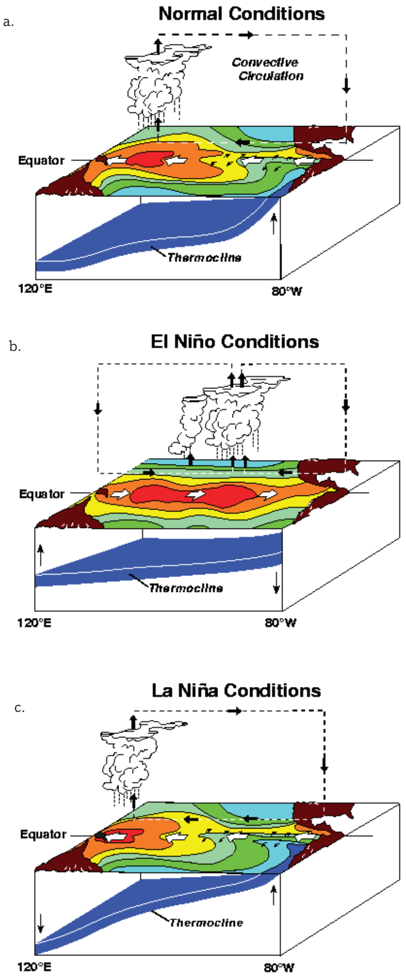

Figure 2-1: *Schematic of the El Niño Southern Oscillation. Sea surface temperature, thermocline depth and atmospheric circulation in the equatorial Pacific Ocean associated with* ***a.*** *normal conditions,* ***b.*** *El Niño,* ***c.*** *La Niña (NOAA)*

The El Niño Southern Oscillation (ENSO) is an interannual mode of climate variability associated with a disturbance of the Walker circulation over the tropical Pacific Ocean (Rasmusson and Carpenter, 1982, Figure 2-1). Over the late 20th century, observations from the tropical

Pacific have shown that at 2-7 year intervals, the easterly trade winds relax, and this allows the pool of warm western Pacific surface waters to migrate towards the central and eastern tropical Pacific. As these warm surface waters shift eastward during an El Niño, so does the zone of strong atmospheric convection. The SST anomalies associated with El Niño disrupt atmospheric circulation within the Walker cell and in doing so, influence weather systems globally (Figure 2-2). As wind stress decreases over the eastern tropical Pacific during an El Niño, the strength of upwelling also decreases and hence, the thermocline deepens across the central and eastern Pacific. In the western Pacific, the subsurface response is just the opposite; the thermocline shoals during an El Niño. In contrast to El Niño, La Niña conditions are characterized by intensified trade winds, leading to unusually warm surface conditions, and a deepening of the thermocline (Figure 2-1). The atmosphere

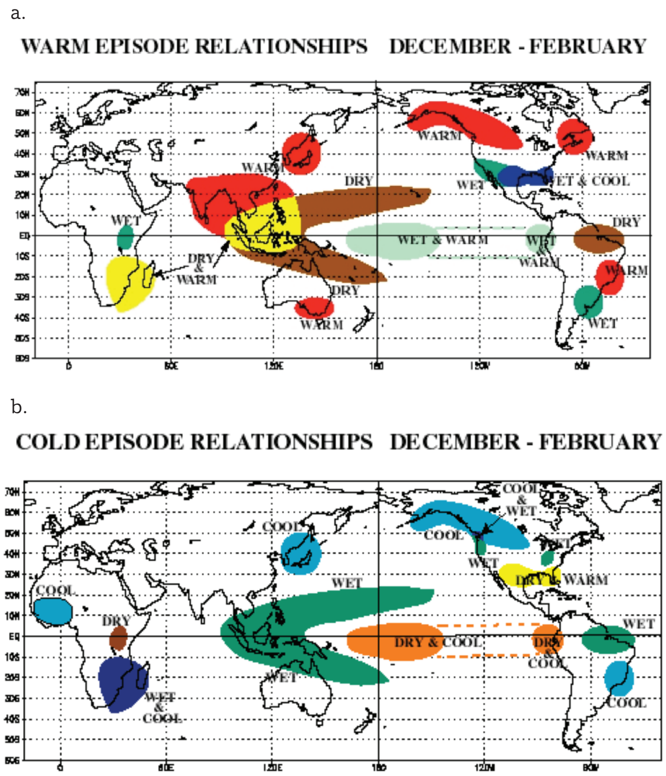

__Figure 2-2:__ Teleconnections associated with __a.__ El Niño and __b.__ La Niña (NOAA)

responds to these oceanic conditions with a seesaw pattern in sea level pressure anomalies between Tahiti and Darwin (Australia), which is referred to as the Southern Oscillation. During an El Niño, unusually high atmospheric sea level pressures develop over the Indo-Pacific Warm Pool, and unusually low sea level pressures develop in the southeastern tropical Pacific. Thus, the coupled ocean-atmosphere process has been termed the El Niño Southern Oscillation (ENSO).

2.1.1. Mechanisms for ENSO

The theoretical explanations for ENSO can be grouped into two frameworks. Classic theories consider ENSO to be a self-sustaining oscillation between two favored states, chaotic in nature, yet deterministic, and its prediction is limited by initial errors (Chen and Cane, 2008). On the other hand, some studies emphasize the role of atmospheric "noise", such as the westerly wind bursts in the western Equatorial Pacific, in triggering an ENSO event. In this view, ENSO is a damped oscillation sustained by stochastic forcing (Chen and Cane, 2008; Guilyardi et al., 2009). However, this theory does not satisfactorily explain the apparent 2-7 year timescale, suggesting that this noise may act more as an enhancer than a trigger for ENSO events (Chen and Cane, 2008). Fedorov et al. (2003) proposed an alternative explanation that attempts to reconcile these two theories. They describe ENSO as a slightly damped periodic oscillation modulated by random noise, in which the timescale of ENSO is controlled by the dynamics of ocean-atmosphere interaction, while the noise sustains the oscillation and makes it irregular. Other studies suggest that the system may alternate between multidecadal periods of more damped vs more freely oscillating dynamics (Guilyardi et al., 2009). In addition, ENSO interacts on different timescales with various climate phenomena, such as the seasonal cycle and decadal oscillations (Fedorov and Philander, 2000; Guilyardi et al., 2009).

According to theoretical studies, ENSO results from the complex interaction of a number of feedbacks either amplifying or dampening the interannual anomalies. ENSO involves the positive ocean-atmosphere feedback described by Bjerknes (1969). Colder temperatures in the east drive stronger easterlies which in turn drive greater upwelling, pull the thermocline up more strongly, and transport cold waters faster, making the temperature even colder. The same feedback applies during an El Niño, reinforcing the warm temperature anomalies in the eastern equatorial Pacific. Although Bjerknes' feedback explains why the system has two favored states, it does not provide an explanation of why it oscillates between them (Cane, 2005). After the onset of an ENSO event, 4 negative feedback loops may act to terminate the growth of positive/negative anomalies in the eastern equatorial Pacific: wave reflection at the ocean western boundary (Battisti and Hirst, 1989; Suarez and Schopf, 1988), a discharge process resulting from Sverdrup transport (Jin, 1997), a western Pacific wind-forced

Kelvin wave of opposite sign (Weisberg and Wang, 1997), and anomalous zonal advection (Picaut et al., 1997). These negative feedbacks may work in various combinations to terminate an ENSO event (Guilyardi et al., 2009).

2.1.2. Is El Niño changing?: Central Pacific ENSO

Two flavors of “El Niño” (Trenberth and Stepaniak, 2001) have been identified, based on the location of the maximum positive SST anomalies (Figure 2-3). Although there are differences among studies that attempt to characterize these different modes of ENSO (Ashok et al., 2007; Kug et al., 2009; Kumar et al., 2006; Larkin and Harrison, 2005a, b; Trenberth and Stepaniak, 2001), the cold tongue El Niño (thereafter, EP El Niño), similar to the canonical El Niño described by Rasmusson and Carpenter (1982), exhibits a maximum sea surface warming in the eastern Pacific (Niño region 1+2 and Niño region 3). In contrast, some events show positive SST anomalies mostly confined to the Niño 4 region. These El Niños have been referred to as “dateline El Niño” (Larkin and Harrison, 2005a, b), “central Pacific (CP) El Niño” (Kao and Yu, 2009), “warm pool El Niño” (Kug et al., 2009), or “El Niño Modoki” (Ashok et al., 2007; Ashok and Yamagata, 2009). This central Pacific warming may be accompanied by a weak cold tongue warming (Kug et al., 2009) or cooling (Ashok et al., 2007; Ashok and Yamagata, 2009; Yeh et al., 2009). Both events are characterized by cooler surface waters than normal in the western tropical Pacific. CP El Niño has

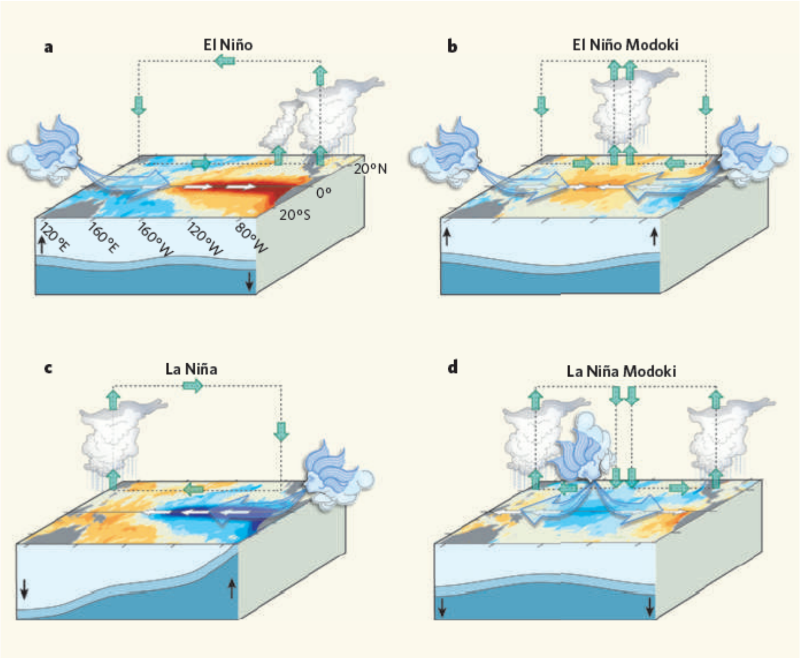

Figure 2-3: *Sea surface temperature, thermocline depth and atmospheric circulation anomalies associated with the EP ENSO (left panels) and the CP ENSO (right panel) (Ashok and Yamagata, 2009).*

occurred more frequently since 1976 in association with a weakening of the easterly trade winds and a flattening of the equatorial thermocline gradient (Ashok et al., 2007; Yeh et al., 2009), although a recent modeling study suggests that the recent increase in the occurrence of CP ENSO could be part of natural variability in the tropical climate system (Yeh et al., in press). Conversely, CP La Niña is characterized by large negative anomalies in the central equatorial Pacific flanked on both sides by positive SST anomalies (Ashok and Yamagata, 2009). Furthermore, the EP type of ENSO tends to produce strong El Niño events, but relatively weak La Niña events. A reverse tendency has been shown for CP ENSO events (Kao and Yu, 2009).

The mechanisms leading to the CP ENSO are not well understood. Recently, Yu et al. (2010) demonstrated that some ENSO events are actually of both types.

For instance, the 1982/83 El Niño was a weak CP event followed by a strong EP event. On the other hand, Ashok et at al. (2007) suggested that CP El Niño is not part of the traditional El Niño evolution and that these two types of ENSO behavior are fundamentally different phenomena, especially after the 1970's. Indeed, the transition mechanism and dynamical subsurface structure of a CP El Niño is inconsistent with the traditional delayed oscillator/discharge concept (Kao and Yu, 2009; Kug et al., 2009). SST variations in the cold tongue are mainly controlled by vertical displacements of the thermocline in response to westerly stress anomalies while changes in SST in the warm pool stem from zonal advection and surface heat flux variations (Chen and Cane, 2008; Kug et al., 2009). However, the CP El Niño also involves ocean-atmosphere coupled processes which include a tripolar sea level pressure pattern, similar to the Southern Oscillation (Ashok et al., 2007; Kug et al., 2010). The CP ENSO is more stochastic in nature than an oscillatory phenomenon, a characteristic associated with the transition mechanism to the CP El Niño. Since the discharge of the CP El Niño is quite weak because of its spatial distribution of ocean dynamic field (Kug et al., 2010), the zonal mean sea level cannot overshoot to a negative sea level anomaly and instead returns to its mean climatological state. Because CP ENSO events primarily occur in the warm phase, its occurrence and existence have the potential to alter the mean state of the tropical Pacific ocean toward warmer conditions (Kug et al., 2009). Furthermore, according to model simulations, warmer mean conditions are favorable to the development of CP ENSO (Kug et al., 2010).

The pattern, amplitude, and even sign of the extratropical atmospheric teleconnections associated with these two types of ENSO are also different (i.e., Ashok et al., 2007; Larkin and Harrison, 2005a). For instance, changes in the extent and location of tropical Pacific warming have been shown to alter the teleconnection with rainfall and temperature anomalies over Asia, North America and Australia (Ashok et al., 2007; Hendon et al., 2009; Larkin and Harrison, 2005a, b; Lim et al., 2009; Wang and Hendon, 2007; Weng et al., 2009), the Indian monsoon (Kumar et al., 2006), and the frequency of tropical cyclones in the North Atlantic (Kim et al., 2009).

2.2. Modern Oceanography of the Indonesian Seas

The Indonesian Seas are a series of basins connected through shallow sills (Figure 2-4), from which a complex and unique oceanography arises (Gordon, 2005; Gordon et al., 2003a; Gordon et al., 2003b). The Indo-Pacific Warm Pool represents the largest reservoir of warm surface waters in the world's ocean, acting as the source of moist static energy for the rising limb of the Hadley and Walker circulation cells (Qu et al., 2005). Therefore, changes in SSTs in this region directly impact global atmospheric circulation, including climate systems

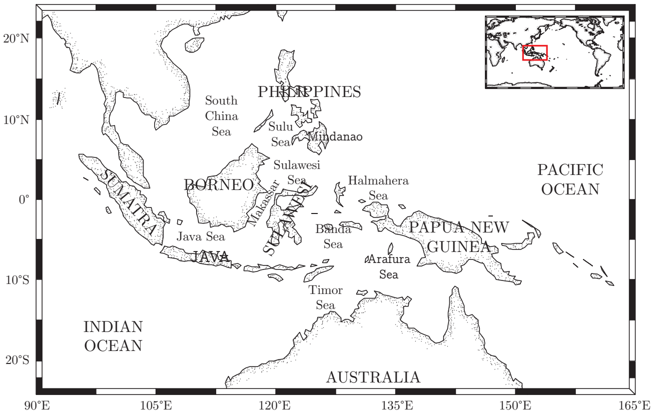

Figure 2-4: *Major islands and seas of the Indonesian Archipelago*

such as the East Asian monsoon (Webster et al., 1998) and ENSO. Indeed, numerical models have shown that tropical dynamics is very sensitive to the SST of the Indonesian Seas (Jochum and Potemra, 2008; McBride et al., 2003; Neale and Slingo, 2003; Qu et al., 2005).

The Indonesian Seaway is also the primary conduit for the exchange of Pacific waters with the Indian Ocean and is therefore a critical component of the global thermohaline circulation system (Bray et al., 1996; Gordon, 1986). The transport of upper ocean waters from the North Pacific through the Indonesian Seas to the Indian Ocean, referred to as the Indonesian Throughflow (ITF), occurs primarily within the thermocline (100-200m, (Sprintall et al., 2009; Susanto and Gordon, 2005)), resulting in a net transfer of cool and relatively fresh water from the Pacific to the Indian Ocean.

2.2.1. Surface Hydrography

Mean annual surface temperatures are high, on the order of ~28.5°C (Locarnini et al., 2010, Figure 2-5). Mean annual surface salinities vary between ~32psu in the Java Sea and Southern Makassar Strait to ~34psu in the Timor

Sea, Banda Sea and Sulawesi Sea (Antonov et al., 2010, Figure 2-5). Surface hydrographic variability in the region is strongly controlled by the seasonal reversal of winds that accompanies the monsoon (Kida and Richards, 2009), the position of the Inter-Tropical Convergence Zone (ITCZ), and to a lesser extent ENSO and intense tidal mixing between surface and thermocline waters (Gordon, 2005; Qu et al., 2005). The ITCZ is in its southernmost position from January to

A. Mean Annual

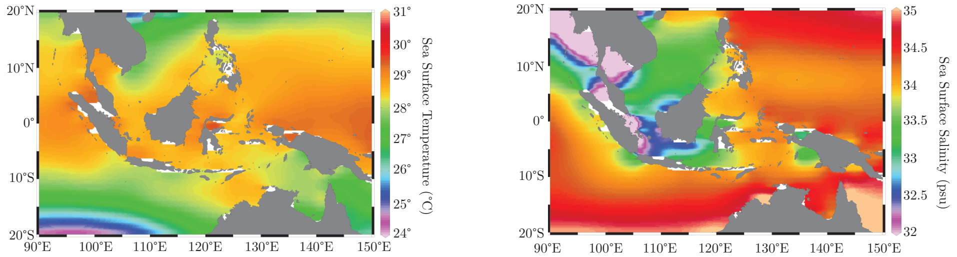

B. Southeastern monsoon (JAS)

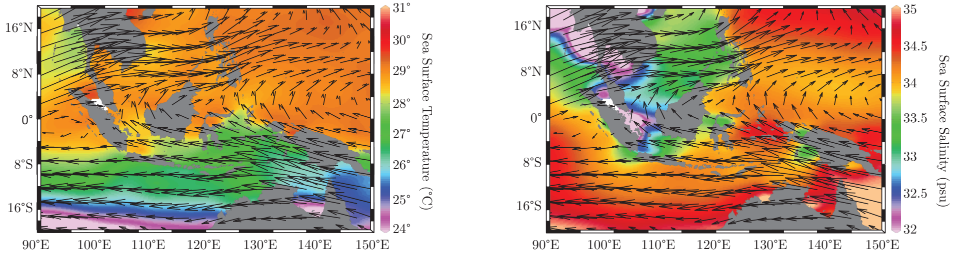

C. Northwestern monsoon (JFM)

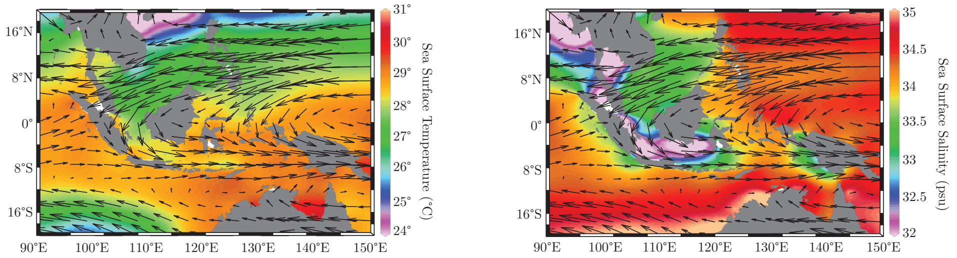

Figure 2-5: *Surface hydrography of the Indonesian Seas. Mean annual, JAS, and JFM sea surface temperature (left panels, Locarnini et al., 2010) and salinity (right panels, Antonov et al., 2010). The wind vectors (NCEP reanalysis) associated with the northwestern monsoon (DJF) and southeastern monsoon (JAS) are superimposed on the temperature/ salinity maps.*

March along the Sunda archipelago and is located over the South China Sea from July to September. The seasonal migration of the ITCZ is echoed in the SSTs, warmer north of the equator during boreal summer (Figure 2-5). However, changes in SSTs accompanying the seasonal migration of the ITCZ are modulated by the seasonal upwelling associated with the monsoon cycle in the region (Gordon, 2005). During the boreal summer southeastern monsoon (JAS), large areas off the southwest coast of Sumatra, the southwestern part of the Makassar Strait, the south coast of Java, the Banda Sea, the Arafura Sea, and the south coast of Bali experience upwelling (Tomascik et al., 1997). This seasonal upwelling is particularly evident in the chlorophyll distribution derived from satellite data (Qu et al., 2005) and in the large increase in primary productivity (Kinkade et al., 1997). It is also evident in foraminiferal fluxes documented in a sediment trap study south of Java (Mohtadi et al., 2009).

Seasonal changes in SSSs are large in the region and reflect changes in precipitation patterns that accompany the migration of the ITCZ and the monsoons, as well as advection of waters from adjacent seas. The largest seasonal changes occur in the Southern Makassar Strait (Figure 2-5) in response to advection of South China Sea water during the boreal winter. During the boreal winter northwestern monsoon (DJF), the winds are directed toward Australia, transporting the low-salinity waters from the South China Sea into the Makassar

Strait through the Java Sea, essentially creating a "plug" for surface waters and increasing transport through the thermocline (Gordon et al., 2008; Gordon et al., 2003b). During the southeastern monsoon (JAS), the winds are directed toward Asia, transferring more saline Banda Sea water into the Makassar Strait and virtually eliminating the salinity gradient between the northern and southern ends of the Makassar Strait (Gordon, 2005; Gordon et al., 2003b, Figure 2-5). This "freshwater plug" controls the amount of heat being transferred from the Pacific to the Indian Ocean via the Makassar Strait. Modeling experiments suggest that in the absence of the transfer of South China Sea water in the Southern Makassar Strait during the winter monsoon, maximum ITF transport occurs at the surface, resulting in an increase in heat transfer of 0.18PW toward the Indian Ocean, corresponding to a transport-weighted temperature increase of ~2°C (Tozuca et al., 2007). Such a situation would have occurred during the last glacial since sea level was 130m lower than present, effectively severing the link between the South China Sea and the Makassar Strait (Hanebuth et al., 2000; Sathiamurthy and Voris, 2006).

The Sulu Sea is a semi-enclosed basin connected to the South China Sea through the Mindoro Passage (420m deep) and to the Sulawesi Sea through the Sibutu Passage (250m deep), which can freely exchange water with the Pacific Ocean, and directly to the western equatorial Pacific through shallower passages in the Philippine Archipelago (110 and 65m, Rosenthal et al., 2003). Mean annual salinities are low (~33 psu, Antonov et al., 2010) and seasonal changes in SSS reflect the interaction between monsoon-driven surface circulation, and net precipitation and riverine input driven by the migration of the ITCZ (Wyrtki, 1961). Precipitation is highest in the northern part of the Sea due to the combined effect of the ITCZ migration and maximum rainfall from the East Asian monsoon (Waliser and Gautier, 1993), which corresponds to the period of lowest salinities (Antonov et al., 2010). However, the seasonal cycle is dampened by the monsoon-driven injection of saltier surface waters from the Sulawesi Sea in JAS (Oppo et al., 2003). On interannual timescales, the temperature and salinity of the Sulu Sea are influenced by ENSO such that during La Niña (El Niño) precipitation increases (decreases) slightly (Oppo et al., 2003).

The Sulawesi Sea exhibits higher mean SSSs since it is directly connected to the western tropical Pacific. The seasonal cycle is similar to that of the Sulu Sea with a minimum in SSS in JAS reflecting the combined effect of the ITCZ and East Asian monsoon rainfall (Antonov et al., 2010, Figure 2-5). Interannual variability associated with ENSO is larger than in the Sulu Sea with increased (decreased) SSSs during El Niño (La Niña).

In the Timor Sea, located at the edge of the Indian Ocean, highest precipitation occurs during the boreal winter northwestern monsoon (Aldrian and

Susanto, 2003) when the ITCZ is at its southernmost position above Australia and correlates with slightly lower salinity in this region (Antonov et al., 2010, Figure 2-5).

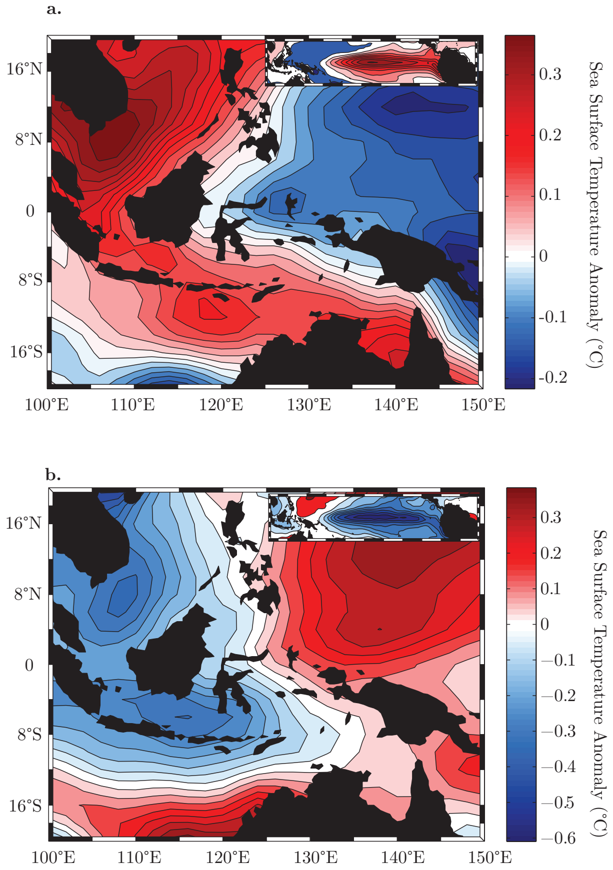

Figure 2-6: *Surface hydrography associated with ENSO variability in the Indonesian Seas.* ***a.*** *El Niño.* ***b.*** *La Niña*

In order to investigate the complex surface expression of the interannual SST variability associated with ENSO, a plot of SST anomaly (compared the 1961-1990 average) for El Niño and La Niña events was constructed from the NOAA extended SST dataset (ERSST_V3, Smith et al., 2007, Figure 2-6). For this composite the moderate to strong El Niño and La Niña events were selected based on the NOAA consensus list of ENSO events (http://ggweather.com/enso/oni.htm). The Halmahera Sea, the northern edge of the Arafura Sea, the Sulawesi Sea and the Northern Makassar Strait warm (cool) during a La Niña (El Niño). This situation reverses in the Southern Makassar Strait, the Java Sea, large areas of the Banda Sea and the Timor Sea. However, Weng et al. (2009) argued that during a CP El Niño, much of the Indonesian Seas will cool, rather than warm; introducing another complexity in the relationship between SST in this region and ENSO.

2.2.2. Subsurface Hydrography: The Indonesian Throughflow

The main characteristic of the oceanography of the Indonesian Seas is the presence of a thermocline-intensified (100-200m) current that links the Pacific and the Indian Ocean, the so-called Indonesian Throughflow (ITF), which plays a critical role in the thermohaline circulation (Bray et al., 1996; Gordon, 1986). The ITF flows primarily as a response to the sea level height difference between the Pacific and Indian Oceans. Further, since the ITF primarily flows within the thermocline, it has a net cooling effect on the Indian Ocean, with a transport-weighted temperature estimated at ~15°C (Gordon, 2005).

Thermocline salinity can be used to identify the major ITF sources and pathways. In the Makassar Strait and the Banda Sea, the ITF is primarily composed of North Pacific Intermediate Water, which flows southward from the Mindanao Current, east of the Philippines (Gordon, 2005, Figure 2-7). However, in the eastern seas, the saltier waters characteristic of the South Pacific Intermediate Water occupy the lower thermocline, spreading from its entrance portal in the Halmahera Sea (Figure 2-7). This water is too dense to make a substantial contribution to the upper thermocline (Gordon, 2005). The distribution of North Pacific and South Pacific Intermediate waters in the eastern seas seem to vary seasonally, with greater amounts of South Pacific water during the northwestern monsoon (Gordon, 2005).

At present, ~80% of the ITF flows through the Makassar Strait (Gordon, 2005). At the southern end of the Makassar Strait, the ITF encounters a sill depth of 680m (Gordon, 2005; Sprintall, 2009). There, a branch of the ITF enters the Indian Ocean directly through the Lombok Strait with a sill depth of ~300m, while the Bulk of the Makassar transport turns eastward toward the Flores Sea and into the Banda Sea where it is mixed with its eastern counterpart (Gordon, 2005; Sprintall, 2009). Eventually, the ITF passes into the Indian Ocean on either side of Timor through many connections, with sill depths varying between 1000 and 1500m (Gordon, 2005).

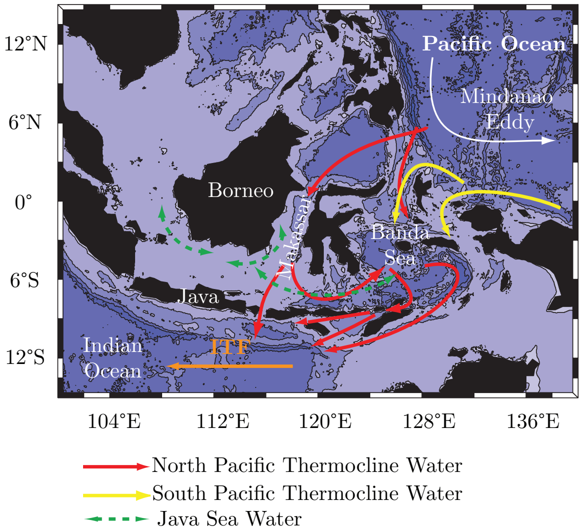

Figure 2-7: Schematic of the ITF and related currents in the Indonesian Seas adapted from Gordon et al. (2005).

Seasonal changes in ITF properties and transport are largely driven by the seasonal changes in monsoonal winds. The seasonal reversal of monsoon winds intensifies thermocline flow within the ITF during both monsoons (Gordon, 2005; Gordon et al., 2008). During the northwestern monsoon, the “freshwater plug” constrains surface flow and, consequently, increases thermocline transport (Gordon, 2005; Gordon et al., 2003b; Susanto and Gordon, 2005). The southeastern monsoon winds constrain southward surface flow out of the Makassar Strait (Figure 2-7), and this too enhances transport within the thermocline from July to September (Gordon, 2005; Gordon et al., 2003b). Transport of waters through the ITF within the thermocline is highest and shallowest (lowest and deepest) during the southeastern (northwestern) monsoon (Gordon et al., 2008).

On interannual timescales, the transport and water mass properties of the ITF vary with ENSO. Since the ITF is primarily driven by the difference in sea level height between the western tropical Pacific and Indian Ocean, its transport varies with the phase of ENSO such that the weakening of the trade winds and the associated displacement of the western Pacific warm pool that occurs during an El Niño reduces the sea level gradient between the two ocean basins, reducing the ITF (Bray et al., 1996; England and Huang, 2005; Fieux et al., 1996; Gordon, 2005; Gordon and Fine, 1996; Gordon and Susanto, 1999; Gordon et al., 1999; Meyers, 1996; Sprintall, 2009). The correlation between ITF transport and ENSO may be as high as 0.73, although the time series is too short to be statistically significant (Gordon et al., 1999). Furthermore, temperature anomalies within the thermocline of the Makassar Strait are highly correlated with the SOI (r=0.77) as evidenced in a 15-yr database of XBT data (Ffield et al., 2000), an observation crucial for the development of an ENSO proxy for this region (Chapter 6).

Chapter 3:

Effect of salinity on *Globigerinoides ruber* (white) Mg/Ca: Implications for paleoceanographic reconstructions

3.1. Summary

The use of Mg/Ca in marine carbonates as a paleothermometer has been challenged recently by observations that indicate there is a salinity influence on Mg incorporation into biogenic calcite. Here I use foraminiferal Mg/Ca measurements from 165 core top and sediment trap data with a global geographic distribution to show that (1) the Mg/Ca sensitivity to temperature is less than previously estimated (6%/°C vs 9%/°C) and (2) that although the effect of salinity on foraminiferal Mg/Ca is small between 33psu and 37psu, it needs to be taken into consideration to derive unbiased sea surface temperature and salinity estimates. I propose a new set of calibration equations for estimating sea surface temperature and salinity in the 15-30°C/33-37psu range based on the paired measurements of Mg/Ca and $\delta^{18}O_c$ in the same foraminiferal sample. I then apply these newly-derived equations to two previously-published marine time series from the Western Tropical Pacific that span the last 25,000 years. The new SST reconstruction suggests that the Last Glacial Maximum (LGM) to interglacial temperature change was ~4°C whereas previous estimates were ~3°C. The revised sea surface salinity estimates also suggest fresher conditions during the LGM

compared to modern; an observation consistent with a more southerly position of the Inter-Tropical Convergence Zone and enhanced moisture transport from the Atlantic to the Pacific.

3.2. Introduction

One of the most common techniques being used to reconstruct sea surface temperatures (SST) is Mg/Ca of foraminiferal shells, which has been shown to co-vary with temperature (i.e., Anand et al., 2003; Dekens et al., 2002; Lea et al., 2000; Nürnberg et al., 1996). When used in conjunction with measurements of the stable oxygen isotope composition ($\delta^{18}O_{calcite}$) from the same foraminiferal sample, it is potentially possible to deconvolve the temperature, local salinity (i.e. local seawater $\delta^{18}O_{sw(l)}$) and, on long timescales, global ice volume influences on the calcite $\delta^{18}O$ (Elderfield and Ganssen, 2000; Lea et al., 2000; Stott et al., 2002). To do so, however, requires the assumption that temperature is the dominant control on Mg incorporation into foraminiferal calcite. Earlier studies recognized that Mg incorporation in foraminiferal shells can be affected by other localized influences such as pressure (Elderfield et al., 1996), carbonate dissolution (Barker et al., 2005; Berger et al., 1982; Brown and Elderfield, 1996; de Villiers, 2003; Dekens et al., 2002; Nouet and Bassinot, 2007; Regenberg et al., 2006; Rosenthal and Lohmann, 2002), carbonate ion concentration (Russell et al., 2004), shell size (Elderfield et al., 2002), and, more recently, salinity (Arbuszewski et al., 2010;

Dueñas-Bohorquez et al., 2009; Ferguson et al., 2008; Kisakürek et al., 2008; Lea et al., 1999; Mathien-Blard and Bassinot, 2009; Nürnberg et al., 1996). In combination, these effects can create a serious bias on reconstructions derived from Mg/Ca alone.

Culturing and core-tops studies have reported an effect of salinity on foraminiferal Mg/Ca, as evidenced by the presence of "excess Mg/Ca" or 'excess temperature" than would be predicted from existing Mg/Ca-temperature relationships (Arbuszewski et al., 2010; Dueñas-Bohorquez et al., 2009; Kisakürek et al., 2008; Lea et al., 1999; Mathien-Blard and Bassinot, 2009). The purpose of the present study is to assess whether a systematic correction for salinity is necessary in the 33-37psu range, which would be applicable to the equatorial Pacific Ocean on glacial/interglacial timescales. I then propose a new calibration for Mg/Ca, which I apply to two previously published sedimentary records from the western tropical Pacific warm pool (Stott et al., 2007) in order to evaluate the impact of the salinity effect on Mg/Ca in paleoceanographic studies.

3.3. Mg/Ca and δ^{18}O systematics in *Globigerinoides ruber*

3.3.1. *Globigeriniodes ruber*

Globigerinoides ruber is a symbiont-bearing planktonic foraminifer commonly found in the surface water of the tropics and subtropics and often used in paleoceanographic studies as a SST proxy. *Globigerinoides ruber* has been shown to tolerate hyposaline conditions and has been recovered from waters having salinities of 30.5 to 31 psu (Bé and Tolderund, 1971). *G. ruber* exhibits two varieties, a pink and a white form. The pink variety occurs usually in the warmer waters of the Atlantic Ocean, whereas the white variety thrives at lower temperatures (Hemleben et al., 1989). The pink variety disappeared from the Indian and Pacific Oceans during the Pleistocene (Thompson et al., 1979).

Two morphotypes of these species have been identified (Wang, 2000): *G ruber* sensu stricto (s.s.) and *G. ruber* sensu lato (s.l.). These two morphotypes exhibit different taxonomic criteria, shell stable isotopic composition of oxygen and carbon, and habitat depths (Wang, 2000). *G. ruber* s.s. (Figure 3-1, 1-4.) refers to specimens with spherical chambers sitting symmetrically over previous sutures, with a wide, high-arched aperture bordered by a rim. On the other hand, *G. ruber* s.l. refers to specimens with more compressed chambers sitting asymmetrically over the previous sutures, with a small round or medium arched opening bordered by a rim and two small to medium size, round supplementary suture apertures situated opposite to sutures of previous chambers (Wang, 2000, Figure 3-1, 5-9.). The differences in stable oxygen and carbon isotope values between *G. ruber* s.l. and *G. ruber* s.s. are -0.21±0.21‰ and -0.28±0.29‰, respectively. Despite large standard errors on the mean values, these differences are significant at the 95% significance level (Wang, 2000). These isotopic

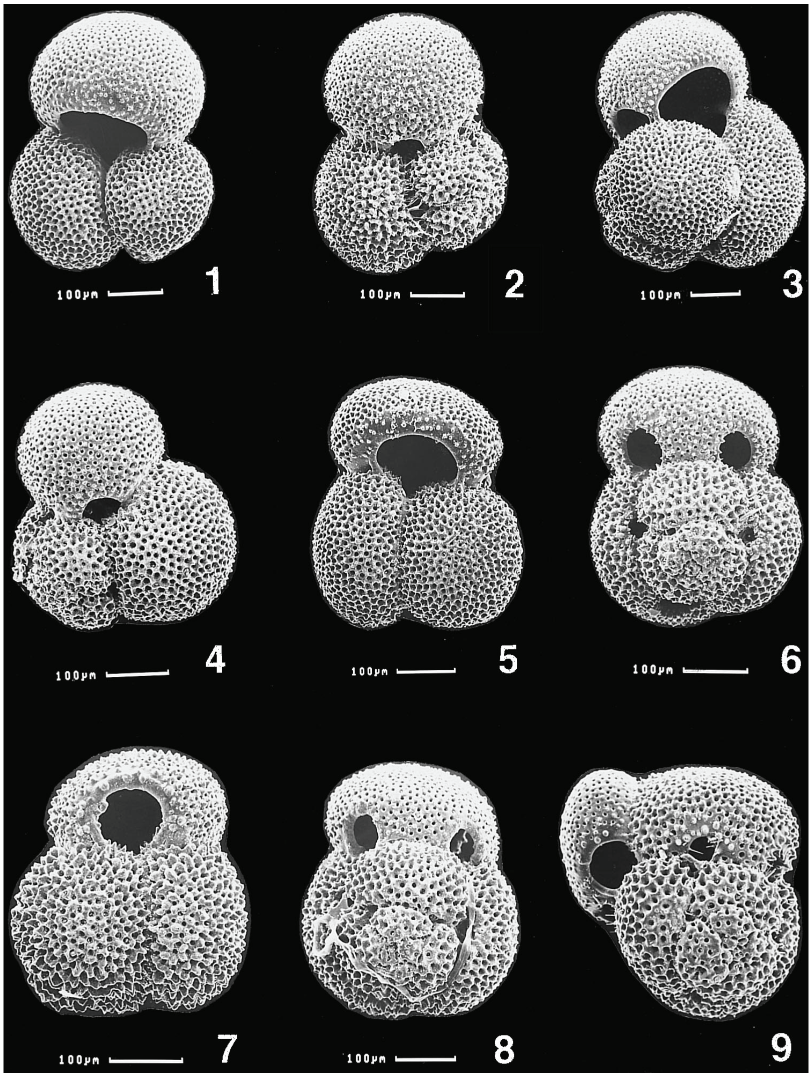

Figure 3-1: *Representatives of the two morphotypes of G. ruber (white) from the surface and downcore sediment samples in the South China Sea. Horizontal bar below each figure indicated the 100um scale (Wang, 2000). 1-4: Globigerinoides ruber s.s., 5-9 Globigerinoides ruber s.l.*

variations are representative of different calcification depths for the two morphotypes, with *G. ruber* s.s. calcifying in the upper 30m of the water column, and *G. ruber* s.l. living at depths of 30-50m (Kawahata, 2005; Wang, 2000). These estimated calcification depths contrast with a recent sediment trap study from South Java (Mohtadi et al., 2009), which show that the $\delta^{18}O$ values of the two morphotypes are virtually identical and consistent with an habitat depth between 0 and 30m.

3.3.2. Systematics of $\delta^{18}O$ in *Globigerinoides ruber*

The fractionation of oxygen isotopes between water and calcium carbonate is temperature sensitive, which prompted H.C. Urey in 1947 to propose that this phenomenon could be used as a paleothermometer. The isotope exchange reaction between calcium carbonate and water takes the form:

$$\frac{1}{3}\mathrm{CaC^{16}O_3+H_2{}^{18}O} \rightleftarrows \frac{1}{3}\mathrm{CaC^{18}O_3+H_2{}^{16}O}$$

The isotope composition of oxygen in a carbonate samples is measured by mass spectrometry using CO_2 gas released when carbonate samples are treated with 100% phosphoric acid in an evacuated vessel at a controlled temperature, typically 90°C (McCrea, 1950). The stable oxygen isotope ratios are usually expressed using the δ-notation referenced to the Vienna Pee Dee Belemnite (VPDB). The δ value of a sample is defined as and is expressed in per mil (‰):

$$\delta^{18}\mathrm{O}=\left(\frac{\left({}^{18}\mathrm{O}/{}^{16}\mathrm{O}\right)_{\mathrm{sample}}}{\left({}^{18}\mathrm{O}/{}^{16}\mathrm{O}\right)_{\mathrm{standard}}}\text{-1}\right)\times 1000$$

The temperature dependence of the fractionation has been determined by several groups of investigators and has been expressed in different forms. The classic temperature equation derived by Epstein et al. (1953) takes the form:

$$T(^\circ C)=16.9-4.2\left(\delta^{18}O_{calcite}-\delta^{18}O_{sw(VSMOW)}\right)+0.13\left(\delta^{18}O_{calcite}-\delta^{18}O_{sw(VSMOW)}\right)^2$$

where $\delta^{18}O_{sw}$ represents the stable oxygen isotopic composition of seawater in which the carbonate precipitated.

However, paleothermometry based on the temperature dependence of the fractionation of oxygen isotopes between marine carbonates and water must satisfy a set of assumptions concerning: (1) the existence of isotopic equilibrium between oxygen in the water and in biogenic calcite or the presence of "vital effects", (2) the preservation of the isotope composition of oxygen in the solid carbonate shell as subsequent dissolution and/or replacement by calcium carbonate that equilibrated at a different temperature with water having a different isotope composition of oxygen may occur, (3) the presence of crystals of diagenetic calcite in foraminiferal shells, whose oxygen isotope composition is different from that of the shell, and (4) the constancy of the isotope composition of water in the oceans (Sharp, 2007).

Violating these assumptions can limit the use of $\delta^{18}O$ of biogenic calcite as a true paleothermometer. Planktonic foraminifera tend to secrete their shells in isotopic equilibrium with seawater. However, divergence from equilibrium, termed "vital effects", has been observed and is related to environmental factors such as sunlight intensity, temperature stress, and nutrient supply (Sharp, 2007). This has led to species-specific calibration equation (i.e., Bemis et al., 1998).

Oxygen isotope ratios of biogenic calcite can be changed by two diagenetic processes: (1) the addition of new carbonate by cementation, and (2) the dissolution of unstable carbonate and the re-precipitation of a stable mineral. Great care is taken to avoid the effects of diagenesis, but there is no foolproof method to prove that no diagenesis has taken place.

The stable oxygen isotopic composition of surface waters is influenced by evaporation, precipitation, advection, mixing and river runoff. These processes also control sea surface salinity, and therefore, there is a strong linear relationship between local salinity and $\delta^{18}O_{sw}$ (i.e., LeGrande and Schmidt, 2006). On longer time scales, the $\delta^{18}O_{sw}$ of the entire ocean is also controlled by ice volume changes that accompany the glacial-interglacial cycles. During glacials, the $\delta^{18}O_{sw}$ increases when isotopically light water is transferred from the ocean to the continental ice sheets. Therefore, an estimation of paleo-salinity and ice volume changes must be made in order to use the $\delta^{18}O_{calcite}$ as a paleothermometer. Conversely, if the temperature at which the biogenic calcite precipitated can be estimated through other means, then the $\delta^{18}O_{calcite}$ can be used to infer past changes in $\delta^{18}O_{sw}$ (i.e. salinity).

3.3.3. Mg/Ca paleothermometry

Early thermodynamics studies showed that the Mg content of inorganically precipitated calcite increased with increasing temperature (Chilingar, 1962;

Mucci, 1987). This reflects the endothermic substitution of Mg ions in the calcite lattice as temperature is increased (Katz, 1973; Lea et al., 1999; Oomori et al., 1987). Studies of Mg/Ca in biogenic calcite from cultures, sediment traps, and core-top samples have also found a temperature dependence of foraminiferal Mg/Ca, but these studies clearly demonstrated additional non-equilibrium processes as reflected in species-dependent Mg/Ca offsets (Elderfield and Ganssen, 2000; Rosenthal et al., 2000). First, foraminifer biomineralization actively discriminates against Mg as reflected in lower distribution coefficient between shell calcite and seawater than would be predicted from thermodynamics of inorganic calcite alone (Bender et al., 1975; Lea et al., 2003; Nürnberg et al., 1996; Oomori et al., 1987; Zeebe and Sanyal, 2002). Furthermore, the exponential temperature dependence for the incorporation of Mg into the foraminifer's shell is much greater (6-10%/°C) than that for inorganic experiments. Finally, several studies have shown that Mg is heterogeneously distributed throughout the shells, with Mg-rich and Mg-poor bands corresponding to a diurnal cycle evident in many species (Bentov and Erez, 2006; Elderfield et al., 1996; Hathorne et al., 2003; Kunioka et al., 2006; Sadekov et al., 2005). This recognition of the role of biology in controlling Mg incorporation into foraminiferal tests led to species-specific calibrations (Anand et al., 2003; Cleroux et al., 2008; Dekens et al., 2002; Delaney et al., 1985; Elderfield and Ganssen, 2000; Lea et al., 1999; Lea et al., 2000; Nürnberg et al., 1996).

Thermodynamic and calibration studies have shown that the empirical regression of Mg/Ca to temperature is exponential of the form: $\mathrm{Mg}/\mathrm{Ca} = \mathrm{B}\exp^{\mathrm{AT}}$, where T is the temperature of calcification in °C and A is the temperature-sensitivity constant, which has been shown to be close to 0.09 for surface-dwelling planktonic foraminifera (Anand et al., 2003; Dekens et al., 2002; Lea et al., 2000).

However, other factors can influence foraminiferal Mg/Ca. Carbonate dissolution is a well-documented influence on the Mg/Ca of biogenic calcite. Dissolution within the water column, at the sediment-water interface, and also within the sediments can occur when the *in situ* carbonate ion concentration ($[CO_3^{2-}]_{act}$) is lower than the saturation concentration ($[CO_3^{2-}]_{sat}$) (Berger et al., 1982) and this will result in a preferential removal of Mg-rich calcite that could result in a cold temperature bias (Barker et al., 2005; Brown and Elderfield, 1996; de Villiers, 2003; Dekens et al., 2002; Nouet and Bassinot, 2007; Regenberg et al., 2006). Several correction procedures for deep-sea sediment cores have been proposed (Dekens et al., 2002; Rosenthal and Lohmann, 2002). The carbonate ion concentration appears to play a minor role in the assimilation of Mg into foraminiferal calcite (Russell et al., 2004), although this role disappears at carbonate concentrations greater than 200µmol/kg (Russell et al., 2004) and is smaller than the influence of salinity on Mg incorporation (Dueñas-Bohorquez et al., 2009).

Culturing and core-top studies have reported an effect of salinity on foraminiferal Mg/Ca (Arbuszewski et al., 2010; Dueñas-Bohorquez et al., 2009; Kisakürek et al., 2008; Lea et al., 1999; Mathien-Blard and Bassinot, 2009). For the species *Globigerinoides sacculifer*, this effect translates into a temperature bias of 1°C for a change of 4psu (Dueñas-Bohorquez et al., 2009). Further, the salinity influence on Mg incorporation is species-dependent and is reportedly as much as 5%/psu for the planktonic foraminifer *G. ruber* (Kisakürek et al., 2008). Although this change is relatively small compared to the temperature effect on Mg incorporation, it can be significant on glacial-interglacial timescales when changes in salinity are expected to be large, or in regions with large salinity gradients. Further, a recent study based on core top data has shown that this effect may be larger than that reported in culture studies, up to 1.6°C/psu (Mathien-Blard and Bassinot, 2009), emphasizing the need to take salinity into account in paleoceanographic studies.

The mechanism(s) responsible for the salinity effect on foraminiferal Mg/Ca is (are) not well-understood. Arbuszewski et al. (2010) recently hypothesized that the dependence of foraminiferal Mg/Ca on salinity in a reflection of increased metabolic rates at higher salinities, which can promote faster calcification rates and kink defect incidence. Indeed, early culture studies (Hemleben et al., 1987) have shown an increase in the metabolic rate in planktonic foraminifera at higher salinity. From this, Nürnberg et al. (1996) speculated that enhanced Mg uptake should take place as a direct consequence of increased metabolic activity, a conclusion supported by Dueñas-Bohórquez et al. (2009), who hypothesized that this effect could be related to the efficiency of the cellular Mg channels and pumps to keep a low-Mg parent solution. Furthermore, inorganic calcification experiments show that the growth rate of calcite increases as a function of ionic strength (i.e. salinity) (Stephenson et al., 2009). This experiment also suggests that preferential incorporation of Mg into the calcite lattice occurs at higher growth rate due to a greater incidence of kink defect sites where Mg^{2+} can substitute for Ca^{2+} (Stephenson et al., 2009). If true, this implies a kinetic uptake of Mg into foraminiferal shells which may lead to highly nonlinear relationships between sea surface temperature, salinity, and Mg/Ca in foraminiferal shells.

3.4. Materials and Methods

3.4.1. Analytical Techniques

In order to investigate the effect of salinity on *Globigerinoides ruber* (white) Mg/Ca, the core-top dataset (25 core tops from 24 locations) from Mathien-Blard and Bassinot (2009) was merged with previously-published core-top data from the Indo-Pacific warm pool (Mohtadi et al., in press), sediment trap study data from the North Atlantic (Anand et al., 2003) and the Guaymas Basin (McConnell and Thunell, 2005; Wejnert et al., 2010), and unpublished core-top data from the

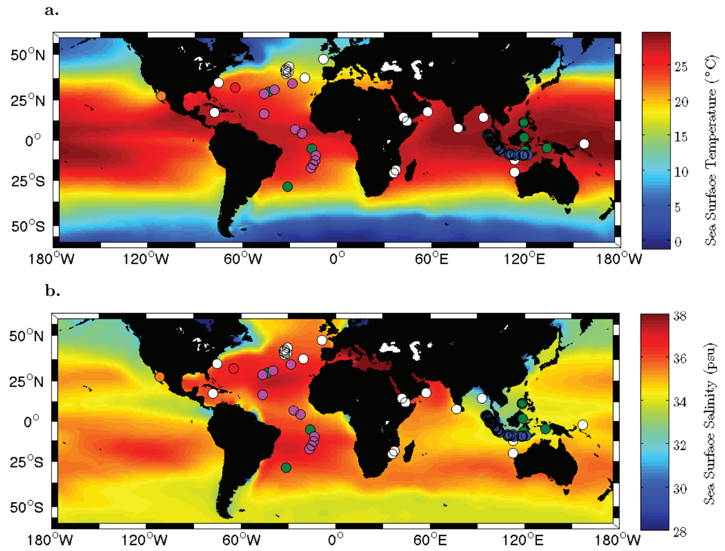

Figure 3-2: *Core tops and sediment trap study location plotted on a map of a. mean annual temperature and b. mean annual salinity from the World Ocean Atlas 09 [Antonov et al., 2010; Locarnini et al., 2010]. White symbols represent the core top database from Mathien-Blard and Bassinot (2009), blue symbols the core top database of Mohtadi et al. (in press), pink symbols the unpublished data from L.D. Stott, and green symbols from this study. The red and orange circle represent the location of the sediment trap study of Anand et al. (2003) and McConnell and Thunell (2005)/Wejnert et al. (2010) respectively.*

Atlantic Ocean (L.D. Stott) as well as additional measurements on 10 core tops from the Indonesian Seas and the subtropical/ tropical Atlantic Ocean (Figure 3-2, Appendix A1). Combining these datasets (n=165) provides a wide SST/SSS rang over which *G. ruber* calcifies. Late Holocene age control on the core top samples was confirmed by either radiometric dating, foraminiferal counts (i.e. % of *Globorotalia hirsute* left coiling in the North Atlantic) or isotope stratigraphy.

For the present study, the core top bulk sediment samples were disaggregated in a sodium hexametaphosphate solution and wet-sieved through a 63µm mesh to remove the clay fraction. This >63µm fraction was then dry-sieved for the 250-350µm fraction in order to minimize possible size effects on the incorporation of Mg in the calcite lattice (Elderfield et al., 2002), although this effect was not confirmed in another study (Ni et al., 2007). Approximately 150-200 specimens of *G. ruber* from each sample were picked under a binocular microscope. The foraminifera were gently cracked open between two glass plates in order to expose the chambers for cleaning. The foraminifera were then cleaned according to the Barker et al. (2003) protocol, which consists of a series of water and methanol rinses designed to remove clays and other impurities, an oxidative step to remove organic matter, and a weak acid leach designed to remove adsorbed contaminants (Appendix A2). This cleaning protocol was also employed in the previous studies used to create the combined dataset.

An interlaboratory study has found that different cleaning protocols can lead to differences in the the absolute foraminiferal Mg/Ca (Rosenthal et al., 2004). The cleaning techniques commonly employed for Mg/Ca analysis fall into two broad categories: the "Mg cleaning" protocol and the "Cd cleaning" protocol. The "Mg cleaning" protocol is a short version of the Boyle and Keigwin (1985) method and consists of a series of water and methanol rinses designed to remove clays and other impurities, an oxidative step designed to remove organic matter and a weak acid leach designed to remove any adsorbed contaminants (Barker et al., 2003, Appendix A2). On the other hand, in the "Cd cleaning" method (Boyle and Keigwin, 1985), additional weak acid leaches, as well as a reductive step designed to remove any Mn-, and Fe-oxides adhering to the shells are performed. This cleaning protocol is designed for other trace elements analysis (i.e. Cd/Ca, Ba/Ca, and U/Ca) performed in addition to Mg/Ca, typically in laboratories equipped with an ICP-MS. Laboratory experiments have shown that shells cleaned using the “Cd cleaning” method tend to have Mg/Ca 6-15% lower than those cleaned using the short “Mg cleaning” protocol (Arbuszewski et al., 2010; Barker et al., 2003; Xu et al., 2010). Since the Barker et al. (2003) procedure was employed for the Mg/Ca measurements presented in this study, it is very unlikely that differences in the absolute foraminiferal Mg/Ca are entirely due to the cleaning protocol alone.

The samples were then split in two aliquots for stable isotope and trace element analyses. The $\delta^{18}O_c$ values were measured using a Multiprep Dual Inlet system attached to an Isoprime stable isotope ratio mass spectrometer. Each sequential run on the Multiprep included 30-50 foraminiferal samples together with 10-15 calcite standards (USC Ultissima marble) used to monitor analytical precision. The long-term precision of the Ultissima standard $\delta^{18}O$ values measured during this study was 0.09‰. Replicate analyses performed on the foraminiferal samples yield an overall precision of 0.14‰. For Mg/Ca analysis, the foraminiferal samples were dissolved in 500μL of 5% nitric acid solution and analyzed on a Jobin Yvon ICP AES. Each sample measurement was bracketed by a standard solution made from solid Mg and reagent grade $CaCO_3$ in an elemental ratio of 5.63mmol/mol, used to adjust the foraminiferal sample Mg/Ca for instrument drift. The average precision on foraminiferal samples replicates is 0.23mmol/mol. Fe/Ca and Mn/Ca ratios were used to monitor potential contamination. A summary of the trace element and isotope analysis for each core top is given in Appendix A3.

3.4.2. Hydrographic conditions

Mean annual, summer and winter temperature and salinity data at each core top locations were extracted from the World Ocean Atlas 09 (Antonov et al., 2010; Locarnini et al., 2010) and averaged over the 0-50m depth horizon, a calcification range that applies to *G. ruber* (Mohtadi et al., 2009; Wang, 2000). Similarly, mean annual $\delta^{18}O_{sw}$ values over this calcification range was extracted from the Legrande and Schmidt (2006) gridded dataset.

Carbonate dissolution is a well-documented influence on the Mg/Ca of biogenic calcite. Dissolution within the water column, at the sediment-water interface, and also within the sediments can occur when the *in situ* carbonate ion concentration ($[CO_3^{2-}]_{act}$) is lower than the saturation concentration ($[CO_3^{2-}]_{sat}$) (Berger et al., 1982) and this will result in a preferential removal of Mg-rich calcite that could result in a cold temperature bias (Barker et al., 2005; Brown and Elderfield, 1996; de Villiers, 2003; Dekens et al., 2002; Nouet and Bassinot, 2007; Regenberg et al., 2006). I estimated, at each site, the departure from calcite saturation: $\Delta CO_3^{2-}=[CO_3^{2-}]_{obs}-[CO_3^{2-}]_{sat}$ based on the gridded alkalinity and total DIC data from the GLODAP database (Key et al., 2004), and temperature, salinity, phosphate and silicate data obtained from the World Ocean Atlas 09 (Antonov et al., 2010; Garcia et al., 2010; Locarnini et al., 2010). This data was used to calculate ΔCO_3^{2-} at each site using the Program Developed for CO_2 Calculations adapted for the MATLAB software (van Hueven et al., 2009). At most locations, the calculated bottom ΔCO_3^{2-} is above 20μmol/kg, and, therefore, dissolution should have a minor influence on the foraminiferal Mg/Ca.

3.5. Results: Calibration equations

3.5.1. *G. ruber* Mg/Ca sensitivity to temperature and salinity

In order to confirm the presence of a salinity effect on *G. ruber* Mg/Ca, I first calculate the "excess Mg/Ca" and "excess temperature" for each datapoint. Here, I define "excess Mg/Ca" as the difference between the measured foraminiferal Mg/Ca and the expected Mg/Ca calculated from the Anand et al. (2003) *G. ruber* specific equation for the 250-350μm size fraction:

$$\text{Excess Mg/Ca}=\text{Mg/Ca}_{\text{measured}}-0.449e^{0.09\text{SST}}$$

And "excess temperature" is defined as:

$$\text{Excess Temperature}=0.09^{-1}\ln\left(\frac{\text{Mg/Ca}}{0.449}\right)-\text{SST}$$

Because SST/SSS data are not available for the duration of the sediment trap studies, I used the oxygen isotope temperature (T_{iso}) as SST. Traditionally, two equations have been used to calculate T_{iso} for *G. ruber:*

$$T_{iso} = 16.9 - 4.31(\delta^{18}O_c - \delta^{18}O_{sw} + 0.27) + 0.1(\delta^{18}O_c - \delta^{18}O_{sw} + 0.27)^2$$ (Shackleton, 1974)

$$T_{iso} = 14.9 - 4.8(\delta^{18}O_c - \delta^{18}O_{sw} + 0.27)$$ (Bemis et al., 1998)

where 0.27‰ represents a correction from VSMOW to VPDB (Bemis et al., 1998). A plot (Figure 3-3) of the isotopic temperatures calculated using the Shackleton (1974) and the Bemis et al. (1998) equation in combination with the $\delta^{18}O_{sw}$ values from the Legrande and Schmidt (2006) gridded dataset versus mean annual temperatures at each of the core location shows that the Shackleton (1974) equation overpredicts SST, an observation especially apparent in the high-temperature regions. Least square linear regressions between mean annual SST and T_{iso} obtained from the Shackleton (1974) and the Bemis et al. (1998) equations both return a slope of 1.0 but an

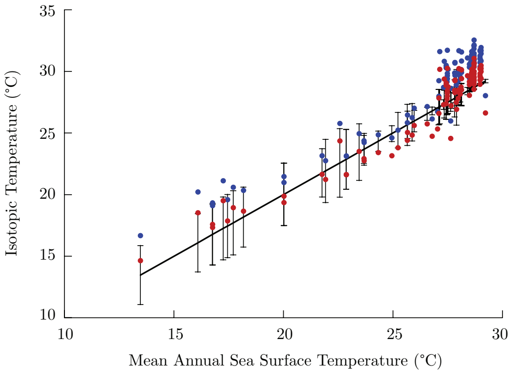

Figure 3-3: *T_{iso} calculated from the Shakleton (1974) oxygen isotope temperature equation (in blue) and the high-light oxygen isotope equation of Bemis et al. (1998) (in red) compared to mean annual sea surface temperature at the core locations extracted from the World Ocean Atlas 09 (Locarnini et al., 2010). The error bars represent the amplitude of the annual cycle.*

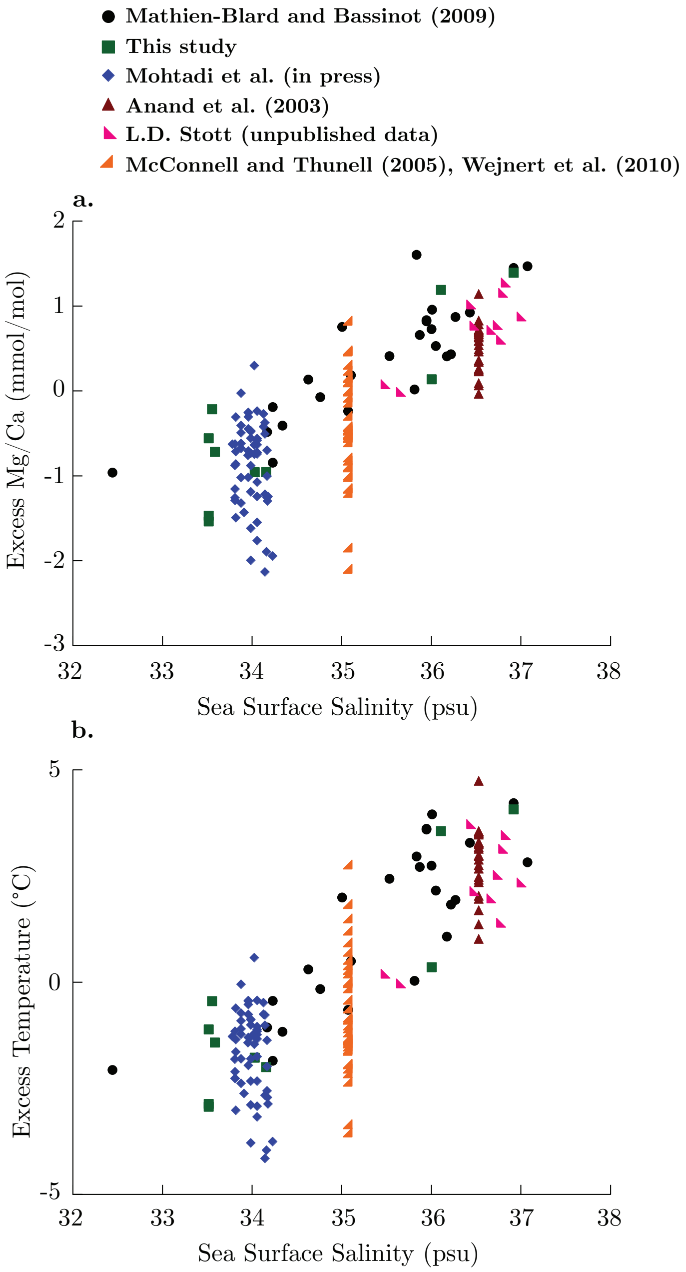

Figure 3-4: ***a.*** *Temperature-independent "excess Mg/Ca" calculated from the calibration dataset. "Excess Mg/Ca" was calculated as the difference between measured and expected Mg/Ca values calculated from* T_{iso} *(using the high-light oxygen isotope temperature equation from Bemis et al. (1998)) and using the Anand et al. (2003) G. ruber specific equation.* ***b.*** *"Excess Temperature" calculated from the calibration dataset as the difference between the temperature values estimated from the measured Mg/Ca using the Anand et al. (2003) G. ruber specific equation and* T_{iso} *(using the high-light oxygen isotope temperature equation from Bemis et al. (1998)).*

intercept of 1.9°C and -0.18°C respectively, confirming the warm bias produced by the Shackleton (1974) equation. Therefore, I will use the isotopic temperature obtained from the Bemis et al. (1998) equation to calculate the "excess Mg/Ca" and "excess temperature" for the dataset (Figure 3-4). For the sediment trap studies of Anand et al. (2003) and Wejnert et al. (2010), T_{iso} was calculated based on the measured $\delta^{18}O_c$ and the mean annual $\delta^{18}O_{sw}$ extracted from the gridded dataset of Legrande and Schmidt (2006). Since at these locations, seasonal changes in SSS are small (~0.2psu as estimated from the World Ocean Atlas 09 (Antonov et al., 2010)), most of the variability in $\delta^{18}O_c$ can be attributed to changes in SST and assuming a constant $\delta^{18}O_{sw}$ should not produce a bias in the T_{iso} estimates.

Mathien-Blard and Bassinot (2009) have argued for a linear relationship between "excess temperature" and SSS while Arbuszewski et al. (2010) argued for a similar relationship between "excess Mg/Ca" and SSS for the salinity range applicable to their Atlantic study. However, these observation yield to different types of equations relating Mg/Ca, SST (as T_{iso}), and SSS. Specifically, a relationship between "excess temperature" and SSS would yield to equations of the type $\mathrm{Mg/Ca} = \exp\left(\alpha \mathrm{SST} + f(\mathrm{SSS}) + \beta\right)$ while a relationship between "excess Mg/Ca" and SSS would give rise to equations of the form $\mathrm{Mg/Ca} = \exp\left(\alpha \mathrm{SST} + \beta\right) + f(\mathrm{SSS})$. In order to define the correct regression model, I used the Root Mean Square Error (RMSE) of each of the following models in combination with a cross-validation using a n-m jacknife and a bootstrap approach:

_ Model 1: $\mathrm{Mg/Ca} = \exp\left(\alpha \mathrm{SST} + \beta\right)$

_ Model 2: $\mathrm{Mg/Ca} = \exp\left(\alpha \mathrm{SST} + \beta \mathrm{SSS} + \gamma\right)$

_ Model 3: $\mathrm{Mg/Ca} = \exp\left(\alpha \mathrm{SST} + \beta \mathrm{SSS} + \gamma \mathrm{SST} \times \mathrm{SSS} + \delta\right)$

_ Model 4: $\text{Mg/Ca} = \exp\left(\alpha\text{SST} + \beta\text{SSS}^2 + \gamma\text{SSS} + \delta\right)$

_ Model 5: $\text{Mg/Ca} = \exp\left(\alpha\text{SST} + \beta\text{SSS}^2 + \gamma\text{SSS} + \delta\text{SST} \times \text{SSS} + \varepsilon\right)$

_ Model 6: $\text{Mg/Ca} = \exp\left(\alpha\text{SST} + \beta\right) + \gamma\text{SSS} + \delta$

_ Model 7: $\text{Mg/Ca} = \exp\left(\alpha\text{SST} + \beta\right) + \gamma\text{SSS} + \delta\text{SST} \times \text{SSS} + \varepsilon$

_ Model 8: $\text{Mg/Ca} = \exp\left(\alpha\text{SST} + \beta\right) + \gamma\text{SSS}^2 + \delta\text{SSS} + \varepsilon$

_ Model 9: $\text{Mg/Ca} = \exp\left(\alpha\text{SST} + \beta\right) + \gamma\text{SSS}^2 + \delta\text{SSS} + \varepsilon\text{SST} \times \text{SSS} + \lambda$

Models 3, 5 ,7, and 9 are used to test for possible interactions between SSS and SST, which would bias the coefficients of the regression. The results are summarized in Table 3-1. Adding a salinity component results in a lower RMSE. However, there is no difference between the models based on a "excess Mg/Ca"/ SSS relationship and those based on a "excess temperature"/SSS. Because models 2-5 (based on "excess temperature") prove easier to handle to develop the calibration equations presented in section 2.5.2., I will test only the performance of these models.

The purpose of cross-validation is to obtain an independent dataset on which to test the accuracy of the model. To this end, a jacknife (removing 10 and 50

Table 3-1: *Coefficients of the multivariate regression between Mg/Ca, SST and SSS and RMSE.*

Model Number	**Model Type**	**RMSE**	**Cross-Validation**		
			n-10	**n-50**	**Bootstrap**
1	$Mg/Ca = \exp\left(\alpha SST + \beta\right)$	0.48	0.48±0.0005	0.48±0.0013	0.48±0.0054
2	$Mg/Ca = \exp\left(\alpha SST + \beta SSS + \gamma\right)$	0.43	0.43±0.0005	0.43±0.0015	0.44±0.0111
3	$Mg/Ca = \exp\left(\alpha SST + \beta SSS + \gamma SST \times SSS + \delta\right)$	0.43	0.43±0.0030	0.43±0.0020	0.44±0.0068
4	$Mg/Ca = \exp\left(\alpha SST + \beta SSS^2 + \gamma SSS + \delta\right)$	0.42	0.42±0.0009	0.42±0.0026	0.42±0.0092
5	$Mg/Ca = \exp\left(\alpha SST + \beta SSS^2 + \gamma SSS + \delta SST \times SSS + \varepsilon\right)$	0.42	0.42±0.0045	0.42±0.0118	0.43±0.0176
6	$Mg/Ca = \exp\big(\alpha SST + \beta) + \gamma SSS + \delta\big)$	0.43	N/A	N/A	N/A
7	$Mg/Ca = \exp\big(\alpha SST + \beta) + \gamma SSS + \delta SST \times SSS + \varepsilon\big)$	0.43	N/A	N/A	N/A
8	$Mg/Ca = \exp\big(\alpha SST + \beta) + \gamma SSS^2 + \delta SSS + \varepsilon\big)$	0.42	N/A	N/A	N/A
9	$Mg/Ca = \exp\big(\alpha SST + \beta) + \gamma SSS^2 + \delta SSS + \varepsilon SST \times SSS + \lambda\big)$	0.42	N/A	N/A	N/A

datapoints, respectively) and bootstrap approach were used to create subsets of the developmental database. All 5 models were then fitted to the subsets and the coefficients of the robust nonlinear regression performed on these subsets used to predict Mg/Ca on the entire dataset. One thousand Monte-Carlo trials were performed for each of the cross-validation technique and the RMSE was calculated for each trial. The mean RMSE±2σ confidence interval is presented in Table 3-1. From this experiment, I conclude that there is no interaction between SSS and SST in the dataset that could bias the coefficients of the nonlinear regression. Furthermore, since fitting a second-order polynomial (with respect to SSS) to the data does not improve the model's prediction, I choose the following model to describe Mg/Ca as a function of SST/SSS (n=165, 95% confidence interval given in parenthesis in terms of %error):

$$\mathrm{Mg/Ca} = \exp\left(0.064\left(\pm 9\%\right)\mathrm{SST} + 0.059\left(\pm 32\%\right)\mathrm{SSS} - 2.188\left(\pm 37\%\right)\right) \quad (1)$$

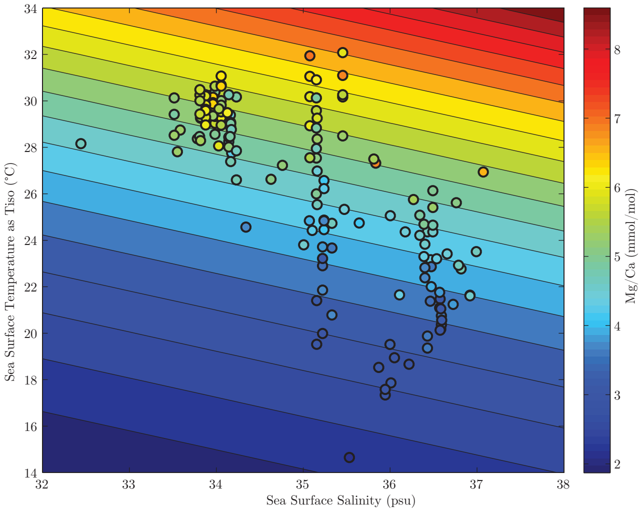

Figure 3-5: *The color field shows the estimated Mg/Ca based on the equation Mg/Ca=exp(0.064SST+0.059SSS-2.188) for the T-S range applicable to this study. The color fill on the inner circle represents the measured Mg/Ca.*

The difference in the error associated with the SST and SSS terms is attributed to the difference in dynamic range between the two variables. The range of SST applicable to this study is ~15°C while the range of SSS covered by my dataset is only ~4psu. The multivariate fit based on mean annual SSS and T_{iso} to the Mg/Ca dataset is presented on Figure 3-5. This equation is statistically indistinguishable from that of Sadekov et al. (2009) and Kisakürek et al. (2008):

$$\mathrm{Mg/Ca} = \exp\left(0.075\left(\pm 8\%\right)\mathrm{SST} + 0.057\left(\pm 21\%\right) - 2.56\left(\pm 18\%\right)\right)$$

$$\mathrm{Mg/Ca} = \exp\left(0.08\left(\pm 25\%\right)\mathrm{SST} + 0.06\left(\pm 30\%\right) - 2.8\left(\pm 36\%\right)\right)$$

From this regression the sensitivity to salinity is ~6%/psu, in line with previous work from Sadekov et al. (2009) on core tops covering a salinity range between 33.5 and 35.5psu and from Kisakürek et al. (2008) using cultured specimens of *G. ruber* over a salinity range between 32 and 44psu, but about 5 times less than that predicted by Arbuszewski et al. (2010) from their higher salinity Atlantic dataset. This equation also suggests a temperature sensitivity of ~6.4%/°C, which is in good agreement with Arbuszewski et al. (2010), Sadekov et al. (2009) and Kisakürek et al. (2008) but is lower than the canonical 9% (Anand et al., 2003; Elderfield and Ganssen, 2000). This temperature sensitivity is also in line with results from sediment trap studies conducted at lower salinity (~0.06-0.07 (McConnell and Thunell, 2005; Mohtadi et al., 2009)).

3.5.2. Deriving a paleotemperature equation for the effect of salinity

I develop two equations to derive unbiased temperature and $\delta^{18}O_{sw}$ estimates from the paired measurements of Mg/Ca and $\delta^{18}O_c$ on the same foraminiferal sample. This approach is similar to that of Mathien-Blard and Bassinot (2009) and Arbuszewski et al. (2010) since it takes advantage of the dual influence of temperature and salinity on both $\delta^{18}O_c$ and Mg/Ca.

Past SSS are expressed as the sum of modern SSS (SSS_0), local changes in salinity (ΔSSS_l) related to evaporation/precipitation, advection, mixing and river runoff (Benway and Mix, 2004), and global salinity changes related to the size of the ice sheets (ΔSSS_g):

$$SSS = SSS_0 + \Delta SSS_l + \Delta SSS_g \quad (2)$$

Each of these salinity influences are expressed in terms of changes in $\delta^{18}O_{sw}$, either local ($\Delta\delta^{18}O_l$), or global ($\Delta\delta^{18}O_g$). Changes in $\delta^{18}O_{sw}$ that accompany the growth and decay of the continental ice sheets can be related to salinity using the following equation, which is based on changes in salinity obtained from sea level variations and in $\delta^{18}O_{sw}$ inferred from benthic foraminifera at the Last Glacial Maximum, LGM (Adkins et al., 2002; Duplessy et al., 2002; Fairbanks, 1989; Labeyrie et al., 1987):

$$\Delta\delta^{18}O_g = 1.1\Delta SSS_g \ (3)$$

This relationship carries some uncertainty and may not be fully representative of the SSS and $\delta^{18}O_{sw}$ changes due to ice volume (Waelbroeck et al., 2002). First, the relative sea level changes at one location do not necessarily reflect the eustatic sea level changes. Second, the actual enrichment in $\delta^{18}O_{sw}$ due to ice volume at the LGM is not precisely known. Direct evidence from measurements of sediment pore water $\delta^{18}O$ shows an enrichment of 1.0±0.1‰ (Adkins and Schrag, 2003; Schrag et al., 1996) while indirect evidence suggests a value between 0.87‰ and 1.3‰ (Duplessy et al., 2002; Fairbanks, 1989; Labeyrie et al., 1987). Third, the exact shape of the ΔSSS_g-$\Delta\delta^{18}O_g$ is not known and should be time-dependent due to the temporal variations in the isotopic composition of the ice stored in the ice sheets (Mix and Ruddiman, 1984). Since the ice isotopic composition is primarily a reflection of the temperature of precipitation and the water vapor trajectory (Delaygue et al., 2000; Lorius and Merlivat, 1977), the ice that first accumulated would be isotopically lighter than that accumulated at the LGM. This effect would, in turn, induce a time-dependent regression between ΔSSS_g and $\Delta\delta^{18}O_g$. However, this effect is small (Chappell and Shackleton, 1986) and I will therefore adopt a first-order regression to simplify the steps in the calibration.

I also take advantage of the linear relationship between $\delta^{18}O_{sw}$ and SSS_l in the ocean. I derive a $\delta^{18}O_{sw}$-SSS relationship for the core tops used in this study of the form (n=104, R^2=0.95, 95% confidence interval given in parenthesis):

$$\delta^{18}O_{sw}=0.28(\pm 0.02)SSS-9.12(\pm 0.41) \quad (4)$$

I acknowledge that this relationship does not take into account spatial variability observed in the world's ocean (LeGrande and Schmidt, 2006). However, since the goal of this study is to provide a calibration for a paleothermometer based on the paired $\delta^{18}O_c$ and Mg/Ca measurements and the errors associated with such an approach, the correction equations should not be overly-sensitive to the regression coefficients of the $\delta^{18}O_{sw}$-SSS relationship as these may have varied through time and the slope of the modern relationship may be inappropriate to quantify the temporal $\delta^{18}O_{sw}$-SSS relationship (LeGrande and Schmidt, 2010). By combining equations (2) with (3) and (4), I can then write an equation that relates SSS with modern surface $\delta^{18}O_{sw}$ ($\delta^{18}O_{sw0}$) and local ($\Delta\delta^{18}O_l$) as well as global ($\Delta\delta^{18}O_g$) changes in $\delta^{18}O_{sw}$:

$$SSS=\frac{\delta^{18}O_{sw0}+9.12}{0.28}+\frac{\Delta\delta^{18}O_l}{0.28}+\frac{\Delta\delta^{18}O_g}{1.1} \quad (5)$$

Since I can also express past $\delta^{18}O_{sw}$ as the sum of modern $\delta^{18}O_{sw0}$, local changes in $\delta^{18}O_{sw}$ ($\Delta\ \delta^{18}O_{l}$) and global changes in $\delta^{18}O_{sw}$ ($\Delta\ \delta^{18}O_{g}$), I re-write equation (5) as:

$$SSS = \frac{\delta^{18}O_{sw}}{0.28} + 2.66\Delta\delta^{18}O_{sw} + 32.57 \quad (6)$$

Combining equation (6) with equation (1) and the oxygen temperature equation of Bemis et al. (1998), I write an equation that links $\delta^{18}O_{sw}$ to ln(Mg/Ca) and $\delta^{18}O_{c}$:

$$\delta^{18}O_{sw} = 1.94\ln\left(\mathrm{Mg/Ca}\right) + 0.59\delta^{18}O_{c} + 0.31\Delta\delta^{18}O_{g} - 1.17 \quad (7)$$

SST can then be estimated by replacing $\delta^{18}O_{sw}$ in the Bemis et al. (1998) isotope equation by equation (7). The $\Delta\delta^{18}O_{g}$ can be estimated using the Waelbroeck et al. (2002) dataset.

In order to test for the accuracy of the newly developed calibration equation, I calculate SST and $\delta^{18}O_{sw}$ for each of the paired Mg/Ca and $\delta^{18}O_{c}$ measurements from the calibration dataset. The precision as expressed by the RMSE of the regression between the estimates obtained using the calibration equations and the mean annual SST and $\delta^{18}O_{sw}$ estimates at each core top location is 1.14°C and 0.17‰, respectively.

3.6. Discussion: Paleoceanographic implications in the western Pacific warm pool

I now apply the newly developed equations to two sedimentary records (core MD98-2181 (MD81), 6.3°N, 125.82°E, 2114m depth; core MD98-2176 (MD76), 5°S, 133.44°E, 2382m depth) from the Indonesian Seas at the edge of the western Pacific warm pool (Stott et al., 2007). The seasonal cycle in both SST and SSS at the core locations is small (1.5-2.5°C, ~0.3psu), reducing the uncertainty associated with changes in the seasonal productivity of *G. ruber*. The Mg/Ca and $\delta^{18}O_c$ records from each of these sites were generated in the same laboratory, eliminating possible biases due to laboratory offsets. Furthermore, although the cleaning procedure used in this laboratory is slightly different from that of Barker et al. (2003), a cleaning test using both methodologies reveal no significant difference in the Mg/Ca ratios obtained with either procedure (Chapter 5). Finally, isotope-enabled global climate model (GCM) simulations suggest that the SSS-$\delta^{18}O_{sw}$ spatial relationship has not changed over the Holocene in the western tropical Pacific (LeGrande and Schmidt, 2010), reducing the uncertainty associated with the calibration equations derived in section 3.5.2. However, there is still no constraint on this relationship at the LGM.

The SST reconstructions were originally published using the general Anand et al. (2003) calibration equation: $\mathrm{Mg/Ca} = 0.38\exp^{0.09\mathrm{SST}}$, which yields a modern

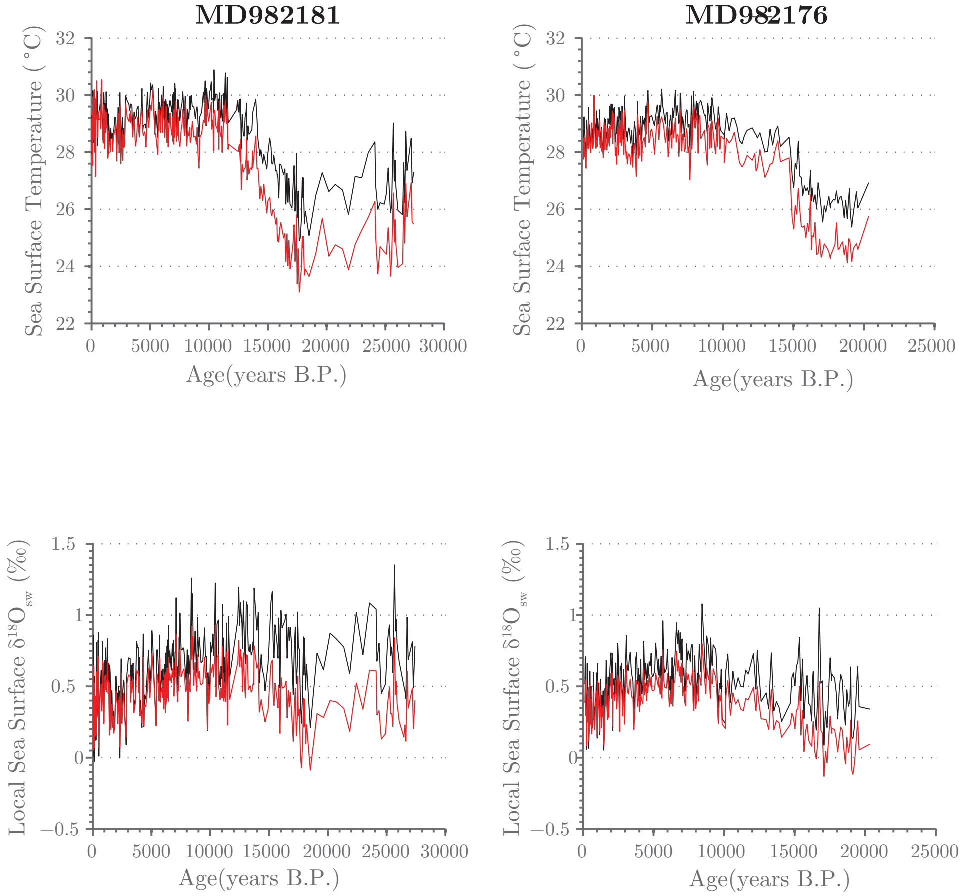

Figure 3-6: Top Panel: *MD98-2181,* ***Bottom Panel:*** *MD98-2176.* ***Top:*** *Sea surface temperature reconstructions using the Anand et al. (2003) general equation (black), and the calibration taking into consideration the effect of salinity (red)* ***Bottom:*** *Same as top for local changes in sea surface* $\delta^{18}O_{sw}$ *after taking into account the influence of global ice volume using the Waelbroeck et al. (2002) dataset.* $\delta^{18}O_{sw}$ *were estimated from the Anand et al. (2003) SST estimates using the Bemis et al. (1998) high-light equation (black) and from the calibration equation:* $\delta^{18}O_{sw}=1.94\ln(Mg/Ca)+0.59\delta^{18}O_c+0.31\Delta\delta^{18}O_g-1.17$ *(red).*

SST estimate (as estimated from the mean SST over the first 2,000 years of the records) of 29.1°C (28.7°C) for MD81 (MD76), which compares well with the mean annual SST of ~28.5°C inferred from the World Ocean Atlas 09 (Locarnini et al., 2010). Core-top $\delta^{18}O_{sw}$ values estimated from the Bemis et al. (1998) isotope temperature equation are 0.44‰ for MD81 and 0.40‰ for MD76, slightly larger than the 0.24‰ extracted from the Legrande and Schmidt (2006) gridded dataset. Core-top SST and $\delta^{18}O_{sw}$ obtained from the calibration equations derived in section 2.5.2 are 28.9°C (28.4°C) and 0.38‰ (0.34‰) for MD81 (MD76), which are also consistent with modern estimates.

On the other hand, the LGM SST estimates obtained with the calibration equation developed in this study suggest a glacial cooling on the order of ~4-4.5°C in the western Pacific warm pool as opposed to ~3°C obtained from the Anand et al. (2003) general equation (Figure 3-6). The magnitude of this cooling is similar to that obtained through another procedure that takes into account the effect of salinity on Mg/Ca (Mathien-Blard and Bassinot, 2009) for another sedimentary record from the southern Indonesian archipelago, in the Indian Ocean (core MD98-2165, 9.65°S, 118.34°E, 2100m) as well as unbiased SST estimates from the tropical Atlantic Ocean (Arbuszewski et al., 2010). After correcting for the effect of ice volume on $\delta^{18}O_{sw}$, the estimates obtained through the new calibration equations suggest relatively fresher conditions in the western Pacific warm pool at the LGM (Figure 3-6), a condition consistent with a more southerly position of the Inter-Tropical Convergence Zone (ITCZ) and enhanced ^{18}O-depleted vapor transport from the Atlantic (Oppo et al., 2007; Schmittner et al., 2000), and an essential element to explain the last glacial termination (Denton et al., 2010).

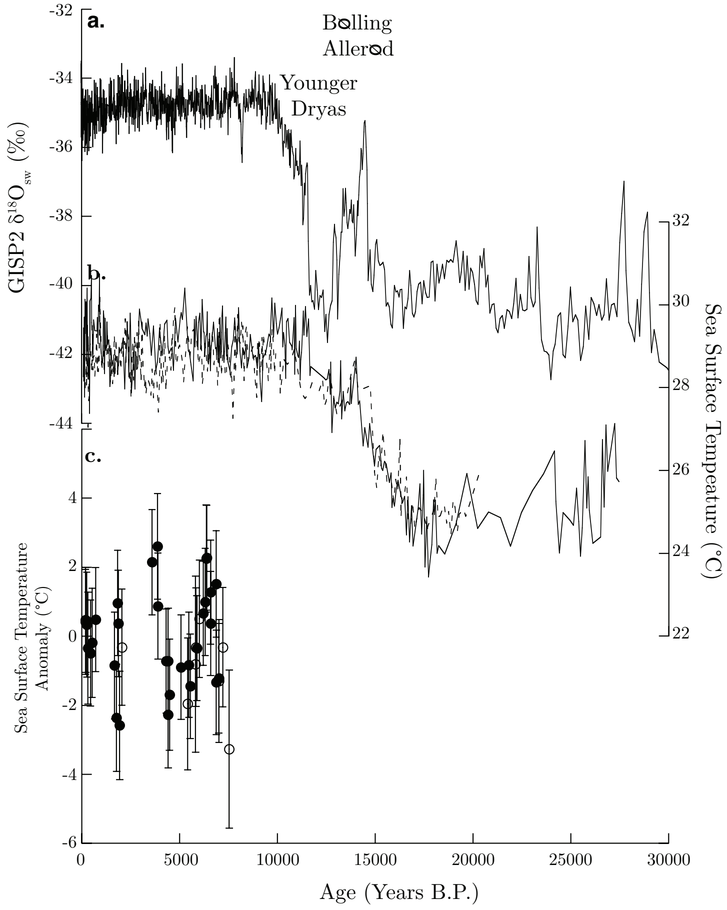

Figure 3-7: ***a.*** *GISP2* $\delta^{18}O_{ice}$ *record taken to represent surface air temperature variations over Greenland (Grootes and Stuiver, 1997).* ***b.*** *SST records from marine sediment cores MD98-2181 (solid line) and MD98-2176 (dashed line).* ***c.*** *SST anomalies derived from coral Sr/Ca paleothermometry from Sumatra (open circles) and Papua New Guinea (filled circles) over the Holocene (Abram et al., 2009). The error bars represent the 2*σ *uncertainty on the temperature estimates.*

Furthermore, the new SST estimates do not support the presence of an early thermal maximum in the Holocene as previously inferred from Mg/Ca calibration based on temperature only (Linsley et al., 2010; Stott et al., 2004). Instead, the records show no-long trend in SST over the Holocene with some millennial-scale SST oscillations; a result consistent with Sr/Ca coral records from the Indonesian Archipelago (Abram et al., 2009, Figure 3-7). The newly derived $\delta^{18}O_{sw}$ estimates also suggest a long-term freshening of the warm pool over the Holocene (Figure 3-6) in response to a southerly displacement of the ITCZ (Oppo et al., 2007;

Stott et al., 2004). Assuming a modern slope of 0.3‰/psu, the ~0.2‰ decrease in $\delta^{18}O_{sw}$ corresponds to a freshening of ~0.7psu as opposed to ~1-1.5psu derived form the Anand et al. (2003) general equation (Stott et al., 2004). This ~0.7psu freshening is more consistent with the ~0.3psu estimates from a GCM study (LeGrande and Schmidt, 2010). Given the importance of the Indo-Pacific Warm Pool to the global atmospheric and oceanic circulation (Qu et al., 2005), including systems such as the East Asian Monsoon (Webster et al., 1998) and the El Niño Southern Oscillation, unbiased SSS and SST estimates are needed to assess the role of this region in climate change. A full assessment of SST and freshwater balance changes in the Indo-Pacific is presented in Chapter 4.

3.7. Conclusions

The Mg/Ca of planktonic foraminifera has traditionally been used as a paleothermometer, which, if used in conjunction with the $\delta^{18}O_c$ can provide estimates of salinity variability (Elderfield and Ganssen, 2000). However, this technique relies on the assumption that temperature is the only influence on Mg incorporation in the calcite lattice of planktonic foraminifers; a hypothesis that has recently been challenged by the recognition that salinity can be an important factor in controlling foraminiferal Mg/Ca (Arbuszewski et al., 2010; Dueñas-Bohorquez et al., 2009; Kisakürek et al., 2008; Lea et al., 1999; Mathien-Blard and Bassinot, 2009; Nürnberg et al., 1996). Using 165 core top and sediment trap data with a global geographical coverage (Figure 3-2), I have shown that (1) the Mg/Ca sensitivity to temperature is lower (~6%/°C) than the canonical 9% inferred from studies in the high-salinity regions of the North Atlantic and (2) although the effect of salinity on Mg/Ca is small in the 33-37psu range, it needs to be taken into consideration in paleoceanographic studies to derive unbiased SST and SSS estimates through time.

I have presented two calibration equations for the planktonic foraminifer *G. ruber* (white variety) that use paired measurements of Mg/Ca and $\delta^{18}O_c$ from the same foraminiferal sample to derive unbiased SST and $\delta^{18}O_{sw}$ estimates. The major caveat in using these equations for routine paleoceanographic reconstructions is their reliance on the assumption that the $\delta^{18}O_{sw}$-SSS relationship has remained constant over time, a hypothesis that should be independently validated for each study site, perhaps with the help of isotope-enabled climate models. I applied this calibration to two sedimentary records from the western tropical Pacific covering the last 25,000 years. The corrected estimates for the effect of salinity in the 32-37psu range suggest that glacial-interglacial temperature changes were on the order of 4-4.5°C compared to the previously estimated 2.5-3°C inferred from the general Anand et al. (2003) calibration. Corrected $\delta^{18}O_{sw}$ values also suggest fresher conditions (after removal of the global salinity change due to changes in ice volume) during the LGM compared to modern, an observation consistent with a more southerly position of the ITCZ resulting in enhanced moisture transport from the Atlantic.

Chapter 4:

A Reevaluation of the Deglacial and Holocene History of the Indo-Pacific Warm Pool

4.1. Summary

A calibration that takes into account the effect of salinity on *Globigerinoides ruber* (white) for a range applicable to the western tropical Pacific on glacial/interglacial timescale is applied to 8 high-resolution sedimentary records from the Indonesian Seas, an important region for the global atmospheric and oceanic circulation. The estimates corrected for the effect of salinity on foraminiferal Mg/Ca suggest a ~4-4.5°C cooling at the Last Glacial Maximum (LGM) compared to ~2.5-3°C from traditional Mg/Ca calibration equations. This cooling was accompanied by a region-wide local freshening, consistent with a more southerly position of the Inter-Tropical Convergence Zone (ITCZ) and enhanced transport of ^{18}O-depleted moisture from the Atlantic at the LGM. The corrected composite record also suggests the presence of a temperature change of ~0.3-0.5°C during the deglaciation, coincident with the Northern Hemisphere Bølling-Allerød/Younger Dryas. This millennial temperature change is accompanied by sea surface salinity (SSS) variations, coincident with a change in the intensity of the summer East Asian Monsoon. Both the corrected and uncorrected records suggest that SSS reached a maximum in the early Holocene. SSS then decreased over the

Holocene, an observation consistent with a southerly displacement of the ITCZ. The flooding of the Sunda Shelf and the re-establishment of the “freshwater plug” in the southern Makassar Strait at 9.5ky B.P. is apparent in the corrected SSS record, although there is no definite evidence for associated changes in heat transport from the Pacific to the Indian Ocean from the SST records.

4.2. Introduction

Since the Indo-Pacific Warm Pool (IPWP) represents the largest reservoir of warm waters in the world’s ocean and acts as a source of convective energy for the rising limb of the Hadley and Walker circulations (Qu et al., 2005), small changes in SSTs in this region can have a profound impact on the global atmospheric circulation, including systems such as the East Asian monsoon (Webster et al., 1998) and ENSO. Further, this region plays an important role in the global thermohaline circulation since it represents the only low-latitude conduit for the exchange of surface waters between ocean basins (Bray et al., 1996; Gordon, 1986), the so-called Indonesian Throughflow (ITF). Therefore, an assessment of the magnitude and spatial pattern of sea surface temperature and salinity changes in this region during periods of rapid climate change such as the last glacial termination is necessary to understand the connection between the monsoon, ENSO, and the Earth’s climate system. In order to derive unbiased SST and SSS in this region spanning the past 25,000 years, the calibration

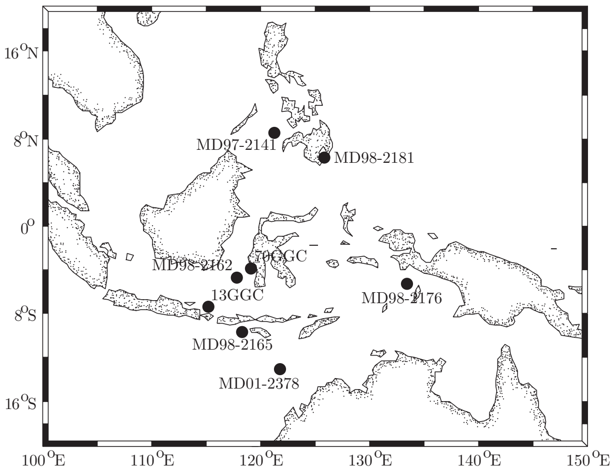

Figure 4-1: *Location of the sedimentary records*

equations derived in Chapter 3 were applied to 8 previously-published sedimentary records (Figure 4-1, Table 4-1) from the Indonesian Seas (Levi et al., 2007; Linsley et al., 2010; Rosenthal et al., 2003; Stott et al., 2007; Visser et al., 2003; Xu et al., 2008). The sedimentary records used in this study are also strategically located (Figure 4-1) to investigate the impact of the flooding of the Sunda Shelf between 10.2ka and 9.5ka (Sathiamurthy and Voris, 2006), which changed the structure of the Indonesian Throughflow from a surface flow to a more thermocline-intensified one, resulting in lower heat transfer from the Pacific to the Indian Ocean in model experiments (Tozuca et al., 2007).

4.3. Methodology

4.3.1. Sea Surface Temperature and Sea Surface Salinity

In order to evaluate hydrographic variability in the Indonesian region on glacial/interglacial timescale, I will examine 8 published high-resolution records from this region spanning the past 25,000 years (Figure 4-1, Table 4-1). These records have very good radiocarbon age control and they are presented on their original age model. For each of the sedimentary Mg/Ca and $\delta^{18}O_c$ records, SST

Table 4-1: *Sediment cores used to evaluate glacial-interglacial SST and SSS changes in the Indo-Pacific Warm Pool.*

Location	**Core ID**	**Latitude**	**Longitude**	**Water Depth (m)**	**Mg/Ca cleaning method**	**Reference**
Mindanao, Western Pacific	MD98-2181 (MD81)	6°27'N	125°50'E	2114	Modified from Boyle et al. (1985)[a]	Stott et al. (2007)
Arafura Sea	MD98-2176 (MD76)	5°18'S	133°26'E	2382	Modified from Boyle et al. (1985)[a]	Stott et al. (2007)
Sulu Sea	MD97-2141 (MD41)	8°47'N	121°17'E	3633	Rosenthal et al. (1999)	Rosenthal et al. (2003)
Makassar Strait	MD98-2162 (MD62)	4°41'S	117°54'E	1855	Boyle et al. (1985)	Visser et al. (2003)
Makassar Strait	70GGC	3°34'S	119°23'E	482	Rosenthal et al. (1999)	Linsley et al. (2010)
Makassar Strait	13GGC	7°24'S	115°12'E	594	Rosenthal et al. (1999)	Linsley et al. (2010)
Sumba	MD98-2165 (MD85)	9°39'S	118°20'E	2100	Barker et al. (2003)	Levi et al. (2007)
Timor Sea	MD01-2378 (MD78)	13°5'S	121°47'E	1783	Martin and Lea (2002)	Xu et al. (2008)

[a] *Cleaning method adapted from Boyle et al. (1985). The foraminiferal samples are rinsed 3 times in DIW. These rinses are followed by a methanol rinse and another DIW rinse. The samples are then rinsed twice with an oxidizing reagent (0.15% H_2O_2 in 0.1M NaOH) at 90°C for 5 min, followed by a DIW and methanol rinse. The samples are then dried and the shells are cracked between two glass slides to expose the chambers' interior. This step is followed by a weak acid leach (0.001M HNO_3), then a DIW rinse (2×) and a final rinse with methanol. The samples are then placed in a drying oven. The samples are sonicated to help dislodge the contaminants and the supernatant is removed after each rinse. Before analysis, the samples are examined under a microscope to remove any impurities.*

and $\delta^{18}O_{sw}$ estimates were derived using the more traditional approach as well as the calibration equations derived in Chapter 3, which take into account the effect of salinity on foraminiferal Mg/Ca. Since the Anand et al. (2003) general calibration equation provides good estimates of modern SST in the region (Linsley et al., 2010; Newton et al., 2006, 2011; Oppo et al., 2009), SST were first determined using the following relationship:

$$\mathrm{Mg/Ca} = 0.38e^{0.09T} \quad (1)$$

Local $\delta^{18}O_{sw}$ estimates were then derived from the calculated temperatures using the Bemis et al. (1998) high-light equation for *O. universa* after removal of the global ice volume signal on $\delta^{18}O_c$ using the Waelbroeck et al. (2002) dataset:

$$T_{iso} = 14.9 - 4.8(\delta^{18}O_c - \delta^{18}O_{sw} + 0.27) \qquad (2)$$

Unbiased SST and $\delta^{18}O_{sw}$ were then estimated from the calibration equation derived in Chapter 3 in combination with equation (2):

$$\delta^{18}O_{sw} = 1.94\ln\left(\mathrm{Mg/Ca}\right) + 0.59\delta^{18}O_c + 0.31\Delta\delta^{18}O_g - 1.17 \qquad (3)$$

In order to account for the differences in cleaning methodologies (Table 4-1), the mean SST, SSS, and $\delta^{18}O_{sw}$ over the past 2000 years was removed from each record. For MD41, I used the mean of the 4,000-5,000B.P. interval, which corresponds to the first 1,000 years of the record. The records are presented in Figure 4-2.

4.3.2. Composite records

Given the relatively good agreement among the records on glacial/interglacial timescale, a composite record spanning the past 25,000 years was created based on 6 of the sedimentary records; namely MD81, MD76, MD41, MD62, MD65, and MD78. Because the records from sediment cores 70GGC and 13GGC covers only the past 14,000 and 10,000 years respectively, they were excluded from this composite. The composite was created after binning the SST, SSS, and $\delta^{18}O_{sw}$ in

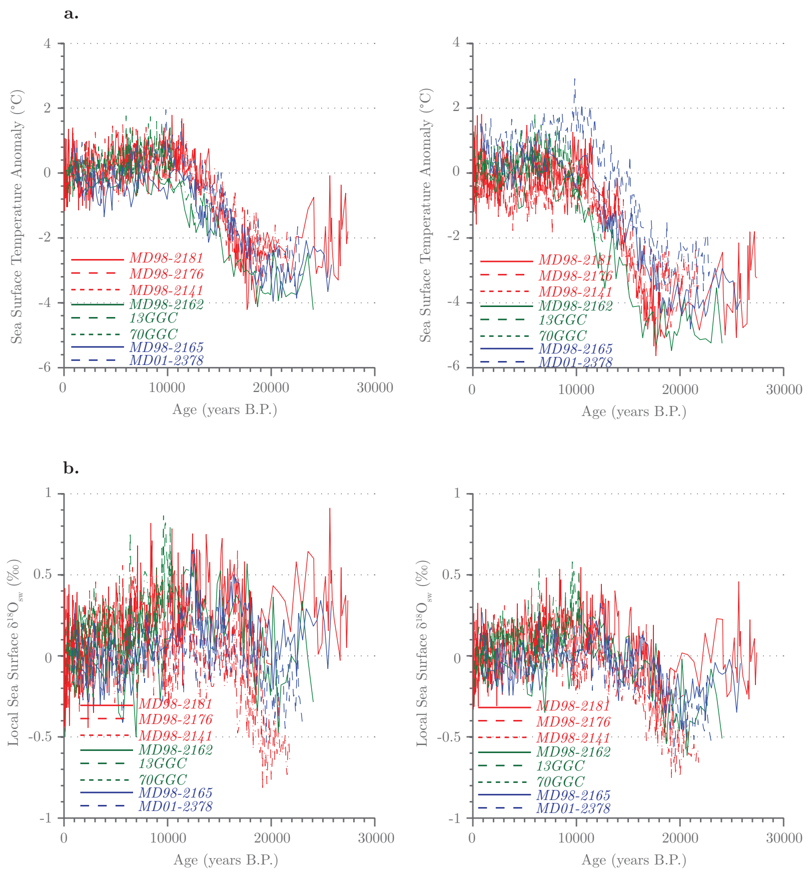

Figure 4-2: ***a.*** *Sea surface temperature anomalies from all eight cores using the Anand et al. (2003) general equation (left panel) and the equation that takes the salinity effect on Mg/Ca into account* ***b.*** $\delta^{18}O_{sw}$ *anomalies from all eight cores derived from the Anand et al. (2003) general equation and the Bemis et al. (1998) high-light equation (left panel) and the equation that takes the salinity effect on Mg/Ca into account* ($\delta^{18}O_{sw}=1.94\ln(Mg/Ca)+0.59\delta^{18}O_c+0.31\Delta\delta^{18}O_g-1.17$).

200-yr non-overlapping intervals. The choice of the bin size is based on the fact that all records, except for MD62, have a resolution higher than 200 years (Linsley et al., 2010).

For the Holocene, three composite records were generated: a warm pool composite (MD76 and MD81), a Makassar Strait composite (MD62, 70GGC, 13GGC), and an Indian Ocean composite (MD65 and MD78). MD41 was excluded from these composites since the record spans only the second half of the Holocene. Theses composites are used to evaluate the impact of the Indonesian Throughflow (ITF) on the regional surface hydrography.

4.4. Results and Discussion: Hydrographic history of the IPWP over the past 25,000 years

4.4.1. The Last Glacial Maximum in the Indonesian Seas

Taking into consideration the effect of salinity on Mg incorporation in the calcite lattice results in a Last Glacial Maximum (LGM)-Holocene temperature change on the order of 4-4.5°C, as opposed to 3-3.5°C obtained from the traditional Anand et al. (2003) general calibration equation. These results are in line with that of Mathien-Blard and Bassinot (2009) for MD65 and that of Arbuszewski et al. (2010) for the tropical Atlantic using a calibration appropriate for the higher salinity values characteristic of this region.

The deglacial IPWP history inferred from the composite is consistent with that of the GISP2 ice core record (Grootes and Stuiver, 1997, Figure 4-3). SST started to rise ~16ka (compared to ~19ka for the composite which does not take the salinity effect into account) and reached a first maximum at ~14.5ka, which corresponds to the Bølling-Allerød period in the GISP2 record. SSTs then dropped by ~0.3-0.5°C during the Younger Dryas, a magnitude similar to that inferred from alkenone records from the South China Sea (Kienast et al., 2001; Steinke et al., 2008, Figure 4-3). This millennial oscillation is not apparent in the SST estimates derived from the Anand et al. (2003) equation, a well-known fact in this region (Rosenthal et al., 2003). The Bølling-Allerød/Younger Dryas

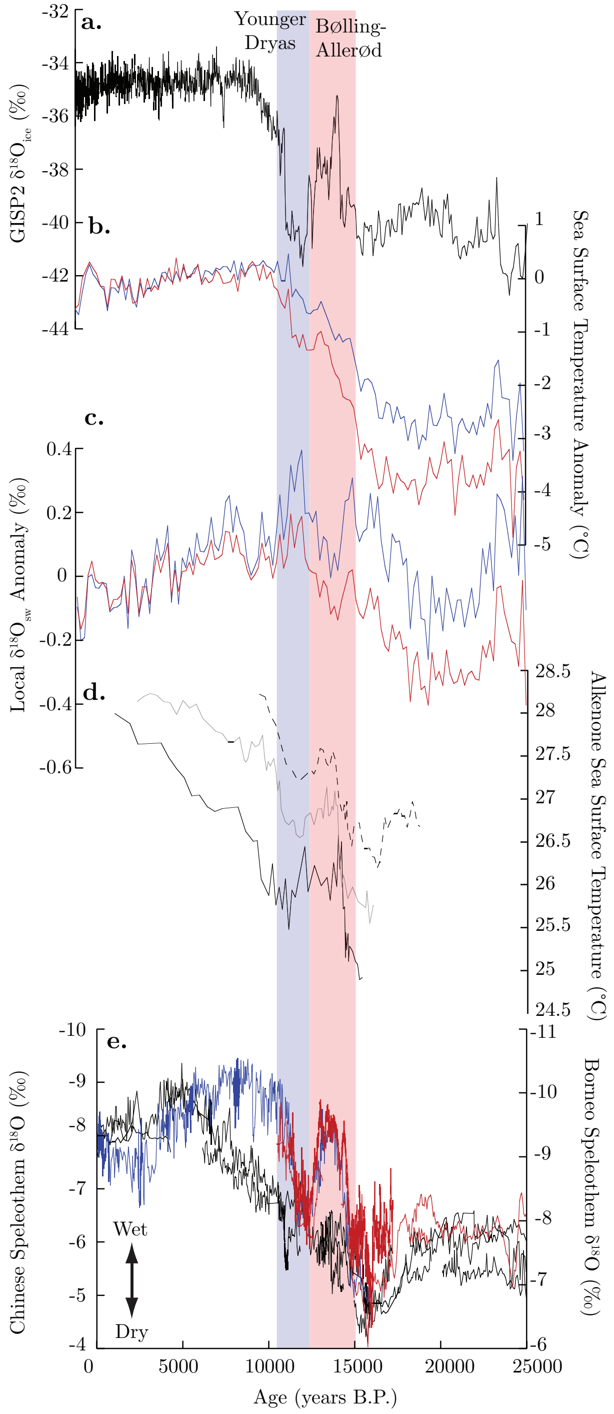

Figure 4-3: Glacial/Interglacial. ***a.*** *GISP2 $\delta^{18}O_{ice}$ record taken to represent surface air temperature variations over Greenland over the past 25,000 years (Grootes and Stuiver, 1997).* ***b.*** *SST composite record for the Indonesian Archipelago over the past 25,000 years (Blue line, using the general Anand et al. (2003) calibration equation, Red line using the calibration that takes salinity into account). Cores 70GGC and 13GGC are excluded from this composite since there is no Mg/Ca and $\delta^{18}O$ data prior to 14ka and 10ka respectively.* ***c.*** *Same as* ***b.*** *for $\delta 1^{8}O_{sw}$.* ***d.*** *Alkenone SST estimates for the South China Sea over the past 25,000 years from marine cores 18252-3 (9°14'N, 109°23'E, black line), 18287-3 (5°39'N, 110°39'E, grey line, Kienast et al., 2001), and MD01-2390 (6°N38'N, 113°25'E, dashed line, Steinke et al., 2008).* ***e.*** *Chinese Speleothem $\delta^{18}O$ (blue, Dongge Cave, Dykoski et al. (2005); red, Hulu Cave, Wang et al. (2001)) taken to represent the intensity of the East Asian monsoon. Northern Borneo speleothem $\delta^{18}O$ (black, Partin et al. (2007)) taken to represent the strength of the Indonesian monsoon.*

climate reversal is particularly apparent in the MD62 record (Figure 4-2).

Direct evidence from measurements of sediment pore water $\delta^{18}O$ shows an enrichment of 1.0±0.1‰ at the LGM due to the growth of continental ice sheets (Adkins and Schrag, 2003; Schrag et al., 1996) while indirect evidence suggests a value between 0.87‰ and 1.3‰ (Duplessy et al., 2002; Fairbanks, 1989; Labeyrie et al., 1987). Here, I used a relationship of 1.1‰/psu according to

Waelbroeck et al. (2002) to correct for the effect of ice volume on $\delta^{18}O_c$. Therefore, the $\delta^{18}O_{sw}$ curves presented on Figure 4-2 and 4-3 represents local variability in SSS (i.e. changes in SSS not due to ice volume). The composite record for the IPWP suggests relatively fresher conditions at the LGM (Figure 4-3); in other words the overall change in $\delta^{18}O_{sw}$ was less than 1.1‰ in the Indonesian Seas. This local freshening is particularly pronounced in the records corrected for the salinity effect on Mg/Ca (Figure 4-3) and is consistent across the region (Figure 4-2), although more pronounced in the Sulu Sea (MD41, Figure 4-2) due to the flow restriction of the relatively saltier western tropical Pacific water into the Sulu Sea as sea level was lower at the LGM (Rosenthal et al., 2003). On the basis on the modern $\delta^{18}O_{sw}$-SSS relationship derived in Chapter 3 (Equation 4), a ~0.2‰ decrease in surface $\delta^{18}O_{sw(l)}$ between modern values and the LGM translates into a ~0.7psu relative freshening of surface waters at the LGM compared to modern conditions. This freshening is consistent with a more southerly mean position of the Atlantic ITCZ, resulting in an increase of ^{18}O-depleted moisture export from the Atlantic to the Pacific Ocean (Oppo et al., 2007; Schmittner et al., 2000).

SSS started to rise ~19ka, 1.5ky before the onset of SST rise in the region, and reached a first maximum at ~15.5ka, at the onset of the Northern Hemisphere Bølling-Allerød/Younger Dryas oscillation. The composite record suggests a region-wide freshening during the Bølling-Allerød followed by a large increase in salinity during the Younger Dryas, a pattern consistent with wetter/ drier conditions over China as a result of East Asian Monsoon variability (Dykoski et al., 2005; Wang et al., 2001). However, a speleothem record from Northern Borneo shows a gradual increase in precipitation over the Maritime Continent from the LGM to the Holocene with no abrupt changes corresponding to the Bølling-Allerød/Younger Dryas (Partin et al., 2007, Figure 4-3). Therefore, the composite SSS records a larger-scale reorganization of atmospheric patterns in the Northern Hemisphere rather than local convective processes over the warm pool region. A southward shift in the mean position of the Atlantic ITCZ accompanied by enhanced transport of ^{18}O-depleted vapor from the Atlantic into the Pacific is an unlikely explanation for the relatively fresh conditions characteristic of the Bølling-Allerød as the ITCZ would have shifted toward the warmer Northern Hemisphere during this time period (Broccoli et al., 2006). Rosenthal et al. (2003) hypothesized that this decrease in salinity could reflect an increase in the intensity of the East Asian summer monsoon during the Bølling-Allerød period as evidenced in the Dongge Cave and Hulu Cave speleothem records (Dykoski et al., 2005; Wang et al., 2001, Figure 4-3). This low-salinity surface water could have then be transferred from the Sulawesi Sea to the Indian Ocean through the Indonesian Throughflow (ITF), which would have flowed at the surface in the absence of a winter "freshwater plug" (Tozuca et al., 2007) due to lower sea level.

4.4.2. Holocene changes and the role of the Indonesian Throughflow

SSTs reached deglacial values at ~11ka. The uncorrected record shows the presence of an early Holocene Thermal Maximum, which has been interpreted to reflect both an expansion and a repositioning of the western Pacific Warm Pool during the early Holocene (Linsley et al., 2010) and which was followed by a region-wide cooling throughout the Holocene on the order of ~0.5°C (Figure 4-3). On the other hand, the corrected composite shows no long-term trend in SST over the Holocene, a result consistent with coral Sr/Ca records from Sumatra and Papua New Guinea (Abram et al., 2009). Region-wide millennial temperature oscillation over the Holocene were small (<0.5°C, Figure 4-3 and 4-4), and probably within the uncertainty associated with the analytical techniques as well as the statistical treatment of the data employed for the composite. This is in contrast with coral Sr/Ca records from Sumatra and Papua New Guinea (Abram et al., 2009), which shows larger millennial-scale variability during the Holocene (Figure 4-4). However, since each data point in the coral record represents only ~10-30 years of coral growth, this record may be more representative of interannual to decadal variability than millennial oscillations. The last millennial oscillation apparent in the composite record corresponds to the Medieval Climate

Figure 4-4: Holocene. a. *Composite of SST records derived from the general Anand et al. (2003) equation (left panel) and the calibration that takes salinity into account (right panel) for the western Pacific Warm Pool (red), the Makassar Strait (green) and the Timor Sea (blue) covering the past 14ka.* ***b.*** *SST anomalies derived from coral Sr/Ca paleothermometry from Sumatra (empty symbols) and Papua New Guinea (filled symbols) over the Holocene (Abram et al., 2009). The error bars represent the 2σ uncertainty on the temperature estimates.* ***c.*** *Same as* ***a.*** *for* $\delta^{18}O$*sw.* ***d.*** *Difference in* $\delta^{18}O_{sw}$ *between the warm pool and the Makassar Strait composites (purple). Difference in SST between the warm pool and the Indian Ocean composites (orange).*

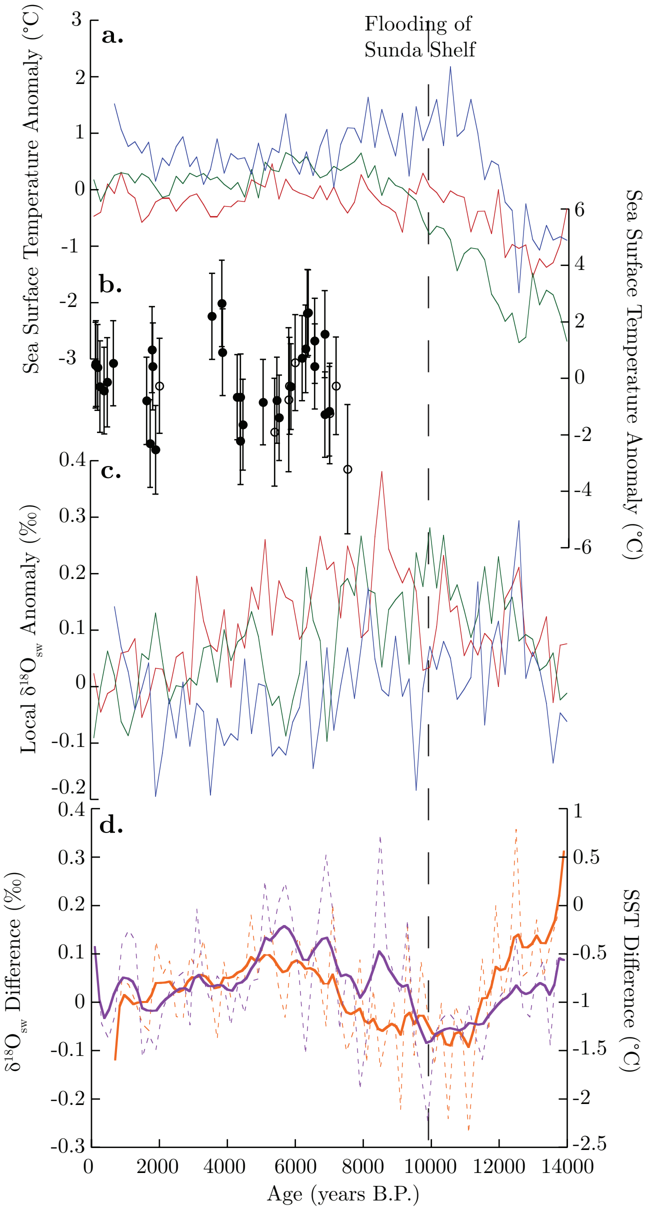

Anomaly/Little Ice Age, which is the subject of Chapter 5.

Local SSS reached a maximum at the peak of the Younger Dryas and decreased throughout the end of the deglaciation and the Holocene. $\delta^{18}O_{sw}$ decreased by ~0.2‰ (~0.7psu) throughout the Holocene, which is consistent with a southward displacement of the ITCZ as previously hypothesized (Oppo et al., 2007; Stott et al., 2004). The amplitude of the Holocene freshening is lower in the composite record corrected for the effect of salinity on Mg/Ca than the ~1.5psu previously inferred (Stott et al., 2004) and is more consistent with the ~0.3psu decrease inferred from a recent modeling

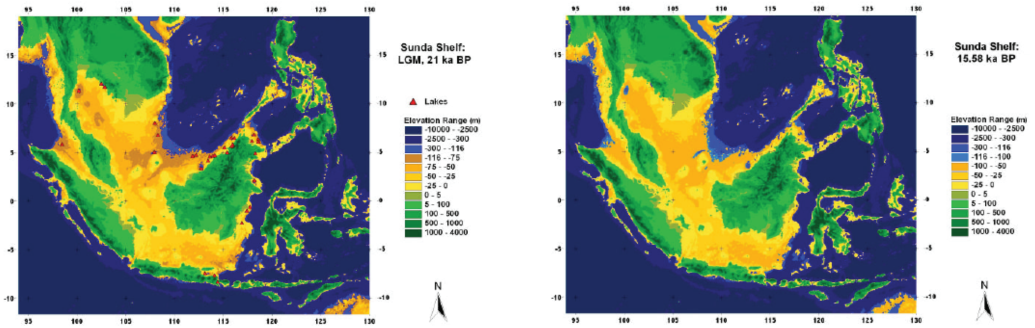

-116m below present-day sea level

-100 m below present-day sea level

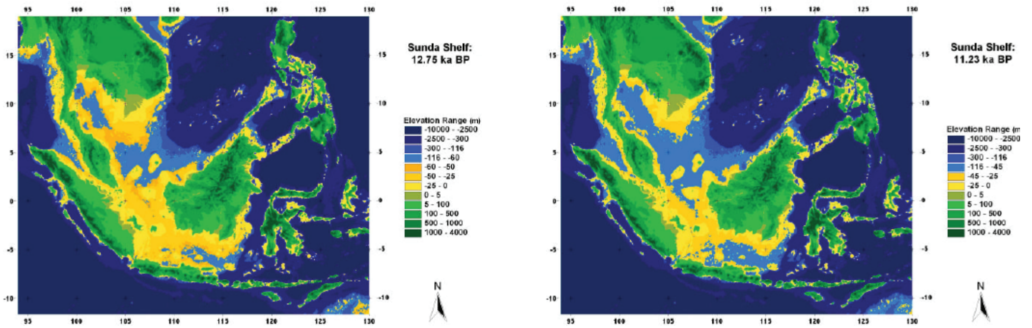

-60 m below present-day sea level

-45 m below present-day sea level

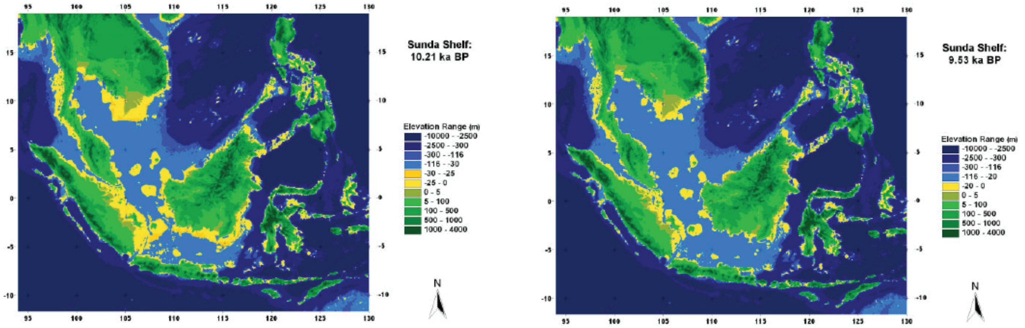

-30 m below present-day sea level

-20 m below present-day sea level

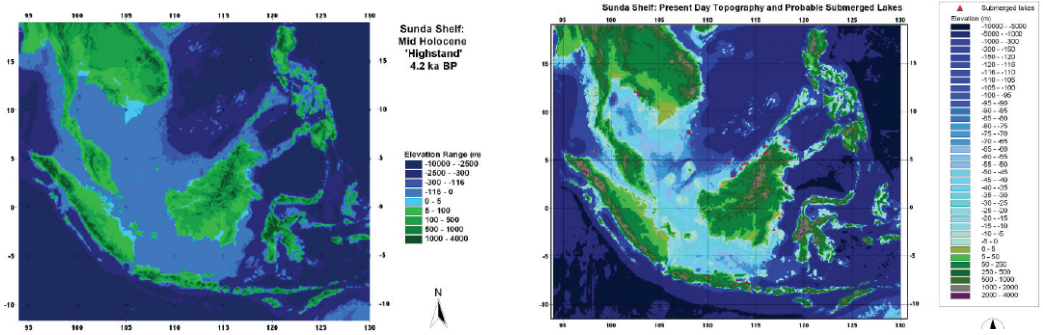

+5 m above present-day sea level

Figure 4-5: *Flooding of the Sunda Shelf. Maps from Sathiamurthy and Voris (2006).*

study (LeGrande and Schmidt, 2009). Legrande and Schmidt (2010) have also argued that the slope of the spatial relationship between $\delta^{18}O_{sw}$ and SSS cannot be used to constrain temporal changes in SSS from the $\delta^{18}O_{sw}$ changes. Instead, they argue for a temporal slope of 0.65‰/psu for the western tropical Pacific over the Holocene. Using this relationship, the ~0.2‰ decrease in $\delta^{18}O_{sw}$ corresponds to a freshening of surface waters of 0.3psu, which is consistent with their model results (LeGrande and Schmidt, 2009).

When post-glacial sea level rise reached ~30m below present sea level at 10-9.5kyr B.P, the Karimata Strait (Sunda Shelf) flooded (Figure 4-5), reconnecting the South China Sea with the Makassar Strait (Hanebuth et al., 2000; Sathiamurthy and Voris, 2006). The establishment of the modern "freshwater plug" is evidenced in the Indonesian composites by a sudden decrease in the $\delta^{18}O_{sw}$ of the cores located in the southern Makassar Strait and the Indian Ocean and a simultaneous increase in the $\delta^{18}O_{sw}$ of the cores located north and east of the Makassar Strait (warm pool composite, Figure 4-4). Taking the difference between the warm pool and Makassar composites, the $\delta^{18}O_{sw}$ gradient between these two regions increased by 0.2‰ in the 1,000 years following the flooding of the Sunda Shelf and the reestablishment of the freshwater plug. Legrande and Schmidt (2010) argue that although the temporal relationship is different from the slope of the spatial relationship, the spatial relationship has remained strikingly similar over the Holocene. Taking their 0.23‰/psu obtained from GCM simulations at 9000y B.P., this 0.3‰ change corresponds to an increase in the salinity gradient of 0.8psu, which is in line with predicted modern changes of ~1psu in mean annual salinity in the absence of a winter "freshwater plug" (Gordon et al., 2003b).

The reconnection of the South China Sea with the Southern Makassar Strait should also have affected heat transport through the region. Specifically, in the absence of a "freshwater plug", modeling results suggest that the ITF was surface-intensified and heat transport to the Indian Ocean increased by 0.18PW (Tozuca et al., 2007). As a consequence of a deeper flow, the ITF today acts to cool the Indian Ocean (Gordon, 2005; Gordon et al., 2003b), resulting in a mean annual temperature gradient of ~0.5°C inferred from the World Ocean Atlas 09 (Locarnini et al., 2010) between surface waters in the warm pool and those of the Indian Ocean. In order to investigate the impact of the flooding of the Sunda Shelf on heat transport through the ITF, the Indian Ocean SST composite was subtracted from the warm pool record (MD81/MD76). The temperature gradient between the warm pool and the Indian Ocean starts increasing at ~11ka, prior to the flooding of the Sunda Shelf and the re-establishment of the "freshwater plug", until ~9ka. In this context, there does not seem to be any large change in heat flux from the Pacific to the Indian Ocean as suggested by modeling results

(Tozuca et al., 2007). An increase in ITF strength would act to further cool the Indian Ocean and, therefore, should result in an increase in the temperature gradient between the western Pacific warm pool and the Indian Ocean. Taking this gradient as a measure of the strength of the ITF, there is a long term increase in ITF strength from about ~11ka to ~4.4ka as evidenced by the increase in the SST difference between the warm pool and Indian Ocean composites. This is followed by a long-term decreased in ITF intensity to the present.

4.5. Conclusions

In this study, I applied the calibration procedure derived in Chapter 3 that takes into account the effect of salinity on *G. ruber* Mg/Ca to 8 previously-published records from the Indonesian Seas, a region important for global atmospheric (Qu et al., 2005) and oceanic circulation (Bray et al., 1996). These records provide the spatial coverage needed to assess regional vs. large-scale climate variability over the last glacial termination and the Holocene. Taking into consideration the effect of salinity in foraminiferal Mg/Ca results in a deglacial warming of 4-4.5°C compared to 2.5-3°C without correction. The results also suggest a regional freshening of the surface waters consistent with a southward displacement of the Inter-Tropical Convergence Zone and enhanced ^{18}O-depleted moisture from the Atlantic into the Pacific Ocean (Oppo et al., 2007; Schmittner et al., 2000; Stott et al., 2004). Regional-scale freshening is less evident in the records not corrected for the effect of salinity on Mg/Ca.

The composite record corrected for the effect of salinity on Mg/Ca also reveals the presence of a ~0.3-0.5°C SST reversal during the deglaciation which corresponds to the Bølling-Allerød/Younger Dryas in the GISP2 ice core record. The SST variability associated with these events in the composite records are of the same magnitude as that inferred from alkenone records from the South China Sea (Kienast et al., 2001; Steinke et al., 2008). These temperature changes also coincide with large SSS variability in the region taken to represent an increase in the intensity of the summer East Asian monsoon during the Bølling-Allerød as previously suggested by Rosenthal et al. (2003).

SST reaches deglacial values at ~11ka. The corrected composite does not support the presence of an early Holocene thermal maximum in the region, which has been attributed to the westward expansion of the Western Pacific Warm Pool (Linsley et al., 2010). Instead, SSTs stay stable throughout the Holocene in the region, a result consistent with a Sr/Ca coral record from Sumatra and Papua New Guinea (Abram et al., 2009). Local $\delta^{18}O_{sw}$ (SSS) decreased by ~0.2‰ (~0.3-0.7psu) through the Holocene, a reflection of a southward displacement of the ITCZ and enhanced ^{18}O-depleted moisture transport from the Atlantic into the Pacific Ocean (Oppo et al., 2007; Schmittner et al., 2000; Stott et al., 2004).

The corrected composite record also suggests a change in the salinity structure at 9.5ky B.P., consistent with the flooding of the Sunda Shelf and the re-establishment of the modern “freshwater plug” in the southern Makassar Strait. No associated changes in the heat flux between the Pacific and Indian Ocean could be inferred from the composite records.

Chapter 5:

Hydrographic Variability in the Indonesian Seas during the Common Era

5.1. Summary

The hydrographic variability associated with the East Asian Monsoon, the relative mean position of the ITCZ, and the El Niño Southern Oscillation (ENSO) is investigated using five high-resolution SST/SSS records from different locations within the Indonesian Seas spanning the last 2,000 years. The results suggest that hydrographic variability in this region was strongly associated with the Northern Hemisphere Medieval Climate Anomaly/Little Ice Age (MCA/LIA). Taken together, the records indicate a ~0.5-1°C temperature change between the MCA and LIA. One of the records also indicates that, on average, the MCA was cooler than the 20th century, although several decades during the MCA show a warming comparable to that of the 20th century. The results also indicate a strengthening (weakening) of the East Asian Monsoon over the MCA (LIA), coincident with a northward (southward) migration of the ITCZ. However, the results do not indicate a preponderant role for ENSO in controlling the surface hydrographic variability found in this region over the past 2,000 years. Most importantly, this study highlights the need for several high-resolution records

from the same region in order to put hydrographic changes in a more global context.

5.2. Introduction

Over the past 150 years, global temperatures have increased by ~0.6°C (Manning et al., 2007). It has been suggested that this increase in temperature, especially since 1980, has been unprecedented over the last millennium (Jansen et al., 2007). This is particularly apparent in the Mann et al. (1999) "hockey stick" reconstruction, although other reconstructions suggest the presence of a warm episode centered around 1,000 A.D., the Medieval Climate Anomaly (Mann et al., 2008; Moberg et al., 2005, Figure 5-1). In order to put the current warming trend and associated climate change into context, efforts are needed to reconstruct the longer pre-instrumental history of climate variability (Jones and Mann, 2004), especially over the past 2,000 years, a period referred to as the Common Era.

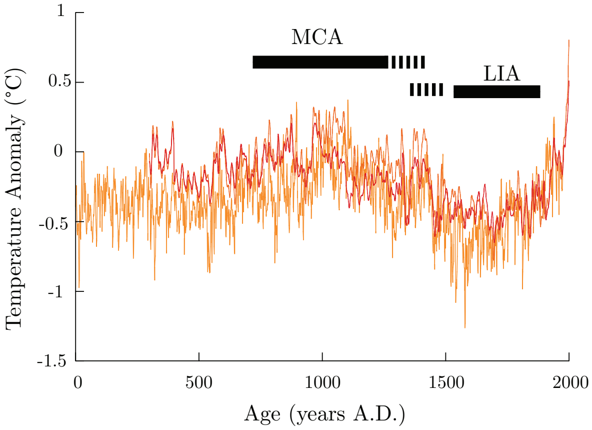

Figure 5-1: *Northern Hemisphere temperature anomaly reconstructions from Moberg et al. (2005, orange), and Mann et al. (2008) (land EIV temperature composite, dark orange, land + ocean EIV composite, red).*

These efforts should include an assessment of sea surface temperature (SST) and salinity (SSS) variability in the Indonesian Seas, a region important for the global atmospheric (Qu et al., 2005) and oceanic (Bray et al., 1996; Gordon et al., 2003a) circulation, including systems such as the East Asian Monsoon (Webster et al., 1998) and ENSO. However, given the oceanographic complexity of this region, coherent regional reconstructions are needed to separate global and local climate influence. To date, two major studies have attempted to detail the hydrographic variability of this region over the Common Era (Newton et al., 2006, 2011; Oppo et al., 2009). These records are confined to the Southern Makassar Strait (cores MD98-2160 and BJ8, Figure 5-2), which experiences large seasonal swings in SST and SSS associated with the southeastern and northwestern monsoons (Chapter 2). The purpose of the current study is to place these 2,000-year records of hydrographic variability into a larger regional context by adding SST/SSS records from locations within the Indonesian Seas influenced to varying degrees by the southeastern and northwestern monsoon as well as ENSO (Figure 5-2, Table 5-1).

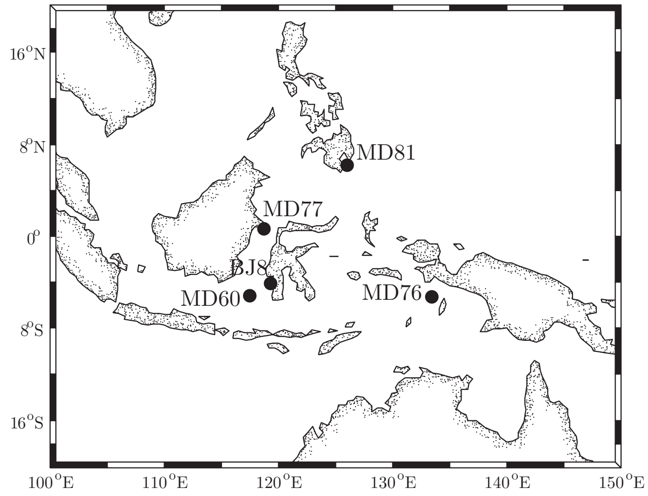

Figure 5-2: *Location of the sediment cores used in this study*

5.3. Climate of the Common Era

As early as the beginning of the 20th century, evidence has been gathered for climate changes occurring over the past two millennia, particularly in North America, Scandinavia, and Eastern Europe (Brooks, 1922). Historical evidence also suggested that Iceland was cultivated in the 10th century and that the Norse were able to settle in Greenland, as the absence of sea ice facilitated navigation at high latitudes (Pettersson, 1914). The Norse left their settlements in the 14th century as conditions worsened and prevented navigation (Brooks, 1922). Lamb (1965) used the term "Medieval Warm Epoch" to describe the emerging picture of warm conditions leading up to the end of the first millennium, at least in the North Atlantic. However, Lamb (1982) also recognized that the precise timing of the warmest conditions was different in different areas. Further, more quantitative studies confirmed Lamb's original assessment; that the "Medieval Warm Epoch" was heterogeneous in terms of its precise timing and geographical extent, especially in the Southern Hemisphere (Bradley et al., 2003; Crowley and Lowery, 2000; D'Arrigo et al., 2006; Esper et al., 2002; Hughes and Diaz, 1994; Jones and Mann, 2004; Mann et al., 2009). Taking the uncertainty associated with paleo-reconstructions into account, the warmest period prior to the 20th century likely occurred between A.D. 950 and 1100 (Figure 5-1), when global temperatures were probably 0.1-0.2°C below that of the 20th century (Jansen et al., 2007), although the medieval warmth may have exceeded that of the 20th century in some regions (Mann et al., 2009).

Furthermore, the medieval times were accompanied by hydrologic changes in Asia, Europe, North America and Africa, evident in several proxy records (Cobb et al., 2003; Cook et al., 2010; Cook et al., 2004; Graham et al., 2007; Haug et al., 2001; Holmgren et al., 1999; Seager et al., 2008; Verschuren et al., 2000; Zhang et al., 2008). Therefore, a more appropriate designation for the climate changes that occurred during Medieval times is the "Medieval Climate Anomaly" (MCA), as this term emphasizes other important changes besides temperature (Bradley et al., 2003). The centuries leading to the cold conditions of the 17th century have been termed the "Little Ice Age" (LIA).

The cause of the MCA/LIA is still highly debated. This climate oscillation seems to be part of a 1500-yr cycle that has been operating since the last glacial (Bond et al., 2001; Bond et al., 1997), in response to either a change in solar radiation further amplified in the climate system (Ammann et al., 2007; Crowley, 2000) or changes in the thermohaline circulation (Broecker, 2000, 2001). The coldest part of the LIA corresponds to the Maunder Minimum in sun spots activity, with other minima occurring during the LIA (Spörer and Wolf), while the MCA coincides with the Medieval Maximum.

Table 5-1: *Hydrographic Parameters at the location of the sediment cores used to evaluate changes in SST and SSS during the Medieval Climate anomaly/Little Ice Age in the Indo-Pacific Warm Pool.*

Location	**Core ID**	**Latitude**	**Longitude**	**Water Depth (m)**	**Mean Annual Temperature (°C)**	**JAS Temperature (°C)**	**Mean Annual Salinity (psu)**	**JAS Salinity (psu)**	**Mg/Ca cleaning method**	**Reference**
Mindanao, Western Pacific	MD98-2181 (MD81)	6°27'N	125°50'E	2114	28.7	28.9	34.1	34.2	Modified from Boyle et al. (1985)	Stott et al. (2004)/this study
Arafura Sea	MD98-2176 (MD76)	5°18'S	133°26'E	2382	28.3	26.1	34.0	34.2	Modified from Boyle et al. (1985)	Stott et al. (2004)
Northern Makassar Strait	MD98-2177 (MD77)	1°24'N	117°5'E	968	28.8	28.7	33.8	34.0	Modified from Boyle et al. (1985)	Saikku (2009)/this study
Southern Makassar Strait	MD98-2160 (MD60)	5°12'S	117°29'E	1185	28.6	27.5	33.1	34.0	Barker et al. (2003)	Newton et al. (2011)
Southern Makassar Strait	BJ8	3°53'S	119°27'E	500	28.8	27.7	33.1	34.1	Barker et al. (2003)	Oppo et al. (2009)

5.4. Materials and Methods

5.4.1. Age models for core MD98-2177 and MD98-2181

An age model for marine sediment cores MD98-2177 (MD77) and MD98-2181 (MD81) was constructed based on 6 and 7 AMS dates respectively (Table 5-2). All ages were calibrated using the CALIB 6.0 software and the Marine09 calibration (Stuiver and Reimer, 1993) with a standard reservoir age correction (ΔR) of 74±70 years estimated for South Borneo (Southon et al., 2002). A plot of calibrated age vs. depth in the sediment core is shown on Figure 5-3. The plot shows a fairly constant accumulation rate for sediment core MD77 over the past 2,000 years. However, the radiocarbon content of the sample taken at 12cm indicates a modern age at this horizon; an age reversal supported by the presence

Table 5-2: *AMS results for core MD98-2177 and MD98-2181. UCI: University of California Irvine. LLNL: Lawrence Livermore National Laboratory*

Core ID	Depth	AMS Laboratory	CAMS#	^{14}C Age	Standard Deviation	Calendar Age (years A.D.)	1σ range (years A.D.)
MD77	0cm	LLNL	95299	580	±45	1852	1801-1903
MD77	12cm	UCI	OS-38302	395	±90	>modern	N/A
MD77	50cm	LLNL	100234	1110	±60	1350	1280-1419
MD77	94cm	LLNL	100235	1745	±45	730	647-812
MD77	109cm	UCI	OS-38335	1870	±110	584	448-719
MD77	130cm	LNNL	100236	2260	±45	168	67-268
MD81	8cm	UCI	OS-36493	580	±110	1806	1709-1903
MD81	55cm	UCI	OS-37308	815	±200	1596	1418-1774
MD81	99cm	UCI	OS-37292	1010	±100	1401.5	1307-1496
MD81	145cm	UCI	OS-37306	1090	±120	1351	1241-1461
MD81	201cm	UCI	OS-90357	1750	±15	721	652-790
MD81	238cm	UCI	OS-36485	1900	±100	562	439-685
MD81	402cm	UCI	OS-37289	3960	±150	-1908	-2129--1687

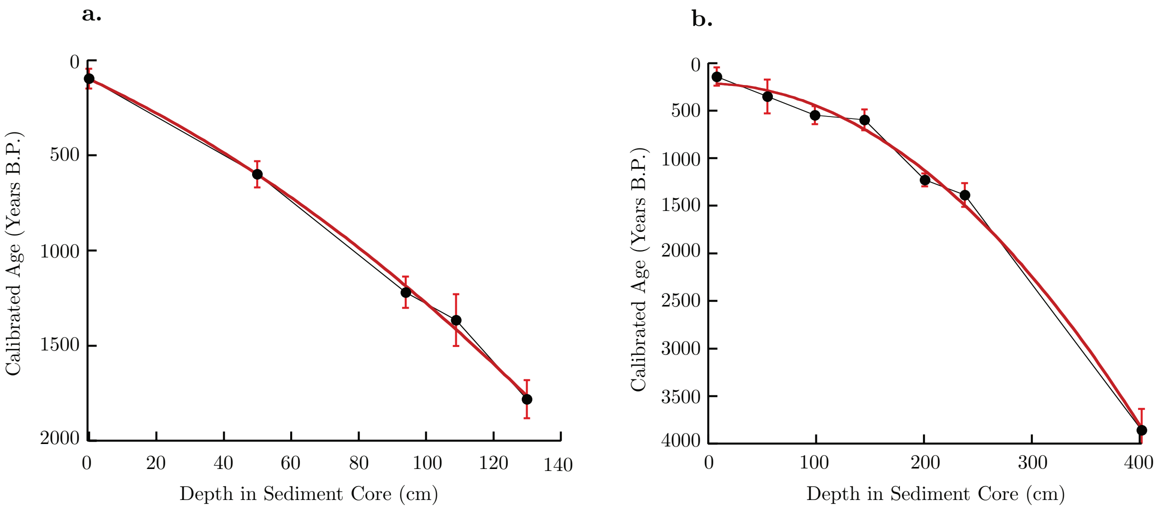

Figure 5-3: *Age model for sediment cores* ***a.*** *MD98-2177 and* ***b.*** *MD98-2181. The black line represents a linear interpolation between adjacent AMS dates while the red line represents a quadratic fit to the entire AMS dataset. The red error bars represent the 1σ uncertainty associated with the analytical measurements and the age calibration.*

of excess Pb-210. The reversal is assumed to be a result of bioturbation with the age reversal due to the localized presence of a burrow that contains some modern material. The uppermost sample does not seem to be greatly affected. It lacks significant excess Pb-210 (Table 5-3), suggesting negligible modern contamination and that the upper few cm of the sediment column are missing. The ^{14}C age of the top interval is consistent with the absence of excess Pb-210.

Table 5-3: *^{210}Pb and ^{214}Pb measurements for core MD98-2177. ^{a,b} represent duplicate samples*

Depth	**Layer Thickness**	**^{214}Pb (±1σ) Bq/kg**	**^{210}Pb (±1σ) Bq/kg**	**Excess ^{210}Pb (±1σ) Bq/kg**
2.5cm	0.8cm	68±11	0±115	--
3.3cm	0.4cm	84±12	0±150	--
3.7cm	0.4cm	69±12	0±172	--
11.5cm^{a}	1cm	24±4	53±43	29±43
11.5cm^{b}	1cm	29±6	82±68	53±68
12.5cm^{a}	1cm	33±3	84±28	51±28
12.5cm^{b}	1cm	28±4	61±41	33±41

Isotopes were measured with gamma spectrometry, based on the 46 keV peak for ^{210}Pb and the 350 keV peak for its progenitor, ^{214}Pb, corrected for ^{222}Rn loss. Excess ^{210}Pb was calculated by subtracting ^{214}Pb activity from total ^{210}Pb activity.

On the other hand, the plot of calibrated age vs depth for sediment core MD81 shows changes in the accumulation rate, such that a simple quadratic fit through the 7 AMS dates may lead to biases in the age model; biases slightly larger than the 1σ dating uncertainty, which takes into consideration not only the error on the ^{14}C measurements but also on the calibration. As a result, the MD81 age model was constructed by linear interpolation between adjacent AMS dates. For consistency, the same procedure was applied to sediment core MD77, ignoring the AMS sample at 12cm, which cannot be calibrated. The previously-published sedimentary records are left on their original age model.

5.4.2. Trace elements and stable isotope analysis

Additional samples from sediment cores MD81 and MD77 were obtained to produce high-resolution records from the original data of Stott et al. (2004) and Saikku (2009). The bulk sediment samples were disaggregated in a sodium hexametaphosphate solution and wet-sieved through a 63µm mesh to remove the clay fraction. The >63µm fraction was then dry-sieved at >180µm. Approximatively 50-100 specimens of the planktonic foraminifer *Globigerinoides ruber* (white, s.s. and s.l.) were picked from the >180µm fraction under a binocular microscope. The foraminifera were then cleaned for trace metal and stable isotope analysis following a method modified from Boyle and Keigwin (1985) and summarized here. The foraminifera are first rinsed three times with deionized (DIW) water followed by a methanol rinse and another DIW rinse. The aim of these rinses is to remove clays from the foraminiferal tests. These steps are followed by two rinses (~5min each) with a hot alkali buffered 1% H_2O_2 solution designed to remove organic material, and another DIW/methanol rinse. The samples are then placed in a drying oven kept at ~50°C. The tests are then cracked open between two glass plates in order to better expose the chambers for further cleaning, and any large coarse-grained silicates contaminants are removed. The samples are then leached with a weak acid solution (0.001M HNO_3) designed to remove coarse-grain silicate contaminants and a final DIW/methanol rinse. The samples were sonified (for a few seconds) after each rinse to help dislodge any contaminants, and the supernatant removed using a syringe. The samples are then placed in a drying oven (50°C) overnight. Prior to analysis, the samples are inspected under a microscope for cleanliness. Remaining silicate grains and strongly discolored calcite shells are disregarded. The calcite preservation in both the MD77 and MD81 samples is excellent because the cores were taken above the present-day lysocline and because they are characterized by very high accumulation rates.

The $\delta^{18}O_c$ values were measured using a Multiprep Dual Inlet system attached to an Isoprime stable isotope ratio mass spectrometer. Each sequential run included 30-50 foraminiferal samples together with 10-15 calcite standards (USC

Ultissima marble) used to monitor analytical precision. The long-term precision of the Ultissima standard $\delta^{18}O$ values measured during this study was 0.09‰. For Mg/Ca analysis, the foraminiferal samples were dissolved in 500μL of 5% nitric acid solution and analyzed on a Jobin Yvon ICP AES. Each sample measurement was bracketed by a standard solution made from solid Mg and reagent grade $CaCO_3$ in an elemental ratio of 5.63mmol/mol, used to adjust the foraminiferal sample Mg/Ca for instrument drift. The nominal precision of the instrument is 0.10 mmol/mol. Fe/Ca and Mn/Ca ratios were used to monitor potential silicate contamination following Barker et al. (2003). The $\delta^{18}O_c$ and Mg/Ca data for cores MD77 and MD81 are presented in Appendix B.

The cleaning procedure used in this study is slightly different from that proposed by Barker et al. (2003), which was used to generate the records for marine sediments cores MD98-2160 (MD60, Newton et al., 2011) and BJ8 (Oppo et al., 2009), which could potentially biased the absolute inferred SST/SSS (Rosenthal et al., 2004). To investigate this potential bias, several samples (Table 5-2) were cleaned according to the Barker et al. (2003) procedure as well as the protocol outlined above and analyzed for Mg/Ca in replicate analysis. For this analysis, ~150-250 *G. ruber* (250-350μm size fraction) were picked under a binocular microscope for each cleaning methodology. The main advantage of using the cleaning protocol described in this study over that of Barker et al.

Table 5-4: *Mg/Ca results for cleaning test*

Core Name	**Latitude (°N)**	**Longitude (°E)**	**Sample Depth (cm)**	**Barker et al. (2003)**		**This study**	
				Mg/Ca	**1σ**	**Mg/Ca**	**1σ**
INMD 48	29.8	-43.2	0-1	4.38	0.35	4.63	0.38
INMD120	-5.5	-16.0	2-3	4.49	0.02	4.59	0.19
MD98-2164	-28.8	-31.2	2-4	4.51	0.10	4.23	0.09
INMD109	-6.6	119.4	0-1	5.29	0.14	5.26	0.13

(2003) is that the shells are not cracked at the beginning of the procedure, limiting the sample loss during the different rinses. Consequently, more replicate analyses could be performed on the samples cleaned according to the protocol described here. There is no systematic difference in Mg/Ca attained by the two procedures, and each replicate for the two cleaning protocols usually lies within the 2σ analytical confidence interval. A student's t-test for the equality of the mean also suggests that the means of the two distributions obtained from the Barker et al. (2003) cleaning and the one outlined previously are not statistically different at the 99% confidence level, although this test may not be entirely reliable given the very small sample size. Other work has shown that the acid leach steps may cause differences in the absolute Mg/Ca of samples cleaned using the "Mg-cleaning" method vs. the "Cd-cleaning" method (Barker et al., 2003; Rosenthal et al., 2004). However, it is not surprising that the Barker et al. (2003) procedure and the one employed in this study leads to similar results since both have only one acid leach step.

$\delta^{18}O_{sw}$ were determined for each of the sedimentary records (Table 5-1, Figure 5-2) using the calibration equation derived in Chapter 3, which takes salinity into account:

$$\delta^{18}O_{sw} = 1.94\ln\left(\mathrm{Mg/Ca}\right) + 0.59\delta^{18}O_{c} + 0.31\Delta\delta^{18}O_{g} - 1.17$$

SSTs are the determined by plugging the $\delta^{18}O_{sw}$ into the Bemis et al. (1998) high-light equation for *O. universa*:

$$T = 14.9 - 4.8\left(\delta^{18}O_{c} - \delta^{18}O_{sw} + 0.27\right)$$

5.5. Results and Discussion: Hydrographic variability during the Common Era

The SST and $\delta^{18}O_{sw}$ records for each of the sediment core are presented on Figure 5-4 and Figure 5-5. Average SST ($\delta^{18}O_{sw}$) taken over the past 2,000 years vary between 28°C and 29°C (0.1-0.3‰), which is in line with modern mean annual sea surface conditions extracted from the World Ocean Atlas 09 (Antonov et al., 2010; Locarnini et al., 2010) and the gridded $\delta^{18}O_{sw}$ dataset of Legrande and Schmidt (2006). However, there are persistent offsets between the sedimentary records (Figure 5-6). These offsets can be explained by (1) interlaboratory analytical accuracy stemming from the use of different calibration standards (0.2°C-0.4°C, Rosenthal et al., 2004), (2) in situ SST/SSS gradients within the region, (3) changes in the seasonality of *G. ruber* productivity, and (4) the accuracy associated with the calibration for a given pair of Mg/Ca/$\delta^{18}O_{sw}$ values.

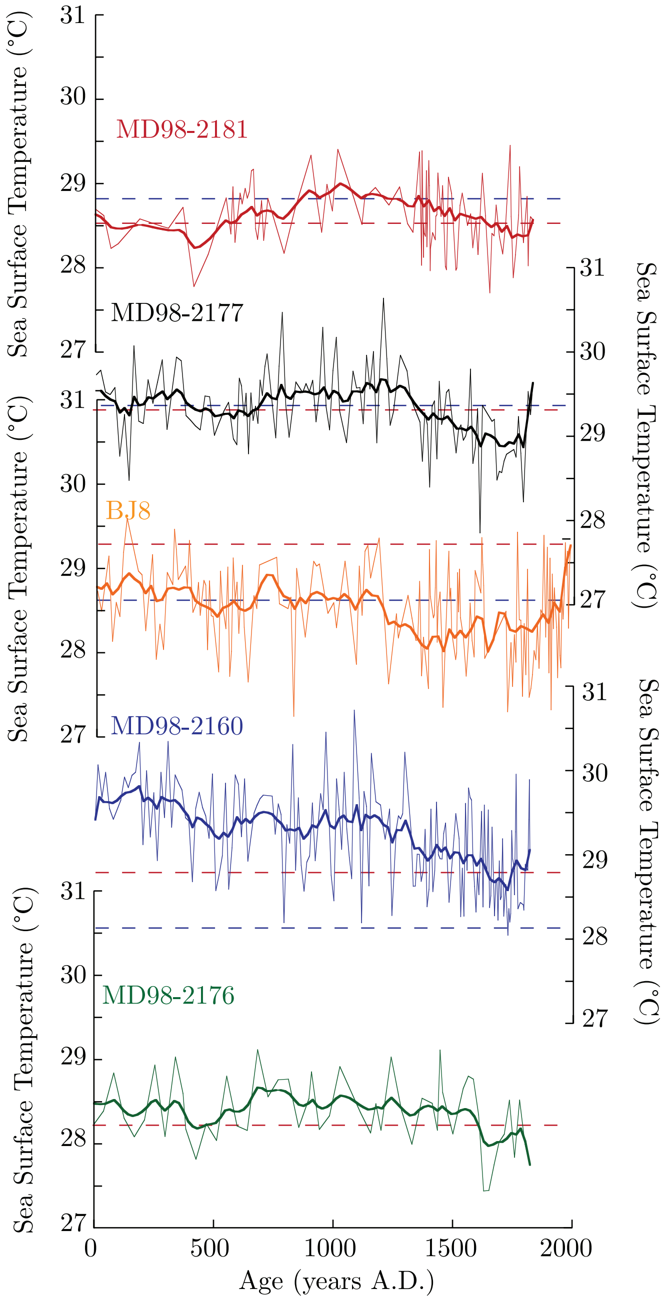

Figure 5-4: *SST variability in the region over the past 2,000 years. The red (blue) dashed line represents modern mean (summer) conditions at the core location extracted from the Word Ocean Atlas 09 (Locarnini et al., 2010).*

SST variability over the past 2,000 years was largely associated with the Northern Hemisphere temperature changes inferred from multi-proxy reconstruction (Figure 5-6). SST were relatively high between ~A.D.900-1350, a period broadly coincident with the Northern Hemisphere MCA. Given that these sedimentary records are presented on independent age models obtained in different laboratories, the timing of the MCA in the Indonesian Seas is a robust feature inferred from these records. SSTs decreased by 0.5-1°C during the LIA. One notable exception is the SST record inferred from MD76, which does not show much variability over the past 2,000 years. Given that the records show a comparable variability despite the fact that the cores were collected from different oceanographic settings with different seasonal amplitude, it is unlikely that this 0.5-1°C cooling over the MCA/LIA transition was only due to a change in the seasonality of production of *G. ruber* or changes in the amplitude of the seasonal cycle. It also suggests that millennial-scale temperature variability in the region may respond to extratropical forcing such as changes in solar radiation

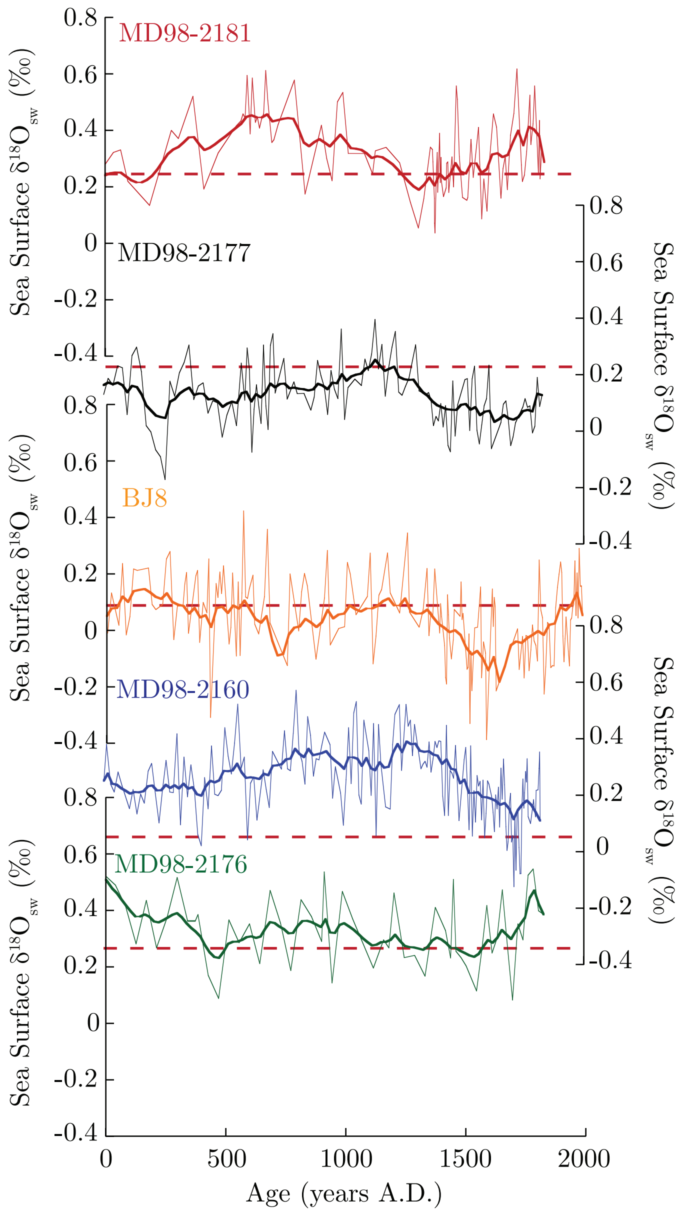

Figure 5-5: *$\delta^{18}O_{sw}$ variability in the region over the past 2000 years. The red dashed line represents modern mean conditions at the core location extracted from the Legrande and Schmidt (2006) gridded dataset.*

(Ammann et al., 2007; Crowley, 2000). The MCA was also preceded by several centuries (from ~A.D. 400 to A.D. 800) of slightly colder conditions, although not as cold as the LIA (Figure 5-6), which broadly corresponds to the "Dark Ages Cold Period" identified in tree-ring records from Northern Europe (Grudd et al., 2002). Only core BJ8 provides a sedimentary record spanning the 20th century. On average, the MCA seems to have been slightly cooler than the 20th century, although several multidecadal periods in the record approached 20th warmth.

SSS increased in the Makassar Strait through the MCA, culminating at ~1250 A.D., concurrent with the SST maximum in this region. However, SSS changes in the western Pacific warm pool seem to be out-of-phase with changes in the Makassar Strait (Figure 5-5 and 5-6). In the following sections, I will examine the relative role of changes in the intensity of the East Asian Monsoon, the position of the ITCZ, and ENSO variability in shaping the different $\delta^{18}O_{sw}$ records.

5.5.1. Monsoon variability over the past 2,000 years

I use the seasonal cycle in SST/SSS described in Chapter 2 as a modern analogue for the combined influence of the ITCZ/monsoon on the records presented in this study. The most profound influence on the seasonal SST variability is the northern Hemisphere summer monsoon, which gives rise to intense upwelling in the Southern Makassar Strait and the Arafura Sea. This is

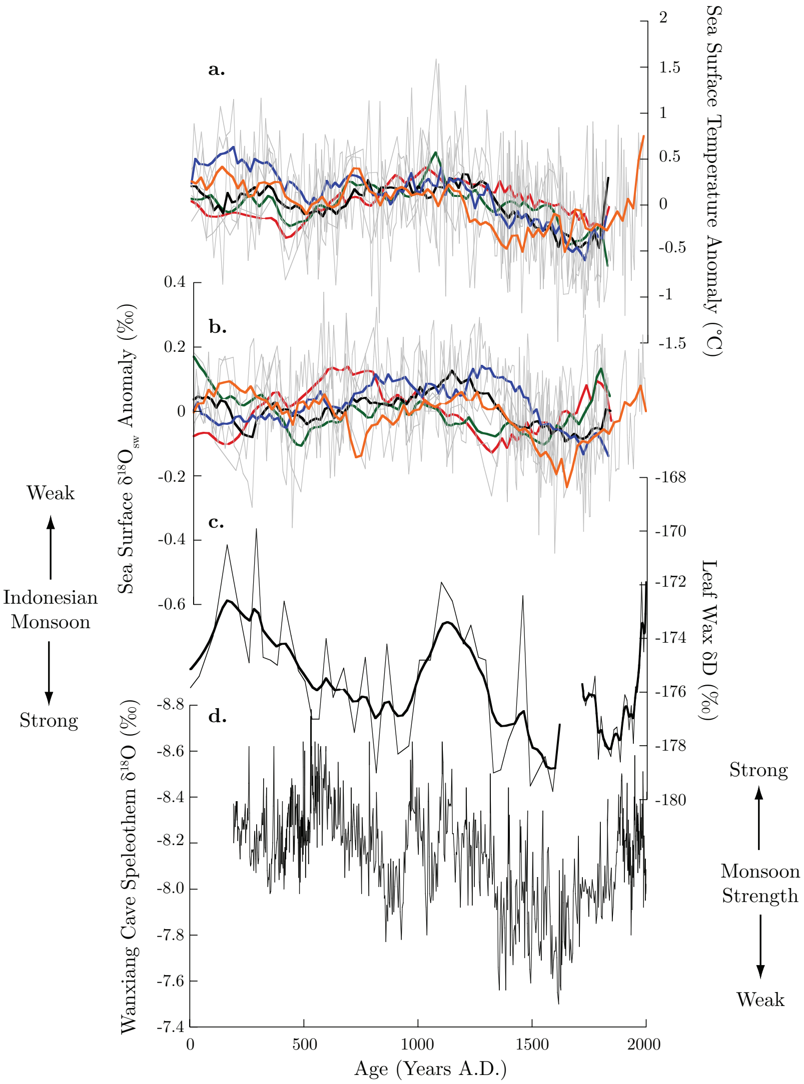

Figure 5-6: ***a.*** *SST records for the 5 sediment cores presented in this study.* ***b.*** *same as* ***a.*** *for* $\delta^{18}O_{sw}$*. The mean for each record was subtracted in order to account for offsets in the record probably due to analytical uncertainties. Red: MD81, Black: MD77, Orange: BJ8, Blue: MD60, and Green: MD76.* ***c.*** *Leaf Wax δD extracted from sediment core BJ8, taken to represent wet/dry conditions over the region associated with the Indonesian Monsoon (Tierney et al., 2010).* ***d.*** *Wanxiang Cave Speleothem* $\delta^{18}O$ *taken to represent wet/dry conditions in association with the intensity of the summer East Asian Monsoon (Zhang et al., 2008)*

especially evident in the large seasonal cycle inferred at the MD76 location (Figure 2-5) and provides a potential explanation for the lack of SST variability over the past 2,000 years at this location. I hypothesize that the lack of MCA warming in the Arafura Sea is caused by stronger upwelling in JAS, which essentially compensated for any expected increase in SST. Because wind-induced upwelling does not create as large a seasonal cycle in the Southern Makassar Strait (Figure 5-4), the MCA warming could still be observed at this location.

Evidence for a stronger summer East Asian monsoon/weaker Indonesian monsoon can also be found in the $\delta^{18}O_{sw}$ records of the cores located in the Makassar Strait. During the summer monsoon, the southeastern winds drive the salty Banda Sea water into the Makassar Strait. In this region, the MCA is characterized by higher SSS (as expressed in higher $\delta^{18}O_{sw}$), in line with other evidence for an increase in the intensity of the East Asian Monsoon (Zhang et al., 2008). However, this higher salinity could also be due to a weaker Indonesian monsoon. A leaf wax δD record, taken to represent precipitation changes associated with the Indonesian Monsoon (Tierney et al., 2010), shows patterns similar to the SSS reconstruction from the same core. For instance, the failure of the Indonesian monsoon at ~1200A.D. certainly contributed to the increased salinity in the region. However, the δD record shows larger, more pronounced variability than the SSS records, a discrepancy that can be attributed to the influence of the East Asian monsoon through advection of Banda Sea water on the SSS records. Tierney et al. (2010) provided a similar explanation for this discrepancy, arguing that the foraminiferal record is representative of regional conditions while the leaf wax δD record provides more local information about precipitation/evaporation. SSS decreased over the course of the LIA, coincident with a decrease in the intensity of the East Asian monsoon inferred from the Chinese speleothem record (Zhang et al., 2008, Figure 5-6). However, this decrease is SSS could also be explained by (1) an increase in the intensity of the northwestern winter monsoon, leading to stronger “freshwater plug”, although this mechanism could not explain the fresher conditions at the MD77 site, and (2) a shift in the mean position of the ITCZ, which is explored in the next section.

5.5.2. ITCZ changes over the past 2,000 years

Changes in the mean position of the ITCZ can help explain some of the SSS variability associated with the past 1,300 years. SSS at the MD81 site was highest at ~A.D.850 and decreased until A.D. 1300. A reverse trend is observed in the cores located in the Makassar Strait (and within age model uncertainty at the MD76 site). This inverse relationship between SSS trends in the Northern and Southern Hemisphere is best explained by the northward migration of the ITCZ over the course of the MCA. Similarly, SSS decreased in the Makassar Strait over the course of the LIA, an observation consistent with a southward displacement of the ITCZ as previously suggested (Newton et al., 2006). The SSS record from sediment core MD76 is out-of-phase with the records from the Makassar Strait and the Sulawesi Sea, which could be due to the relatively poor age control over the past 2,000 years (Stott et al., 2004; Stott et al., 2007) as opposed to the other records presented in this study.

5.5.3. A role for ENSO?

Numerous studies have attempted to explain the climate variability associated with the MCA/LIA in terms of La Niña-like and El Niño-like SST patterns respectively (i.e., Cobb et al., 2003; Conroy et al., 2010; Cook et al., 2007; Cook et al., 2004; Graham et al., 2007; Mann et al., 2009; Seager et al., 2008). The sedimentary records used this study are suitably located to investigate whether ENSO could have played a role in shaping the SST/SSS history of the Indonesian Seas over the past 2,000 years since they are located at a nodal point, at which the sign of the SST anomaly associated with El Niño and La Niña reverses (Chapter 2, Figure 2-6). Specifically, if La Niña (El Niño) conditions would have persisted through the MCA (LIA), the Southern Makassar Strait cores should have seen a large-scale cooling (warming) over the MCA (LIA) while the sedimentary record obtained from sediment core MD81 would have shown a warming (cooling) during the MCA (LIA). However, all the sedimentary records show a period of warmth (cold) in the Indonesian region associated with the MCA (LIA). Therefore, it is highly unlikely that ENSO itself is entirely responsible for the variability associated with the MCA/LIA in this region. A full assessment of ENSO variability over the past 2,000 years in presented in Chapter 6.

5.6. Conclusions

In this study I investigated the relative contribution of changes in the mean position of the ITCZ, the East Asian Monsoon and ENSO on the hydrographic variability of the Indonesian Seas over the past 2,000 years, a time period referred to as the Common Era. To do so, I used the paired measurements of Mg/Ca and $\delta^{18}O_c$ on newly measured and previously published *G. ruber* samples to derive unbiased estimates of past SSS and SST changes from 5 locations within the Indonesian Seas. These sites are influenced to varying degrees by the ITCZ, ENSO, and the East Asian Monsoon. The main limitation of this approach is the fact that the records were generated in different laboratories, which limit interpretation of the data to a semi-quantitive analysis of the relative influence of these climate systems. Moreover, only one of the sedimentary records allows for direct comparison with the 20th century; and this record suggests that the average SST during the MCA was cooler than the 20th century although several multidecadal periods of warming during the MCA approached 20th century warmth. Additional sedimentary records spanning the past 2,000 years (including the 20th century) are needed to fully evaluate the role of natural climate variability in the current warming trend.

Hydrographic variability within the Indonesian Seas was strongly associated with the Northern Hemisphere MCA/LIA. In this region, the MCA was associated with warmer conditions (~0.5-1°C) compared to the LIA (Mann et al., 2008; Moberg et al., 2005, Figure 5-6). The $\delta^{18}O_{sw}$ results indicate a stronger (weaker) East Asian Monsoon during the MCA (LIA), in good agreement with a Chinese speleothem record (Zhang et al., 2008). These changes in the intensity of the East Asian Monsoon were coincident with a northward (southward) migration of the ITCZ during the MCA (LIA). The records do not indicate a strong influence of ENSO on the surface hydrographic variability of the Indonesian Seas over this time period. Most importantly, however, these results illustrate the need for high-resolution, regionally-coherent records, especially in regions with multiple climatic influences, such as the Indonesian Seas.

Chapter 6:

Assessing El Niño Southern Oscillation Variability over the Past Millennium

6.1. Summary

I present a reconstruction of El Niño Southern Oscillation (ENSO) variability spanning the Medieval Climate Anomaly (MCA, A.D. 800-1300) and the Little Ice Age (LIA, A.D. 1500-1850). Changes in ENSO are estimated by comparing the spread and symmetry of $\delta^{18}O$ values of individual specimens of the thermocline-dwelling planktonic foraminifer *Pulleniatina obliquiloculata* extracted from discrete time horizons of a sediment core collected in the Sulawesi Sea, at the edge of the western tropical Pacific warm pool. The spread of individual $\delta^{18}O$ values is interpreted to be a measure of the strength of both phases of ENSO while the symmetry of the $\delta^{18}O$ distributions is used to evaluate the relative strength/frequency of El Niño and La Niña events. In contrast to previous studies, I use robust and resistant statistics to quantify the spread and symmetry of the $\delta^{18}O$ distributions; an approach motivated by the relatively small sample size and the presence of outliers. Furthermore, I use a pseudo-proxy approach to investigate the effects of the different paleo-environmental factors on the statistics of the $\delta^{18}O$ distributions, which could bias the paleo-ENSO reconstruction. I find no systematic difference in the magnitude/strength of ENSO during the Northern

Hemisphere MCA or LIA. However, my results suggest that ENSO during the MCA was skewed toward stronger/more frequent La Niña than El Niño, an observation consistent with the medieval megadroughts documented from sites in western North America.

6.2. Introduction

The El Niño Southern Oscillation (ENSO), centered in the tropical Pacific Ocean, is the leading mode of interannual climate variability in the global climate system. Because of its influence on weather patterns and its associated socio-economic impacts, growing concern about potential changes in ENSO strength and/or frequency in response to future sea surface warming in the tropics have made its study (and, if possible, its prediction) a priority. Climate models that are forced with increased greenhouse gas concentrations simulate changes in ENSO variability but importantly, the models do not agree on the sign of change nor on the mean state of the tropical Pacific Ocean (Meehl et al., 2007). Much of the current understanding of past ENSO variability has been obtained from geochemical data derived from corals (i.e., Cobb et al., 2003; Dunbar et al., 1994; Quinn et al., 2006). The geochemistry of coral skeletons documents hydrographic conditions from the center of action of ENSO; however, most existing coral records span only the last 200 years, limiting their usefulness as long-term recorders of ENSO (Jones and Mann, 2004). Longer ENSO reconstructions can be obtained from high-resolution terrestrial archives located outside the tropical Pacific Ocean (Anderson, 1992; Moy et al., 2002; Quinn, 1992; Thompson et al., 1984). These proxies rely on the assumption that the sign and the strength of the teleconnection with ENSO has remained constant over time; a hypothesis that has yet to be thoroughly tested. Over the past few decades, a variety of proxies has been used to investigate the behavior of ENSO during the Little Ice Age (LIA, defined here as the period between A.D. 1500 and 1850) and the Medieval Climate Anomaly (MCA, A.D. 800 to 1300). The results from these studies paint a very complex and, at times, contradictory picture of ENSO behavior during the past millennium (see, for example, Cobb et al. (2003), and Conroy et al. (2009) vs Conroy et al. (2008), and Moy et al. (2002) or Cobb et al (2003) vs Heired et al. (2009)). This complexity underscores the need for additional high-resolution proxy records from within the tropical Pacific Ocean capable of recording ENSO variability over long time scales. Furthermore, recent observations have identified two apparent "flavors" of ENSO (i.e., Trenberth and Stepaniak, 2001), each characterized by a different spatial pattern of sea surface temperature (SST) anomalies in the tropical Pacific and each having distinct extratropical teleconnection patterns (i.e., Ashok et al., 2007; Kumar et al., 2006). These observations further emphasize the need to expand the network of high-resolution proxy records from the central and western tropical Pacific Ocean.

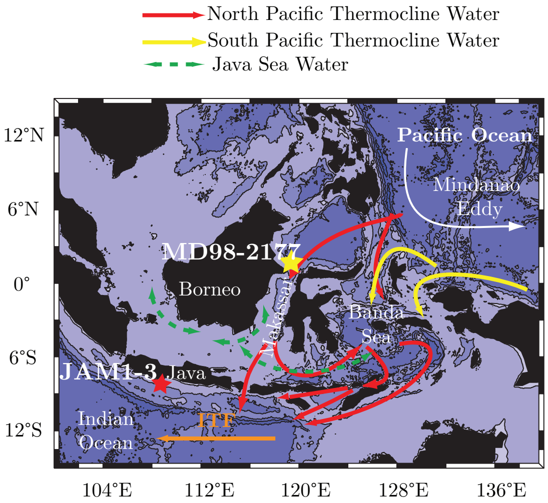

Figure 6-1: *Schematic of the ITF and related current in the Indonesian Seas adapted from Gordon et al. (2005). The location of core MD98-2177 is shown in yellow. The location of the sediment trap study by Mohtadi et al. (2009) is represented in red.*

Marine sediment cores can provide long and continuous archives of ocean conditions within the tropics that contain information about ENSO variability. For instance, core MD98-2177 (hereafter MD77), collected from the northern entrance of the Makassar Strait in the Indo-Pacific warm pool (Figure 6-1), is suitably located to study past changes in ENSO behavior because the thermocline temperatures at this site are highly correlated with ENSO (Ffield et al., 2000, Figure 6-2 and Section 6.3). However, MD77, like most marine sediment cores, cannot provide discrete, annually-resolved samples because sedimentation rates are too low and the sediments are bioturbated. I present a method for extracting ENSO history from samples taken from the MD77 core that overcomes the lack of annual resolution. The method involves the measurements of the oxygen isotopic composition (δ^{18}O) of individual shells of the planktonic foraminifer *Pulleniatina obliquiloculata* that calcifies within the tropical thermocline. Since planktonic foraminifera secrete a calcite shell on a timescale of 2-4 weeks (Spero, 1998), the stable isotope composition of individual foraminiferal tests of a large population of specimens can provide an estimate of the spectrum of monthly surface to sub-surface temperature and salinity changes that accompany the seasonal cycle and interannual variability (Stott and Tang, 1996; Tang and Stott, 1993), including ENSO (Koutavas et al., 2006; Leduc et al., 2009) over the range of calcification depths that apply to *P. obliquiloculata*. In section 6.4, I introduce a conceptual model to explore the relative impact of these parameters on the $\delta^{18}O$ distributions obtained from individual *P. obliquiloculata*. From this pseudo-proxy model, I demonstrate that changes in the spread and symmetry of these distributions are attributable to ENSO variability. Specifically, an increase in the strength and frequency of both El Niño and La Niña events will result in an overall increase in the spread of the individual $\delta^{18}O$ values within a sample while a change in the relative strength of either El Niño or La Niña events will impart a skewness to the distributions (Koutavas et al., 2006; Leduc et al., 2009). For this study, I sampled MD77 at discrete horizons that correspond to the MCA and LIA sections of the core and analyzed ~70 individual specimens of *P. obliquiloculata* at each horizon, resulting in 'snapshots' of ENSO variability over the past millennium.

6.3. Oceanographic Settings

The MD77 sediment core (Figure 6-1) was collected as part of the IMAGES program using the R.V. *Marion Dufresne*. The core location is at the northern entrance of the Makassar Strait (1.4°N, 119°E, and 968m depth) in the Sulawesi Sea.

The ENSO signal is transmitted to the core location through the Indonesian Throughflow (Chapter 2). A 15-year database of XBT (Expendable Bathythermograph) data has shown that thermocline temperatures in the Makassar Strait are highly correlated (r=0.77) with the SOI (Ffield et al., 2000). Unfortunately, there is no long, continuous in situ temperature and salinity data at the MD77 site. I therefore rely on reanalysis data to evaluate the impact of ENSO and the seasonal cycle on temperature and salinity at the surface and within the thermocline at the core location. I use the European Center for Medium-Range Weather Forecasts (ECMWF) ocean reanalysis system 3 covering the period 1959-2009 (thereafter, ORA-S3, (Balmaseda et al., 2008)). My motivation for using the ORA-S3 reanalysis compared to other reanalysis datasets stems from the fact that the artificial vertical velocity fields produced by most ocean models within a few degrees of the equator (Bell et al., 2004) are partially corrected for through the use of an online bias-correction scheme in the pressure field (Balmaseda et al., 2007; Balmaseda et al., 2008). In the absence of this bias-correction algorithm, the artificial velocity field can produce inaccuracies in the temperature estimates (Bell et al., 2004), making an evaluation of ENSO dynamics at the MD77 location impossible. I acknowledge that the reanalysis

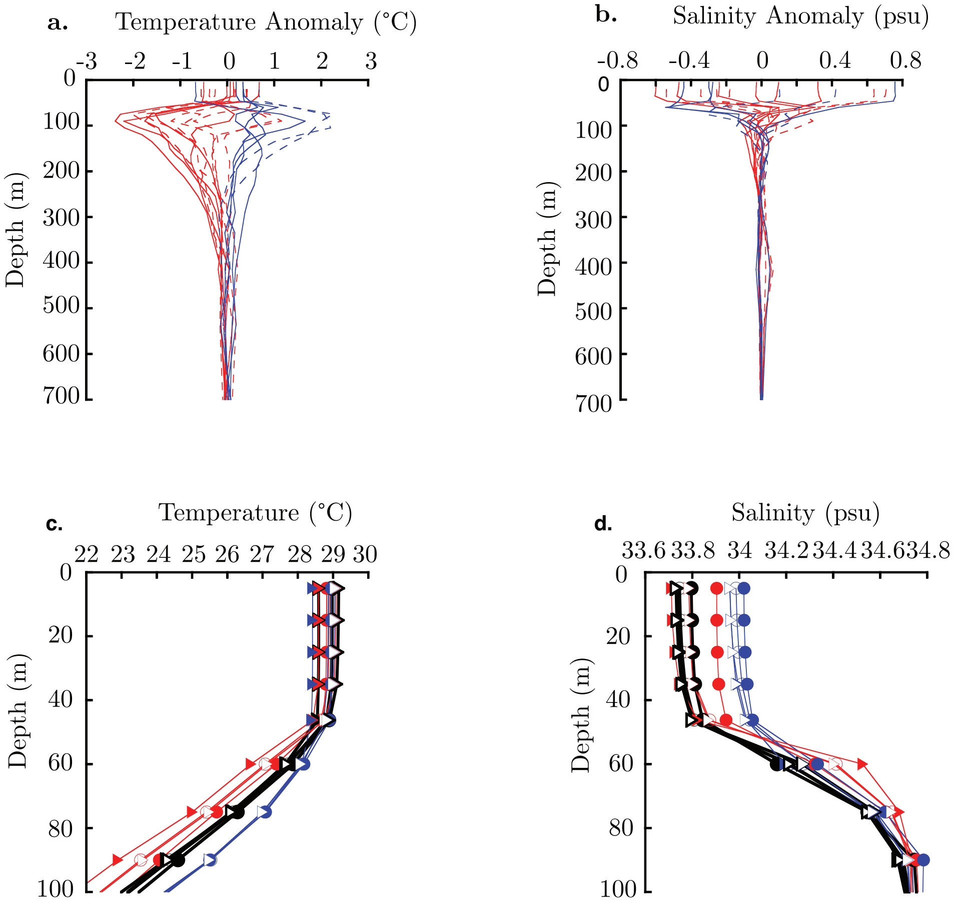

Figure 6-2: ***a.*** *Annual temperature anomalies associated with ENSO dynamics at the MD98-2177 location obtained from the EMCWF ORA-S3 reanalysis.* ***b.*** *Annual salinity anomalies associated with ENSO dynamics. A year was defined from May of year 1 to April of year 2 to accentuate the seasonal locking of the ENSO cycle. Moderate to strong events were selected based on the consensus list of El Niño and La Niña years (http://ggweather.com/enso/omi.htm). El Niño (La Niña) events are represented in red (blue). EP ENSO events are represented by a solid line while CP ENSO events are represented by a dashed line.* ***c.*** *Mean annual (open circle), summer (JAS, filled circle), and winter (DFJ, filled triangle) temperature during El Niño (red), La Niña (blue) and normal years (black).* ***d.*** *Mean annual (open circle), summer (JAS, filled circle), and winter (DFJ, filled triangle) salinity during El Niño (red), La Niña (blue) and normal years (black).*

data may not be completely accurate (a fact further discussed in Section 6-4) but it provides a basis for discussing the impact of ENSO at the MD77 site.

Temperature and salinity anomalies were calculated for the ORA-S3 dataset by removing the annual mean temperature (salinity) of the entire reanalysis period at each depth. Any long-term trends in the data were not removed beforehand in order to evaluate the relative strength of the interannual signal and background climate variability. Temperature anomalies associated with ENSO dynamics at the MD77 location are greater within the thermocline than in the mixed layer. The maximum anomalies occur at ~100m depth and average ~±2°C. In the upper thermocline, the temperature anomalies associated with ENSO are on the order of ~±1°C (Figure 6-2a). On the other hand, salinity changes are largely independent of ENSO (Figure 6-2b). At the surface, the lack of an ENSO-salinity relationship is explained by the long-term decrease (~1psu) in salinity from 1959 to 1982 apparent in the ORA-S3 reanalysis dataset, which masks the interannual variability. Changes in salinity in the sub-surface are small ($<$ 0.1psu) and are not systematically associated with ENSO, although there is a general tendency toward slightly lower (higher) salinities during La Niña (El Niño). However, the interannual anomalies in salinity are of the same magnitude as those associated with the seasonal cycle (Figure 6-2d). On the other hand, the seasonal changes in temperature, which can conceal the surface expression associated with ENSO, are reduced in the thermocline, which enhances the expression of ENSO (Figure 6-2c). At the core location the thermocline temperature (and, to a lesser extent, salinity) anomalies that accompany CP and EP types of ENSO are of the same magnitude and most importantly, of the same sign. This means that the MD77 record is particularly well-suited for documenting the evolution of both types of ENSO events during the past millennium.

6.4. Modeling $\delta^{18}O$ of individual *Pulleniatina obliquiloculata* in the Western Tropical Pacific

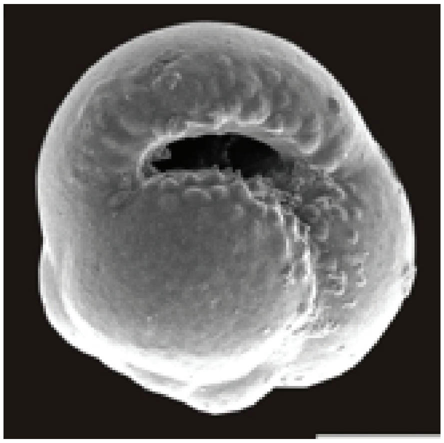

Figure 6-3: Pulleniatina obliquiloculata

Since individual planktonic foraminifera have an average lifespan of 2-4 weeks (Spero, 1998), a suite of $\delta^{18}O$ measurements for individual foraminiferal tests (~50-100) provides a composite sample of thermocline hydrographic variability, including that associated with ENSO (Koutavas et al., 2006; Leduc et al., 2009). *Pulleniatina obliquiloculata* (Figure 6-3) is a warm-water planktonic foraminifer commonly found in upper thermocline waters in tropical to subtropical regions (Cleroux et al., 2007; Wejnert et al., 2010). The calcification depth of *P. obliquiloculata* depends on its ontogenic life cycle with juveniles mainly confined to the mixed layer before migration at greater depth at the time of cortex formation (Erez and Honjo, 1981; Hemleben et al., 1989; Ravelo and Fairbanks, 1992). This was demonstrated in a plankton tow study from the central equatorial Pacific where the largest abundance of adult specimens of *P. obliquiloculata* were found below 60m (Watkins et al., 1996). *P. obliquiloculata* is found in greatest abundance along the seasonal thermocline; in close association with the maximum in chlorophyll concentration (Ravelo and Fairbanks, 1992). Adult specimens of *P. obliquiloculata* can be easily identified from juveniles by the distinctive smooth outer cortex that envelops the final whorl in the adult, and an arched aperture (Watkins et al., 1996). A sediment trap study from south of Java reports calcification depths for this species between 60 and 80m (Mohtadi et al., 2009), which I use as a basis for further assessing the impact of ENSO and the seasonal cycle on the $\delta^{18}O$ distributions of individual specimens of *P. obliquiloculata.*

The $\delta^{18}O_{calcite}$ of *P. obliquiloculata* will vary with both temperature and the isotopic composition of seawater ($\delta^{18}O_{sw}$), the latter reflecting local salinity (and on longer time scales, ice volume changes). Since the contribution of ice volume to the $\delta^{18}O_{sw}$ over the past millennium can be neglected, the $\delta^{18}O_{calcite}$ is interpreted here only in terms of local temperature and salinity. I calculated monthly mean equilibrium $\delta^{18}O_{calcite}$ values at different depths between 1959-2009 from monthly temperature and salinity data taken from the ORA-S3 reanalysis dataset. Evaporation, precipitation, advection, mixing, and river runoff are the physical processes that govern changes in salinity (and $\delta^{18}O_{sw}$) at the study site (Benway and Mix, 2004). There have been several empirical $\delta^{18}O_{sw}$-salinity relationships proposed for the surface waters of the tropical Pacific, including the western tropical Pacific. These relationships were derived from either in situ observations (Fairbanks et al., 1997; Morimoto et al., 2002) or from isotope-enabled climate models (LeGrande and Schmidt, 2006). The slopes of these $\delta^{18}O_{sw}$-salinity relationships vary between 0.27‰/psu (Fairbanks et al., 1997; LeGrande and Schmidt, 2006) and 0.42‰ (Morimoto et al., 2002). Differences in the slope of the $\delta^{18}O_{sw}$-SSS relationship may reflect a large range of evaporation/precipitation conditions across the tropical oceans. Furthermore, these relationships are derived for surface waters and therefore, may not apply to the western Pacific thermocline waters as shown in another study from the Panama Strait in the eastern equatorial Pacific (Benway and Mix, 2004). At that location, the slope of surface waters $\delta^{18}O_{sw}$-salinity relationship is 0.25‰/psu (Benway and Mix, 2004), close to the values reported by Fairbanks et al. (1997) and Legrande and Schmidt (2006), whereas the slope of the thermocline waters (40-100m) $\delta^{18}O_{sw}$-salinity is 0.47‰/psu, closer to the value reported by Morimoto et al. (2002). For the present study modeled salinity values have been converted to $\delta^{18}O_{sw}$ using a linear $\delta^{18}O_{sw}$-salinity relationship where $\delta^{18}O_{sw}$ (VSMOW) $=0.42\text{x}Salinity(psu)-14.3$, following Morimoto et al. (2002). The equilibrium $\delta^{18}O_{calcite}$ was then calculated from the species-specific paleotemperature equation of Russell and Spero (2000): $T(°C)=16.5-4.8(\delta^{18}O_{calcite}(VPDB)- \delta^{18}O_{sw}(VPDB))$

and the VSMOW-VPDB conversion of $\delta^{18}O_{sw}$(VPDB)= $\delta^{18}O_{sw}$(VSMOW)-0.27‰ (Bemis et al., 1998).

The total range of $\delta^{18}O_{calcite}$ values for the 55-85m depth range that are expressed in the ORA-S3 reanalysis dataset is 1.73‰. This large range in $\delta^{18}O_{calcite}$ is indicative of the temperature and salinity variability that accompanies the seasonal cycle, ENSO, and the range of calcification depths for *P. obliquiloculata*. In the following sections I present results of an analysis that distinguishes how the different environmental parameters influence a distribution of $\delta^{18}O$ values within a population of *P. obliquiloculata* and in doing so how the ENSO influence can be differentiated.

6.4.1. The influence of ENSO on $\delta^{18}O$ distributions

The monthly calculated $\delta^{18}O_{calcite}$ values at the calcification depths of *P. obliquiloculata* exhibit a strong interannual variability that correlates significantly with the southern oscillation index (SOI, r=-0.54 at the 90% significant level, effective degrees of freedom corrected for persistence in the dataset N_{eff}=11, Figure 6-4). The interannual variability at the beginning of the ORA-S3 record is reduced compared to the end of the record, which may indicate a bias in the reanalysis as the number of available observations decreases. Indeed, when considering the post-1972 period, the correlation between the monthly calculated $\delta^{18}O_{calcite}$ and the SOI increases to r=-0.58 (90% significance level, N_{eff}=7). This

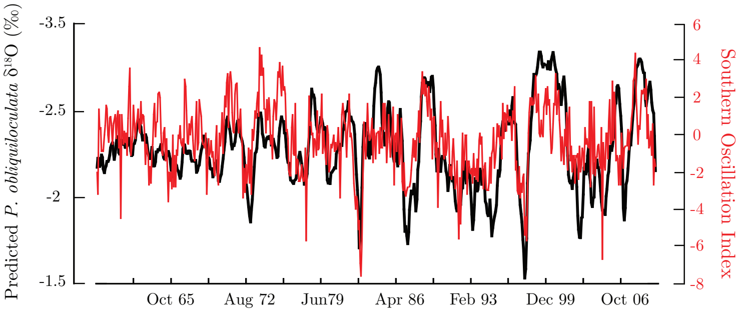

Figure 6-4: *Calculated monthly $\delta^{18}O_{calcite}$ for P. obliquiloculata (black curve) compared to the SOI (red curve)*

also implies that the temperature anomalies associated with ENSO may be slightly larger at this site than inferred from the reanalysis. In order to investigate how well the reanalysis captures ENSO variability, I compare the ORA-S3 dataset to the NOAA consensus list of El Niño and La Niña years, which is based on the Oceanic Niño Index (ONI). According to the ONI index, an ENSO event is defined as 5 consecutive seasons (3-month running average) with an absolute temperature anomaly greater than 0.5°C in the Niño 3.4 region (5°N-5°S, 120°-170°W), based on the 1971-2000 climatology (http://ggweather.com/enso/oni.htm). When applying this criterion to the temperature dataset extracted from the ORA-S3 reanalysis in the Niño 3.4 region, 15 out of the 16 El Niño events occurring over the reanalysis period can be accurately predicted. The reanalysis also produces a false positive, predicting an El Niño in 1992-1993. Further, I am able to accurately predict 13 of the 15 La Niña events occurring during the same period, with no false positive. I define an ENSO event at the MD77 site as 5 consecutive seasons (based on a 3-month running average of the predicted $\delta^{18}O_{calcite}$) with an absolute anomaly greater than one standard

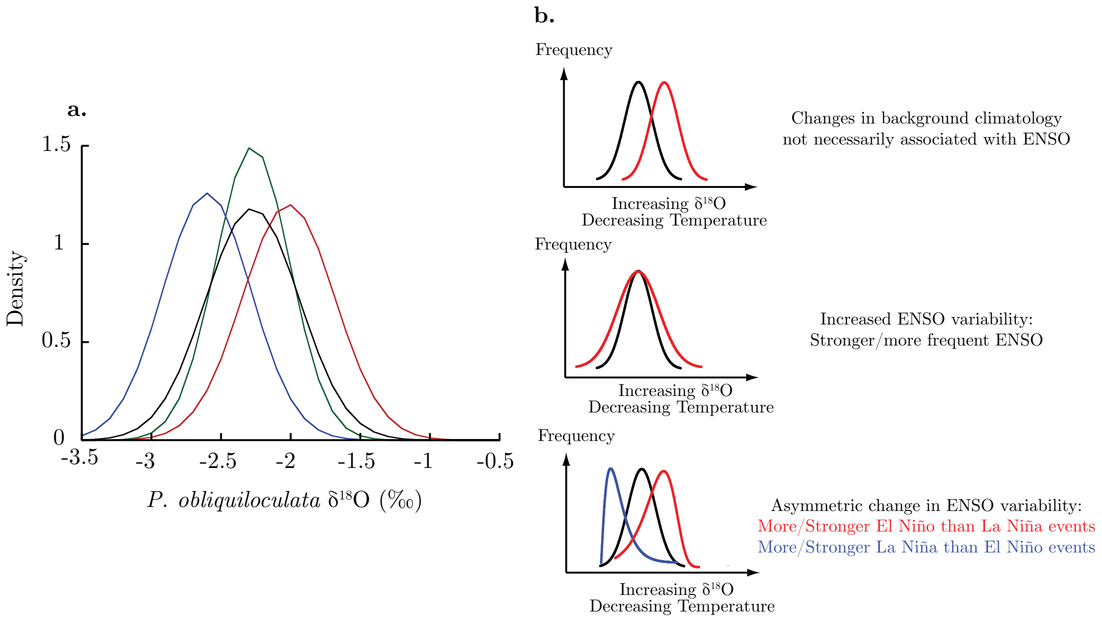

Figure 6-5: ***a.*** *Probability distribution function (PDF) of the calculated δ^{18}O values of P. obliquiloculata that would calcify during El Niño (red), La Niña (blue) and normal (green) years. The black curve represents the overall δ^{18}O distributions for the period 959-2009. Each distribution represents the combined effect of the seasonal cycle, inter-ENSO and interannual variability and the range of calcification depths that apply to P. obliquiloculata.* ***b.*** *Theoretical model for interpreting the statistics of the distributions in terms of ENSO variability (adapted from Leduc et al. (2009)).*

deviation (0.2‰) based on the 1971-2000 climatology. When taking into consideration the entire reanalysis period, this criterion predicts El Niño (La Niña) events with 56% (40%) accuracy when using the NOAA ONI index and 63% (46%) accuracy when using the same index derived from the ORA-S3 reanalysis. This criterion also produces three false positives, predicting an El Niño event in 1992-1993 and a La Niña in 1978-1979 and 2008-2009. When considering the period after 1972, this criterion becomes 75% (83%) accurate in predicting El Niño and 60% accurate in predicting La Niña.

The modeled δ^{18}O distributions depicted in black on Figure 6-5 reflect the accumulated δ^{18}O values of planktonic foraminifera that calcify during El Niño, La Niña, and during normal years. A year is defined here as May to the following April to emphasize the seasonal phase locking of the ENSO cycle. The El Niño and La Niña years are identified using the criterion based on the anomalies in $\delta^{18}O_{calcite}$ defined previously. Each distribution incorporates the influence of the seasonal cycle, inter-annual and inter-ENSO variability, and the range of calcification depths associated with *P. obliquiloculata.* The effect of intra- and interannual changes in the production of *P. obliquiloculata* on the overall $\delta^{18}O$ distribution (black curve on Figure 6-5) is addressed in section 6.4.4. The warmer (cooler) conditions such as those that accompany La Niña (El Niño) lead to lower (higher) population mean $\delta^{18}O$ values as illustrated on Figure 6-5b. Although there is a significant amount of overlap, the means of the distributions are significantly different (90% confidence level on a Student's t-test, N_{eff}=430).

An increase in the strength (taken here as to represent the amplitude of the temperature anomalies) and/or frequency of ENSO (both El Niño and La Niña) events will accentuate the difference in the mean of El Niño and La Niña distributions, resulting in an increase in the spread of the overall distribution, as measured by the standard deviation (Koutavas et al., 2006; Leduc et al., 2009, Figure 6-5). The standard deviation of the distribution for normal years is 0.27‰ compared to 0.34‰ for the overall distribution. This change in spread between a full ENSO model and no ENSO is significant at the 90% confidence level using a

Fischer F-test. Doubling (tripling) the number of ENSO events result in an increase in the standard deviation of 0.03‰ (0.04‰) compared to the original overall distribution, a change that is significant at the 90% confidence level using the F-test.

On the other hand, an asymmetric change in ENSO variability will induce an asymmetry in the δ^{18}O distributions such that stronger or more frequent El Niños (La Niñas) will result in a negative (positive) skewness (Leduc et al., 2009, Figure 6-5). Doubling the number of El Niño (La Niña) compared to normal and La Niña (El Niño) years does not result in an asymmetric distribution. On the other hand, tripling and quadrupling the number of El Niño (La Niña) years result in a change in the Pearson's coefficient of skewness of -0.04‰ and -0.06‰ (0.05‰ and 0.10‰) respectively, which is significant at the 90% significant level. In order to test for the significance of the asymmetry of the modeled δ^{18}O distributions, I use a procedure introduced by Lanzante (1996), which is summarized here. The method consists of partitioning the original distribution into two subsamples; one representing the values greater than the median and the other representing the values on the other side of the median, which have been reflected across the median (Lanzante, 1996). If the original distribution is symmetric, then the medians of the two partitions should be identical. Here, I use a robust rank-order test, based on the Wilcoxon-Mann-Whitney test, for assessing the equality of the medians. It is interesting, to note that the trend toward stronger El Niños in the late 20th century reported in some earlier studies (An and Jin, 2004; Burgers and Stephenson, 1999; Hannachi et al., 2003; Jin et al., 2003; Lau and Weng, 1999; Monahan and Dai, 2004; Rayner et al., 2003; Trenberth, 1997) is not reflected in the skewness of the ORA-S3 dataset. The Pearson's coefficient of skewness for the overall distribution is -0.04‰, which is not statistically significant at the 90% confidence level. This could be due to either the reanalysis model itself, as general circulation models do not generally simulate this bias (Guilyardi et al., 2009)or, to a weaker El Niño signal in the region because of changes in ITF transport that accompanies ENSO.

6.4.2. The influence of the seasonal cycle and background climate on the δ18O distributions

Changes in the spread and to some extent the skewness may also be influenced by changes in the magnitude of the seasonal cycle and/or the magnitude of the interannual variability that is not associated with ENSO. In other words, a change in the spread of the overall distribution could be induced by changes in the spread of the δ18O distributions for planktonic foraminifera that calcify during La Niña, El Niño, and normal years rather than from a change in ENSO variability itself. Therefore, to estimate the potential influence of changes in seasonality on the δ18O distributions, I remove the seasonal cycle from the

ORA-S3 reanalysis. This yields a standard deviation of 0.34‰ for the overall distribution, which is indistinguishable from the original value. Therefore, changes in the seasonal cycle do not significantly impact the statistics of the $\delta^{18}O$ distributions. This experiment also suggests that most of the variability depicted in the distribution functions is due to the varying strength of ENSO itself rather than the seasonal cycle.

A shift in the background climate could also affect the measured $\delta^{18}O$ distributions. A step change in background climate during the period represented in the sediment sample results in bimodal distributions (Leduc et al., 2009), which cannot be interpreted in terms of ENSO variability. A gradual change in temperature could mask some, if not all, of the interannual variability associated with ENSO. The temperature difference between El Niño and La Niña events at my study site is ~1.6°C. If an increase of this magnitude occurred during a sampled period, the years at the beginning (end) of the time interval would plot as El Niño (La Niña) years in Figure 6-5a, and the thermocline variability reflected in the spread of the $\delta^{18}O$ distributions would be mostly attributable to the background warming. However, considering the high sediment accumulation rate that characterizes the MD77 core location, such a temperature change would have to occur within a period of 10-30 years (although the effective time slice is probably larger due to bioturbation, as noted later), a very unlikely scenario since, for example, changes in thermocline temperatures over the last glacial/ interglacial cycle were on the order of 1.9°C (Xu et al., 2008) in the region as estimated from *P. obliquiloculata* Mg/Ca. However, smaller long-term temperature trends may mask or amplify some of the ENSO variability that I infer from the spread of the $\delta^{18}O$ distributions.

6.4.3. The influence of calcification depths on the $\delta^{18}O$ distributions

Changes in the range of calcification depth could have a profound effect on the interpretation of the spread of the $\delta^{18}O$ distributions as a measure of ENSO variability. If only a few individuals calcified deeper (or shallower) during a specific time interval, their $\delta^{18}O$ values may be significantly higher (or lower) than the majority of specimens within the analyzed population and therefore would plot as outliers on a histogram of $\delta^{18}O$ values. Furthermore, changes in the overall calcification depth (for instance from 55-85m to 75-105m) of a large portion of the individuals analyzed from a single sample horizon would produce a bimodal distribution, which is not interpretable in terms of ENSO variability.

An increase in the overall range of calcification depths from 30m to 45m would increase the standard deviation of the calculated $\delta^{18}O_{calcite}$ distribution by 0.10‰, which is significant at the 90% confidence level using the F-test. Similarly, if a distribution of individual *P. obliquiloculata* were skewed because the preferred calcification horizon of *P. obliquiloculata* shoaled (or became deeper), this would induce asymmetry to a δ^{18}O distribution that would be misinterpreted as a change in ENSO variability. Consequently, an additional measure of the depth of calcification is needed. The sharp gradient in $\delta^{18}O_{calcite}$ within the thermocline is echoed in the δ^{13}C of dissolved ΣCO_2 (Figure 6-6). A change in the spread and symmetry of the δ^{13}C can therefore be used in combination with the δ^{18}O distribution to decipher the ENSO influence from any change in habitat. Specifically, a simultaneous increase (decrease) in the standard deviation of the measured δ^{18}O and δ^{13}C values is most likely to indicate a change in the range of habitat depths while opposite changes or no change in the spread of a δ^{13}C distribution would be indicative of shifts in ENSO variability rather than shifting habitat. Similarly, a positive (negative) skewness in the δ^{18}O (δ^{13}C) distribution can be induced by an asymmetric population distribution in the water column toward a shallower habitat. On the other hand, if the sign of the skewness of the δ^{18}O and δ^{13}C distributions co-varies, then a change in skewness of a δ^{18}O distribution can be interpreted in terms of ENSO. This model relies on the notion

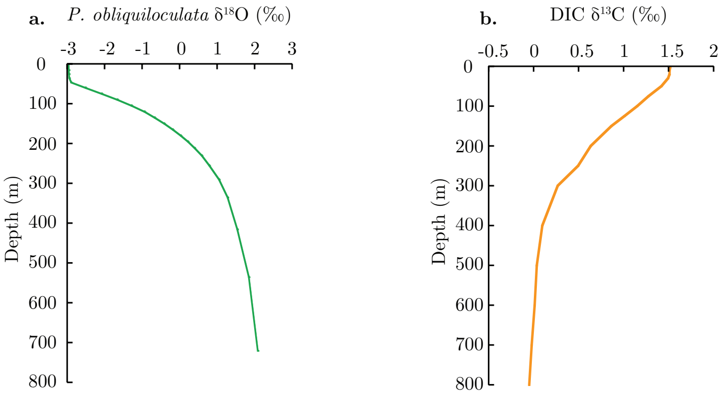

Figure 6-6: ***a.*** *Vertical profile of P. obliquiloculata $\delta^{18}O_{calcite}$ calculated from the temperature and salinity data of the ORA-S3 reanalysis dataset.* ***b.*** *Vertical profile of $\delta^{13}C_{calcite}$ calculated from Apparent Oxygen Utilization data (Kroopnick, 1965) obtained from the World Ocean Atlas 09 (Garcia et al,, 2010).*

the δ^{13}C of *P. obliquiloculata* reflects that of dissolved CO_2 or that the degree of isotopic disequilibrium remains constant. A study by Mulitza et al. (1999) showed that *P. obliquiloculata* does not secrete its test in isotopic equilibrium with dissolved CO_2, but the deviation from isotopic equilibrium is a linear function of temperature. Therefore, although the mean of the δ^{13}C cannot be used to infer the actual calcification depth, the spread and skewness of the individual δ^{13}C measurements should still be representative of the range of calcification depth and habitat preference within the thermocline.

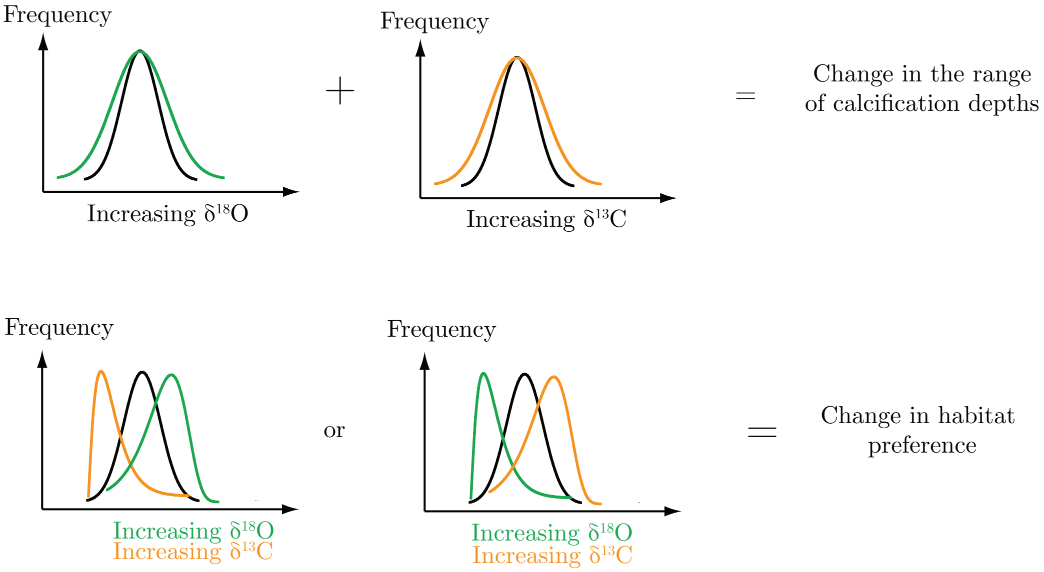

Figure 6-7: *Theoretical model for interpreting the statistics of the δ^{18}O and δ^{13}C distributions in terms of changes in the habitat depth.*

I acknowledge that my approach has several caveats. First, changes in ITF transport related to ENSO (Bray et al., 1996; England and Huang, 2005; Fieux et al., 1996; Gordon, 2005; Gordon and Fine, 1996; Gordon and Susanto, 1999; Gordon et al., 1999; Meyers, 1996; Sprintall, 2009) may affect the thermocline

δ^{13}C gradient. However, since no time series of apparent oxygen utilization is available for this location, the effect of interannual variability on the thermocline δ^{13}C gradient cannot be quantified. Second, my method can contain false negatives since a large change in ENSO variability can be compensated by a reduced range of habitat depth, leaving the statistics of the δ^{18}O distributions unchanged, which I use as my main proxy for ENSO variability. Nevertheless, the statistics of the δ^{13}C distributions provide a basis for assessing how depth habitat influences my interpretation of past ENSO variability (see Section 6.5).

6.4.4. The influence of productivity on the δ^{18}O distributions

The thermocline temperature and salinity changes that accompany the annual monsoon cycle, and to a lesser extent ENSO variability, may influence and change the production and flux of planktonic foraminifera, including *P. obliquiloculata*. A change in the production or flux would affect the distribution of δ^{18}O values. During the southeastern monsoon (JAS), large areas off the southwest coast of Sumatra, the southwestern part of the Makassar Strait, the south coast of Java, the Banda Sea, the Arafura Sea, and the south coast of Bali experience upwelling (Tomascik et al., 1997). This seasonal upwelling is particularly evident in the chlorophyll distribution derived from satellite data (Qu et al., 2005) and in the large increase in primary productivity (Kinkade et al., 1997). It is also evident in foraminiferal fluxes documented in a sediment trap study conducted south of

Java (Mohtadi et al., 2009). However, at the MD77 site primary productivity increases from 0.53±0.36gCm^{-2}day^{-1} during the southeastern monsoon to 1.23±0.22gCm^{-2}day^{-1} during the northwestern monsoon when river runoff is highest (Kinkade et al., 1997). I therefore expect the yearly *P. obliquiloculata* production to be weighted toward the boreal winter season. On an interannual timescale, the amplitude of JAS *P. obliquiloculata* production south of Java is also strongly influenced by ENSO, with JAS production 4 times greater than during a normal year (Mohtadi et al., 2009). At the MD77 site, the relationship between primary productivity and ENSO is largely unknown. However, if I consider that river runoff is the primary influence on primary productivity in the northern Makassar Strait, then primary productivity should be larger (lower) during La Niña (El Niño) when precipitation over the Indonesian archipelago is higher (lower).

To evaluate how a change in the intra- or interannual production and flux of this species influences the distribution of $\delta^{18}O$ values, the predicted monthly $\delta^{18}O$ values from the ORA-S3 reanalysis are weighted according to my different scenarios based on the changes in primary productivity and foraminiferal fluxes as inferred previously. In scenario 1 and 2, I assess how a change in the seasonal cycle influences the $\delta^{18}O$ distributions. In scenario 1 (Table 6-1), the yearly production of foraminifera is kept constant (~200 individuals). The calculated

Table 6-1: Changes in the standard deviation and the Pearson's coefficient of skewness of the modeled $\delta^{18}O$ distributions associated with the variability in the production of P. obliquiloculata

	Unweighted	**Scenario 1**	**Scenario 2**	**Scenario 3**	**Scenario 4**
Standard Deviation	0.34	$0.34^{a}\pm0.00^{b}$	$0.34^{a}\pm0.00^{b}$	$0.40^{a}\pm0.00^{b}$	$0.38^{a}\pm0.00^{b}$
Pearson's Skewness	-0.04	$-0.05^{a}\pm0.03^{b}$	$-0.02^{a}\pm0.03^{b}$	$-0.04^{a}\pm0.04^{b}$	$0.02^{a}\pm0.04^{b}$

a:mean of 1000 MC simulations
b: ±2σ of the 1000 MC simulations

monthly $\delta^{18}O$ values for the entire ORA-S3 dataset are then weighted so that JAS (DJF) represents between 25% and 60% (0-25%) of the yearly total *P. obliquiloculata* production. In scenario 2, I weight the monthly values so that DJF (JAS) represents between 25% and 60% (0-25%) of the yearly total *P. obliquiloculata* production, a scenario more consistent with the observed changes in primary productivity in the northern Makassar Strait (Kinkade et al., 1997). The next two sets of simulations are used to investigate how interannual variations in the production of *P. obliquiloculata* affect the $\delta^{18}O$ distributions. In scenario 3, the DJF production is increased 2 to 6 times compared to that of scenario 2, so that DJF would represent up to 90% of the total yearly production during a given ENSO year. In contrast, scenario 4 emphasizes the role of ENSO in controlling the interannual variations in the production of planktonic foraminifera. The DJF production is increased 2x to 6x compared to that of scenario 2, but only during La Niña years. One thousand Monte Carlo simulations are performed for each of these scenarios. The mean of the standard deviation and the Pearson's coefficient of skewness (±2σ) for the 1,000 simulations are compared to the statistics of the original (non-weighted) predicted $\delta^{18}O$ distribution (Table 6-1). Adding a seasonal productivity component does not affect the spread or the skewness of the $\delta^{18}O$ distributions in the first two scenarios presented. This indicates that intrannual changes in *P. obliquiloculata* production associated with the monsoon do not significantly affect the overall distribution of $\delta^{18}O$ values within a population, a result consistent with the small seasonal cycle associated with the monsoon (Figure 6-2).On the other hand, increasing productivity during the winter months of ENSO years result in an overall increase in the standard deviation of the $\delta^{18}O$ distributions. This result is not surprising since increasing the productivity during these years is essentially equivalent to increasing the number of ENSO years in the reanalysis dataset, which is consistent with the ENSO model developed in section 6.4.1. An increase in the productivity during the La Niña years also results in a change in the statistics of the $\delta^{18}O$ distributions, with an increase in a spread of the $\delta^{18}O$ distributions as well as a shift toward a positive skewness, a result also consistent with the ENSO model developed in section 6.4.1. Therefore, if my inference about productivity is correct, La Niña events should be more readily recorded in the thermocline at the MD77 site, slightly biasing an ENSO reconstruction towards La Niña conditions.

6.5. Analytical Methods

6.5.1. Age Model for MD77

Table 6-2: *AMS results for core MD98-2177. UCI: University of California Irvine. LLNL: Lawrence Livermore National Laboratory*

Depth	**AMS Laboratory**	**CAMS#**	**^{14}C Age**	**Standard Deviation**	**Calendar Age (years A.D.)**	**1σ range (years A.D.)**
0cm	LLNL	95299	580	±45	1852	1801-1903
12cm	UCI	OS-38302	395	±90	>modern	N/A
50cm	LLNL	100234	1110	±60	1350	1280-1419
94cm	LLNL	100235	1745	±45	730	647-812
109cm	UCI	OS-38335	1870	±110	584	448-719
130cm	LNNL	100236	2260	±45	168	67-268

An age model for core MD77 was constructed using a quadratic fit through 5 calibrated AMS dates (Table 6-2). All ages were calibrated using the CALIB 6.00 software and the Marine09 calibration (Stuiver and Reimer, 1993) with a standard reservoir age correction (ΔR) of 74±70 years estimated for South Borneo (Southon et al., 2002). The radiocarbon content of the sample taken at 12cm indicates a modern age at this horizon; an age reversal supported by the presence of some excess Pb-210 (Table 6-3). On the other hand, both the ^{14}C and excess ^{210}Pb of uppermost sample suggest that the top of the core is older and does not contain 20th century material. The reversal is assumed to be a result of bioturbation with the age reversal due to the localized presence of a burrow that contains some modern material. This indicates that the nominal dating uncertainty for each horizon in the MD77 core can be as large as 200 years, although the absence of further age reversals downcore suggests that this

Table 6-3: *^{210}Pb and ^{214}Pb measurements for core MD98-2177. $^{a.b.}$ represent duplicate samples*

Depth	**Layer Thickness**	**^{214}Pb (±1σ) Bq/kg**	**^{210}Pb (±1σ) Bq/kg**	**Excess ^{210}Pb (±1σ) Bq/kg**
2.5cm	0.8cm	68±11	0±115	--
3.3cm	0.4cm	84±12	0±150	--
3.7cm	0.4cm	69±12	0±172	--
11.5cm^{a}	1cm	24±4	53±43	29±43
11.5cm^{b}	1cm	29±6	82±68	53±68
12.5cm^{a}	1cm	33±3	84±28	51±28
12.5cm^{b}	1cm	28±4	61±41	33±41

Isotopes were measured with gamma spectrometry, based on the 46 keV peak for ^{210}Pb and the 350 keV peak for its progenitor, ^{214}Pb, corrected for ^{222}Rn loss. Excess ^{210}Pb was calculated by subtracting ^{214}Pb activity from total ^{210}Pb activity.

represents the upper limit of the dating uncertainty (Table 6-3). Furthermore, this uncertainty is not large enough to prevent a meaningful comparison between the MCA and the LIA, although it prevents comparisons between adjacent intervals.

For the present study 1-cm to 2-cm intervals were sampled at 16 horizons in the MD77 sediment core. These intervals correspond to the MCA and LIA sections of the core (Table 6-4). Each 1-cm (2-cm) sediment interval represents ~10-30 years of accumulated sediment and foraminiferal tests, although the effective time slice for each sample may be larger. Based on modern excess ^{210}Pb measured in a sediment core from the Southern Makassar Strait (Oppo et al., 2009), 2-5% of modern material might be present at ~12cm. Using the upper estimate (5% of modern material mixed with material that is about 200 years older), I determine that the effective time slice for each horizon is 30-50 years. Furthermore, the core was sampled every ~5cm; if I have underestimated the

Table 6-4: *Sedimentary and Statistical Results for each time slice.*

Age	**1843-1851**	**1800-1817**	**1737-1755**	**1681-1700**	**1622-1642**	**1496-1518**	**1452-1464**	**1407-1419**	**1337-1349**	**1290-1302**	**1240-1265**	**1139-1165**	**1060-1087**	**895-923**	**793-823**	**704-734**
Age Uncertainty (1σ)	10	47	97	85	72	58	58	63	69	62	58	56	56	65	76	76
Sample width (cm)	1	2	2	2	2	2	1	1	1	1	2	2	2	2	2	2
Depth in core (cm)	0-1	4-6	11-13	17-19	23-25	35-37	40-41	44-45	50-51	54-55	58-60	65-67	71-73	83-85	90-92	96-98
# of individuals analyzed	67	77	76	81	65	76	72	72	69	60	79	88	67	73	71	72
Median/mean weight of individuals analyzed (μg)	20/21	21/21	19/19	22/22	21/22	25/26	18/21	23/25	24/25	23/27	21/236	23/25	23/24	22/24	23/25	23/26
IQR of weights of individuals analyzed (μg)	11	7	7	8	11	8	11	12	8	10	10	11	10	9	10	13
δ^{18}O Biweigth mean	-2.23	-2.26	-2.15	-2.15	-2.20	-2.12	-2.04	-2.00	-2.10	-2.07	-1.97	-1.98	-2.03	-2.05	-2.08	-2.17
δ^{18}O IQR	0.35	0.39	0.51	0.41	0.53	0.47	0.44	0.51	0.41	0.53	0.47	0.39	0.45	0.49	0.56	0.43
δ^{18}O BSD	0.28	0.34	0.39	0.34	0.38	0.32	0.35	0.40	0.36	0.41	0.38	0.34	0.34	0.39	0.38	0.30
δ^{18}O YKS	0.02	0.02	-0.10	-0.17	0.06	0.03	-0.08	0.16	0.02	0.10	0.49	0.03	0.35	-0.04	0.25	0.13
δ^{18}O σ_{std}	0.09	0.07	0.11	0.10	0.09	0.10	0.11	0.11	0.11	0.11	0.09	0.09	0.10	0.10	0.10	0.10
δ^{13}C Biweigth mean	0.75	0.77	0.85	0.84	0.89	0.86	0.78	0.77	0.78	0.74	0.84	0.82	0.81	0.80	0.77	0.70
δ^{13}C IQR	0.35	0.25	0.23	0.21	0.21	0.21	0.22	0.24	0.21	0.23	0.20	0.27	0.25	0.23	0.29	0.26
δ^{13}C BSD	0.24	0.18	0.18	0.17	0.18	0.18	0.18	0.19	0.15	0.19	0.15	0.24	0.18	0.16	0.19	0.19
δ^{13}C YKS	-0.15	-0.07	-0.21	-0.13	0.15	0.18	0.05	-0.18	0.00	0.28	0.07	0.04	0.01	-0.02	-0.22	0.19
δ^{13}C σ_{std}	0.05	0.08	0.07	0.09	0.08	0.09	0.05	0.05	0.05	0.06	0.06	0.09	0.08	0.06	0.06	0.05

degree of bioturbation inferred from the radiocarbon and excess Pb-210 analysis, adjacent horizons in the sediment core may overlap in time.

6.5.2. Stable Isotope Methodology

The bulk sediment samples from the MD77 core were disaggregated in a sodium hexametaphosphate solution and wet-sieved through a 63μm mesh to remove the clay fraction. This >63μm fraction was then dry-sieved at >250μm. The individual adult *P. obliquiloculata* were picked from this fraction under a binocular microscope. Adult specimens were differentiated from juveniles by the presence of a thick, smooth cortex layer. The foraminifera were then rinsed three times with deionized water (DIW), followed by a methanol rinse. The low viscosity of this reagent helps dislodge clays and other impurities from the carbonate tests (Barker et al., 2003). These steps are followed by a rinse with an alkali buffered 1% H_2O_2 solution designed to remove organic material, a weak acid leach to remove coarse-grain silicates contaminants (Barker et al., 2003) and a final DIW/methanol rinse. The samples were sonified after each rinse to help dislodge any contaminants. The calcite preservation in MD77 sediment samples is excellent because the core was taken above the present-day lysocline and because it is characterized by very high sediment accumulation rates. Approximately 70 adult individual *P. obliquiloculata* were picked for each sample (time horizon), inspected for cleanliness under a microscope, weighed individually and then loaded into individual vials for stable isotope analysis. The median weights of the *P. obliquilocuata* used in this study vary between 18 and 25μg with a interquartile range between 8 and 13μg; suggesting that the individuals used for all climatic periods in this study were of similar size (Table 6-4). The $\delta^{13}C$ and $\delta^{18}O$ values were measured using a Multiprep Dual Inlet system attached to an Isoprime stable isotope ratio mass spectrometer. Each sequential run of the Multiprep included 30-50 individual foraminiferal samples together with 10-15 calcite standards of similar weight (USC Ultissima marble) used to monitor analytical precision. The long-term precision of the Ultissima standard $\delta^{13}C$ and $\delta^{18}O$ values measured during this study was 0.07‰ and 0.09‰ respectively. Individual foraminiferal tests from each discrete sample were run out-of-sequence in order to minimize the effect of analytical uncertainty on the difference in spread among the sampled intervals. There was no observed test weight to $\delta^{18}O$ or $\delta^{13}C$ relationship, suggesting that size was not a factor for depth habitat. A summary of the sedimentary and statistical results is presented in Table 6-4. The measured $\delta^{13}C$, $\delta^{18}O$ and weights of the individual *P. obliquiloculata* are presented in Appendix C.

6.6. Results and Discussion: ENSO changes over the past millennium

6.6.1. ENSO vs calcification depth

Histograms of the δ^{18}O measurements performed on single specimen of *P. obliquiloculata* (Figure 6-8) indicate that in certain core intervals (especially during the MCA), the distribution of individual δ^{18}O values is not Gaussian. Therefore I apply robust statistics (i.e. insensitive to distributional assumptions)

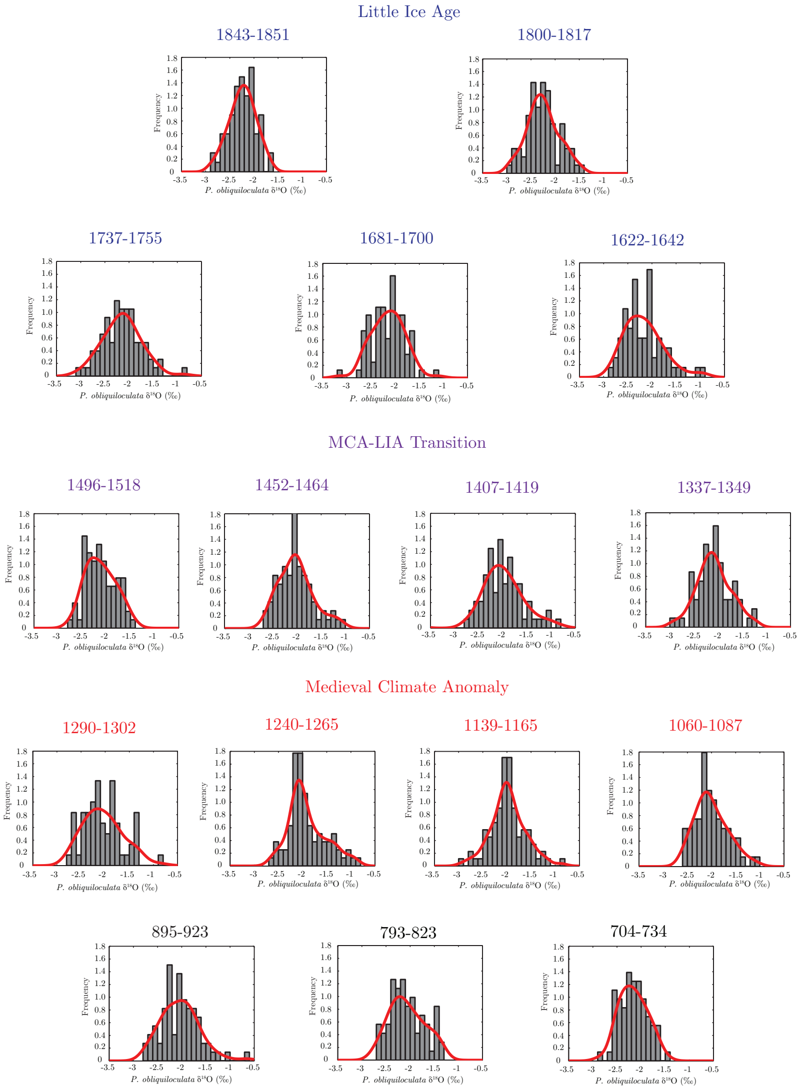

Figure 6-8: *Histograms representing the frequency of individual P. obliquiloculata δ^{18}O values (binned into 0.1‰ intervals) with their respective Kernel density function (red curves) for each time slice.*

to quantify the moments of the δ^{18}O distributions. Furthermore, I need resistant statistics due to (1) the relatively small sample size and (2) the presence of outliers in the distributions. These outliers probably represent individuals of *P. obliquiloculata* that calcified deeper/shallower than the prescribed habitat depth of 55-85m inferred from the sediment trap conducted south of Java (Mohtadi et al., 2009). Specifically, I use the biweight standard deviation (hereafter, BSD (Hoaglin et al., 1983; Lanzante, 1996)) and the Yule-Kendall skewness (YKS, also known as the Bowley or quartile coefficient of skewness (Bowley, 1920)) as measures of spread and of symmetry, respectively. The BSD is estimated through a two-step procedure. First, the median and the median absolute deviation are calculated for each distribution; these estimates are used to discard outliers (Lanzante, 1996). The median absolute deviation is the median of the absolute deviations of the δ^{18}O values from the median of the distribution. Then a weighting scheme is applied such that values that are further away from the median are given less weight. In a Gaussian case, if a value falls more than 5 standard deviations away from the median, it is given a weight of zero (Lanzante, 1996). Using resistant statistics reduces sensitivity to individuals that may have calcified deeper/shallower within the thermocline and allows evaluation of changes in the spread and symmetry associated with the bulk of the δ^{18}O distributions, reducing the sensitivity to individuals that may have calcified deeper/shallower within the thermocline.

The BSD and YKS values for the δ^{13}C and δ^{18}O distributions for the sampled intervals are presented in Table 6-4. The BSD for the δ^{18}O distributions varies between 0.28‰ and 0.41‰, with an average of 0.36‰ similar to the 20th century average inferred from the ORA-S3 reanalysis dataset for the calcification depths ascribed to *P. obliquiloculata*. Furthermore, the BSD of the δ^{18}O distributions has remained remarkably constant through time as shown by the lack of significant changes as measured by the Brown-Forsythe test for the analysis of variance (Brown and Forsythe, 1974); this is a nonparametric test based on the absolute deviation from the median (Table 6-5). Similarly, there is almost no significant change in the BSD of the δ^{13}C distributions over the study period (Table 6-6), which suggests that the range of calcification depth for *P. obliquiloculata* has remained fairly constant over the past millennium. Other lines of evidence for a constant habitat range comes from a direct comparison between the location of the δ^{18}O distributions (quantified here using the biweight mean, a robust and resistant measure of location (Lanzante, 1996)) and that of the δ^{13}C distributions as well as the spread of the δ^{18}O distributions. A shift in the calcification depth of *P. obliquiloculata* should be reflected by a negative relationship between the biweight mean of the δ^{18}O and the δ^{13}C distributions. For instance, if *P.*

Table 6-5: Test matrix from the Brown-Forsythe test for the analysis of variance giving the probability (in%) for the two time slices to have a different $\delta^{18}O$ biweight standard deviation

Age	**1843-1851**	**1800-1817**	**1737-1755**	**1681-1700**	**1622-1642**	**1496-1518**	**1452-1464**	**1407-1419**	**1337-1349**	**1290-1302**	**1240-1265**	**1139-1165**	**1060-1087**	**895-923**	**793-823**
1800-1817	X														
1737-1755	≥99	X													
1681-1700	≥90	X	X												
1622-1642	≥99	X	X	X											
1496-1518	X	X	≥90	X	≥90										
1452-1464	X	X	X	X	X	X									
1407-1419	≥99	≥90	X	X	X	≥90	X								
1337-1349	≥90	X	X	X	X	X	X	X							
1290-1302	≥99	≥90	X	X	X	≥95	X	X	X						
1240-1265	≥95	X	X	X	X	X	X	X	X	X					
1139-1165	X	X	X	X	X	X	X	X	X	X	X				
1060-1087	X	X	X	X	X	X	X	X	X	X	X	X			
895-923	≥99	X	X	X	X	≥90	X	X	X	X	X	X	X		
793-823	≥95	X	X	X	X	X	X	X	X	X	X	X	X	X	
704-734	X	X	≥95	X	≥95	X	X	≥95	X	≥95	X	X	X	≥95	≥90

X: The biweight standard deviations of the two intervals are not statistically different (below the 90% confidence level).

obliquiloculata calcified deeper, the biweight mean of the $\delta^{18}O$ distribution should become more positive while the biweight mean of the $\delta^{13}C$ distributions should decrease (Figure 6-6). Such a relationship is not evident in my dataset (Table 4, slope=0.05, R^2=0.01, not significant at the 90% confidence level, N_{eff}=16). Furthermore, assuming that the vertical distribution of *P. obliquiloculata* within

Table 6-6: Test matrix from the Brown-Forsythe test for the analysis of variance giving the probability (in%) for the two time slices to have a different δ13C biweight standard deviation

Age	**1843-1851**	**1800-1817**	**1737-1755**	**1681-1700**	**1622-1642**	**1496-1518**	**1452-1464**	**1407-1419**	**1337-1349**	**1290-1302**	**1240-1265**	**1139-1165**	**1060-1087**	**895-923**	**793-823**
1800-1817	≥95														
1737-1755	≥95	X													
1681-1700	≥99	X	X												
1622-1642	≥90	X	X	X											
1496-1518	≥90	X	X	X	X										
1452-1464	≥95	X	X	X	X	X									
1407-1419	X	X	X	X	X	X	X								
1337-1349	≥95	X	X	X	X	X	X	X							
1290-1302	≥95	X	X	X	X	X	X	X	X						
1240-1265	≥99	X	X	X	X	X	X	X	X	X					
1139-1165	X	≥95	≥95	≥99	X	X	≥90	X	≥90	X	≥95				
1060-1087	≥95	X	X	X	X	X	X	X	X	X	X	≥95			
895-923	≥99	X	X	X	X	X	X	X	X	X	X	≥99	X		
793-823	≥90	X	X	X	X	X	X	X	X	X	X	X	X	≥90	
704-734	≥95	X	X	X	X	X	X	X	X	X	X	≥90	X	X	X

X: The biweight standard deviations of the two intervals are not statistically different (below the 90% confidence level).

the thermocline is Gaussian, an increase in the calcification range and depth would result in a more positive δ^{18}O biweight mean, representing a shift in the main body of the distribution as well as an increase in the BSD of the δ^{18}O distributions. However, such a relationship is not necessary to explain changes in the strength/frequency of ENSO since El Niño and La Niña events represent the tail of the distribution (Figure 6-5), and changes in the spread can then only be explained by an increase the difference in the mean of El Niño and La Niña distributions, which would not affect the mean of the overall distribution. There is no apparent relationship between changes in the spread and the mean of the $\delta^{18}O$ distributions in my dataset (Table 4, slope=0.18, $R^2=0.20$, not significant at the 90% confidence level, $N_{eff}=16$). Taken together, these three lines of evidence suggest that changes in the range of calcification depths may have played a minimal role in shaping the $\delta^{18}O$ record; therefore I interpret the spread and symmetry of the $\delta^{18}O$ distributions mostly in terms of ENSO.

6.6.2. Inferring ENSO variability over the past millennium

Because the paired radiocarbon and excess Pb-210 measurements used to construct the age model for MD77 suggest that this core is bioturbated over a length of at least ~10cm, adjacent distributions of $\delta^{18}O$ of individual specimens of *P. obliquiloculata* may represent the same time period. This implies that changes in the spread between two adjacent distributions may be representative of the reproducibility associated with the technique and the degree of mixing by bioturbation rather than changes in ENSO variability. However, bioturbation should not affect the reconstruction over centennial timescales. Furthermore, the time window inferred from my age model for each distribution is ~10-30 years, although the effective time slice is probably larger due to bioturbation (I estimate

30-50 years). This time windows may not be long enough to truly assess changes in ENSO variability. To take into account the effect of bioturbation and increase the effective time window in order to capture changes in ENSO variability over centennial timescales, I remove the mean of each distribution and group the $\delta^{18}O$ values into 4 time periods corresponding to the LIA (1500-1850A.D.), the MCA (800-1300A.D.), the transition from the MCA to the LIA (1300-1400A.D.), and the Dark Ages Cold Period (450-750A.D.). Histograms of the $\delta^{18}O$ measurements performed on individual specimens of *P. obliquiloculata* for each of the 4 time periods are presented in Figure 6-9. The BSD value for each of these 4 periods is 0.35‰, 0.37‰, 0.35‰, and 0.35‰ respectively. The increase in the BSD value during the MCA is not significant at the 90% confidence level using the Brown-Forsythe tests for the analysis of variance. Indeed, one of the most notable features of my ENSO record from the western tropical Pacific is that there is no systematic difference in the strength/frequency of ENSO associated with the period broadly defined as the MCA and the LIA (Figure 6-9).

To compare my MD77 record to an ENSO reconstruction derived from a coral $\delta^{18}O$ record from Palmyra Island in the central equatorial Pacific (Cobb et al., 2003), I apply a 2-7 year bandpass filter to the monthly-resolved coral $\delta^{18}O$ record in order to isolate the variability associated with ENSO and then bin the $\delta^{18}O$ values into 20 to 50-year intervals. I then calculate the standard deviation for

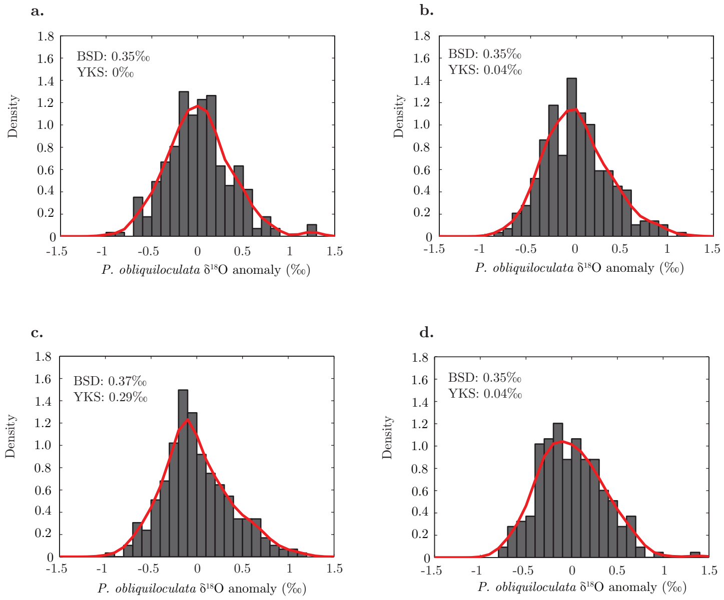

Figure 6-9: *Histograms representing the frequency of individual P. obliquiloculata* $\delta^{18}O$ *values (binned into 0.1‰ intervals) with their respective Kernel density function (red curves) for the* ***a.*** *LIA,* ***b.*** *the transition from the LIA to the MCA,* ***c.*** *the MCA and* ***d.*** *the Dark Ages Cold Period. The spread of the δ18O distributions, as measured by the BSD, is similar among these distributions. This suggests that ENSO has remained remarkably constant on centennial timescales over the past millennium. The MCA was also characterized by a positively skewed distribution, suggesting an increase in the relative strength/frequency of La Niña compared to El Niño.*

each bin (Table 6-7, Figure 6-10). The standard deviation for binned coral δ^{18}O values varies between 0.07‰ and 0.13‰, after exclusion of the 0.04‰ value that corresponds to a window of only 14 years. Albeit small, these differences are significant at the 90% confidence level (Table 6-8) and suggest that the LIA (standard deviation=0.11‰) was characterized by periods of greater ENSO variability than the MCA (standard deviation=0.08‰) or the 20th century (standard deviation=0.10‰);

Table 6-7: *Statistical results for each time slice sampled from the Palmyra coral record*

Time Slice	Standard Deviation (‰)	Pearson's coefficient of skewness (‰)
928-961	0.09	0.00
1149-1199	0.08	0.07
1200-1220	0.08	0.61
1317-1367	0.07	-0.32
1368-1406	0.10	-0.56
1326-1357	0.09	-0.16
1398-1448	0.08	-0.21
1349-1363	0.04	0.15
1405-1448	0.09	-0.15
1412-1443	0.07	-0.39
1635-1666	0.13	-0.32
1653-1695	0.11	1.22
1665-1703	0.10	0.03
1915-1937	0.09	0.16
1886-1936	0.11	0.00
1937-1998	0.11	0.02

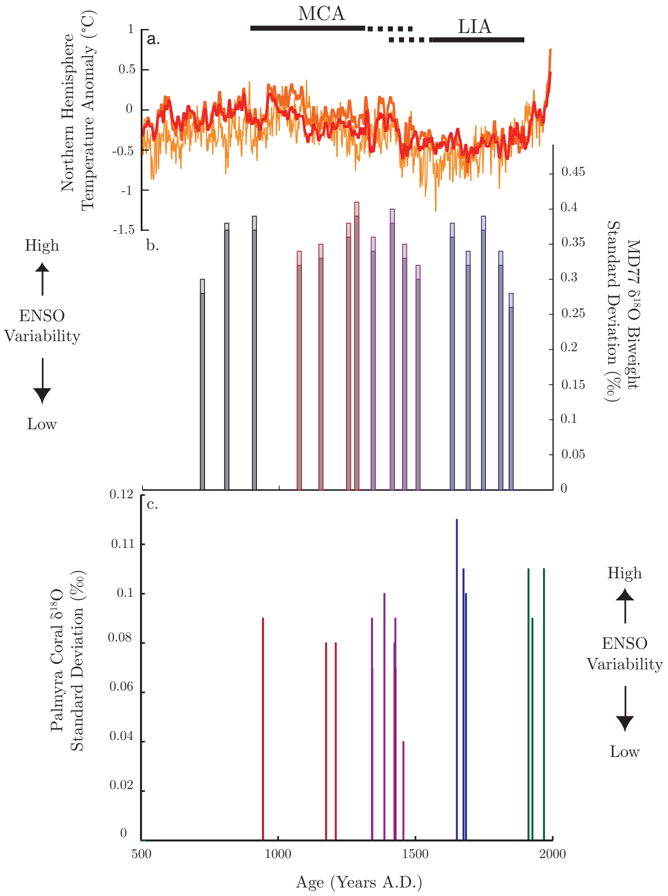

Figure 6-10: Changes in ENSO variability over the past millennium. a. *Northern Hemisphere temperature anomaly reconstructions from Moberg et al. (2005, orange), and Mann et al. (2008) (land EIV temperature composite, dark orange, land + ocean EIV composite, red).* ***b.*** *Biweight standard deviation values for each time slice sampled from MD98-2177. The light grey bars represent the BSD values for the entire dataset. The dark grey bars represent the BSD values for the trimmed dataset in which the highest and lowest $\delta^{18}O$ values were removed from the original dataset. The statistics of the trimmed dataset are not significantly different from that of the full distribution, which is consistent with the use of resistant statistics to quantify the moments of the distribution. Changes in ENSO variability, as measured by the BSD, are small and not significant on centennial time scale.* ***c.*** *Standard deviation values for each time slice sampled from the Palmyra Island coral $\delta^{18}O$ record (Cobb et al., 2003). The blue, purple, red and black bars correspond to the intervals representing the LIA, the transition form the LIA to the MCA, the MCA, and the Dark Ages Cold Period respectively.*

a conclusion consistent with that of Cobb et al. (2003). However, a closer examination of the record suggests that changes in ENSO variability within the MCA and the LIA have the same (or greater) magnitude than differences between the MCA and LIA. The standard deviation for the binned coral $\delta^{18}O$ values corresponding to the period ~900-1450 A.D. varies between 0.07‰ and 0.1‰; changes that are significant at the 90% confidence level using a F-test (Table 6-8). Similarly, the standard deviation for the binned coral $\delta^{18}O$ values corresponding to LIA varies between 0.10‰ and 0.13‰. This 0.03% range within

Table 6-8: *Test matrix from the Fischer F-test for the analysis of variance giving the probability that two time slices have a different $\delta^{18}O$ standard deviation.*

Age	**928-961**	**1149-1199**	**1200-1220**	**1317-1367**	**1368-1406**	**1326-1357**	**1398-1448**	**1349-1363**	**1405-1448**	**1412-1443**	**1635-1666**	**1653-1695**	**1665-1703**	**1915-1937**	**1886-1936**
1149-1199	≥95														
1200-1220	X	X													
1317-1367	≥99	≥99	≥99												
1368-1406	≥90	≥99	≥99	≥99											
1326-1357	X	≥99	≥90	≥99	X										
1398-1448	≥99	X	≥90	≥99	≥99	≥99									
1349-1363	≥99	≥99	≥99	≥99	≥99	≥99	≥99								
1405-1448	X	≥95	X	≥99	≥99	X	≥99	≥99							
1412-1443	≥99	≥95	≥99	X	≥99	≥99	X	≥99	≥99						
1635-1666	≥99	≥99	≥99	≥99	≥99	≥99	≥99	≥99	≥99	≥99					
1653-1695	≥99	≥99	≥99	≥99	≥99	≥99	≥99	≥99	≥99	≥99	≥99				
1665-1703	≥95	≥99	≥99	≥99	X	X	≥99	≥99	≥99	≥99	≥99	≥99			
1915-1937	X	X	X	≥99	≥95	X	≥99	≥99	X	≥99	≥99	≥99	≥95		
1886-1936	≥99	≥99	≥99	≥99	≥95	≥99	≥99	≥99	≥99	≥99	≥99	X	≥95	≥99	
1937-1998	≥99	≥99	≥99	≥99	≥99	≥99	≥99	≥99	≥99	≥99	≥99	X	≥99	≥99	X

X: The standard deviations of the two intervals are not statistically different (below the 90% confidence level).

the MCA and LIA intervals is significant at the 90% confidence level (Table 6-8) and of similar magnitude as between the MCA and LIA intervals. A similar comparison for the MD77 record is more difficult because of bioturbation, especially for the intervals corresponding to the LIA. However the BSD for the A.D. 1496-1518 intervals is significantly lower (90% confidence level, Table 6-5) than that for the A.D. 1290-1302 and A.D. 895-925 intervals. These intervals are located 18.5cm and 48cm apart, respectively, limiting the effect of biotubation on the statistics of the distribution. This analysis on my MD77 record suggests that decadal changes in the strength/frequency of both El Niño and La Niña events are larger on decadal timescale than on centennial to millennial timescales.

Table 6-9: *Test matrix giving the probability (in %) that the distribution is asymmetric*

Age	δ^{18}O	δ^{13}C
1843-1851	X	X
1800-1817	X	X
1737-1755	X	≥90
1681-1700	≥95	X
1622-1642	X	X
1496-1518	X	X
1452-1464	X	X
1407-1419	X	≥95
1337-1349	X	X
1290-1302	≥90	X
1240-1265	≥99	X
1139-1165	X	X
1060-1087	≥99	X
895-923	X	X
793-823	≥99	≥99
704-734	X	X

6.6.3. El Niño vs. La Niña History

In my western Pacific record, the period that corresponds to the MCA and the transition into the LIA is characterized by stronger/more frequent La Niñas than El Niños (Table 6-4, Figure 6-11) as evidenced by the presence of several

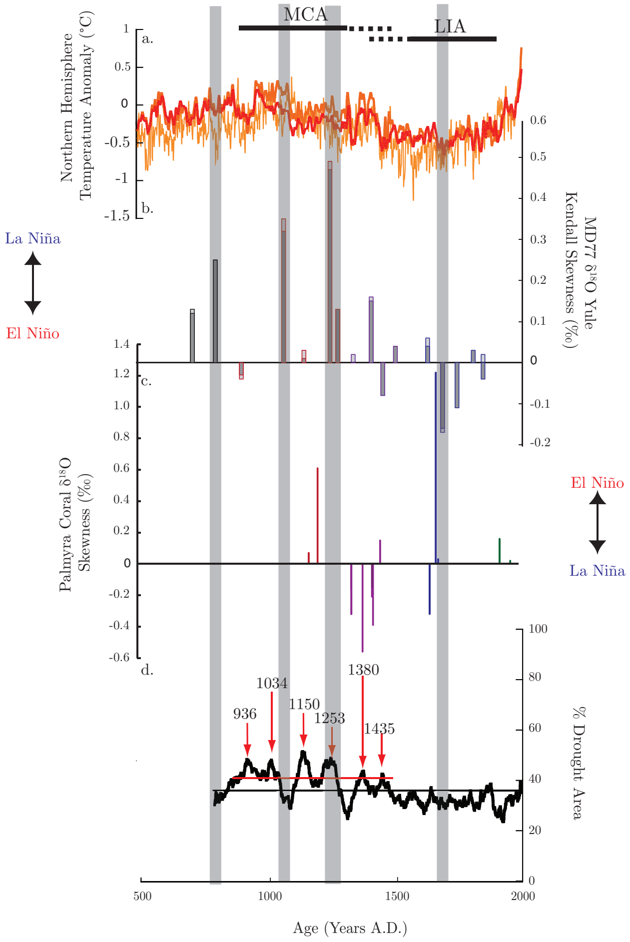

Figure 6-11: El Niño vs. La Niña over the past millennium. a. *Northern Hemisphere temperature anomaly reconstructions from Moberg et al. (2005, orange), and Mann et al. (2008) (land EIV temperature composite, dark orange, land + ocean EIV composite, red).* ***b.*** *Yule Kendall Skewness values for each time slice sampled from MD98-2177. The light grey bars represent the BSD values for the entire dataset. The dark grey bars represent the YKS values for the trimmed dataset in which the highest and lowest* $\delta^{18}O$ *values were removed from the original dataset. The statistics of the trimmed dataset are not significantly different from that of the full distribution, which is consistent with the use of resistant statistics to quantify the moments of the distribution. The intervals with a significant skewness are highlighted in grey. In this record, the MCA is characterized by stronger/more frequent La Niña than El Niño.* ***c.*** *Pearson's coefficient of skewness values for each time slice sampled from the Palmyra Island coral* $\delta^{18}O$ *record (Cobb et al., 2003). The blue, purple, red and black bars correspond to the intervals representing the LIA, the transition form the LIA to the MCA, the MCA, and the Dark Ages Cold Period respectively.* ***d.*** *Drought area index (50-year smooth) for western North America over the past millennium (Cook et al., 2004), with the long-term mean (horizontal black line). The arrows indicate the time of the medieval megadroughts (Cook et al., 2004; Cook et al., 2007; Herweijer et al., 2007; Seager et al., 2008), which correspond within age uncertainty to stronger/more frequent La Niña events than El Niño in the MD77 and Palmyra record.*

significantly (Table 6-5) positively skewed $\delta^{18}O$ distributions during this time interval. When taken together in order to reduce the effect of bioturbation on the MD77 record, the YKS value for the distributions corresponding to the MCA is 0.29‰, which is significant at the 90% significance level. This high YKS value is partly attributable to the assumed increase in *P. obliquiloculata* productivity during La Niña events (Section 6.4.4), which reinforces the original positive skewness attributed to increased strength/frequency of La Niña compared to El Niño. This result is consistent with negative values for the Pearson's coefficient of skewness for the Palmyra coral δ^{18}O distributions (Table 6-9, Figure 6-11) that indicate there was a departure toward stronger La Niña compared to El Niño between A.D. 1300 and A.D. 1450, which corresponds within age uncertainty to the positively skewed intervals between A.D.1240-1265 and A.D. 1290-1302 in the MD77 record.

Table 6-10: *Probability (in%) that the coral $\delta^{18}O$ distributions is asymmetric*

Time slice	Probability (%)
928-961	X
1149-1199	X
1200-1220	≥90
1317-1367	≥99
1368-1406	X
1326-1357	≥90
1398-1448	≥99
1349-1363	X
1405-1448	X
1412-1443	≥99
1635-1666	≥99
1653-1695	X
1665-1703	≥95
1915-1937	≥90
1886-1936	≥99
1937-1998	X

The MCA was a period characterized by recurrent widespread droughts over western North America as reconstructed from a network of drought-sensitive trees. These so-called medieval megadroughts occurred at A.D. 1021-1051, A.D. 1240-1265, and A.D. 1413-1460 (Cook et al., 2007; Cook et al., 2004, Figure 6-11). Modeling studies (Burgman et al., 2010; Herweijer et al., 2007; Seager et al., 2008) link these megadroughts to La Niña-like conditions in the tropical Pacific. Such conditions are evident in the MD77 YKS record as well as in the relatively cooler and more saline (lower precipitation) conditions documented in δ^{18}O values of the Palmyra corals between A.D. 950 and A.D 1250 (Cobb et al., 2003) as well as cooler conditions inferred from a diatom record from El Junco Lake, Galapagos (Conroy et al., 2009). However, this is in sharp contrast with studies by Conroy et al. (2008) and Moy et al. (2002), who inferred greater precipitation over the Galapagos and Southern Ecuador during the MCA, which the authors attributed to increased frequency of El Niño during that period. This discrepancy was pointed out by Conroy et al. (2010), who argued that these disparities are related to different factors influencing the El Junco lake environment. Furthermore, an increase in the strength/frequency of both El Niño and La Niña events (with a larger increase in La Niña vs El Niño events to account for the skewness in the MD77 record) cannot explain this discrepancy in the El Junco records since this simultaneous increase would result in higher BSD/ standard deviation values in the MD77 record or the Palmyra record, which are not observed (Figure 6-10).

The Palmyra record also suggests that there were stronger/more frequent El Niño during the 17th century (Figure 6-11), which corresponds within age model uncertainty to the interval 1681-1700 A.D. in my MD77 record. On the other hand, the YKS value for the LIA distributions is 0, which indicates that El Niño was not significantly stronger/more frequent than La Niña during that period. This discrepancy may be explained by my assumed increase in productivity in *P. obliquiloculata* during La Niña, which would bias the MD77 record against stronger/more frequent El Niño events.

6.7. Conclusions

In this study I explored the use of δ^{18}O and δ^{13}C of individual *P. obliquiloculata* from marine sediment core MD98-2177 to investigate the history of ENSO variability during the past millennium. Changes in ENSO behavior was inferred from both the spread (BSD) and the symmetry (YKS) of individual δ^{18}O values of *P. obliquiloculata* from a sediment sample. Changes in the spread were used as a metric ENSO strength/frequency (i.e. simultaneous change in the strength/frequency of both El Niño and La Niña events) while the symmetry was interpreted in terms of the relative strength of El Niño and La Niña events. The main limitation of this proxy is the possibility that the depth habitat of *P. obliquiloculata* may change. This limitation was evaluated by comparing changes in the spread of the δ^{18}O values to those of the δ^{13}C values to distinguish between changes due to ENSO variability and varying habitat depth.

My results indicate that the strength/frequency of ENSO, as inferred from the spread of the δ^{18}O distributions, during the MCA and during the LIA was not statistically distinguishable and was comparable to that of the 20th century as inferred from the ECMWF-ORA S3 reanalysis dataset. On the other hand, a coral record from the central Pacific (Cobb et al., 2003) shows that the LIA was characterized by an increase in strength/frequency of ENSO events compared to the MCA or the 20th century. Both records document fairly large decadal changes in ENSO strength/frequency but smaller changes at centennial timescales. In my MD77 record, the MCA was also marked by an increase in the amplitude/ frequency of La Niña events compared to El Niño (as evidenced by several positively skewed intervals in the MD77 record), in line with proxy evidence from the central and eastern tropical Pacific that suggests relatively cool conditions prevailed during this time period (Cobb et al., 2003; Conroy et al., 2009). However, these results are in sharp contrast with the studies by Moy et al. (2002) and Conroy et al. (2008), which show an increase in the frequency of El Niño events during this time period. These periods of stronger La Niña as opposed to El Niño correspond within age model uncertainty to the time of medieval megadroughts in western North America (Cook et al., 2007; Cook et al., 2004). These megadroughts have been hypothesized to be caused by an increase in the strength/frequency of La Niña events, a theory supported by my record.

Chapter 7:

Conclusions

The purpose of these studies was to assess the role of natural tropical variability in the current warming trend. More specifically, the studies presented in this dissertation help provide some answers to the five questions presented in the introduction.

7.1. How have topographic changes affected the Indonesian Throughflow?

Studying the past 25,000years of the oceanographic history of the Indonesian Seas provide a unique opportunity to study how topographical barriers can affect the flow of the ITF, and therefore the heat and freshwater fluxes from the Pacific to the Indian Ocean. In the modern ocean, ~80% of the ITF flows within the Makassar Strait (Gordon, 2005), and is mainly composed of North Pacific thermocline water (Sprintall, 2009). Most of the transport occurs within the thermocline as a result of the seasonal changes in monsoonal winds (Gordon, 2005; Gordon et al., 2008). During the Australian (northwestern) monsoon, the wind transports the low-salinity buoyant Java Sea water into the Makassar Strait, essentially creating a surface "plug" and increasing the transport within the thermocline (Gordon, 2005; Gordon et al., 2003a; Susanto and Gordon, 2005). The southeastern monsoon winds constrain southward water flow out of the

Makassar Strait, also enhancing thermocline transport from July to September (Gordon, 2005; Gordon et al., 2003a).

However, at the Last Glacial Maximum, when sea level was ~120m lower than today, the Sunda Shelf was exposed (Sathiamurthy and Voris, 2006), essentially preventing Java Sea water from entering the southern Makassar Strait. According to modeling experiments (Tozuca et al., 2007), this would result in enhanced surface flow and heat transport (0.18PW) to the Indian Ocean. The flooding of the Sunda Shelf and the reestablishment of the winter "freshwater plug" at 9.5k is evident in the $\delta^{18}O_{sw}$ records from the western Pacific Warm Pool and the Makassar Strait. However, there is no evidence for decreased heat flux toward the Indian Ocean at this time. There are two possible explanations for this lack of evidence: (1) the proxies are not sensitive enough to record small changes in the SST gradient resulting from enhanced thermocline flow, or/and (2) the ITF does not play such a vital role in controlling Indian Ocean sea surface temperature as inferred from modeling studies.

7.2. What is the hydrographic variability associated with the East Asian Monsoon and ENSO?

The East Asian monsoon seems to be the dominant control of the SSS variability of the Indonesian Seas on millennial timescale, especially in the Makassar Strait (Chapter 4 and Chapter 5). It also seems to play a role in regions that are prone to upwelling such as the Arafura Sea (Chapter 5). On the other hand, ENSO does not seem to influence the SST in this region as evidenced by the lack of a strong ENSO signal in the Indonesian records over the Common Era (Chapter 5). This is not surprising considering that the surface temperature anomalies associated with the modern ENSO are small in this region (Chapter 2).

Previous attempts have been made to quantify the state of the tropical Pacific in term of El Niño-like or La Niña-like conditions by taking the gradients between sedimentary records from the Indonesian Seas with temperature records from the eastern equatorial Pacific (Conroy et al., 2010; Koutavas et al., 2006). This approach should be used with care as (1) the uncertainty in the age models of the two records can lead to false changes in the SST gradient, and (2) modern ENSO anomalies in this region are small, with a complex signature and a nodal point in the Makassar Strait.

7.3. What was the behavior of ENSO in the past?

ENSO is the leading mode of interannual climate variability with widespread repercussions on weather patterns and their associated socio-economic impacts. Therefore quantifying the behavior of ENSO during warm and cold periods in Earth's history represents the best opportunity we have to validate models that attempt to simulate changes in ENSO when forced with increased greenhouse gas concentrations. Unlike the surface, the thermocline structure of the Northern

Makassar Strait is very sensitive to ENSO. Furthermore, this location allows to capture changes in the variability of the eastern and central Pacific types of ENSO. From the $\delta^{18}O_c$ measurements of hundreds of individuals of the thermocline-dweller *P. obliquiloculata* over the past 1300 years, there does not seem to be changes in the strength/frequency of ENSO as measured by the spread of the $\delta^{18}O$ distributions associated with the warm conditions of the MCA or the cold conditions of the LIA. On the other hand, the MCA was characterized by decades of stronger/more frequent La Niña than El Niño as measured by the symmetry of the $\delta^{18}O$ distributions, corresponding within age uncertainty, to the medieval megadroughts found in tree-ring records from the Southerwestern United States (Cook and Krusic, 2004; Cook et al., 2007; Cook et al., 2004).

7.4. What is the range of sea surface temperature variability that can be expected in the Indonesian Seas?

The new estimates for SST change at the LGM obtained from Mg/Ca/$\delta^{18}O_c$ suggests at 4-4.5°C cooling in the Indonesian region. This is in sharp contrast with the finding of CLIMAP (1976) and MARGO (2009), who reported changes of ~2°C in most of the tropical Pacific, including the Indo-Pacific warm pool. These new results suggest that the tropics are capable of undergoing more profound SST changes than previously thought. SST started to rise ~17ka and reach Holocene temperature at ~11ky B.P. Assuming a linear rate of SST rise, this would correspond to a change of ~0.7°C/1000 years, 10 times less than the modern rate of tropical ocean warming of ~0.6-1°C/century (Deser et al., 2010). However, a closer examination of the composite record (Figure 4-3) shows period of more rapid SST change, such as the Bølling-Allerød period. Then, SST increased by ~2.5°C over the course of 2000 years, or 0.3°C/century. This is about half of the modern rate of tropical warming.

The MCA seems to have been, on average, cooler than the 20th century, although several decades have approached 20th century warmth. The ~0.5-1°C drop is SST from the MCA to the LIA occurred within 5 centuries. Even by taking the upper estimate of SST variability associated with the MCA/LIA, the rate of temperature change is ~0.2°C/century, an estimate close to that inferred for the Bølling-Allerød period. However, the rate of surface warming never approached that of the 20th century over the course of the last 25,000 years in this region.

7.5. Were changes in the Indonesian Seas generally coincident with North Atlantic climate change?

Within the age uncertainty associated with each of the proxy records, the answer to this question seems to be yes. The deglacial history of the Indonesian Seas is similar to that of the North Atlantic. In the Indo-Pacific Warm Pool, the deglaciation started at ~17ka, and was marked by an abrupt warming culminating at ~12.5ka, broadly consistent with the Bølling-Allerød in the Greenland ice core record (GISP2, Figure 4-3). SST then dropped slightly (~0.5°C) during the Younger Dryas. More importantly, however, the Bølling-Allerød/Younger Dray was characterized by large changes in SSS, coincident with changes in the strength of the Asian Monsoon as recorded by Chinese speleothems (Wang et al., 2008; Wang et al., 2001). Taken together, these records indicate a major reorganization of the Northern Hemisphere atmospheric circulation coincident with Greenland temperature change (Figure 4-3). Furthermore, the timing of temperature variability over the past 2000 years is consistent with Northern Hemisphere multi-proxy reconstruction with warmer (cooler) sea surface conditions during the MCA (LIA). However, the age uncertainty associated with each of the records presented in this study prevents a meaningful assessment of the relative timing of Indonesian vs Northern Hemisphere changes; and, therefore, does not allow for assessing a causal link between climate change in the Northern Hemisphere and the tropics.

Bibliography

Abram, N.J., McGregor, H.V., Gagan, M.K., Hantoro, W.S., Suwargadi, B.W., 2009. Oscillations in the southern extent of the Indo Pacific Warm Pool during the mid-Holocene. Quaternary Science Reviews 28, 2794-2863.

Adkins, J.F., McIntyre, K., Schrag, D.P., 2002. The salinity, temperature, and $\delta^{18}O$ of the glacial deep ocean. Science 298, 1769-1773.

Adkins, J.F., Schrag, D.P., 2003. Reconstructing the Last Glacial Maximum bottom water salinities from deep-sea sediment pore fluid profiles. Earth and Planetary Science Letters 216, 109-123.

Aldrian, E., Susanto, R.D., 2003. Identification of three dominant rainfall regions within Indonesia and their relationship to sea surface temperature. International Journal of Climatology 23, 1435-1452.

Ammann, C.M., Joos, F., Schimel, D.S., Otto-Bliesner, B.L., Tomas, R.A., 2007. Solar influence on climate during the past millennium: Results from transient simulations with the NCAR Climate System Model. . Proceeding of the National Academy of Sciences 104, 3713-3718.

An, S.-I., Jin, F.-F., 2004. Nonlinearity and asymmetry of ENSO. Journal of Climate 17, 2399-2412.

Anand, P., Elderfield, H., Conte, M.H., 2003. Calibration of Mg/Ca thermometry in planktonic foraminifera from a sediment trap time series. Paleoceanography 18, 1050.

Anderson, R.Y., 1992. Long-term changes in the frequency of occurence of El Niño events, in: Diaz, H.F., Markgraf, V. (Eds.), El Niño: Historical and paleoclimatic aspects of the Southern Oscillation. Cambridge University Press, Cambridge, pp. 193-200.

Antonov, J.I., Seidov, D., Boyer, T.P., Locarnini, R.A., Mishonov, A.V., Garcia, H.E., 2010. World Ocean Atlas 2009, Volume 2: Salinity. U.S. Government Printing Office, Washington, D.C.

Arbuszewski, J., DeMenocal, P., Kaplan, A., Farmer, E.C., 2010. On the fidelity of shell-derived $\delta^{18}O_{seawater}$ estimates. Earth and Planetary Science Letters 300, 186-196.

Ashok, K., Behera, S.K., Rao, S.A., Weng, H., Yamagata, T., 2007. El Niño Modoki and its possible teleconnection. Journal of Geophysical Research 112, C11007.

Ashok, K., Yamagata, T., 2009. The El Niño with a difference. Nature, 481-482.

Babkina, A.M., 2003. El Niño: Overview and Bibliogprahy. Nove Science Publishers, Hauppauge, New York.

Balmaseda, M.A., Dee, D., Vidard, A., Anderson, D.L.T., 2007. A multivariate treatment of bias for sequential data assimilation: Application to the tropical oceans. Quarterly journal of the royal meteorological society 133, 167-179.

Balmaseda, M.A., Vidard, A., Anderson, D.L.T., 2008. The ECMWF Ocean Analysis System: ORA-S3. Monthly Weather Review 136, 3018-3034.

Barker, S., Cacho, I., Benway, H., Tachikawa, K., 2005. Planktonic foraminiferal Mg/Ca as a proxy for past oceanic temperatures: a methodological overview and data compilation for the Last Glacial Maximum. Quaternary Science Reviews 24, 821-834.

Barker, S., Greaves, M., Elderfield, H., 2003. A study of cleaning procedures used for foraminiferal Mg/Ca paleothermometry. Geochemistry, Geophysics, Geosystems 4, 8407.

Battisti, D.S., Hirst, A.C., 1989. Interannual variability in the tropical atmosphere-ocean model: Influence of the basic state, ocean geometry, and nonlinearity. Journal of Atmospheric Science 45, 1687-1712.

Bé, A.W.H., Tolderund, D.S., 1971. Distribution and ecology of living planktonic foraminifera in surface waters of the Atlantic and Indian Oceans, in: Funnell, B.M., Riedel, W.R. (Eds.), The Micropaleoontology of Oceans. Cambridge University Press, Cambridge, U.K., pp. 105-149.

Bell, M.J., Martin, M.J., Nichols, N.K., 2004. Assimilation of data into an ocean model with systematics errors near the equator. Quarterly journal of the royal meteorological society 130, 873-893.

Bemis, B.E., Spero, H.J., Bijma, J., Lea, D.W., 1998. Reevaluation of the oxygen isotopic composition of planktonic foraminifera: Experimental results and revised paleotemperature equations. Paleoceanography 13, 150-160.

Bender, M.L., Lorens, R.B., Williams, D.F., 1975. Sodium, magnesium, and strontium in the tests of planktonic foraminifera. Micropaleontology 21, 448-459.

Bentov, S., Erez, J., 2006. Impact of biomineralization processes on the Mg content of foraminiferal shells: a biologic perspective. Geochemistry, Geophysics, Geosystems 7.

Benway, H.M., Mix, A.C., 2004. Oxygen isotopes, upper-ocean salinity, and precipiation sources in the eastern tropical Pacific. Earth and Planetary Science Letters 224, 493-507.

Berger, W.H., Bonneau, M.C., Parker, F.L., 1982. Foraminifera on the deep-sea floor: Lysocline and dissolution rate. Oceanologica Acta 5, 249-258.

Bjerknes, J., 1969. Atmospheric teleconnection from the equatorial Pacific. Monthly Weather Review 97, 163-172.

Bond, G., Kromer, B., Beer, J., Muscheler, R., Evans, M.N., Showers, W., Hoffmann, S., R., L.-B., Hajdas, I., Bonani, G., 2001. Persistent solar influence on North Atlantic climate during the Holocene. Science 294, 2130-2136.

Bond, G., Showers, W., Cheseby, M., Lotti, R., Almasi, P., deMenocal, P., Priore, P., Cullen, H., Hajdas, I., Bonani, G., 1997. A pervasive millennial-scale cycle in North Atlantic Holocene and glacial climates. Science 278, 1257-1266.

Bowley, A.L., 1920. Elements of statistics. Scribner, New York.

Boyle, E.A., Keigwin, L.D., 1985. Comparison of Atlantic and Pacific paleochemical records for the last 250,000 years: changes in deep ocean circulation and chemical inventories. Earth and Planetary Science Letters 76, 135-150.

Bradley, R.S., Briffa, K.R., Cole, J.E., Hughes, M.K., Osborn, T.J., 2003. The Climate of the Last Millennium, in: Alverson, K.D., Bradley, R.S., Pedersen, T.F. (Eds.), Paleoclimate, global changes and the future. Springer-Verlag, Berlin Heidelberg, Germany, pp. 105-141.

Bray, N.A., Hautala, S., Chong, J., Pariwono, J., 1996. Large-scale sea level, thermocline, and wind variations in the Indonesian Throughflow region. Journal of Geophysical Research 101, 12,239-212,254.

Broccoli, A.J., Dahl, K.A., Stouffer, R.F., 2006. Response of the ITCZ to northern hemisphere cooling. Geophysical Research Letters 33.

Broecker, W.S., 1997. Thermohaline circulation, the Achilles heel of our climate system: will man-made CO_2 upset the current balance? Science 278, 1582-1588.

Broecker, W.S., 1998. Paleocean circulation during the last deglaciation: a bipolar seesaw? Paleoceanography 13, 119-121.

Broecker, W.S., 2000. Was a change in thermohaline circulation responsible for the Little Ice Age? Proceedings of the National Academy of Sciences 97, 1339-1342.

Broecker, W.S., 2001. Was the Medieval Warm Period Global? Science 291, 1497-1499.

Broecker, W.S., Hemming, S., 2001. Climate swings come into focus. Science 294, 2308-2309.

Brooks, C.E.P., 1922. The evolution of climate, London.

Brown, M.B., Forsythe, A.B., 1974. Robust tests for the equality of variances. Journal of the American Statistical Association 69, 364-367.

Brown, S., Elderfield, H., 1996. Variations in Mg/Ca and Sr/Ca ratios of planktonic foraminifera caused by postdepositional dissolution: evidence of shallow Mg-dependent dissolution. Paleoceanography 11, 543-551.

Burgers, G., Stephenson, D.B., 1999. The "normality' of El Niño. Geophysical Research Letters 26, 1027-1030.

Burgman, R., Seager, R., Clement, A., Herweijer, C., 2010. The role of tropical Pacific SSTs in global medieval hydroclimate: A modeling study. Geophysical Research Letters.

Cane, M., 1998. A role for the Tropical Pacific. Science 282, 59-61.

Cane, M.A., 2005. The evolution of El Niño, past and future. Earth and Planetary Science Letters 230, 227-240.

Chagnon, S.A., 2000. El Niño 1997-1998: The Climate Event of the Century. Oxford University Press, Oxford, New York.

Chappell, J., Shackleton, N.J., 1986. Oxygen isotopes and sea level. Nature 324, 137-140.

Chen, D., Cane, M.A., 2008. El Niño prediction and predictability. Journal of Computational Physics 227, 3625-3640.

Chilingar, G.V., 1962. Dependence on temperature of Ca/Mg ratio of skeletal structures of organisms and direct chemical precipitates out of sea water. Bulletin of the Southern California Academy of Sciences 61, 45-61.

Cleroux, C., Cortijo, E., Anand, P., Labeyrie, L., Bassinot, F., Caillon, N., Duplessy, J.C., 2008. Mg/Ca and Sr/Ca ratios in planktonic foraminifera: proxies for upper water column temperature reconstruction. Paleoceanography 23, PA3214.

Cleroux, C., Cortijo, E., Duplessy, J.C., Zahn, R., 2007. Deep-dwelling foraminifera as thermocline temperature recorders. Geochemistry, Geophysics, Geosystems 8, Q04N11.

CLIMAP Project Members, 1976. The surface of the Ice-Age Earth. Science 191, 1131-1137.

Cobb, K.M., Charles, C.D., Cheng, H., Edwards, R.L., 2003. El Niño/Southern Oscillation and tropical Pacific climate during the last millennium. Nature 424, 271-276.

Conroy, J.L., Overpeck, J.T., Cole, J.E., 2010. El Niño/Southern Oscillation and changes in the zonal gradient of tropical Pacific sea surface temperature over the last 1.2ka. PAGES news 18, 32-34.

Conroy, J.L., Overpeck, J.T., Cole, J.E., Shanahan, T.M., Steinitz-Kannan, M., 2008. Holocene changes in eastern tropical Pacific climate inferred from a Galapagos lake sediment record. Quaternary Science Reviews 27, 1166-1180.

Conroy, J.L., Restrepo, A., Overpeck, J.T., Steinitz-Kannan, M., Cole, J.E., Bush, M.B., Colinvaux, P.A., 2009. Unprecendented recent warming of surface temperatures in the eastern tropical Pacific Ocean. Nature geoscience 2, 46-50.

Cook, E., Krusic, P., 2004. North American Summer PDSI reconsctructions. , IGBP PAGES/World Data Center for Paleoclimatology, Data Contribution Series 2004-045. NOAA/NGDC, Paleoclimatology Program, Boulder, CO.

Cook, E.R., Anchukaitis, K.J., Buckley, B.M., D'Arrigo, R.D., Jacoby, G.C., Wright, W.E., 2010. Asian Monsoon failure and megadrought during the last millennium. Science 328, 486-489.

Cook, E.R., Seager, R., Cane, M.A., Stahle, D.W., 2007. North American drought: Reconstructions, causes, and consequences. Earth Science Reviews 81, 93-134.

Cook, E.R., Woodhouse, C.A., Eakin, C.M., Meko, D.M., Stahle, D.W., 2004. Long-term aridity changes in the Western United States. Science 306, 1015-1018.

Crowley, T.J., 2000. Causes of climate change over the past 1000 years. Science 289, 270-277.

Crowley, T.J., Lowery, T.S., 2000. How warm was the Medieval Warm Period? A coment on 'Man-made versus natural climate change'. Ambio 39, 51-54.

D'Arrigo, R., Wilson, R., Jacoby, G., 2006. On the long-term context for late twentieth century warming. Journal of Geophysical Research 111, D03103.

de Villiers, S., 2003. Dissolution effects on foraminiferal Mg/Ca records of sea surface temperature in the western equatorial Pacific. Paleoceanography 18, 1070.

Dekens, P.S., Lea, D.W., Pak, D.K., Spero, H.J., 2002. Core top calibration of Mg/Ca in the tropical foraminifera: Refining paleotemperature estimation. Geochemistry, Geophysics, Geosystems 3, 1022.

Delaney, M.L., Bé, A., Boyle, E.A., 1985. Li, Sr, Mg, and Na in foraminiferal calcite shells from laboratory culture, sediment traps, and sediment cores. Geochimica et Cosmochimica Acta 49, 1327-1341.

Delaygue, G., Jouzel, J., Dutay, J.-C., 2000. Oxygen 18-salinity relationship simulated by an oceanic general circulation model. Earth and Planetary Science Letters 178, 113-123.

Denton, G.H., Anderson, R.F., Toggweiler, J.R., Edwards, R.L., Schaefer, J.M., Putman, A.E., 2010. The last glacial termination. Science 328, 1652-1656.

Deser, C., Phillips, A.S., Alexander, M.A., 2010. Twentieth century tropical sea surface temperature trends revisited. Geophysical Research Letters 37, L10701.

Dueñas-Bohorquez, A., da Rocha, R.E., Kuroyanagi, A., Bijma, J., Reichart, G.-J., 2009. Effect of salinity and seawater calcite saturation state on Mg and Sr incorporation in cultured planktonic foraminifera. Marine Micropaleontology 73, 178-189.

Dunbar, R.B., Wellington, G.M., Colgan, M.W., Glynn, P.W., 1994. Eastern Pacific sea surface temperature since 1600 A.D.: The δ^{18}O record of climate variability in the Galapagos corals. Paleoceanography 9, 291-315.

Duplessy, J.C., Labeyrie, L., Waelbroeck, C., 2002. Constraints on the ocean oxygen isotopic enrichment between the Last Glacial Maximum and the Holocene: Paleoceanographic implications. Quaternary Science Reviews 21, 315-330.

Dykoski, C.A., Edwards, R.L., Cheng, H., Yuan, D., Cai, Y., Zhang, M., Lin, Y., Qing, J., An, Z., Revenaugh, J., 2005. A high-resolution, absolute-dated Holocene and deglacial Asian monsoon record from Dongge Cave, China. Earth and Planetary Science Letters 23, 71-86.

Elderfield, H., Bertram, C.J., Erez, J., 1996. A biomineralization model for the incorporation of trace elements into foraminiferal calcium carbonate. Earth and Planetary Science Letters 142, 409-423.

Elderfield, H., Ganssen, G., 2000. Past temperature and $\delta^{18}O$ of surface ocean waters inferred from foraminiferal Mg/Ca ratios. Nature 405, 442-445.

Elderfield, H., Vautravers, M., Cooper, M., 2002. The relationship between shell size and Mg/Ca, Sr/Ca, $\delta^{18}O$, and $\delta^{13}C$ of species of planktonic foraminifera. Geochemistry, Geophysics, Geosystems 3.

England, M.H., Huang, F., 2005. On the interannual variability of the Indonesian Throughflow and its linkage with ENSO. Journal of Climate 18, 1435-1444.

Epstein, S., Buchsbaum, R., Lowenstam, H.A., Urey, H.C., 1953. Revised carbonate-water isotopic temperature scale. Geological Society of America Bulletin 64, 1315-1326.

Erez, J., Honjo, S., 1981. Comparison of isotopic composition of planktonic foraminifera in plankton tows, sediment traps and sediments. Palaeogeography, palaeoclimatology, palaeoecology 33, 129-156.

Esper, J., Cook, E.R., Schweingruber, F.H., 2002. Low-frequency signals in long tree-ring chronologies for reconstructing past temperature variability. Science 295, 2250-2253.

Fairbanks, R.G., 1989. A 17,000-year glacio-eustatic sea level record: influence of glacial melting rates on the Younger Dryas event and deep-ocean circulation. Nature 342, 637-642.

Fairbanks, R.G., Evans, M.N., Rubenstone, J.L., Mortlock, R.A., Broad, K., Moore, M.D., Charles, C.D., 1997. Evaluating climate indices and their geochemical proxies measured in corals. Coral Reefs 16, S93-S100.

Fedorov, A.V., Harper, S.L., Philander, S.G., Winter, B., Wittenberg, A.T., 2003. How predictable is El Niño? Bulletin of the American Meteorological Society 84, 911-919.

Fedorov, A.V., Philander, S.G., 2000. Is El Niño changing? Science 288, 1997-2002.

Ferguson, J.E., Henderson, G.M., Kucera, M., Rickaby, R.E.M., 2008. Systematic change of foraminiferal Mg/Ca ratios across a strong salinity gradient. Earth and Planetary Science Letters 265, 153-166.

Ffield, A., Vranes, K., Gordon, A.L., Susanto, R.D., 2000. Temperature variability within Makassar Strait. Geophysical Research Letters 27, 237-240.

Fieux, M., Molcard, R., Ilahude, A.G., 1996. Geostrophic transport of the Pacific-Indian Oceans Throughflow. Journal of Geophysical Research 101, 12421-12432.

Ganopolski, A., Rahmstorf, S., 2001. Rapid changes of glacial climate simulated in a coupled climate model. Nature 409, 153-158.

Garcia, H.E., Locarnini, R.A., Boyer, T.P., Antonov, J.I., Zweng, M.M., Baranova, O.K., Johnson, D.R., 2010. World Ocean Atlas 2009, Volume 4: Nitrients (phosphate, nitrate, silicate), in: Levitus, S. (Ed.), NOAA Atlas NESDIS 71. U.S. Government Printing Office, Washington D.C., p. 398.

Gordon, A.L., 1986. Interocean exchange of thermocline water. Journal of Geophysical Research 91, 5037-5046.

Gordon, A.L., 2005. Oceanography of the Indonesian Seas and their throughflow. Oceanography 18, 14-27.

Gordon, A.L., Fine, R.A., 1996. Pathways of water between the Pacific and Indian Oceans in the Indonesian Seas. Nature 379, 146-149.

Gordon, A.L., Giulivi, C.F., Gani Ilahude, A., 2003a. Deep topographic barriers within the Indonesian Seas. Deep Sea Research II 50, 2205-2228.

Gordon, A.L., Susanto, R.D., 1999. Makassar Strait transport: Initial estimate based on Arlindo results. Marine Technology Society Journal 32, 34-45.

Gordon, A.L., Susanto, R.D., Ffield, A., 1999. Throughflow within Makassar Strait. Geophysical Research Letters 26, 3325-3328.

Gordon, A.L., Susanto, R.D., Ffield, A., Huber, B.A., Pranowo, W., Wirasantosa, S., 2008. Makassar Strait throughflow, 2004 to 2006. Geophysical Research Letters 35, L24605.

Gordon, A.L., Susanto, R.D., Vranes, K., 2003b. Cool Indonesian throughflow as a consequence of restricted surface layer flow. Nature 425, 824-828.

Graham, N.E., Hughes, M.K., Ammann, C.M., Cobb, K.M., Hoerling, M.P., Kennett, D.J., Kennett, J.P., Rein, B., Stott, L., Wigand, P.E., Xu, T., 2007. Tropical Pacific-mid-latitude teleconnections in medieval times. Climatic Change 83, 241-285.

Grootes, P.M., Stuiver, M., 1997. Oxygen 18/16 variability in Greenland snow and ice with 10^{-3} to 10^{5}-year time resolution. Journal of Geophysical Research 102, 26455-26470.

Grudd, H., Briffa, K.R., Karlen, W., Bartholin, T.S., Jones, P.D., Kromer, B., 2002. a 7400-year tree-ring chronology in northern Swedish Lapland: natural climatic variability expressed on annual to millennial timescales. The Holocene 12, 657-665.

Guilyardi, E., Wittenberg, A.T., Fedorov, A., Collins, M., Wang, C., Capotondi, A., van Oldenborgh, G.J., Stockdale, T., 2009. Understanding El Niño in ocean-atmosphere general circulation models: Progress and Challenges. Bulletin of the American Meteorological Society.

Hanebuth, T., Stattegger, K., Grootes, P.M., 2000. Rapid flooding of the Sunda Shelf: A late-glacial sea-level record. Science 288, 1033-1035.

Hannachi, A., Stepgenson, D.B., Sperber, K.R., 2003. Probability-based methods for quantifying nonlinearity in the ENSO. Climate Dynamics 20, 241-256.

Hathorne, E.C., Alard, O., James, R.H., Rogers, N.W., 2003. Determination of intratest variability of trace elements in foraminifera by laser ablation inductively coupled plasma-mass spectrometry. Geochemistry, Geophysics, Geosystems 4.

Haug, G.H., Hughen, K.A., Sigman, D.M., Peterson, L.C., Röhl, U., 2001. Southward migration of the intertropical convergence zone through the Holocene. Science 293, 1304-1308.

Heired, K.A., Quinn, T.M., Taylor, F.M., Banner, J., 2009. Interannual to multi-decadal scale climate variability in the Western Pacific Warm Pool recorded by the geochemistry of 16-17th century corals from Papua New Guinea EOS Transactions AGU Fall Meeting Supplement 90, Abstract PP11G-04.

Hemleben, C., Spindler, M., Anderson, O.R., 1989. Modern Planktonic Foraminifera. Springer-Verlag, Berlin.

Hemleben, C., Spindler, M., Breitinger, L., Ott, R., 1987. Morphologic and physiological responses of *G. sacculifer* (Brady) under varying laboratory conditions. Marine Micropaleontology 12, 305-324.

Hendon, H.H., Lim, E., Wang, G., Alves, O., Hudson, D., 2009. Prospects for predicting two flavors of El Niño. Geophysical Research Letters 36, L19713.

Herweijer, C., Seager, R., Cook, E.R., Emile-Geay, J., 2007. North American droughts of the last millennium from a gridded network of tree-ring data. Journal of Climate 2-, 1353-1376.

Hoaglin, D., Mosteller, F., Tukey, J., 1983. Understanding robust and exploratory data analysis. Wiley, New York.

Holmgren, K., Karlén, W., Lauritzen, S.-E., Lee-Thorp, J.A., Partridge, T.C., Piketh, S., Repinski, P., Stevenson, C., Svanered, O., Tyson, P.D., 1999. A 3000-year high resolution stalagmite based record of palaeoclimate for northeastern South Africa. The Holocene 9, 295-308.

Hughes, K.M., Diaz, H.F., 1994. Was there a "Medieval Warm Period", and if so, where and when? Climatic Change 26.

Jansen, E., Overpeck, J., Briffa, K.R., Duplessy, J.-C., Joos, F., Masson-Delmotte, V., Olago, D., Otto-Bliesner, B.L., Peltier, W.R., Rahmstorf, S., Ramesh, R., Raynaud, D., Rind, D., Solomina, O., Villalba, R., Zhang, D., 2007. Paleoclimate, in: Solomon, S., Qin, D., Manning, M., Chen, Z., Maquis, M., Averyt, K.B., Tignor, M., Miller, H.L. (Eds.), Climate change 2007: The Physical Science Basis. Contribution of working group I to the Fourth Assessment Report of the Intergovernmental Panel on climate change. Cambridge University Press, Cambridge, United Kingdom and New York, NY, USA.

Jin, F.-F., 1997. An equatorial ocean recharge paradigm for ENSO. Part I: Conceptual model. Journal of Atmospheric Science 54, 811-829.

Jin, F.-F., An, S.-I., Timmermman, A., Zhao, J., 2003. Strong El Niño events and nonlinear dynamical heating Geophysical Research Letters 30, 1120.

Jochum, M., Potemra, J., 2008. Sensitivity of tropical rainfall to Banda Sea diffusivity in the Community Climate System Model. Journal of Climate 21, 6445-6454.

Jones, P.D., Mann, M.E., 2004. Climate over past millennia. Reviews of Geophysics 42, RG2002.

Kao, H.-Y., Yu, J.-Y., 2009. Contrasting Eastern-Pacific and Central-Pacific types of ENSO. Journal of Climate 22.

Katz, A., 1973. The interaction of magnesium with calcite during crystal growth at 25-90 ° C and one atmosphere. Geochimica et cosmochimica acta 37, 1563-1586.

Kawahata, H., 2005. Stable isotopic composition of two morphotypes of *Globigerinoides ruber* (white) in the subtropical gyre in the North Pacific. Paleontological Research 9, 27-35.

Key, R.M., Kozyr, A., Sabine, C., Lee, K., Wanninkhof, R., Bullister, J.L., Feely, R.A., Millero, F.J., Mordy, C., Peng, T.-H., 2004. A global ocean carbon climatology: Results from Global Data Analysis Project (GLODAP). Global Biogeochemical Cycles 18, GB4031.

Kida, S., Richards, K.J., 2009. Seasonal sea surface temperature variability in the Indonesian Seas. Journal of Geophysical Research 114, C06016.

Kienast, M., Steinke, S., Stattegger, K., calvert, S.E., 2001. Synchronous tropical South China Sea SST change and Greenland warming during deglaciation. Science 291, 2132-2134.

Kim, H.-M., Webster, P.J., Curry, J.A., 2009. Impact of shifting patterns of Pacific Ocean warming on North Atlantic tropical cyclones. Science 325, 77-80.

Kinkade, C., Marra, J., Langdon, C., Knudson, C., Gani Ilahude, A.G., 1997. Monsoonal differences in phytoplankton biomass and production in the Indonesian Seas: tracing vertical mixing using temperature. Deep-Sea Research I 44, 581-592.

Kisakürek, B., Eisenhauer, A., Böhm, F., Garbe-Schönberg, D., Erez, J., 2008. Controls on shell Mg/Ca and Sr/Ca in cultured planktonic foraminiferan, *Globigeriniodes ruber* (white). Earth and Planetary Science Letters 273, 260-269.

Koutavas, A., deMenocal, P.B., Olive, G.C., Lynch-Stieglitz, J., 2006. Mid-Holocene El Nino-Southern Oscillation (ENSO) attenuation revealed by individual foraminifera in eastern tropical Pacific sediments. Geology 34, 993-996.

Kug, J.-S., Choi, J., An, S.-I., Jin, F.-F., Wittenberg, A.T., 2010. Warm pool and cold tongue El Niño events as simulated by the GFDL 2.1 coupled GCM. Journal of Climate 23, 1226-1239.

Kug, J.-S., Jin, F.-F., An, S.-I., 2009. Two types of El Nino events: cold tongue El Niño and Warm Pool El Niño. Journal of Climate 22, 1499-1515.

Kumar, K.K., Rajagopalan, B., Hoerling, M., Bates, G., Cane, M., 2006. Unraveling the mystery of Indian Monsoon failure during El Niño. Science 314, 115-119.

Kunioka, D., Shirai, K., Takachata, N., Y., S., Toyofuku, T., Ujie, Y., 2006. Microdistribution of Mg/Ca, Sr/Ca, and Ba/Ca ratios in *Pulleniatina obliquiloculata* test by using a NanoSIMS: Implication for the vital effect mechanism. Geochemistry, Geophysics, Geosystems 7.

Labeyrie, L., Duplessy, J.C., Blanc, P.L., 1987. Variations in mode of formation and temperature of oceanic deep waters over the past 125,000 years. Nature 327, 477-482.

Lamb, H.H., 1965. The early medieval warm epoch and its sequel. Palaeogeography, palaeoclimatology, palaeoecology 1, 13-37.

Lamb, H.H., 1982. Climate History and the Modern World. Routledge, London and New York.

Lanzante, J.R., 1996. Resistant, robust and non-parametric techniques for the analysis of climate data: theory and examples, including applications to historical radiosonde station data. International Journal of Climatology 16, 1197-1226.

Larkin, N.K., Harrison, D.E., 2005a. Global seasonal temperature and precipitation anomalies during El Niño autumn and winter. Geophysical Research Letters 32, L16705.

Larkin, N.K., Harrison, D.E., 2005b. On the definition of El Niño and associated seasonal average U.S. weather anomalies. Geophysical Research Letters 32, L13705.

Lau, K.M., Weng, H., 1999. Interannual, decadal-interdecadal, and global warming signals in sea surface temperature during 1955-97. Journal of Climate 12, 1257-1267.

Lea, D.W., Mashiotta, T.A., Spero, H.J., 1999. Controls on magnesium and strontium uptake in planktonic foraminifera determined by live culturing. Geochimica et cosmochimica acta 63, 2369-2379.

Lea, D.W., Pak, D.K., Peterson, L.C., Hughen, K.A., 2003. Synchroneity of tropical and high-latitude Atlantic temperatures over the last glacial termination. Science 301, 1361-1364.

Lea, D.W., Pak, D.K., Spero, H.J., 2000. Climate impact of Late Quaternary equatorial Pacific sea surface temperature variations. Science 289, 1719-1724.

Leduc, G., Vidal, L., Cartapanis, O., Bard, E., 2009. Modes of eastern equatorial Pacific thermocline variability: Implications for ENSO dynamics over the last glacial period Paleoceanography 24, PA3202.

LeGrande, A.N., Schmidt, G.A., 2006. Global gridded data set of the oxygen isotopic composition in seawater. Geophysical Research Letters 33, L12604.

LeGrande, A.N., Schmidt, G.A., 2009. Sources of Holocene variability of oxygen isotopes in paleoclimate archives. Climate of the Past 5, 441-455.

LeGrande, A.N., Schmidt, G.A., 2010. Water isotopes as a quantitative paleosalinity proxy, International Conference on Paleoceanography, Scripps Institution of Oceanography, La Jolla.

Levi, C., Labeyrie, L., Bassinot, F., Guichard, F., Cortijo, E., Waelbroeck, C., Caillon, N., Duprat, J., De Garidel-Thoron, T., Elderfield, H., 2007. Low-latitude hydrological cycle and rapid climate changes during the last deglaciation. Geochemistry, Geophysics, Geosystems 8, Q05N12.

Lim, E.-P., Hendon, H.H., Hudson, D., Wang, G., Alves, O., 2009. Dynamical forecasts of inter-El Niño variations of tropical SST and Australian spring rainfall. Monthly Weather Review in press.

Linsley, B.K., Rosenthal, Y., Oppo, D.W., 2010. Holocene evolution of the Indonesian Throughflow and the Western Pacific warm pool. Nature geoscience 3, 578-583.

Locarnini, R.A., Mishonov, A.V., Antonov, J.I., Boyer, T.P., Garcia, H.E., 2010. World Ocean Atlas, Volume 1: Temperature. U.S. Government Printing Office, Washington, D.C.

Lorius, C., Merlivat, L., 1977. Distribution of mean surface stable isotope values in East Antarctica. Observed changes with depth in a coastal area, in: IAHS (Ed.). IAHS, Vienna, pp. 125-137.

Mann, M.E., Bradley, R.S., Hughes, M.K., 1999. Northern Hemisphere temperatures during the past millennium: Inferences, Uncertainties, and Limitations. Geophysical Research Letters 26, 759.

Mann, M.E., Zhang, Z., Hughes, M.K., Bradley, R.S., Miller, S.K., Rutherford, S., Ni, F., 2008. Proxy-based reconstructions of hemispheric and global surface temperature variations over the past two millennia. Proceeding of the National Academy of Sciences 105, 13252-13257.

Mann, M.E., Zhang, Z., Rutherford, S., Bradley, R., Hughes, M.K., Shindell, D.T., Ammann, C.M., Faluvegi, G., Ni, F., 2009. Global signatures and dynamical origins of the Little Ice Age and Medieval Climate Anomaly. Science 326, 1256-1260.

Manning, M., Qin, D., Marquis, M., Averyt, K.E., 2007. Climate Change 2007: the physical science basis. Working group 1 contribution to the intergovernmental panel on climate change fourth assessment report. Cambridge University Press.

MARGO project Members, 2009. Constraints on the magnitude and patterns of ocean cooling at the Last Glacial Maximum. 2007.

Mathien-Blard, E., Bassinot, F., 2009. Salinity bias on the foraminifera Mg/Ca thermometry: correction procedure and implications for past ocean hydrographic reconstructions. Geochemistry, Geophysics, Geosystems 10, Q12011.

McBride, J.L., Haylock, M.R., Nichols, N., 2003. Relationships between the maritime continent heat source and the El Niño Southern Oscillation phenomenon. Journal of Climate 16, 2905-2914.

McConnell, M.C., Thunell, R.C., 2005. Calibration of the planktonic foraminiferal Mg/Ca paleothermometer: Sediment trap results from the Guaymas Basin, Gulf of California. Paleoceanography 20, PA2016.

McCrea, J.M., 1950. On the isotopic chemistry of carbonates and a paleotemperature scale. Journal of Chemical Physics 18, 849-857.

Meehl, G.A., Stocker, T.F., Collins, W.D., Friedlingstein, P., Gaye, A.T., Gregory, J.M., Kitoh, A., Knutti, R., Murphy, J.M., Noda, A., Raper, S.C.B., Watterson, I.G., Weaver, A.J., Zhao, Z.-C., 2007. Global Climate Projections, in: Solomon, S., Qin, D., Manning, M., Chen, Z., Marquis, M., Averyt, K., Tignor, M., Miller, H.L. (Eds.), Climate Change 2007: The Physical Science Basis. Contribution of Working Group I to the Fourth Assessment Report of the Intergovernmental Panel on Climate Change. Cambridge University Press, Cambridge, United Kingdom and New York, NY, USA.

Meyers, G., 1996. Variation of Indonesian throughflow and the El Niño-Southern Oscillation. journal of Geophysical Research 101, 12255-12263.

Mix, A.C., Ruddiman, W.F., 1984. Oxygen-isotope analyses and Pleistocene ice volumes. Quaternary Research 21, 1-20.

Moberg, A., Sonechkin, D.M., Holmgren, K., Datsenko, N.M., Karlen, W., 2005. Highly variable Northern Hemisphere temperatures reconstructed from low- and high-resolution proxy data. Nature 433, 613-617.

Mohtadi, M., Oppo, D., Luckge, A., DePol-Holz, R., Steinke, S., Groeneveld, J., Hemme, N., Hebbeln, D., in press. Reconstructing the thermal structure of the upper ocean: insights from planktic foraminifera shell chemistry and alkenones in modern sediments of the tropical eastern Indian Ocean. Paleoceanography.

Mohtadi, M., Steinke, S., Groeneveld, J., Fink, H.G., Rixen, T., Hebbeln, D., Donner, B., Herunadi, B., 2009. Low-latitude control on seasonal and interannual changes in planktonic foraminiferal flux and shell geochemistry off south Java: A sediment trap study. Paleoceanography 24, PA1201.

Monahan, A.H., Dai, A., 2004. The spatial and temporal structure of ENSO nonlinearity. Journal of Climate 17, 3026-3036.

Morimoto, M., Abe, O., Kayanne, H., Kurita, N., Matsumoto, E., Yoshida, N., 2002. Salinity records for the 1997-98 El Niño from Western Pacific corals. Geophysical Research Letters 29, 1540.

Moy, C.M., Seltzer, G.O., Rodbell, D.T., Anderson, D.M., 2002. Variability of El Niño/Southern Oscillation activity at millennial timescales during the Holocene epoch. Nature 420, 162-165.

Mucci, A., 1987. Influence of temperature on the composition of magnesian calcite overgrowths precipitated from seawater. Geochimica et cosmochimica acta 51, 1977-1984.

Mulitza, S., Arz, H., Kemle-von Mucke, S., Moos, C., Niebler, H., -S., Patzold, J., Segl, M., 1999. The South Atlantic Carbon Isotope Record of Planktic Foraminifera, in: Fischer, G., Wefer, G. (Eds.), Use of proxies in paleoceanography: Examples from the South Atlantic. Springer, Berlin, Germany, pp. 427-445.

Neale, R.B., Slingo, J.M., 2003. The maritime continent and its role in the global climate: A GCM study. Journal of Climate 16, 834-848.

Newton, A., Thunell, R., Stott, L., 2006. Climate and hydrographic variability in the Indo-Pacific Warm Pool during the last millennium. Geophysical Research Letters 33, L19710.

Newton, A., Thunell, R., Stott, L., 2011. Changes in the Indonesian Throughflow during the past 2000 yr. Geology 39, 63-66.

Ni, Y., G.L., F., Bailey, T., Elliot, T., Schmidt, D.N., Pearson, P., Haley, B., Coath, C., 2007. A core top assessment of proxies for the ocean carbonate systen in surface-dwelling foraminifers. Paleoceanography 22, PA3212.

Nouet, J., Bassinot, F., 2007. Dissolution effects on the crystallography and Mg/Ca content of planktonic foraminifera *Globorotalia tumida* (Rotalina) revealed by X-ray diffractometry. Geochemistry, Geophysics, Geosystems 8, A10007.

Nürnberg, D., Bijma, J., Hemleben, C., 1996. Assessing the reliability of magnesium in foraminiferal calcite as a proxy for water mass temperatures. Geochimica et Cosmochimica Acta 60, 803-814.

Oomori, T., Kaneshima, H., Maezato, Y., 1987. Distribution coefficient of Mg^{2+} ions between calcite and solution at 10-50°C. Marine Chemistry 20, 327-336.

Oppo, D., Linsley, B.K., Rosenthal, Y., Dannenmann, S., Beaufort, L., 2003. Orbital and suborbital climate variability in the Sulu Sea, western tropical Pacific. Geochemistry, Geophysics, Geosystems 4, 1003.

Oppo, D.W., Rosenthal, Y., Linsley, B.K., 2009. 2,000-year-long temperature and hydrology reconstructions from the Indo-Pacific warm pool. Nature 460, 1113-1116.

Oppo, D.W., Schmidt, G.A., LeGrande, A.N., 2007. Seawater isotope constraints on tropical hydrology during the Holocene. Geophysical Research Letters 34, L13701.

Partin, J.W., Cobb, K.M., Adkins, J.F., Clark, B., Fernandez, D.F., 2007. Millennial-scale trends in west Pacific warm pool hydrology since the Last Glacial Maximum. Nature 449, 452-455.

Peixoto, J.P., Oort, A.H., 1992. Physics of climate. American Institute of Physics, New York.

Pettersson, O., 1914. Climate variations in historic and prehistoric time. Svenska Hydrogr. - Biol. Komm. Skriften 5, 1-26.

Picaut, J., Masia, F., du Penhoat, Y., 1997. An adevective-reflective conceptual model for the oscillatory nature of the ENSO. Science 277, 663-666.

Qu, T., Du, Y., Strachan, J., Meyers, G., Slingo, J., 2005. Sea surface temperature and its variability in the Indonesian region. Oceanography 18, 50-61.

Quinn, T.M., Taylor, F.W., Crowley, T.J., 2006. Coral-based climate variability in the western Pacific warm pool. Journal of Geophysical Research 111, C11006.

Quinn, W.H., 1992. A study of Southern Oscillation-related climatic activity for A.D. 622-1990 incorporating Nile River flood data, in: Diaz, H.F., Markgraf, V. (Eds.), El Nino: Historical and paleoclimatic aspects of the Southern Oscillation. Cambridge University Press, Cambridge, pp. 119-149.

Rasmusson, E.M., Carpenter, T.H., 1982. Variations in tropical sea surface temperatures and surface wind fields associated with the Southern Oscillation/El Nino. Monthly Weather Review 110, 354-384.

Ravelo, A.C., Fairbanks, R.G., 1992. Oxygen isotopic composition of multiple species of planktonic foraminifera: recorders of the modern photic zone temperature gradient. Paleoceanography 7, 815-831.

Rayner, N.A., Parker, D.E., Horton, E.B., Folland, C.K., Alexander, L.V., Rowell, D.P., Kent, E.C., Kaplan, A., 2003. Global analyses of sea surface temperature, sea ice and night marine air temperature since the late nineteenth century. Journal of Geophysical Research 108, 4407.

Regenberg, M., Nurnberg, D., Steph, S., Groeneveld, J., Garbe-Schonberg, D., Tiedemann, R., Dullo, W.-C., 2006. Assessing the effect of dissolution on planktonic foraminiferal Mg/Ca ratios: Evidence from Caribbean core tops. Geochemistry, Geophysics, Geosystems 7, Q07P15.

Rosenthal, Y., Lohmann, G.P., 2002. Accurate estimation of sea surface temperatures using dissolution-corrected calibrations for Mg/Ca paleothermometry. Paleoceanography 17, 1044.

Rosenthal, Y., Lohmann, G.P., Lohmann, K.C., Sherrell, R.M., 2000. Incorporation and preservation of Mg in *Globigerinoides sacculifer*: implications for the reconstructing the temperature and O-18/O-16 of seawater. Paleoceanography 15, 135-145.

Rosenthal, Y., Oppo, D.W., Linsley, B.K., 2003. The amplitude and phasing of climate change during the last deglaciation in the Sulu Sea, western equatorial Pacific. Geophysical Research Letters 30, 1428.

Rosenthal, Y., Perron-Cashman, S., Lear, C.H., Bard, E., Barker, S., Billups, K., Bryan, M., Delaney, M.L., deMenocal, P.B., Dwyer, G.S., Elderfield, H., German, C.R., Greaves, M., Lea, D.W., Marchitto, T.M., Pak, D.K., Paradis, G.L., Russell, A.D., Schneider, R.R., Scheiderich, K., Stott, L., Tachikawa, K., Tappa, E., Thunell, R., Wara, M., Weldeab, S., Wilson, P.A., 2004. Interlaboratory comparison study of Mg/Ca and Sr/Ca measurements in planktonic foraminifera for paleoceanographic research. Geochemistry, Geophysics, Geosystems 5, Q04D09.

Russell, A.D., Hönisch, B., Spero, H.J., Lea, D.W., 2004. Effects of seawater carbonate ion concentration and temperature on shell U, Mg. and Sr in cultured planktonic foraminifera. Geochimica et cosmochimica acta 68, 4347-4361.

Russell, A.D., Spero, H.J., 2000. Field examination of the oceanic carbonate ion effect on stable isotopes in planktonic foraminifera. Paleoceanography 15, 43-52.

Sadekov, A.Y., Eggins, S.M., De Deckker, P., 2005. Characterization of Mg/Ca distributions in planktonic foraminifera species by electron microprobe mapping. Geochemistry, Geophysics, Geosystems 6.

Sadekov, A.Y., Eggins, S.M., De Dekker, P., Ninnemann, U.S., Kuhnt, W., Bassinot, F., 2009. Surface and sub-surface seawater temperature reconstruction using Mg/Ca microanalysis of planktonic foraminifera *Globigerinoides ruber*, *Globigerinoides sacculifer* and *Pelluniatina obliquiloculata*. . Paleoceanography 24, PA3201.

Saikku, R., 2009. Abrupt climate variability during the last glacial and the late Holocene from the western tropical Pacific perspective, Department of Earth Sciences. University of Southern California, Los Angeles, p. 169.

Sathiamurthy, E., Voris, H.K., 2006. Maps of Holocene sea level transgression and submerged lakes on the Sunda Shelf. The natural history journal of Chulalongkorn university Suppl. 2, 1-44.

Schmittner, A., Appenzeller, C., Stocker, T.F., 2000. Enhanced Atlantic freshwater export during El Niño. Geophysical Research Letters 27, 1163-1166.

Schrag, D.P., Hampt, G., D.W., M., 1996. Pore fluid constraints on the temperature and oxygen isotopic composition of the glacial ocean. Science 272, 1930-1932.

Seager, R., Burgman, R., Kushnir, Y., Clement, A., Cook, E., Naik, N., Velez, J., 2008. Tropical Pacific forcing of North American Medieval megadroughts: Testing the concept with an atmosphere model forced by coral-reconstructed SSTs. Journal of Climate 21, 6175-6190.

Shackleton, N.J., 1974. Attainment of isotopic equilibrium between ocean wtaer and benthonic foraminifera genus Uvigerina: Isotopic changes in the ocean during the last glacial, Les méthodes quantitatives d'étude des variations du climat au cours du Pleistocène. Centre National de la Recherche Scientifique, Gif-sur-Yvette, France, pp. 203-209.

Sharp, Z., 2007. Principles of stable isotope geochemistry. Pearson Prentice Hall, Upper Saddle River, New Jersey.

Shen, C., Wang, W.-C., Hao, Z., Gong, W., 2007. Exceptional drought events over eastern China during the last five centuries. Climatic Change 85, 453-471.

Smith, T.M., Reynolds, R.W., Perterson, T.C., Lawrimore, J., 2007. Improvements to NOAA's historical merged land-ocean surface temperature analysis (1880-2006). Journal of Climate.

Southon, J., Kashgarian, M., Fontugne, M.R., Metivier, B., Yim, W.W.-S., 2002. Marine reservoir corrections for the Indian ocean and southeast Asia. Radiocarbon 44, 167-180.

Spero, H.J., 1998. Life history and stable isotope geochemistry of planktonic foraminifera, in: Norris, R.D., Corfield, R.M. (Eds.), Isotope paleobiology and paleoecology. Paleontological Society Papers, Pittsburg, Pennsylvania, pp. 7-36.

Sprintall, J., 2009. Indonesian Throughflow, in: Steele, J.H., Turekian, K.K., Thorpe, S.A. (Eds.), Encyclopedia of Ocean Sciences. Academic Press, pp. 237-243.

Sprintall, J., Wijffels, S.E., Molcard, R., Jaya, I., 2009. Direct estimates of the Indonesian Throughflow entering the Indian Ocean: 2004-2006. Journal of Geophysical Research 114, C07001.

Steinke, S., Kienast, M., Groeneveld, J., Lin, L.-C., Chen, M.-T., Rendle-Bühring, R., 2008. Proxy dependence of the temporal patterns of deglacial warming in the tropical South China Sea: toward resolving seasonality. Quaternary Science Reviews 27, 688-700.

Stephenson, A.E., Hunter, J.L., Han, M., Dove, P.M., 2009. Relative influence of salinity and growth rate on calcite Mg/Ca. Geochimica et Cosmochimica Acta 73, A1272-A.

Stott, L., Cannariato, K., Thunell, R., Haug, G.H., Koutavas, A., Lund, S., 2004. Decline of surface temperature and salinity in the western tropical Pacific Ocean in the Holocene epoch. Nature 431, 56-59.

Stott, L., Poulsen, C., Lund, S., Thunell, R., 2002. Super ENSO and global climate oscillations at millennial time scales. Science 297, 222-226.

Stott, L., Timmermman, A., Thunell, R., 2007. Southern Hemisphere and Deep-Sea Warming led to deglacial atmospheric CO_2 rise and tropical warming. Science 318, 435-438.

Stott, L.D., Tang, C.M., 1996. Reassessment of tropical sea surface $\delta^{18}O$ paleotemperatures. Paleoceanography 11, 37-56.

Stuiver, M., Reimer, P.J., 1993. Extended ^{14}C data base and revised CALIB 3.0 ^{14}C age calibration program. Radiocarbon 35, 215-230.

Suarez, M.J., Schopf, P.S., 1988. A delayed action oscillator for ENSO. Journal of Atmospheric Science 45, 3283-3287.

Susanto, R.D., Gordon, A.L., 2005. Velocity and transport of the Makassar Strait throughflow. Journal of Geophysical Research 110, C01005.

Tang, C.M., Stott, L.D., 1993. Seasonal salinity changes during Mediterranean sapropel deposition 9,000 years B.P.: Evidence from isotopic analyses of individual planktonic foraminifera. Paleoceanography 8.

Thompson, L.G., Mosley-Thompson, E., Morales Arnao, B., 1984. El Niño-Southern Oscillation events recorded in the stratigraphy of the tropical Quelccaya ice cap, Peru. Science 226, 50-53.

Thompson, P.R., Bè, A.W.H., Duplessy, J.C., Shackleton, N.J., 1979. Disappearance of pink-pigmented *Globigerinoides ruber* at 120,000 yr BP in the Indian and Pacific Ocean. Nature 280, 554-558.

Tierney, J.E., Oppo, D.W., Rosenthal, Y., Russell, J.M., Linsley, B.K., 2010. Coordinated hydrological regimes in the Indo-Pacific region during the past two millennia. Paleoceanography 25, PA1102.

Tomascik, T., Mah, A.J., Nontji, A., Moosa, M.K., 1997. The Ecology of the Indonesian Seas. Periplus Editions, Singapore.

Tozuca, T., Qu, T., Yamagata, T., 2007. Dramatic impact of the South China Sea on the Indonesian Throughflow. Geophysical Research Letters 34, L12612.

Trenberth, K.E., 1997. The definition of El Niño. Bulletin of the American Meteorological Society 78, 2771-2777.

Trenberth, K.E., Stepaniak, D.P., 2001. Indices of El Niño evolution. Journal of Climate 14, 1697-1701.

van Hueven, S., Pierrot, D., Lewis, E., Wallace, W.R., 2009. MATLAB program developed for CO2 System Calculations.

Verschuren, D., Laird, K.R., Cumming, F., 2000. Rainfall and drought in equatorial east Africa in the pat 1,100 years. Nature 403, 410-414.

Visser, K., Thunell, R., Stott, L., 2003. Magnitude and timing of temperature change in the Indo-Pacific warm pool during deglaciation. Nature 421, 152-155.

Waelbroeck, C., Labeyrie, L., Michel, E., Duplessy, J.C., McManus, J.F., Lambeck, K., Balbon, E., Labracherie, M., 2002. Sea level and deep water temperature changes derived from benthic foraminifera isotopic records. Quaternary Science Reviews 21, 295-305.

Waliser, D.E., Gautier, C., 1993. A satellite-derived climatology of the ITCZ. Journal of Climate 6, 2162-2174.

Wang, G., Hendon, H.H., 2007. Sensitivity of Australian rainfall to inter-El Niño variations. Journal of Climate 20, 4211-4226.

Wang, L., 2000. Isotopic signale in two morphoypes of *Globigerinoides ruber* (white) from the South China Sea: implications for monsoon climate change during the last glacial cycle. . Palaeogeography, palaeoclimatology, palaeoecology 161, 381-394.

Wang, Y., Cheng, H., Edwards, R.L., Kong, X., Shao, X., Chen, S., Wu, J., Jiang, X., Wang, X., An, Z., 2008. Millennial- and orbital-scale changes in the East Asian monsoon over the past 224,000 years. Nature 451, 1090-1093.

Wang, Y.J., Cheng, H., Edwards, R.L., An, Z.S., Wu, J.Y., Shen, C.-C., J.A., D., 2001. A high-resolution absolute-dated late Pleistocene monsoon record from Hulu Cave, China. Science 294, 2345-2348.

Watkins, J.M., Mix, A.C., Wilson, J., 1996. Living planktonic foraminifera: tracers of circulation and productivity in the central equatorial Pacific. Deep Sea Research II 43, 1257-1282.

Webster, P.J., Magaña, V.O., Palmer, T.N., Shukla, J., Tomas, R.A., Yanai, M., Yasunari, T., 1998. Monsoons: Processes, predictability, and the prospects for prediction. Journal of Geophysical Research 103, 14,451-414,510.

Weisberg, R.H., Wang, C., 1997. A western Pacific oscillator paradigm for the El Niño Southern Oscillation. Geophysical Research Letters 24, 779-782.

Wejnert, K.E., Pride, C.J., Thunell, R.C., 2010. The oxygen isotope composition of planktonic foraminifera from the Guaymas Basin, Gulf of California: seasonal, annual, and interspecies variability. Marine Micropaleontology 74, 29-37.

Weng, H., Behera, S.K., Yamagata, T., 2009. Anomalous winter climate conditions in the Pacific rim during recent El Niño Modoki and El Niño events. Climate Dynamics 32, 663-674.

Wyrtki, K., 1961. Scientific results of marine investigations of the South China Sea and the Gulf of Thailand, physical oceanography of the Southeast Asian waters, NAGA Rep. 2. University of California, Scripps Institute of Oceanography, La Jolla, CA.

Xu, J., Holbourn, A., Kuhnt, W., Jian, Z., Kawamura, H., 2008. Changes in the thermocline structure of the Indonesia outflow during Terminations I and II. Earth and Planetary Science Letters 273, 152-162.

Xu, J., Kuhnt, W., Holbourn, A., Regenberg, M., Andersen, N., 2010. Indo-Pacific warm pool variability during the Holocene and Last Glacial Maximum. Paleoceanography, PA4230.

Yeh, S.-W., Kirtman, B.P., Kug, J.-S., Park, W., Latif, M., in press. Natural variability of the central Pacific El Niño event on multi-centennial timescales. Geophysical Research Letters.

Yeh, S.-W., Kug, J.-S., Dewitte, B., Kwon, M.-H., Kirtman, B.P., Jin, F.-F., 2009. El Niño in a changing climate. Nature 461, 511-515.

Yu, J.-Y., Kao, H.-Y., Lee, T., Kim, S.T., 2010. Subsurface Ocean Indices for Central-Pacific and Eastern-Pacific types of El Niño and La Niña events. Theoretical and applied climatology.

Zeebe, R.E., Sanyal, A., 2002. Comparison of two potential strategies of planktonic foraminifera for house building: Mg^{2+} or H^+ removal? Geochimica et cosmochimica acta 66, 1159-1169.

Zhang, P., Cheng, H., Edwards, R.L., Chen, F., Wang, Y., Yang, X., Liu, J., Tan, M., Wang, X., Liu, J., An, C., Dai, Z., Zhou, J., Zhang, D., Jia, J., Jin, L., Johnson, K.R., 2008. A test of climate, sun, and culture relationships from 1810-year Chinese Cave Record. Science 322, 940-042.

Appendix A

Supplementary Information for Chapter 3

A1. Core Location and Stratigraphic Control

Area	Core Name	Latitude (°N)	Longitude (°E)	Water Depth (km)	Age Control	ΔCO32- (µmol/kg)	T_{iso}	Mean annual SSS	δ18Osw	Reference
North Atlantic	INMD48	29.80	-43.20	2.836	1	35.05	21.6	36.9	1.19	This study
Tropical Atlantic	INMD109	-5.50	-16.00	3.895	1	7.28	25.1	36.0	0.81	This study
South Atlantic	INMD 120	-28.80	-31.20	1.918	1	38.66	21.7	36.1	0.88	This study
Indonesia	MD98-2177	1.40	119.10	0.968	1	16.37	29.7	34.0	0.26	This study
Indonesia	MD98 2164	-6.60	119.40	0.750	1	21.19	27.8	33.6	0.23	This study
Indonesia	MD98-2176	-5.00	133.40	2.382	1	6.20	28.5	34.2	0.28	This study
Indonesia	GGC 8	11.60	118.70	1.305	1	12.47	28.5	33.5	0.19	This study
Indonesia	GGC 9	11.60	118.60	1.465	4	10.71	30.1	33.5	0.19	This study
Indonesia	GGC 10	11.70	118.50	1.605	4	7.99	29.4	33.5	0.19	This study
Indonesia	GGC 13	10.60	118.30	0.990	1	15.58	28.7	33.6	0.20	This study
North Atlantic	INMD 42	28.57	-46.36	3.774	2 and 4	66.59	23.5	37.0	1.20	L.D. Stott (unpublished)
North Atlantic	INMD 50	31.18	-39.68	3.481	2 and 4	68.83	21.2	36.7	1.16	L.D. Stott (unpublished)
North Atlantic	INMD 68	34.81	-28.36	2.520	2 and 4	87.28	19.4	36.4	1.04	L.D. Stott (unpublished)
Tropical Atlantic	INMD 97	16.65	-46.13	3.619	2 and 4	62.50	25.6	36.8	0.92	L.D. Stott (unpublished)
Tropical Atlantic	INMD 101	6.95	-26.45	4.093	2 and 4	52.43	24.7	35.6	0.76	L.D. Stott (unpublished)
Tropical Atlantic	INMD 104	4.25	-21.92	3.279	2 and 4	65.31	25.3	35.5	0.74	L.D. Stott (unpublished)
Tropical Atlantic	INMD 110	-10.04	-13.39	1.959	2 and 4	79.91	23.2	36.5	0.87	L.D. Stott (unpublished)
Tropical Atlantic	INMD 111	-12.64	-13.85	3.069	2 and 4	62.34	23.4	36.7	0.90	L.D. Stott (unpublished)
Tropical Atlantic	INMD 113	-15.26	-14.96	3.471	2 and 4	58.00	22.9	36.8	0.92	L.D. Stott (unpublished)
Tropical Atlantic	INMD 115	-17.64	-16.21	3.427	2 and 4	60.57	22.8	36.8	0.96	L.D. Stott (unpublished)
North Atlantic	INMD48BX.1	29.80	-43.20	2.836	3 and 4	35.05	21.6	36.9	1.19	Mathien-Blard and Bassinot (2009)
North Atlantic	INMD68BX.6	34.80	-28.40	2.520	3 and 4	41.44	19.9	36.4	1.04	Mathien-Blard and Bassinot (2009)
North Atlantic	MD952038	37.80	-20.20	2.310	4	43.46	18.7	36.2	0.93	Mathien-Blard and Bassinot (2009)
North Atlantic	paleo SU 9007P	42.50	-32.40	3.290	4	26.57	17.6	35.9	0.78	Mathien-Blard and Bassinot (2009)
North Atlantic	paleo SU 9004P	41.00	-32.00	2.865	4	33.39	19.5	36.0	0.81	Mathien-Blard and Bassinot (2009)
North Atlantic	paleo SU 9002P	40.60	-31.00	2.220	3	42.24	17.9	36.0	0.83	Mathien-Blard and Bassinot (2009)
North Atlantic	paleo SU 9003P	40.10	-32.00	2.475	2 and 3	39.24	18.9	36.1	0.84	Mathien-Blard and Bassinot (2009)
North Atlantic	paleo SU 9008P	43.80	-30.60	3.800	3 and 4	18.42	18.5	35.9	0.74	Mathien-Blard and Bassinot (2009)
North Atlantic	paleo SU 9006P	42.00	-32.70	3.510	3	22.68	17.3	35.9	0.78	Mathien-Blard and Bassinot (2009)
Tropical Atlantic	CHO 288-54	17.40	-77.70	1.020	1	38.08	27.5	35.8	0.83	Mathien-Blard and Bassinot (2009)
North Atlantic	MD95-2002	47.50	-8.50	2.174	3 and 4	44.58	14.7	35.5	0.56	Mathien-Blard and Bassinot (2009)
North Atlantic	MD99-2203	35.00	-75.20	0.620	1	109.30	24.4	36.2	0.82	Mathien-Blard and Bassinot (2009)
Mozambique	MD79-255	-19.00	37.50	1.226	4	22.47	24.8	35.1	0.44	Mathien-Blard and Bassinot (2009)
Mozambique	MD79-257	-20.40	36.30	1.262	2	21.90	24.4	35.1	0.44	Mathien-Blard and Bassinot (2009)
Arabian Sea	MD92-1002	12.00	44.30	1.327	1	15.08	25.8	36.3	0.77	Mathien-Blard and Bassinot (2009)
Indonesia	MD00-2359 PC	-9.20	114.70	2.775	4	8.77	26.6	34.2	0.27	Mathien-Blard and Bassinot (2009)
Indonesia	MD98-2165	-9.70	118.30	2.100	1	13.00	27.4	34.2	0.28	Mathien-Blard and Bassinot (2009)
Andaman Sea	MD77-176	14.50	93.10	1.375	1	13.33	28.16	32.4	0.01	Mathien-Blard and Bassinot (2009)
Southeast Indian	MD00-2360top	-20.10	112.70	0.980	4	22.14	23.8	35.0	0.42	Mathien-Blard and Bassinot (2009)
Red Sea	MD92-1008	14.40	42.20	0.708	1	35.49	26.9	37.1	0.92	Mathien-Blard and Bassinot (2009)
Indonesia	MD002358top	-12.30	112.70	2.520	4	38.99	24.6	34.3	0.31	Mathien-Blard and Bassinot (2009)
Indonesia	MD00-2359 G	-9.20	114.70	2.775	4	8.77	27.8	34.2	0.27	Mathien-Blard and Bassinot (2009)
Arabian Sea	ODP117-723	18.10	57.60	0.808	1	20.63	27.3	35.8	0.61	Mathien-Blard and Bassinot (2009)
Central Indian	MD77-191	7.50	76.70	1.254	1	13.79	27.2	34.8	0.40	Mathien-Blard and Bassinot (2009)

Area	Core Name	Latitude (°N)	Longitude (°E)	Water Depth (km)	Age Control	ΔCO32- (µmol/kg)	T_{iso}	Mean annual SSS	δ18Osw	Reference
West Pacific	ERDC92BX	-2.20	157.00	1.598	2	11.57	26.6	34.6	0.27	Mathien-Blard and Bassinot (2009)
Indian Ocean	SO189-118MC	3.52	96.31	0.804	1	33.17	30.5	33.8	0.22	Mohtadi et al. (in press)
Indian Ocean	SO189-114MC	3.49	95.33	1.535	1	28.91	29.4	33.8	0.22	Mohtadi et al. (in press)
Indian Ocean	SO-189-121MC	3.27	96.15	1.031	1	30.19	30.0	33.8	0.22	Mohtadi et al. (in press)
Indian Ocean	SO189-104MC	3.20	96.78	1.013	1	30.37	30.2	33.8	0.22	Mohtadi et al. (in press)
Indian Ocean	SO189-84MC	2.99	96.22	0.861	1	32.26	29.6	33.9	0.24	Mohtadi et al. (in press)
Indian Ocean	SO189-80MC	2.95	96.50	1.088	1	30.39	29.0	33.9	0.24	Mohtadi et al. (in press)
Indian Ocean	SO189-72MC	2.83	96.39	0.913	1	30.67	29.3	33.9	0.24	Mohtadi et al. (in press)
Indian Ocean	SO189-76MC	2.82	96.61	1.108	1	30.58	29.6	33.9	0.24	Mohtadi et al. (in press)
Indian Ocean	SO189-89MC	2.78	96.42	0.916	1	30.99	29.8	33.9	0.24	Mohtadi et al. (in press)
Indian Ocean	SO189-97MC	2.56	96.76	1.136	1	29.48	30.2	33.9	0.24	Mohtadi et al. (in press)
Indian Ocean	SO189-101MC	2.49	97.12	0.767	1	36.37	30.3	33.9	0.24	Mohtadi et al. (in press)
Indian Ocean	SO189-139MC	1.76	96.77	1.854	1	31.50	29.9	34.0	0.24	Mohtadi et al. (in press)
Indian Ocean	GeoB 10014-1	1.68	96.98	1.158	1	29.86	29.8	34.0	0.24	Mohtadi et al. (in press)
Indian Ocean	GeoB 10016-2	1.60	96.66	1.900	1	34.86	29.3	34.0	0.24	Mohtadi et al. (in press)
Indian Ocean	SO189-60MC	1.45	98.05	0.551	1	55.29	29.5	34.0	0.24	Mohtadi et al. (in press)
Indian Ocean	SO189-59MC	1.15	98.07	0.479	1	56.23	29.9	34.0	0.24	Mohtadi et al. (in press)
Indian Ocean	SO189-53MC	1.00	98.03	0.082	1	216.71	30.2	34.0	0.24	Mohtadi et al. (in press)
Indian Ocean	SO189-48MC	0.95	98.13	0.457	1	70.79	29.5	34.1	0.21	Mohtadi et al. (in press)
Indian Ocean	SO189-41MC	0.34	98.13	0.674	1	40.15	29.5	34.1	0.21	Mohtadi et al. (in press)
Indian Ocean	GeoB 10022-6	-0.5	98.85	0.706	1	39.85	31.1	34.1	0.21	Mohtadi et al. (in press)
Indian Ocean	GeoB 10025-3	-0.67	99.12	1.149	1	29.00	29.0	34.1	0.21	Mohtadi et al. (in press)
Indian Ocean	SO189-147MC	-0.69	98.07	1.052	1	30.64	29.5	34.1	0.21	Mohtadi et al. (in press)
Indian Ocean	GeoB10028-4	-0.7	99.76	0.522	1	57.47	30.6	34.1	0.21	Mohtadi et al. (in press)
Indian Ocean	SGeoB 10024-3	-0.77	99.27	1.381	1	30.92	29.8	34.1	0.21	Mohtadi et al. (in press)
Indian Ocean	SO189-38MC	-0.79	99.91	0.517	1	57.51	29.3	34.1	0.21	Mohtadi et al. (in press)
Indian Ocean	GeoB 10027-3	-0.81	99.65	0.875	1	33.64	30.7	34.1	0.21	Mohtadi et al. (in press)
Indian Ocean	SO189-35MC	-0.87	99.80	0.755	1	35.94	29.5	34.1	0.21	Mohtadi et al. (in press)
Indian Ocean	GeoB 10026-2	-0.94	99.52	1.641	1	34.60	30.0	34.1	0.21	Mohtadi et al. (in press)
Indian Ocean	GeoB 10008-4	-0.95	98.26	0.936	1	32.66	29.2	34.1	0.21	Mohtadi et al. (in press)
Indian Ocean	GeoB 10010-1	-1.18	97.98	2.937	1	32.04	28.6	34.0	0.23	Mohtadi et al. (in press)
Indian Ocean	SO189-31MC	-1.30	99.72	1.734	1	35.05	29.3	34.0	0.23	Mohtadi et al. (in press)
Indian Ocean	SO189-34MC	-1.46	100.23	0.560	1	52.15	29.6	34.0	0.23	Mohtadi et al. (in press)
Indian Ocean	GeoB 10029-3	-1.50	100.13	0.794	1	37.83	30.6	34.0	0.23	Mohtadi et al. (in press)
Indian Ocean	GeoB 10033-3	-1.56	99.95	1.756	1	34.78	30.4	34.0	0.23	Mohtadi et al. (in press)
Indian Ocean	SO189-32MC	-1.62	100.0	1.751	1	34.84	29.4	34.0	0.23	Mohtadi et al. (in press)
Indian Ocean	SO189-28MC	-1.67	99.68	1.758	1	34.75	29.0	34.0	0.23	Mohtadi et al. (in press)
Indian Ocean	SO189-27MC	-1.88	99.61	1.002	1	31.82	30.0	34.0	0.23	Mohtadi et al. (in press)
Indian Ocean	SO189-11MC	-3.83	101.23	0.911	1	35.63	29.3	34.0	0.20	Mohtadi et al. (in press)
Indian Ocean	SO189-09MC	-4.16	101.64	1.128	1	33.15	29.2	34.0	0.20	Mohtadi et al. (in press)
Indian Ocean	GeoB 10034-3	-4.16	101.50	0.995	1	33.79	28.9	34.0	0.20	Mohtadi et al. (in press)
Indian Ocean	SO189-03MC	-4.70	101.96	1.707	1	36.96	28.1	34.0	0.20	Mohtadi et al. (in press)
Indian Ocean	GeoB 10036-3	-5.34	103.66	1.502	1	33.76	29.3	33.8	0.20	Mohtadi et al. (in press)
Indian Ocean	SO189-02MC	-5.48	103.01	1.972	1	36.28	28.3	33.8	0.20	Mohtadi et al. (in press)
Indian Ocean	GeoB 10039-3	-5.87	103.29	1.799	1	34.56	29.2	33.8	0.20	Mohtadi et al. (in press)
Indian Ocean	GeoB 10038-3	-5.94	103.25	1.891	1	33.31	29.3	33.8	0.20	Mohtadi et al. (in press)
Indian Ocean	GeoB 10041-3	-6.27	103.09	1.540	1	33.17	28.5	33.8	0.22	Mohtadi et al. (in press)
Indian Ocean	GeoB 10040-3	-6.48	102.86	2.605	1	32.65	30.2	33.9	0.23	Mohtadi et al. (in press)
Indian Ocean	GeoB 10042-2	-7.11	104.64	2.457	1	34.90	28.4	33.8	0.24	Mohtadi et al. (in press)
Indian Ocean	GeoB 10044-3	-8.5	109.16	3.346	1	28.29	28.0	34.1	0.24	Mohtadi et al. (in press)
Indian Ocean	GeoB 10058-1	-8.68	112.64	1.103	1	35.84	28.4	34.1	0.24	Mohtadi et al. (in press)
Indian Ocean	GeiB 10059-1	-8.68	112.87	1.372	1	34.35	30.3	34.1	0.24	Mohtadi et al. (in press)
Indian Ocean	GeoB 10049-5	-8.78	110.50	1.288	1	35.49	28.2	34.1	0.24	Mohtadi et al. (in press)
Indian Ocean	GeoB 10047-1	-9.31	109.16	1.780	1	34.20	28.8	34.2	0.28	Mohtadi et al. (in press)
Indian Ocean	GeoB 10050-1	-9.47	110.45	1.221	1	34.81	27.8	34.2	0.28	Mohtadi et al. (in press)
Indian Ocean	GeoB 10061-5	-9.73	113.20	2.170	1	32.70	30.2	34.2	0.27	Mohtadi et al. (in press)

Area	Core Name	Latitude (°N)	Longitude (°E)	Water Depth (km)	Age Control	ΔCO32- (μmol/ kg)	T$_{iso}$	Mean annual SSS	δ18Osw	Reference
Indian Ocean	GeoB 10065-9	-9.22	118.89	1.284	1	34.05	29.0	34.2	0.28	Mohtadi et al. (in press)
Indian Ocean	GeoB 10064-5	-9.54	118.30	2.035	1	35.36	29.1	34.2	0.28	Mohtadi et al. (in press)
Indian Ocean	GeoB 10063-5	-9.65	118.15	2.495	1	33.33	28.9	34.2	0.28	Mohtadi et al. (in press)
Indian Ocean	GeoB 10068-2	-9.60	121.15	2.002	1	35.58	29.4	34.2	0.30	Mohtadi et al. (in press)
North Atlantic	Sediment trap	32.09	-64.26				20.1	36.5	1.09	Anand et al. (2003)
North Atlantic	Sediment trap	32.09	-64.26				22.8	36.5	1.09	Anand et al. (2003)
North Atlantic	Sediment trap	32.09	-64.26				24.2	36.5	1.09	Anand et al. (2003)
North Atlantic	Sediment trap	32.09	-64.26				24.6	36.5	1.09	Anand et al. (2003)
North Atlantic	Sediment trap	32.09	-64.26				21.8	36.5	1.09	Anand et al. (2003)
North Atlantic	Sediment trap	32.09	-64.26				21.0	36.5	1.09	Anand et al. (2003)
North Atlantic	Sediment trap	32.09	-64.26				22.9	36.5	1.09	Anand et al. (2003)
North Atlantic	Sediment trap	32.09	-64.26				25.4	36.5	1.09	Anand et al. (2003)
North Atlantic	Sediment trap	32.09	-64.26				22.4	36.5	1.09	Anand et al. (2003)
North Atlantic	Sediment trap	32.09	-64.26				25.1	36.5	1.09	Anand et al. (2003)
North Atlantic	Sediment trap	32.09	-64.26				24.4	36.5	1.09	Anand et al. (2003)
North Atlantic	Sediment trap	32.09	-64.26				21.4	36.5	1.09	Anand et al. (2003)
North Atlantic	Sediment trap	32.09	-64.26				23.3	36.5	1.09	Anand et al. (2003)
North Atlantic	Sediment trap	32.09	-64.26				21.1	36.5	1.09	Anand et al. (2003)
North Atlantic	Sediment trap	32.09	-64.26				20.6	36.5	1.09	Anand et al. (2003)
North Atlantic	Sediment trap	32.09	-64.26				21.5	36.5	1.09	Anand et al. (2003)
North Atlantic	Sediment trap	32.09	-64.26				23.8	36.5	1.09	Anand et al. (2003)
North Atlantic	Sediment trap	32.09	-64.26				26.1	36.5	1.09	Anand et al. (2003)
North Atlantic	Sediment trap	32.09	-64.26				20.4	36.5	1.09	Anand et al. (2003)
North Atlantic	Sediment trap	32.09	-64.26				22.0	36.5	1.09	Anand et al. (2003)
North Atlantic	Sediment trap	32.09	-64.26				24.7	36.5	1.09	Anand et al. (2003)
North Atlantic	Sediment trap	32.09	-64.26				24.4	36.5	1.09	Anand et al. (2003)
North Atlantic	Sediment trap	32.09	-64.26				23.2	36.5	1.09	Anand et al. (2003)
North Atlantic	Sediment trap	32.09	-64.26				20.8	36.5	1.09	Anand et al. (2003)
North Atlantic	Sediment trap	32.09	-64.26				20.2	36.5	1.09	Anand et al. (2003)
Guaymas Basin	Sediment trap	27.88	111.67				30.9	35.1	0.09	McConnell and Thunell (1995)/ Wejnert et al. (2010)
Guaymas Basin	Sediment trap	27.88	111.67				29.3	35.1	0.09	McConnell and Thunell (1995)/ Wejnert et al. (2010)
Guaymas Basin	Sediment trap	27.88	111.67				27.0	35.1	0.09	McConnell and Thunell (1995)/ Wejnert et al. (2010)
Guaymas Basin	Sediment trap	27.88	111.67				19.5	35.1	0.09	McConnell and Thunell (1995)/ Wejnert et al. (2010)
Guaymas Basin	Sediment trap	27.88	111.67				23.2	35.1	0.09	McConnell and Thunell (1995)/ Wejnert et al. (2010)
Guaymas Basin	Sediment trap	27.88	111.67				20.0	35.1	0.09	McConnell and Thunell (1995)/ Wejnert et al. (2010)
Guaymas Basin	Sediment trap	27.88	111.67				24.8	35.1	0.09	McConnell and Thunell (1995)/ Wejnert et al. (2010)
Guaymas Basin	Sediment trap	27.88	111.67				26.2	35.1	0.09	McConnell and Thunell (1995)/ Wejnert et al. (2010)
Guaymas Basin	Sediment trap	27.88	111.67				28.0	35.1	0.09	McConnell and Thunell (1995)/ Wejnert et al. (2010)
Guaymas Basin	Sediment trap	27.88	111.67				28.8	35.1	0.09	McConnell and Thunell (1995)/ Wejnert et al. (2010)
Guaymas Basin	Sediment trap	27.88	111.67				30.1	35.1	0.09	McConnell and Thunell (1995)/ Wejnert et al. (2010)
Guaymas Basin	Sediment trap	27.88	111.67				27.6	35.1	0.09	McConnell and Thunell (1995)/ Wejnert et al. (2010)
Guaymas Basin	Sediment trap	27.88	111.67				30.2	35.1	0.09	McConnell and Thunell (1995)/ Wejnert et al. (2010)
Guaymas Basin	Sediment trap	27.88	111.67				32.1	35.1	0.09	McConnell and Thunell (1995)/ Wejnert et al. (2010)
Guaymas Basin	Sediment trap	27.88	111.67				30.3	35.1	0.09	McConnell and Thunell (1995)/ Wejnert et al. (2010)
Guaymas Basin	Sediment trap	27.88	111.67				28.4	35.1	0.09	McConnell and Thunell (1995)/ Wejnert et al. (2010)

Area	**Core Name**	**Latitude (°N)**	**Longitude (°E)**	**Water Depth (km)**	**Age Control**	**ΔCO32- (µmol/ kg)**	**T_{iso}**	**Mean annual SSS**	**δ18Osw**	**Reference**
Guaymas Basin	Sediment trap	27.88	111.67				25.5	35.1	0.09	McConnell and Thunell (1995)/ Wejnert et al. (2010)
Guaymas Basin	Sediment trap	27.88	111.67				24.7	35.1	0.09	McConnell and Thunell (1995)/ Wejnert et al. (2010)
Guaymas Basin	Sediment trap	27.88	111.67				23.7	35.1	0.09	McConnell and Thunell (1995)/ Wejnert et al. (2010)
Guaymas Basin	Sediment trap	27.88	111.67				21.4	35.1	0.09	McConnell and Thunell (1995)/ Wejnert et al. (2010)
Guaymas Basin	Sediment trap	27.88	111.67				21.9	35.1	0.09	McConnell and Thunell (1995)/ Wejnert et al. (2010)
Guaymas Basin	Sediment trap	27.88	111.67				22.9	35.1	0.09	McConnell and Thunell (1995)/ Wejnert et al. (2010)
Guaymas Basin	Sediment trap	27.88	111.67				24.5	35.1	0.09	McConnell and Thunell (1995)/ Wejnert et al. (2010)
Guaymas Basin	Sediment trap	27.88	111.67				26.0	35.1	0.09	McConnell and Thunell (1995)/ Wejnert et al. (2010)
Guaymas Basin	Sediment trap	27.88	111.67				27.5	35.1	0.09	McConnell and Thunell (1995)/ Wejnert et al. (2010)
Guaymas Basin	Sediment trap	27.88	111.67				29.6	35.1	0.09	McConnell and Thunell (1995)/ Wejnert et al. (2010)
Guaymas Basin	Sediment trap	27.88	111.67				28.9	35.1	0.09	McConnell and Thunell (1995)/ Wejnert et al. (2010)
Guaymas Basin	Sediment trap	27.88	111.67				28.5	35.1	0.09	McConnell and Thunell (1995)/ Wejnert et al. (2010)
Guaymas Basin	Sediment trap	27.88	111.67				20.8	35.1	0.09	McConnell and Thunell (1995)/ Wejnert et al. (2010)
Guaymas Basin	Sediment trap	27.88	111.67				23.7	35.1	0.09	McConnell and Thunell (1995)/ Wejnert et al. (2010)
Guaymas Basin	Sediment trap	27.88	111.67				24.9	35.1	0.09	McConnell and Thunell (1995)/ Wejnert et al. (2010)
Guaymas Basin	Sediment trap	27.88	111.67				26.6	35.1	0.09	McConnell and Thunell (1995)/ Wejnert et al. (2010)
Guaymas Basin	Sediment trap	27.88	111.67				31.1	35.1	0.09	McConnell and Thunell (1995)/ Wejnert et al. (2010)
Guaymas Basin	Sediment trap	27.88	111.67				31.9	35.1	0.09	McConnell and Thunell (1995)/ Wejnert et al. (2010)
Guaymas Basin	Sediment trap	27.88	111.67				31.1	35.1	0.09	McConnell and Thunell (1995)/ Wejnert et al. (2010)
Guaymas Basin	Sediment trap	27.88	111.67				30.2	35.1	0.09	McConnell and Thunell (1995)/ Wejnert et al. (2010)

Age control levels are given from 1 to 4, corresponding to different level of uncertainty: Level 1: ^{14}C AMS control within 0-2ka, Level 2: ^{14}C AMS control within 0-6ka, Level 3: specific biostratigraphic control (i.e., % of *Globorotalia hirsuta* left coiling in the North Atlantic). Level 4: other stratigraphic control such as oxygen isotope stratigraphy.

A2. Barker et al. (2003) Cleaning Procedure

The following method is designed around cleaning approximately 10-15 samples at one time. Procedures in part modified after Boyle (1981) and Boyle and Keigwin (1985).

Crushing

Foraminiferal tests are crushed using two clean glass plates. The aim here is to allow any chamber fill to escape during subsequent cleaning stages.

1. Place the tests in a single layer on the lower glass slide. Keep the sample moist with excess water.
2. In a controlled manner, lower the second plate onto the sample and apply gentle pressure in order to open every shell chamber. Take care not to over-crush the sample; this will lead to excessive loss of sample during cleaning
3. Remove the upper glass plate and transfer all particles to the lower plate.

At this time, a piece of light colored paper should be positioned beneath the sample while under a microscope. This will reveal the presence of any large silicate grains that may not be removed during the following clay removal steps. It is not necessary to remove such grains at this stage but only to note their presence so that action may be taken later on.

Steps (4) to (6) should be followed if the sample is intended for paired analyses of trace metals and stable isotopes or similar.

4. Add water to the sample in order to bring the shell particles into suspension.
5. Mix particles thoroughly with a brush with the aim of homogenizing the sample as far as possible.
6. Remove any excess water
7. Using a moistened brush, transfer the crushed sample to an acid cleaned 500µL microcentrifuge tube.

Clay Removal

During this stage, all samples should be treated individually in order to maximize cleaning effectiveness (batch treatment for ultrasonification is appropriate). It is important to use separate pipette tips for adding and removing reagents.

Having opened the test chambers during crushing, much of the test fill will be loosened and easily brought into suspension.

1. Squirt 500uL of UHQ H_2O onto the crushed sample (trapped air bubbles may be freed by flicking the tube end with a fingernail).
2. Allow the sample to settle for 30 seconds or so.
3. Remove the overlying solution (supernatant) with a separate pipette. The size of the 500µL pipette tip is suitable for removing most of the overlying liquid from the tube without risk of sample loss.
At this stage, all tubes should still contain about 10-20µL of H_2O.
4. Place the sample rack in an ultrasonic bath for 1-2minutes. This will encourage separation of more tightly bound clays from the test surfaces.

Suspended clays will appear as a milky residue in the liquid just above the sample.

5. Squirt 500µL of UHO H_2O onto each sample. This will agitate the sample and bring loose clays into suspension.

6. Briefly allow the sample to settle (minimal settling technique). Sufficient settling will only take a number of seconds (long enough for the distinct carbonate grains to reach the bottom). After this period the remaining settling material will mainly comprise unwanted silicate particles.

7. Remove the overlying solution.

8. Repeat steps (4) to (7) a further 4 times. More repetitions may be necessary for as long as clays are being visibly brought into suspension by ultrasonication.

After the water cleaning steps, methanol is used for further clay removal. The lower viscosity of thus reagent should dislodge material still attached to the carbonate tests.

9. Squirt 250µL of Aristar methanol into each tube.

10. Ultrasonicate the tubes for 1-2 minutes.

11. Treating each tube individually, lift the methanol off the sample with a pipette and quirt straight back in to bring clays into suspension.

12. Allow sample to settle for a few seconds and remove the methanol.

13. Repeat steps (9) to (12).

14. Repeat steps (5) to (7) in order to remove any remaining methanol (further ultrasonication may be applied if desired).

Removal of organic matter

1. Add 250µL of alkali buffered 1% H_2O_2 solution to each tube and secure the rack with a lid to prevent tubes popping while under pressure.

2. Place the sample rack in a boiling water bath for 10 minutes. At 2.5 and 7.5 minutes remove the rack momentarily and rap on the bench top to release any gaseous build-up. At 5 minutes place the rack in an ultrasonic bath for a few seconds and return to the water bath after rapping on the bench. The aim of these interim steps is to maintain contact between reagent and sample.

3. Remove the oxidizing reagent using a pipette.

4. Repeat steps (1) to (3).

5. Remove any remaining oxidizing reagent by filing the tube with UHQ and removing after settling. This step should be repeated 1-2 times.

Removal of coarse-grained silicates

This step is necessary if silicates were observed in the sample after crushing. It is a good idea to follow this step even if no large particles were seen; any foreign body that has entered the sample during the preceding steps might bias the desired measurement.

Particle removal at this stage is less time consuming than straight after crushing as the clay treatment and oxidation steps will have broken down and removed some particles already.

A 100µL pipette is used to transfer the sample into a 1mL glass micro-beaker.

Squirt 100µL of UHQ H_2O into the sample and immediately transfer to a micro-beaker avoiding settling.

2. Repeat step (1) 3-4 times ensuring that the entire sample is transferred.

3. Remove excess H_2O leaving approximately 100µL overlying the sample.

The sample is viewed under a microscope using a dark and light background in turn.

4. Remove any particles that are not apparently carbonate using a fine brush. Strongly discolored carbonate should also be removed.

5. Transfer the sample into a clean microcentrifuge tube using the technique in step (1) and remove excess H_2O.

Note, if particles are not removed using the technique outlined above, it is nevertheless, good practice to transfer all samples to clean tubes before continuing. If a transfer is not performed, thorough cleaning of the sample tube (including cap) with UHQ H2O should be carried out to ensure that all oxidizing reagent is removed.

Weak acid leach

A weak acid leach is used to remove any adsorbed contaminants from the test fragments.

1. Add 250µL of 0.001M HNO_3 to each sample.

2. Ultrasonicate all samples for 30 seconds

3. Remove acid from each sample

4. Squirt UHQ H_2O into each tube.

It is important to replace the leach acid with H_2O as soon as possible for all samples in order to prevent excess dissolution.

5. Remove the overlying H_2O

6. Repeat steps (4) and (5)

7. Using a 10µL pipette, carefully remove any remaining solution from each sample.

Dissolution

Dissolution should be performed with consideration given to any non-carbonate particles that may still be present in the sample. The following steps should act to reduce the risk of contamination from such phases.

1. Add 500µL of 0.075M HNO_3 to each sample (for small samples 300µL is adequate).

2. Place the sample rack in an ultrasonic bath to promote reaction

3. Momentarily remove each tube in turn and flick with a fingernail to allow any build-up of CO_2 to escape and the reaction to continue. As soon as production of CO_2 ceases in any sample tube, remove that tube from the ultrasonic bath and leave to settle.

4. Once all samples are dissolved, they should be transferred to clean sample tubes.

A3. Mg/Ca and δ^{18}O data for the core tops used in the calibration

Area	Core Name	Latitude (°N)	Longitude (°E)	Water Depth (km)	Mg/Ca	$\delta^{18}O_c$	Reference
North Atlantic	INMD48	29.80	-43.20	2.836	4.54	-0.49	This study
Tropical Atlantic	INMD109	-5.50	-16.00	3.895	4.42	-1.58	This study
South Atlantic	INMD 120	-28.80	-31.20	1.918	4.34	-0.80	This study
Indonesia	MD98-2177	1.40	119.10	0.968	5.52	-3.09	This study
Indonesia	MD98 2164	-6.60	119.40	0.750	5.27	-2.73	This study
Indonesia	MD98-2176	-5.00	133.40	2.382	4.86	-2.82	This study
Indonesia	GGC 8	11.60	118.70	1.305	5.29	-2.91	This study
Indonesia	GGC 9	11.60	118.60	1.465	5.22	-3.25	This study
Indonesia	GGC 10	11.70	118.50	1.605	4.87	-3.10	This study
Indonesia	GGC 13	10.60	118.30	0.990	5.25	-2.96	This study
North Atlantic	INMD 42	28.57	-46.36	3.774	4.60	-0.86	L.D. Stott (unpublished)
North Atlantic	INMD 50	31.18	-39.68	3.481	3.81	-0.43	L.D. Stott (unpublished)
North Atlantic	INMD 68	34.81	-28.36	2.520	3.58	-0.16	L.D. Stott (unpublished)
Tropical Atlantic	INMD 97	16.65	-46.13	3.619	5.11	-1.58	L.D. Stott (unpublished)
Tropical Atlantic	INMD 101	6.95	-26.45	4.093	4.15	-1.56	L.D. Stott (unpublished)
Tropical Atlantic	INMD 104	4.25	-21.92	3.279	4.47	-1.70	L.D. Stott (unpublished)
Tropical Atlantic	INMD 110	-10.04	-13.39	1.959	4.38	-1.12	L.D. Stott (unpublished)
Tropical Atlantic	INMD 111	-12.64	-13.85	3.069	4.41	-1.15	L.D. Stott (unpublished)
Tropical Atlantic	INMD 113	-15.26	-14.96	3.471	4.69	-1.02	L.D. Stott (unpublished)
Tropical Atlantic	INMD 115	-17.64	-16.21	3.427	4.76	-0.95	L.D. Stott (unpublished)
North Atlantic	INMD48BX.1	29.80	-43.20	2.836	4.59	-0.48	Mathien-Blard and Bassinot (2009)
North Atlantic	INMD68BX.6	34.80	-28.40	2.520	3.61	-0.27	Mathien-Blard and Bassinot (2009)
North Atlantic	MD952038	37.80	-20.20	2.310	2.84	-0.12	Mathien-Blard and Bassinot (2009)
North Atlantic	paleo SU 9007P	42.50	-32.40	3.290	3.02	-0.05	Mathien-Blard and Bassinot (2009)
North Atlantic	paleo SU 9004P	41.00	-32.00	2.865	3.33	-0.42	Mathien-Blard and Bassinot (2009)
North Atlantic	paleo SU 9002P	40.60	-31.00	2.220	3.20	-0.06	Mathien-Blard and Bassinot (2009)
North Atlantic	paleo SU 9003P	40.10	-32.00	2.475	3.00	-0.27	Mathien-Blard and Bassinot (2009)
North Atlantic	paleo SU 9008P	43.80	-30.60	3.800	3.04	-0.29	Mathien-Blard and Bassinot (2009)
North Atlantic	paleo SU 9006P	42.00	-32.70	3.510	2.96	0.00	Mathien-Blard and Bassinot (2009)
Tropical Atlantic	CHO 288-54	17.40	-77.70	1.020	5.35	-2.06	Mathien-Blard and Bassinot (2009)
North Atlantic	MD95-2002	47.50	-8.50	2.174	2.09	0.34	Mathien-Blard and Bassinot (2009)
North Atlantic	MD99-2203	35.00	-75.20	0.620	4.43	-1.42	Mathien-Blard and Bassinot (2009)
Mozambique	MD79-255	-19.00	37.50	1.226	3.96	-1.90	Mathien-Blard and Bassinot (2009)
Mozambique	MD79-257	-20.40	36.30	1.262	4.23	-1.81	Mathien-Blard and Bassinot (2009)
Arabian Sea	MD92-1002	12.00	44.30	1.327	5.43	-1.76	Mathien-Blard and Bassinot (2009)
Indonesia	MD00-2359 PC	-9.20	114.70	2.775	4.73	-2.44	Mathien-Blard and Bassinot (2009)
Indonesia	MD98-2165	-9.70	118.30	2.100	4.80	-2.59	Mathien-Blard and Bassinot (2009)
Andaman Sea	MD77-176	14.50	93.10	1.375	4.70	-3.02	Mathien-Blard and Bassinot (2009)
Southeast Indian	MD00-2360top	-20.10	112.70	0.980	4.58	-1.71	Mathien-Blard and Bassinot (2009)
Red Sea	MD92-1008	14.40	42.20	0.708	6.54	-1.86	Mathien-Blard and Bassinot (2009)
Indonesia	MD002358top	-12.30	112.70	2.520	3.69	-1.97	Mathien-Blard and Bassinot (2009)
Indonesia	MD00-2359 G	-9.20	114.70	2.775	4.66	-2.70	Mathien-Blard and Bassinot (2009)
Arabian Sea	ODP117-723	18.10	57.60	0.808	6.85	-2.25	Mathien-Blard and Bassinot (2009)
Central Indian	MD77-191	7.50	76.70	1.254	5.13	-2.44	Mathien-Blard and Bassinot (2009)
West Pacific	ERDC92BX	-2.20	157.00	1.598	5.07	-2.44	Mathien-Blard and Bassinot (2009)
Indian Ocean	SO189-118MC	3.52	96.31	0.804	5.69	-3.30	Mohtadi et al. (in press)
Indian Ocean	SO189-114MC	3.49	95.33	1.535	5.72	-3.08	Mohtadi et al. (in press)
Indian Ocean	SO-189-121MC	3.27	96.15	1.031	5.53	-3.20	Mohtadi et al. (in press)
Indian Ocean	SO189-104MC	3.20	96.78	1.013	5.57	-3.25	Mohtadi et al. (in press)
Indian Ocean	SO189-84MC	2.99	96.22	0.861	6.03	-3.09	Mohtadi et al. (in press)
Indian Ocean	SO189-80MC	2.95	96.50	1.088	6.06	-2.96	Mohtadi et al. (in press)
Indian Ocean	SO189-72MC	2.83	96.39	0.913	5.78	-3.03	Mohtadi et al. (in press)
Indian Ocean	SO189-76MC	2.82	96.61	1.108	5.79	-3.10	Mohtadi et al. (in press)
Indian Ocean	SO189-89MC	2.78	96.42	0.916	5.96	-3.14	Mohtadi et al. (in press)

Area	Core Name	Latitude (°N)	Longitude (°E)	Water Depth (km)	Mg/Ca	$\delta^{18}O_c$	Reference
Indian Ocean	SO189-97MC	2.56	96.76	1.136	5.79	-3.22	Mohtadi et al. (in press)
Indian Ocean	SO189-101MC	2.49	97.12	0.767	5.52	-3.23	Mohtadi et al. (in press)
Indian Ocean	SO189-139MC	1.76	96.77	1.854	6.30	-3.15	Mohtadi et al. (in press)
Indian Ocean	GeoB 10014-1	1.68	96.98	1.158	6.29	-3.13	Mohtadi et al. (in press)
Indian Ocean	GeoB 10016-2	1.60	96.66	1.900	5.28	-3.04	Mohtadi et al. (in press)
Indian Ocean	SO189-60MC	1.45	98.05	0.551	5.70	-3.08	Mohtadi et al. (in press)
Indian Ocean	SO189-59MC	1.15	98.07	0.479	6.38	-3.16	Mohtadi et al. (in press)
Indian Ocean	SO189-53MC	1.00	98.03	0.082	6.33	-3.21	Mohtadi et al. (in press)
Indian Ocean	SO189-48MC	0.95	98.13	0.457	6.11	-3.10	Mohtadi et al. (in press)
Indian Ocean	SO189-41MC	0.34	98.13	0.674	5.96	-3.10	Mohtadi et al. (in press)
Indian Ocean	GeoB 10022-6	-0.5	98.85	0.706	6.28	-3.43	Mohtadi et al. (in press)
Indian Ocean	GeoB 10025-3	-0.67	99.12	1.149	5.50	-2.99	Mohtadi et al. (in press)
Indian Ocean	SO189-147MC	-0.69	98.07	1.052	5.68	-3.11	Mohtadi et al. (in press)
Indian Ocean	GeoB10028-4	-0.7	99.76	0.522	6.33	-3.34	Mohtadi et al. (in press)
Indian Ocean	SGeoB 10024-3	-0.77	99.27	1.381	5.33	-3.17	Mohtadi et al. (in press)
Indian Ocean	SO189-38MC	-0.79	99.91	0.517	6.03	-3.06	Mohtadi et al. (in press)
Indian Ocean	GeoB 10027-3	-0.81	99.65	0.875	5.34	-3.35	Mohtadi et al. (in press)
Indian Ocean	SO189-35MC	-0.87	99.80	0.755	5.77	-3.11	Mohtadi et al. (in press)
Indian Ocean	GeoB 10026-2	-0.94	99.52	1.641	5.14	-3.21	Mohtadi et al. (in press)
Indian Ocean	GeoB 10008-4	-0.95	98.26	0.936	5.68	-3.05	Mohtadi et al. (in press)
Indian Ocean	GeoB 10010-1	-1.18	97.98	2.937	4.99	-2.89	Mohtadi et al. (in press)
Indian Ocean	SO189-31MC	-1.30	99.72	1.734	5.10	-3.05	Mohtadi et al. (in press)
Indian Ocean	SO189-34MC	-1.46	100.23	0.560	5.87	-3.10	Mohtadi et al. (in press)
Indian Ocean	GeoB 10029-3	-1.50	100.13	0.794	5.45	-3.32	Mohtadi et al. (in press)
Indian Ocean	GeoB 10033-3	-1.56	99.95	1.756	4.92	-3.27	Mohtadi et al. (in press)
Indian Ocean	SO189-32MC	-1.62	100.0	1.751	5.84	-3.06	Mohtadi et al. (in press)
Indian Ocean	SO189-28MC	-1.67	99.68	1.758	5.66	-2.99	Mohtadi et al. (in press)
Indian Ocean	SO189-27MC	-1.88	99.61	1.002	5.92	-3.18	Mohtadi et al. (in press)
Indian Ocean	SO189-11MC	-3.83	101.23	0.911	5.53	-3.08	Mohtadi et al. (in press)
Indian Ocean	SO189-09MC	-4.16	101.64	1.128	5.56	-3.04	Mohtadi et al. (in press)
Indian Ocean	GeoB 10034-3	-4.16	101.50	0.995	5.32	-2.99	Mohtadi et al. (in press)
Indian Ocean	SO189-03MC	-4.70	101.96	1.707	5.91	-2.81	Mohtadi et al. (in press)
Indian Ocean	GeoB 10036-3	-5.34	103.66	1.502	5.41	-3.07	Mohtadi et al. (in press)
Indian Ocean	SO189-02MC	-5.48	103.01	1.972	5.42	-2.86	Mohtadi et al. (in press)
Indian Ocean	GeoB 10039-3	-5.87	103.29	1.799	5.53	-3.06	Mohtadi et al. (in press)
Indian Ocean	GeoB 10038-3	-5.94	103.25	1.891	4.78	-3.07	Mohtadi et al. (in press)
Indian Ocean	GeoB 10041-3	-6.27	103.09	1.540	4.94	-2.87	Mohtadi et al. (in press)
Indian Ocean	GeoB 10040-3	-6.48	102.86	2.605	5.39	-3.23	Mohtadi et al. (in press)
Indian Ocean	GeoB 10042-2	-7.11	104.64	2.457	5.14	-2.84	Mohtadi et al. (in press)
Indian Ocean	GeoB 10044-3	-8.5	109.16	3.346	5.21	-2.76	Mohtadi et al. (in press)
Indian Ocean	GeoB 10058-1	-8.68	112.64	1.103	5.30	-2.85	Mohtadi et al. (in press)
Indian Ocean	GeiB 10059-1	-8.68	112.87	1.372	4.71	-3.23	Mohtadi et al. (in press)
Indian Ocean	GeoB 10049-5	-8.78	110.50	1.288	4.49	-2.81	Mohtadi et al. (in press)
Indian Ocean	GeoB 10047-1	-9.31	109.16	1.780	4.68	-2.88	Mohtadi et al. (in press)
Indian Ocean	GeoB 10050-1	-9.47	110.45	1.221	4.22	-2.67	Mohtadi et al. (in press)
Indian Ocean	GeoB 10061-5	-9.73	113.20	2.170	4.84	-3.18	Mohtadi et al. (in press)
Indian Ocean	GeoB 10065-9	-9.22	118.89	1.284	4.86	-2.93	Mohtadi et al. (in press)
Indian Ocean	GeoB 10064-5	-9.54	118.30	2.035	5.14	-2.94	Mohtadi et al. (in press)
Indian Ocean	GeoB 10063-5	-9.65	118.15	2.495	5.34	-2.90	Mohtadi et al. (in press)
Indian Ocean	GeoB 10068-2	-9.60	121.15	2.002	4.43	-2.99	Mohtadi et al. (in press)
North Atlantic	Sediment trap	32.09	-64.26		2.98	-0.27	Anand et al. (2003)
North Atlantic	Sediment trap	32.09	-64.26		3.75	-0.83	Anand et al. (2003)
North Atlantic	Sediment trap	32.09	-64.26		4.56	-1.12	Anand et al. (2003)
North Atlantic	Sediment trap	32.09	-64.26		4.77	-1.21	Anand et al. (2003)
North Atlantic	Sediment trap	32.09	-64.26		3.86	-0.61	Anand et al. (2003)
North Atlantic	Sediment trap	32.09	-64.26		3.05	-0.46	Anand et al. (2003)

Area	Core Name	Latitude (°N)	Longitude (°E)	Water Depth (km)	Mg/Ca	$\delta^{18}O_c$	Reference
North Atlantic	Sediment trap	32.09	-64.26		3.61	-0.84	Anand et al. (2003)
North Atlantic	Sediment trap	32.09	-64.26		5.25	-1.37	Anand et al. (2003)
North Atlantic	Sediment trap	32.09	-64.26		3.71	-0.74	Anand et al. (2003)
North Atlantic	Sediment trap	32.09	-64.26		4.88	-1.30	Anand et al. (2003)
North Atlantic	Sediment trap	32.09	-64.26		4.56	-1.15	Anand et al. (2003)
North Atlantic	Sediment trap	32.09	-64.26		3.54	-0.53	Anand et al. (2003)
North Atlantic	Sediment trap	32.09	-64.26		4.35	-0.93	Anand et al. (2003)
North Atlantic	Sediment trap	32.09	-64.26		4.14	-0.47	Anand et al. (2003)
North Atlantic	Sediment trap	32.09	-64.26		3.22	-0.36	Anand et al. (2003)
North Atlantic	Sediment trap	32.09	-64.26		3.07	-0.55	Anand et al. (2003)
North Atlantic	Sediment trap	32.09	-64.26		4.56	-1.04	Anand et al. (2003)
North Atlantic	Sediment trap	32.09	-64.26		4.98	-1.52	Anand et al. (2003)
North Atlantic	Sediment trap	32.09	-64.26		3.30	-0.32	Anand et al. (2003)
North Atlantic	Sediment trap	32.09	-64.26		3.92	-0.66	Anand et al. (2003)
North Atlantic	Sediment trap	32.09	-64.26		4.93	-1.22	Anand et al. (2003)
North Atlantic	Sediment trap	32.09	-64.26		4.65	-1.15	Anand et al. (2003)
North Atlantic	Sediment trap	32.09	-64.26		4.34	-0.91	Anand et al. (2003)
North Atlantic	Sediment trap	32.09	-64.26		3.61	-0.40	Anand et al. (2003)
North Atlantic	Sediment trap	32.09	-64.26		3.12	-0.28	Anand et al. (2003)
Guaymas Basin	Sediment trap	27.88	111.67		6.10	-3.52	McConnell and Thunell (1995)/ Wejnert et al. (2010)
Guaymas Basin	Sediment trap	27.88	111.67		5.80	-3.17	McConnell and Thunell (1995)/ Wejnert et al. (2010)
Guaymas Basin	Sediment trap	27.88	111.67		4.48	-2.70	McConnell and Thunell (1995)/ Wejnert et al. (2010)
Guaymas Basin	Sediment trap	27.88	111.67		3.07	-1.15	McConnell and Thunell (1995)/ Wejnert et al. (2010)
Guaymas Basin	Sediment trap	27.88	111.67		3.22	-1.92	McConnell and Thunell (1995)/ Wejnert et al. (2010)
Guaymas Basin	Sediment trap	27.88	111.67		2.95	-1.24	McConnell and Thunell (1995)/ Wejnert et al. (2010)
Guaymas Basin	Sediment trap	27.88	111.67		3.73	-2.25	McConnell and Thunell (1995)/ Wejnert et al. (2010)
Guaymas Basin	Sediment trap	27.88	111.67		4.21	-2.54	McConnell and Thunell (1995)/ Wejnert et al. (2010)
Guaymas Basin	Sediment trap	27.88	111.67		4.67	-2.90	McConnell and Thunell (1995)/ Wejnert et al. (2010)
Guaymas Basin	Sediment trap	27.88	111.67		4.87	-3.08	McConnell and Thunell (1995)/ Wejnert et al. (2010)
Guaymas Basin	Sediment trap	27.88	111.67		4.91	-3.35	McConnell and Thunell (1995)/ Wejnert et al. (2010)
Guaymas Basin	Sediment trap	27.88	111.67		5.46	-2.82	McConnell and Thunell (1995)/ Wejnert et al. (2010)
Guaymas Basin	Sediment trap	27.88	111.67		5.89	-3.37	McConnell and Thunell (1995)/ Wejnert et al. (2010)
Guaymas Basin	Sediment trap	27.88	111.67		5.96	-3.76	McConnell and Thunell (1995)/ Wejnert et al. (2010)
Guaymas Basin	Sediment trap	27.88	111.67		5.64	-3.38	McConnell and Thunell (1995)/ Wejnert et al. (2010)
Guaymas Basin	Sediment trap	27.88	111.67		5.26	-2.99	McConnell and Thunell (1995)/ Wejnert et al. (2010)
Guaymas Basin	Sediment trap	27.88	111.67		4.63	-2.40	McConnell and Thunell (1995)/ Wejnert et al. (2010)
Guaymas Basin	Sediment trap	27.88	111.67		4.64	-2.23	McConnell and Thunell (1995)/ Wejnert et al. (2010)
Guaymas Basin	Sediment trap	27.88	111.67		3.64	-2.01	McConnell and Thunell (1995)/ Wejnert et al. (2010)
Guaymas Basin	Sediment trap	27.88	111.67		3.23	-1.54	McConnell and Thunell (1995)/ Wejnert et al. (2010)
Guaymas Basin	Sediment trap	27.88	111.67		3.68	-1.63	McConnell and Thunell (1995)/ Wejnert et al. (2010)
Guaymas Basin	Sediment trap	27.88	111.67		3.52	-1.85	McConnell and Thunell (1995)/ Wejnert et al. (2010)

Area	Core Name	Latitude (°N)	Longitude (°E)	Water Depth (km)	Mg/Ca	$\delta^{18}O_c$	Reference
Guaymas Basin	Sediment trap	27.88	111.67		4.16	-2.17	McConnell and Thunell (1995)/ Wejnert et al. (2010)
Guaymas Basin	Sediment trap	27.88	111.67		4.97	-2.49	McConnell and Thunell (1995)/ Wejnert et al. (2010)
Guaymas Basin	Sediment trap	27.88	111.67		5.06	-2.82	McConnell and Thunell (1995)/ Wejnert et al. (2010)
Guaymas Basin	Sediment trap	27.88	111.67		5.65	-3.24	McConnell and Thunell (1995)/ Wejnert et al. (2010)
Guaymas Basin	Sediment trap	27.88	111.67		5.99	-3.10	McConnell and Thunell (1995)/ Wejnert et al. (2010)
Guaymas Basin	Sediment trap	27.88	111.67		5.29	-3.01	McConnell and Thunell (1995)/ Wejnert et al. (2010)
Guaymas Basin	Sediment trap	27.88	111.67		3.74	-1.41	McConnell and Thunell (1995)/ Wejnert et al. (2010)
Guaymas Basin	Sediment trap	27.88	111.67		3.80	-2.02	McConnell and Thunell (1995)/ Wejnert et al. (2010)
Guaymas Basin	Sediment trap	27.88	111.67		3.79	-2.26	McConnell and Thunell (1995)/ Wejnert et al. (2010)
Guaymas Basin	Sediment trap	27.88	111.67		4.09	-2.61	McConnell and Thunell (1995)/ Wejnert et al. (2010)
Guaymas Basin	Sediment trap	27.88	111.67		6.36	-3.55	McConnell and Thunell (1995)/ Wejnert et al. (2010)
Guaymas Basin	Sediment trap	27.88	111.67		6.95	-3.73	McConnell and Thunell (1995)/ Wejnert et al. (2010)
Guaymas Basin	Sediment trap	27.88	111.67		6.82	-3.56	McConnell and Thunell (1995)/ Wejnert et al. (2010)
Guaymas Basin	Sediment trap	27.88	111.67		6.26	-3.36	McConnell and Thunell (1995)/ Wejnert et al. (2010)

Appendix B:

Supplementary Information for Chapter 5

B1. Mg/Ca and $\delta^{18}O$ data for marine sediment core MD98-2177

Depth in sediment core (cm)	Age (Years A.D.)	Mg/Ca (mmol/mol)	$\delta^{18}O$ (‰)
2.5	1827	5.22	-3.21
3.5	1817	5.06	-3.17
4.5	1807	5.25	-3.13
5.5	1797	4.89	-3.17
6.5	1787	4.66	-3.05
7.5	1777	4.92	-3.08
8.5	1767	5.05	-3.17
9.5	1757	4.93	-3.04
10.5	1746	4.93	-3.09
13.5	1716	4.86	-3.13
14.5	1706	4.79	-3.17
15.5	1696	4.72	-3.17
16.5	1686	4.81	-3.08
17.5	1676	4.84	-2.99
18.5	1666	5.05	-3.15
19.5	1656	4.98	-3.21
23.5	1616	4.95	-3.35
24.5	1606	4.77	-2.74
25.5	1596	5.11	-3.16
26.5	1586	4.94	-3.09
27.5	1576	4.82	-3.12
28.5	1566	5.10	-3.42
29.5	1556	4.94	-3.23
30.5	1545	5.12	-2.98
31.5	1535	5.06	-3.01
32.5	1525	4.94	-3.23
33.5	1515	5.10	-3.04

Depth in sediment core (cm)	**Age (Years A.D.)**	**Mg/Ca (mmol/mol)**	**δ^{18}O (‰)**
34.5	1505	5.01	-2.98
37.5	1475	5.16	-3.23
38.5	1465	5.04	-3.33
39.5	1455	5.15	-3.08
40.5	1445	4.87	-3.31
41.5	1435	5.05	-3.39
42.5	1425	4.90	-3.06
43.5	1415	5.04	-3.28
44.5	1405	5.10	-3.18
45.5	1395	4.75	-3.05
46.5	1385	4.99	-3.19
47.5	1375	5.00	-3.25
48.5	1365	4.91	-3.04
49.5	1355	5.08	-3.11
50.5	1342.4	5.10	-3.13
51.5	1328.3		-3.16
52.5	1314.2	5.18	-3.16
53.5	1300.1	5.45	-3.06
54.5	1286.0		-3.21
55.5	1271.9	5.39	-3.22
56.5	1257.9	5.25	-3.18
57.5	1243.8	5.11	-3.14
58.5	1229.7	5.07	-3.10
59.5	1215.6	5.55	-3.05
60.5	1201.5	5.74	-3.25
61.5	1187.4	5.41	-3.17
62.5	1173.3	4.99	-3.07
63.5	1159.2	5.53	-3.11
64.5	1145.1	5.29	-3.10
65.5	1131.0	5.61	-3.01
66.5	1116.9	5.21	-2.97
67.5	1102.9	5.29	-3.11
68.5	1088.8	5.33	-3.07
69.5	1074.7	5.30	-3.21

Depth in sediment core (cm)	Age (Years A.D.)	Mg/Ca (mmol/mol)	δ^{18}O (‰)
70.5	1060.6		-2.99
71.5	1046.5	5.05	-3.01
72.5	1032.4		-3.18
73.5	1018.3	5.14	-3.12
74.5	1004.2	5.31	-3.41
75.5	990.1	5.51	-3.01
76.5	976.0	5.03	-3.11
77.5	961.9	5.15	-3.13
78.5	947.9	5.53	-3.26
79.5	933.8	5.12	-3.26
80.5	919.7	5.10	-3.09
81.5	905.6	5.30	-3.15
82.5	891.5	5.31	-3.07
83.5	877.4	5.21	-3.22
84.5	863.3	5.13	-3.24
85.5	849.2		-3.24
86.5	835.1	5.23	-3.21
87.5	821.0	5.03	
88.5	806.9	5.02	-3.07
89.5	792.9	5.18	-3.11
90.5	778.8	4.98	-3.90
91.5	764.7	5.27	-3.27
92.5	750.6	5.14	-2.95
93.5	736.5		-3.04
94.5	724.60		-3.07
95.5	714.87	5.34	-3.28
96.5	705.14	5.51	-3.04
97.5	695.40	5.35	-3.01
98.5	685.67	5.11	-3.34
99.5	675.94	5.03	-3.15
100.5	666.20	5.31	-2.98
101.5	656.47	4.98	-3.22
102.5	646.74	5.14	-3.23
103.5	637.00	4.99	-3.00

Depth in sediment core (cm)	Age (Years A.D.)	Mg/Ca (mmol/mol)	$\delta^{18}O$ (‰)
104.5	627.27	5.13	-3.24
105.5	617.54	4.90	-3.33
106.5	607.80	5.30	-3.11
107.5	598.07	5.41	-3.06
108.5	588.34	4.97	-3.08
109.5	574	5.12	-2.96
110.5	554	5.04	-3.27
111.5	534	5.09	-3.17
112.5	514	5.00	-3.18
113.5	494	4.88	-3.23
114.5	474	5.14	-3.21
115.5	455	5.15	-3.20
116.5	435	4.98	-3.16
117.5	415	5.10	-3.06
118.5	395	5.11	-3.09
119.5	375	5.08	-3.15
120.5	356	5.49	-3.09
121.5	336	5.44	-3.16
122.5	316	5.26	-3.11
123.5	296	5.04	-3.10
124.5	276	5.36	-3.22
125.5	257	4.93	-3.51
126.5	237	4.93	-3.38
127.5	217	5.04	-3.41
128.5	197	4.94	-3.24
129.5	177	4.97	-3.23
130.5	157	5.45	-3.22
131.5	138	5.02	-2.80
132.5	118	5.24	-2.99
133.5	98	4.88	-3.10
134.5	78	5.30	-3.10
135.5	58	5.28	-3.08
136.5	39	5.22	-3.16
137.5	19	5.33	-3.18

Depth in sediment core (cm)	**Age (Years A.D.)**	**Mg/Ca (mmol/mol)**	**δ^{18}O (‰)**
138.5	-1	5.25	-3.23
139.5	-21	5.39	-3.32
141	-51	5.22	
142.5	-80	4.89	-2.98
143.5	-100	5.35	-3.16
144.5	-120	5.26	-3.05
145.5	-140	5.39	-3.15

B2. Mg/Ca and $\delta^{18}O$ data for marine sediment core MD98-2181

Depth in sediment core (cm)	Age (Years A.D.)	Mg/Ca (mmol/mol)	$\delta^{18}O$ (‰)
2.5	1831	5.04	-2.83
5	1819	5.10	-2.79
6.5	1813	4.93	-2.85
7	1810	5.01	-2.57
8	1806	5.09	-2.93
11.5	1790	5.22	-2.50
13	1784	5.17	-2.69
15	1775	5.30	-2.90
16	1770	5.29	-2.61
19	1757	4.95	-2.71
21	1748	4.79	-2.73
23	1739	4.98	-2.91
24	1734	5.31	-3.02
28	1717	5.36	-2.49
31	1703	5.08	-2.57
34	1690	5.07	-2.69
37	1676	5.00	-2.96
39	1667	5.00	-2.77
41	1659	4.97	-2.82
43	1650	4.66	-2.78
47	1632	5.18	-2.72
50	1618	5.39	-2.78
54	1600	4.90	-2.76
56	1592	4.87	-3.00
59	1578	4.88	-2.82
61	1569	4.87	-3.05
64	1556	5.14	-2.69
69	1534	5.09	-2.95
71	1525	5.17	-2.78
74	1512	4.75	-2.84
75	1508	4.73	-2.84

Depth in sediment core (cm)	Age (Years A.D.)	Mg/Ca (mmol/mol)	δ^{18}O (‰)
79	1490	5.02	-3.02
82	1477	5.22	-2.92
84	1468	5.07	-2.49
85	1463	5.13	-2.45
87.5	1452	5.08	-3.00
89	1446	5.07	-2.82
92	1432	5.11	-3.05
93	1428	5.06	-2.84
94	1424	5.05	-2.84
94.5	1421	4.88	-2.87
97	1410	4.88	-2.92
99	1401	4.87	-2.83
100	1400	4.87	-2.69
103.5	1397	5.10	-2.99
105.5	1394	5.37	-2.87
113	1386	4.84	-2.87
115	1384	5.26	-2.92
118	1381	4.93	-2.84
120	1378	5.03	-2.84
123	1375	4.76	-3.05
125	1373	4.82	-3.04
126	1372	4.78	-2.87
131	1366	5.30	-3.00
133	1364	4.92	-2.67
141	1355	5.35	-2.95
147	1329	4.87	-2.93
149	1306	4.80	-3.05
152	1272	5.02	-3.05
156	1227	5.09	-2.87
161	1171	5.21	-2.86
165	1126	5.16	-2.84
166	1115	4.98	-2.86
169	1081	5.15	-2.85

Depth in sediment core (cm)	Age (Years A.D.)	Mg/Ca (mmol/mol)	$\delta^{18}O$ (‰)
175	1014	5.34	-2.97
177	991	5.32	-2.61
179	969	5.39	-2.70
181	946	4.93	-2.87
183	924	5.14	-2.87
185	901	5.42	-2.86
191	834	4.97	-2.97
195	789	5.20	-2.46
201	721	5.25	-2.75
205	704	5.04	-2.70
207	695	5.18	-2.81
211	678	5.18	-2.56
213	669	5.33	-2.48
215	661	5.41	-2.78
217	652	5.38	-2.80
219	644	5.27	-2.78
221	635	5.28	-2.72
223	627	5.30	-2.77
226	614	5.40	-2.57
228	605	5.24	-2.80
231	592	5.35	-2.52
233	584	5.11	-2.62
235	575	5.34	-2.74
237	566	5.13	-2.65
239	547	5.25	-2.76
244	472	4.94	-2.71
248	411	4.71	-2.76
251	366	5.32	-2.63
255	306	5.09	-2.73
257	276	5.13	-2.70
263	185	4.90	-2.99
269	95	4.89	-2.84
271	65	4.98	-2.72

Depth in sediment core (cm)	Age (Years A.D.)	Mg/Ca (mmol/mol)	δ^{18}O (‰)
273	35	5.09	-2.81
279	-56	5.04	-2.96
285	-146	4.77	-3.06
286	-161	5.02	-2.81
289	-206	4.77	-2.86
297	-327	4.97	-2.96

Appendix C:

Supplementary Information for Chapter 6

$\delta^{18}O$ data for core MD98-2177

Depth in sediment core	Time slice	$\delta^{13}C$ (‰)	$\delta^{18}O$ (‰)	Weight (µg)
0-1cm	1843-1851	0.936	-2.254	34
0-1cm	1843-1851	0.895	-2.356	37
0-1cm	1843-1851	0.514	-2.630	20
0-1cm	1843-1851	0.900	-2.480	25
0-1cm	1843-1851	0.957	-2.094	29
0-1cm	1843-1851	0.754	-2.664	28
0-1cm	1843-1851	1.023	-2.147	19
0-1cm	1843-1851	0.844	-1.862	13
0-1cm	1843-1851	1.027	-2.202	35
0-1cm	1843-1851	0.376	-2.012	18
0-1cm	1843-1851	2.111	-2.043	29
0-1cm	1843-1851	0.441	-2.198	25
0-1cm	1843-1851	1.027	-2.374	26
0-1cm	1843-1851	0.702	-2.339	24
0-1cm	1843-1851	1.086	-2.239	23
0-1cm	1843-1851	0.814	-2.307	13
0-1cm	1843-1851	0.597	-2.589	24
0-1cm	1843-1851	1.077	-2.610	25
0-1cm	1843-1851	0.936	-2.363	26
0-1cm	1843-1851	1.114	-2.040	33
0-1cm	1843-1851	0.803	-1.811	16
0-1cm	1843-1851	0.920	-1.815	14
0-1cm	1843-1851	0.804	-2.203	12
0-1cm	1843-1851	0.797	-2.090	12
0-1cm	1843-1851	0.678	-2.498	32
0-1cm	1843-1851	0.710	-2.263	20
0-1cm	1843-1851	0.456	-2.251	12

Depth in sediment core	Time slice	δ^{13}C (‰)	δ^{18}O (‰)	Weight (μg)
0-1cm	1843-1851	0.776	-1.939	16
0-1cm	1843-1851	0.747	-2.397	24
0-1cm	1843-1851	0.728	-2.433	22
0-1cm	1843-1851	0.606	-2.538	26
0-1cm	1843-1851	0.966	-1.697	15
0-1cm	1843-1851	0.352	-2.058	18
0-1cm	1843-1851	0.933	-2.163	18
0-1cm	1843-1851	0.828	-2.097	11
0-1cm	1843-1851	1.078	-1.835	31
0-1cm	1843-1851	0.813	-2.386	15
0-1cm	1843-1851	0.554	-2.458	28
0-1cm	1843-1851	0.628	-2.067	19
0-1cm	1843-1851	0.815	-1.955	31
0-1cm	1843-1851	-0.437	-2.416	12
0-1cm	1843-1851	0.589	-2.865	9
0-1cm	1843-1851	0.244	-2.865	15
0-1cm	1843-1851	0.766	-1.825	14
0-1cm	1843-1851	0.865	-2.249	14
0-1cm	1843-1851	0.847	-2.140	23
0-1cm	1843-1851	0.534	-1.666	14
0-1cm	1843-1851	0.548	-2.320	15
0-1cm	1843-1851	0.720	-2.073	15
0-1cm	1843-1851	0.451	-2.194	12
0-1cm	1843-1851	0.682	-1.915	13
0-1cm	1843-1851	0.387	-2.553	11
0-1cm	1843-1851	0.728	-1.984	20
0-1cm	1843-1851	0.723	-2.277	16
0-1cm	1843-1851	0.453	-2.700	20
0-1cm	1843-1851	0.868	-2.345	27
0-1cm	1843-1851	0.951	-2.157	17
0-1cm	1843-1851	0.945	-1.889	15
0-1cm	1843-1851	0.888	-2.191	24
0-1cm	1843-1851	0.454	-2.719	27
0-1cm	1843-1851	1.089	-2.104	35

Depth in sediment core	Time slice	$\delta^{13}C$ (‰)	$\delta^{18}O$ (‰)	Weight (µg)
0-1cm	1843-1851	0.859	-2.033	14
0-1cm	1843-1851	0.394	-2.440	17
0-1cm	1843-1851	0.295	-2.293	27
0-1cm	1843-1851	0.252	-2.563	19
0-1cm	1843-1851	0.630	-2.283	25
0-1cm	1843-1851	0.713	-2.088	21
4-6cm	1800-1817	0.550	-2.555	22
4-6cm	1800-1817	0.874	-2.132	38
4-6cm	1800-1817	0.632	-2.409	29
4-6cm	1800-1817	1.000	-2.262	22
4-6cm	1800-1817	0.851	-2.452	29
4-6cm	1800-1817	1.149	-1.848	24
4-6cm	1800-1817	0.970	-2.196	15
4-6cm	1800-1817	0.405	-2.957	23
4-6cm	1800-1817	0.583	-1.825	18
4-6cm	1800-1817	0.865	-2.466	29
4-6cm	1800-1817	0.716	-2.159	22
4-6cm	1800-1817	0.603	-2.572	27
4-6cm	1800-1817	0.970	-2.221	16
4-6cm	1800-1817	0.004	-2.013	21
4-6cm	1800-1817	0.691	-2.369	23
4-6cm	1800-1817	0.743	-2.403	16
4-6cm	1800-1817	0.767	-2.155	12
4-6cm	1800-1817	0.699	-2.126	15
4-6cm	1800-1817	1.048	-2.125	23
4-6cm	1800-1817	0.585	-2.882	10
4-6cm	1800-1817	0.695	-2.206	23
4-6cm	1800-1817	0.963	-2.066	18
4-6cm	1800-1817	0.535	-2.292	14
4-6cm	1800-1817	0.543	-2.322	21
4-6cm	1800-1817	0.489	-2.868	18
4-6cm	1800-1817	0.625	-2.431	14
4-6cm	1800-1817	0.818	-2.538	21
4-6cm	1800-1817	0.604	-2.726	14

Depth in sediment core	Time slice	δ^{13}C (‰)	δ^{18}O (‰)	Weight (µg)
4-6cm	1800-1817	1.059	-1.796	20
4-6cm	1800-1817	0.717	-2.357	24
4-6cm	1800-1817	0.353	-2.869	25
4-6cm	1800-1817	0.875	-2.054	21
4-6cm	1800-1817	0.916	-1.746	19
4-6cm	1800-1817	0.693	-2.223	15
4-6cm	1800-1817	0.885	-2.418	20
4-6cm	1800-1817	0.856	-2.284	22
4-6cm	1800-1817	0.661	-2.522	17
4-6cm	1800-1817	0.942	-2.483	26
4-6cm	1800-1817	0.721	-2.259	14
4-6cm	1800-1817	0.693	-2.372	18
4-6cm	1800-1817	0.788	-1.940	21
4-6cm	1800-1817	0.635	-2.357	13
4-6cm	1800-1817	0.733	-2.424	19
4-6cm	1800-1817	0.938	-1.791	23
4-6cm	1800-1817	0.866	-2.166	31
4-6cm	1800-1817	0.896	-1.859	16
4-6cm	1800-1817	0.764	-1.860	23
4-6cm	1800-1817	0.861	-1.507	10
4-6cm	1800-1817	0.783	-2.206	28
4-6cm	1800-1817	0.564	-2.705	16
4-6cm	1800-1817	0.780	-1.680	23
4-6cm	1800-1817	1.079	-1.874	27
4-6cm	1800-1817	0.772	-2.337	30
4-6cm	1800-1817	1.126	-1.475	27
4-6cm	1800-1817	0.593	-2.505	14
4-6cm	1800-1817	0.721	-2.363	22
4-6cm	1800-1817	0.625	-2.744	28
4-6cm	1800-1817	0.923	-1.682	32
4-6cm	1800-1817	0.810	-2.249	22
4-6cm	1800-1817	1.113	-2.001	11
4-6cm	1800-1817	0.732	-2.009	15
4-6cm	1800-1817	0.880	-2.070	20

Depth in sediment core	Time slice	$\delta^{13}C$ (‰)	$\delta^{18}O$ (‰)	Weight (µg)
4-6cm	1800-1817	0.591	-2.383	22
4-6cm	1800-1817	0.740	-1.833	16
4-6cm	1800-1817	0.790	-2.575	22
4-6cm	1800-1817	0.669	-2.402	22
4-6cm	1800-1817	0.741	-2.289	17
4-6cm	1800-1817	0.827	-2.215	15
4-6cm	1800-1817	1.228	-1.600	20
4-6cm	1800-1817	0.546	-2.693	29
4-6cm	1800-1817	0.921	-2.180	22
4-6cm	1800-1817	0.496	-2.457	17
4-6cm	1800-1817	0.901	-2.158	32
4-6cm	1800-1817	0.826	-2.150	13
4-6cm	1800-1817	0.695	-2.632	21
4-6cm	1800-1817	0.787	-2.418	18
4-6cm	1800-1817	0.766	-2.592	18
11-13cm	1737-1755	1.118	-1.759	37
11-13cm	1737-1755	0.873	-2.085	20
11-13cm	1737-1755	0.742	-2.045	15
11-13cm	1737-1755	0.984	-2.201	20
11-13cm	1737-1755	1.064	-2.213	19
11-13cm	1737-1755	0.723	-2.767	25
11-13cm	1737-1755	0.953	-1.972	18
11-13cm	1737-1755	0.667	-2.135	13
11-13cm	1737-1755	1.008	-2.248	24
11-13cm	1737-1755	0.877	-2.270	13
11-13cm	1737-1755	1.033	-1.815	23
11-13cm	1737-1755	0.687	-2.515	11
11-13cm	1737-1755	0.729	-2.334	22
11-13cm	1737-1755	0.936	-2.047	19
11-13cm	1737-1755	1.072	-2.097	25
11-13cm	1737-1755	0.770	-2.003	23
11-13cm	1737-1755	0.867	-1.975	12
11-13cm	1737-1755	0.980	-2.594	31
11-13cm	1737-1755	1.068	-1.916	22

Depth in sediment core	Time slice	$\delta^{13}C$ (‰)	$\delta^{18}O$ (‰)	Weight (µg)
11-13cm	1737-1755	0.933	-2.015	16
11-13cm	1737-1755	0.842	-2.121	22
11-13cm	1737-1755	0.424	-2.782	13
11-13cm	1737-1755	0.686	-2.547	16
11-13cm	1737-1755	0.817	-1.876	13
11-13cm	1737-1755	0.813	-2.418	21
11-13cm	1737-1755	0.349	-2.482	23
11-13cm	1737-1755	0.562	-2.464	16
11-13cm	1737-1755	0.672	-2.311	23
11-13cm	1737-1755	0.943	-1.882	27
11-13cm	1737-1755	0.939	-2.406	24
11-13cm	1737-1755	0.686	-1.782	19
11-13cm	1737-1755	0.876	-1.692	20
11-13cm	1737-1755	0.867	-2.206	18
11-13cm	1737-1755	0.863	-1.727	18
11-13cm	1737-1755	0.884	-2.198	28
11-13cm	1737-1755	1.162	-1.903	23
11-13cm	1737-1755	0.959	-2.318	40
11-13cm	1737-1755	0.674	-1.999	14
11-13cm	1737-1755	1.020	-1.688	17
11-13cm	1737-1755	0.935	-1.564	17
11-13cm	1737-1755	0.808	-1.607	11
11-13cm	1737-1755	0.953	-1.379	20
11-13cm	1737-1755	0.231	-2.489	22
11-13cm	1737-1755	0.918	-1.936	17
11-13cm	1737-1755	0.974	-2.253	12
11-13cm	1737-1755	1.013	-2.161	22
11-13cm	1737-1755	0.892	-2.280	18
11-13cm	1737-1755	0.885	-2.231	11
11-13cm	1737-1755	0.867	-2.124	26
11-13cm	1737-1755	0.625	-2.428	18
11-13cm	1737-1755	0.546	-2.199	15
11-13cm	1737-1755	0.814	-1.786	15
11-13cm	1737-1755	0.541	-2.675	10

Depth in sediment core	Time slice	δ^{13}C (‰)	δ^{18}O (‰)	Weight (μg)
11-13cm	1737-1755	1.044	-1.989	13
11-13cm	1737-1755	0.791	-2.536	12
11-13cm	1737-1755	0.463	-2.347	21
11-13cm	1737-1755	0.818	-2.041	19
11-13cm	1737-1755	0.829	-1.389	20
11-13cm	1737-1755	0.972	-1.849	24
11-13cm	1737-1755	0.728	-2.591	34
11-13cm	1737-1755	0.776	-2.434	15
11-13cm	1737-1755	0.977	-2.144	22
11-13cm	1737-1755	0.357	-3.095	27
11-13cm	1737-1755	1.044	-1.639	20
11-13cm	1737-1755	1.171	-2.048	17
11-13cm	1737-1755	0.862	-1.484	17
11-13cm	1737-1755	0.710	-2.617	20
11-13cm	1737-1755	0.844	-2.835	22
11-13cm	1737-1755	0.635	-2.769	22
11-13cm	1737-1755	1.102	-2.107	15
11-13cm	1737-1755	0.594	-2.956	13
11-13cm	1737-1755	0.819	-0.884	18
11-13cm	1737-1755	0.844	-2.279	14
11-13cm	1737-1755	0.837	-1.545	17
11-13cm	1737-1755	0.894	-1.978	15
11-13cm	1737-1755	0.878	-2.687	13
17-19cm	1681-1700	1.081	-2.207	25
17-19cm	1681-1700	0.727	-1.779	17
17-19cm	1681-1700	0.826	-2.626	34
17-19cm	1681-1700	1.025	-1.863	18
17-19cm	1681-1700	0.540	-1.834	28
17-19cm	1681-1700	0.797	-2.672	44
17-19cm	1681-1700	0.691	-2.586	28
17-19cm	1681-1700	0.830	-2.116	33
17-19cm	1681-1700	1.053	-2.010	22
17-19cm	1681-1700	0.637	-1.964	18
17-19cm	1681-1700	0.861	-1.961	21

Depth in sediment core	Time slice	$\delta^{13}C$ (‰)	$\delta^{18}O$ (‰)	Weight (μg)
17-19cm	1681-1700	0.908	-2.523	35
17-19cm	1681-1700	0.942	-2.072	31
17-19cm	1681-1700	1.142	-2.050	26
17-19cm	1681-1700	0.519	-2.515	23
17-19cm	1681-1700	0.930	-1.761	19
17-19cm	1681-1700	1.024	-1.778	18
17-19cm	1681-1700	1.157	-1.667	17
17-19cm	1681-1700	0.843	-2.241	12
17-19cm	1681-1700	1.046	-1.642	13
17-19cm	1681-1700	1.150	-1.824	27
17-19cm	1681-1700	0.923	-1.855	14
17-19cm	1681-1700	1.001	-1.492	22
17-19cm	1681-1700	0.711	-2.541	23
17-19cm	1681-1700	0.785	-2.642	22
17-19cm	1681-1700	0.907	-2.578	36
17-19cm	1681-1700	0.557	-2.667	26
17-19cm	1681-1700	0.974	-2.084	25
17-19cm	1681-1700	0.890	-1.876	12
17-19cm	1681-1700	0.706	-2.582	39
17-19cm	1681-1700	0.893	-2.453	33
17-19cm	1681-1700	0.868	-1.940	22
17-19cm	1681-1700	0.859	-2.288	20
17-19cm	1681-1700	0.457	-3.153	23
17-19cm	1681-1700	0.820	-2.307	25
17-19cm	1681-1700	0.919	-2.080	25
17-19cm	1681-1700	1.081	-2.318	25
17-19cm	1681-1700	0.998	-2.519	17
17-19cm	1681-1700	0.817	-2.187	20
17-19cm	1681-1700	0.681	-2.193	19
17-19cm	1681-1700	0.981	-2.015	27
17-19cm	1681-1700	0.935	-2.090	24
17-19cm	1681-1700	0.836	-2.312	22
17-19cm	1681-1700	0.717	-1.633	18
17-19cm	1681-1700	0.978	-2.308	32

Depth in sediment core	Time slice	δ^{13}C (‰)	δ^{18}O (‰)	Weight (µg)
17-19cm	1681-1700	0.596	-1.959	14
17-19cm	1681-1700	0.887	-2.296	30
17-19cm	1681-1700	0.833	-2.000	23
17-19cm	1681-1700	0.880	-2.086	24
17-19cm	1681-1700	0.910	-1.832	24
17-19cm	1681-1700	1.079	-1.962	44
17-19cm	1681-1700	0.841	-2.073	16
17-19cm	1681-1700	0.826	-2.397	24
17-19cm	1681-1700	0.899	-1.943	22
17-19cm	1681-1700	1.109	-1.117	20
17-19cm	1681-1700	0.790	-2.263	13
17-19cm	1681-1700	0.723	-1.866	19
17-19cm	1681-1700	0.764	-2.268	21
17-19cm	1681-1700	0.861	-2.346	28
17-19cm	1681-1700	0.821	-2.149	17
17-19cm	1681-1700	1.016	-1.664	24
17-19cm	1681-1700	0.873	-2.409	26
17-19cm	1681-1700	0.513	-2.287	15
17-19cm	1681-1700	0.762	-2.228	19
17-19cm	1681-1700	0.638	-2.351	21
17-19cm	1681-1700	1.049	-1.655	14
17-19cm	1681-1700	0.921	-1.975	13
17-19cm	1681-1700	0.663	-2.656	17
17-19cm	1681-1700	0.872	-2.009	20
17-19cm	1681-1700	0.564	-2.234	15
17-19cm	1681-1700	0.847	-2.339	17
17-19cm	1681-1700	0.839	-2.733	18
17-19cm	1681-1700	0.708	-2.537	18
17-19cm	1681-1700	0.688	-1.956	21
17-19cm	1681-1700	0.794	-1.630	14
17-19cm	1681-1700	0.813	-2.072	22
17-19cm	1681-1700	0.551	-2.616	13
17-19cm	1681-1700	0.593	-1.819	15
17-19cm	1681-1700	0.713	-2.376	15

Depth in sediment core	Time slice	δ^{13}C (‰)	δ^{18}O (‰)	Weight (μg)
17-19cm	1681-1700	1.119	-2.075	20
17-19cm	1681-1700	0.814	-2.195	23
23-25cm	1622-1642	0.998	-1.375	14
23-25cm	1622-1642	1.142	-2.064	24
23-25cm	1622-1642	0.805	-2.641	23
23-25cm	1622-1642	0.803	-2.506	23
23-25cm	1622-1642	0.898	-2.306	22
23-25cm	1622-1642	1.110	-2.027	28
23-25cm	1622-1642	0.932	-2.279	31
23-25cm	1622-1642	1.152	-2.472	34
23-25cm	1622-1642	1.115	-2.580	21
23-25cm	1622-1642	1.050	-2.230	34
23-25cm	1622-1642	0.783	-2.483	30
23-25cm	1622-1642	0.682	-2.030	12
23-25cm	1622-1642	0.927	-1.524	16
23-25cm	1622-1642	1.012	-1.666	28
23-25cm	1622-1642	1.144	-1.683	45
23-25cm	1622-1642	0.680	-2.525	17
23-25cm	1622-1642	1.036	-2.100	17
23-25cm	1622-1642	0.999	-2.106	20
23-25cm	1622-1642	0.794	-2.827	27
23-25cm	1622-1642	0.856	-2.546	33
23-25cm	1622-1642	1.148	-2.315	36
23-25cm	1622-1642	1.011	-1.962	31
23-25cm	1622-1642	0.878	-2.423	32
23-25cm	1622-1642	0.959	-2.200	15
23-25cm	1622-1642	0.816	-2.433	39
23-25cm	1622-1642	0.832	-2.077	13
23-25cm	1622-1642	1.036	-1.665	45
23-25cm	1622-1642	0.810	-1.855	21
23-25cm	1622-1642	0.829	-2.041	17
23-25cm	1622-1642	0.861	-2.375	26
23-25cm	1622-1642	0.592	-2.612	22
23-25cm	1622-1642	0.910	-1.889	21

Depth in sediment core	Time slice	δ^{13}C (‰)	δ^{18}O (‰)	Weight (µg)
23-25cm	1622-1642	0.207	-2.585	17
23-25cm	1622-1642	0.757	-2.275	13
23-25cm	1622-1642	0.768	-2.301	27
23-25cm	1622-1642	0.941	-2.385	35
23-25cm	1622-1642	0.997	-2.229	25
23-25cm	1622-1642	-0.083	-2.786	26
23-25cm	1622-1642	0.819	-2.517	11
23-25cm	1622-1642	0.943	-2.382	18
23-25cm	1622-1642	0.786	-2.029	25
23-25cm	1622-1642	0.358	-1.911	18
23-25cm	1622-1642	1.145	-1.800	23
23-25cm	1622-1642	0.632	-2.688	16
23-25cm	1622-1642	1.000	-2.787	15
23-25cm	1622-1642	0.807	-1.814	28
23-25cm	1622-1642	0.836	-2.301	21
23-25cm	1622-1642	0.977	-2.335	27
23-25cm	1622-1642	0.946	-2.490	17
23-25cm	1622-1642	1.013	-2.085	21
23-25cm	1622-1642	0.895	-2.389	27
23-25cm	1622-1642	0.800	-1.876	18
23-25cm	1622-1642	1.190	-2.091	17
23-25cm	1622-1642	0.692	-2.643	18
23-25cm	1622-1642	1.140	-0.958	17
23-25cm	1622-1642	0.724	-1.773	16
23-25cm	1622-1642	0.841	-2.052	16
23-25cm	1622-1642	0.896	-1.748	11
23-25cm	1622-1642	0.554	-2.569	12
23-25cm	1622-1642	0.613	-2.144	12
23-25cm	1622-1642	0.801	-1.414	13
23-25cm	1622-1642	0.996	-1.025	13
23-25cm	1622-1642	0.587	-2.161	12
23-25cm	1622-1642	0.939	-2.084	13
23-25cm	1622-1642	0.789	-2.378	20
35-37cm	1496-1518	0.770	-2.340	39

Depth in sediment core	Time slice	δ^{13}C (‰)	δ^{18}O (‰)	Weight (µg)
35-37cm	1496-1518	0.694	-2.676	30
35-37cm	1496-1518	1.067	-2.120	24
35-37cm	1496-1518	1.017	-2.046	35
35-37cm	1496-1518	0.973	-2.133	35
35-37cm	1496-1518	0.844	-2.343	29
35-37cm	1496-1518	1.091	-2.015	36
35-37cm	1496-1518	0.967	-1.832	32
35-37cm	1496-1518	0.916	-1.788	29
35-37cm	1496-1518	1.113	-1.607	33
35-37cm	1496-1518	1.007	-1.682	22
35-37cm	1496-1518	1.325	-1.433	22
35-37cm	1496-1518	0.768	-2.487	26
35-37cm	1496-1518	0.761	-2.288	18
35-37cm	1496-1518	0.844	-2.414	20
35-37cm	1496-1518	1.040	-2.081	42
35-37cm	1496-1518	1.137	-2.345	22
35-37cm	1496-1518	0.936	-1.653	30
35-37cm	1496-1518	0.868	-2.411	22
35-37cm	1496-1518	0.734	-2.463	30
35-37cm	1496-1518	0.671	-2.403	13
35-37cm	1496-1518	0.956	-2.322	14
35-37cm	1496-1518	1.104	-1.933	31
35-37cm	1496-1518	1.003	-1.546	22
35-37cm	1496-1518	0.816	-2.179	21
35-37cm	1496-1518	0.646	-2.275	32
35-37cm	1496-1518	1.224	-2.113	22
35-37cm	1496-1518	0.150	-2.394	19
35-37cm	1496-1518	-0.239	-2.023	32
35-37cm	1496-1518	0.751	-2.431	23
35-37cm	1496-1518	0.876	-2.421	26
35-37cm	1496-1518	0.810	-2.393	23
35-37cm	1496-1518	0.680	-2.176	28
35-37cm	1496-1518	0.657	-2.459	35
35-37cm	1496-1518	1.024	-2.091	36

Depth in sediment core	Time slice	δ^{13}C (‰)	δ^{18}O (‰)	Weight (μg)
35-37cm	1496-1518	0.780	-2.124	34
35-37cm	1496-1518	1.174	-1.523	32
35-37cm	1496-1518	0.364	-2.357	26
35-37cm	1496-1518	0.840	-1.832	30
35-37cm	1496-1518	0.927	-1.744	26
35-37cm	1496-1518	0.757	-2.343	30
35-37cm	1496-1518	0.593	-2.733	27
35-37cm	1496-1518	0.868	-1.878	34
35-37cm	1496-1518	0.939	-2.044	31
35-37cm	1496-1518	0.804	-1.970	28
35-37cm	1496-1518	0.924	-2.024	23
35-37cm	1496-1518	0.851	-1.880	32
35-37cm	1496-1518	0.805	-2.289	30
35-37cm	1496-1518	0.783	-2.187	27
35-37cm	1496-1518	0.808	-1.760	24
35-37cm	1496-1518	0.828	-2.101	23
35-37cm	1496-1518	0.478	-1.971	24
35-37cm	1496-1518	0.840	-2.203	27
35-37cm	1496-1518	0.851	-2.275	29
35-37cm	1496-1518	1.194	-1.743	22
35-37cm	1496-1518	0.797	-2.250	17
35-37cm	1496-1518	0.683	-2.344	23
35-37cm	1496-1518	0.678	-2.512	18
35-37cm	1496-1518	0.834	-1.944	19
35-37cm	1496-1518	0.918	-2.432	20
35-37cm	1496-1518	1.100	-1.611	20
35-37cm	1496-1518	0.847	-2.009	16
35-37cm	1496-1518	0.626	-2.129	19
35-37cm	1496-1518	0.884	-1.940	30
35-37cm	1496-1518	0.863	-1.764	19
35-37cm	1496-1518	0.767	-2.443	28
35-37cm	1496-1518	0.960	-2.289	16
35-37cm	1496-1518	0.665	-2.116	24
35-37cm	1496-1518	1.039	-1.797	17

Depth in sediment core	Time slice	$\delta^{13}C$ (‰)	$\delta^{18}O$ (‰)	Weight (µg)
35-37cm	1496-1518	0.791	-1.890	17
35-37cm	1496-1518	0.884	-1.679	22
35-37cm	1496-1518	0.965	-2.240	23
35-37cm	1496-1518	0.974	-2.471	20
35-37cm	1496-1518	0.628	-2.623	23
35-37cm	1496-1518	1.010	-1.677	24
35-37cm	1496-1518	0.542	-2.606	34
40-41cm	1452-1464	NaN	-2.050	26
40-41cm	1452-1464	NaN	-2.011	13
40-41cm	1452-1464	NaN	-2.537	25
40-41cm	1452-1464	NaN	-2.526	15
40-41cm	1452-1464	NaN	-2.076	16
40-41cm	1452-1464	NaN	-2.472	22
40-41cm	1452-1464	NaN	-1.994	17
40-41cm	1452-1464	NaN	-2.438	30
40-41cm	1452-1464	NaN	-2.058	22
40-41cm	1452-1464	NaN	-2.337	27
40-41cm	1452-1464	NaN	-1.236	44
40-41cm	1452-1464	NaN	-2.108	25
40-41cm	1452-1464	0.952	-1.615	18
40-41cm	1452-1464	0.685	-2.111	33
40-41cm	1452-1464	0.472	-2.406	18
40-41cm	1452-1464	0.916	-2.373	38
40-41cm	1452-1464	0.909	-1.957	33
40-41cm	1452-1464	0.812	-1.853	17
40-41cm	1452-1464	0.787	-2.509	37
40-41cm	1452-1464	0.330	-2.372	29
40-41cm	1452-1464	0.926	-1.086	14
40-41cm	1452-1464	0.735	-2.117	19
40-41cm	1452-1464	0.579	-1.766	24
40-41cm	1452-1464	0.733	-2.260	32
40-41cm	1452-1464	0.499	-2.375	27
40-41cm	1452-1464	0.788	-2.044	13
40-41cm	1452-1464	0.627	-2.225	19

Depth in sediment core	Time slice	$\delta^{13}C$ (‰)	$\delta^{18}O$ (‰)	Weight (µg)
40-41cm	1452-1464	0.894	-2.297	16
40-41cm	1452-1464	0.760	-2.039	15
40-41cm	1452-1464	0.790	-1.768	14
40-41cm	1452-1464	0.363	-1.702	15
40-41cm	1452-1464	0.574	-1.450	50
40-41cm	1452-1464	0.149	-2.237	14
40-41cm	1452-1464	0.777	-2.275	16
40-41cm	1452-1464	0.749	-2.041	38
40-41cm	1452-1464	0.994	-2.006	15
40-41cm	1452-1464	0.804	-2.394	19
40-41cm	1452-1464	1.186	-1.912	18
40-41cm	1452-1464	0.738	-1.863	15
40-41cm	1452-1464	0.814	-1.851	25
40-41cm	1452-1464	0.705	-1.960	18
40-41cm	1452-1464	0.742	-2.108	22
40-41cm	1452-1464	0.929	-1.862	13
40-41cm	1452-1464	0.909	-1.148	13
40-41cm	1452-1464	0.913	-1.953	32
40-41cm	1452-1464	0.770	-1.828	21
40-41cm	1452-1464	0.790	-2.066	18
40-41cm	1452-1464	1.099	-1.717	31
40-41cm	1452-1464	0.725	-2.046	36
40-41cm	1452-1464	0.879	-1.911	15
40-41cm	1452-1464	0.815	-2.069	17
40-41cm	1452-1464	0.618	-2.135	14
40-41cm	1452-1464	0.575	-2.069	12
40-41cm	1452-1464	0.834	-1.430	18
40-41cm	1452-1464	0.933	-1.739	14
40-41cm	1452-1464	0.634	-2.427	20
40-41cm	1452-1464	0.720	-2.153	16
40-41cm	1452-1464	0.967	-2.042	16
40-41cm	1452-1464	0.567	-2.642	18
40-41cm	1452-1464	0.830	-2.243	35
40-41cm	1452-1464	0.788	-1.594	15

Depth in sediment core	Time slice	δ13C (‰)	δ18O (‰)	Weight (μg)
40-41cm	1452-1464	0.937	-1.663	21
40-41cm	1452-1464	0.684	-2.020	22
40-41cm	1452-1464	1.111	-1.235	16
40-41cm	1452-1464	0.331	-2.293	16
40-41cm	1452-1464	0.719	-2.674	18
40-41cm	1452-1464	0.861	-1.818	21
40-41cm	1452-1464	0.844	-1.606	16
40-41cm	1452-1464	0.852	-1.355	13
40-41cm	1452-1464	0.445	-1.997	13
40-41cm	1452-1464	0.691	-2.472	22
40-41cm	1452-1464	0.966	-2.438	27
44-45cm	1407-1419	NaN	-2.246	27
44-45cm	1407-1419	NaN	-2.208	35
44-45cm	1407-1419	NaN	-2.265	21
44-45cm	1407-1419	NaN	-1.860	30
44-45cm	1407-1419	NaN	-2.241	33
44-45cm	1407-1419	NaN	-1.602	34
44-45cm	1407-1419	NaN	-2.518	28
44-45cm	1407-1419	NaN	-2.111	26
44-45cm	1407-1419	NaN	-2.081	33
44-45cm	1407-1419	NaN	-2.192	33
44-45cm	1407-1419	NaN	-2.124	15
44-45cm	1407-1419	NaN	-2.111	23
44-45cm	1407-1419	0.290	-2.201	22
44-45cm	1407-1419	0.535	-2.393	37
44-45cm	1407-1419	0.886	-1.877	25
44-45cm	1407-1419	0.884	-2.066	25
44-45cm	1407-1419	0.804	-2.021	25
44-45cm	1407-1419	0.968	-1.856	32
44-45cm	1407-1419	0.770	-1.283	14
44-45cm	1407-1419	0.933	-1.815	48
44-45cm	1407-1419	0.690	-1.740	33
44-45cm	1407-1419	0.782	-1.413	14
44-45cm	1407-1419	0.654	-2.221	23

Depth in sediment core	Time slice	δ^{13}C (‰)	δ^{18}O (‰)	Weight (µg)
44-45cm	1407-1419	1.141	-1.818	31
44-45cm	1407-1419	0.929	-1.665	21
44-45cm	1407-1419	0.810	-2.269	21
44-45cm	1407-1419	0.590	-2.233	43
44-45cm	1407-1419	0.894	-1.655	24
44-45cm	1407-1419	0.871	-1.981	21
44-45cm	1407-1419	0.651	-2.334	24
44-45cm	1407-1419	0.954	-2.063	29
44-45cm	1407-1419	0.849	-1.613	15
44-45cm	1407-1419	0.794	-1.999	15
44-45cm	1407-1419	0.893	-2.030	39
44-45cm	1407-1419	0.803	-2.423	43
44-45cm	1407-1419	0.495	-2.344	44
44-45cm	1407-1419	0.251	-2.423	17
44-45cm	1407-1419	0.965	-1.110	19
44-45cm	1407-1419	1.062	-1.034	15
44-45cm	1407-1419	0.654	-2.348	23
44-45cm	1407-1419	0.911	-2.011	24
44-45cm	1407-1419	0.976	-0.814	19
44-45cm	1407-1419	0.652	-1.858	25
44-45cm	1407-1419	0.252	-2.064	18
44-45cm	1407-1419	0.817	-1.395	17
44-45cm	1407-1419	0.875	-1.648	17
44-45cm	1407-1419	0.983	-1.403	22
44-45cm	1407-1419	0.651	-2.510	27
44-45cm	1407-1419	0.597	-2.406	18
44-45cm	1407-1419	0.580	-2.526	15
44-45cm	1407-1419	0.708	-2.068	17
44-45cm	1407-1419	0.828	-2.325	16
44-45cm	1407-1419	0.581	-2.670	18
44-45cm	1407-1419	0.850	-1.964	34
44-45cm	1407-1419	0.767	-1.784	25
44-45cm	1407-1419	0.769	-1.953	20
44-45cm	1407-1419	0.567	-2.306	27

Depth in sediment core	Time slice	δ^{13}C (‰)	δ^{18}O (‰)	Weight (μg)
44-45cm	1407-1419	0.677	-1.966	16
44-45cm	1407-1419	0.662	-1.477	18
44-45cm	1407-1419	0.633	-2.775	38
44-45cm	1407-1419	-0.405	-3.780	21
44-45cm	1407-1419	0.838	-1.833	23
44-45cm	1407-1419	0.818	-1.872	20
44-45cm	1407-1419	0.609	-1.754	12
44-45cm	1407-1419	0.970	-1.514	27
44-45cm	1407-1419	1.047	-1.092	18
44-45cm	1407-1419	0.424	-1.719	16
44-45cm	1407-1419	0.749	-1.744	13
44-45cm	1407-1419	0.727	-2.079	29
44-45cm	1407-1419	0.879	-2.063	25
44-45cm	1407-1419	0.787	-2.263	22
44-45cm	1407-1419	0.511	-2.679	50
50-51cm	1337-1349	NaN	-2.064	25
50-51cm	1337-1349	NaN	-1.686	31
50-51cm	1337-1349	NaN	-2.418	24
50-51cm	1337-1349	NaN	-2.128	38
50-51cm	1337-1349	NaN	-2.263	26
50-51cm	1337-1349	NaN	-1.378	19
50-51cm	1337-1349	NaN	-2.166	27
50-51cm	1337-1349	NaN	-1.661	22
50-51cm	1337-1349	NaN	-1.282	25
50-51cm	1337-1349	0.926	-1.901	22
50-51cm	1337-1349	0.948	-2.031	31
50-51cm	1337-1349	0.589	-2.056	20
50-51cm	1337-1349	0.724	-1.810	34
50-51cm	1337-1349	0.868	-2.144	22
50-51cm	1337-1349	0.907	-1.910	33
50-51cm	1337-1349	0.666	-2.127	23
50-51cm	1337-1349	0.881	-2.048	35
50-51cm	1337-1349	0.895	-1.980	33
50-51cm	1337-1349	0.581	-2.472	23

Depth in sediment core	Time slice	δ^{13}C (‰)	δ^{18}O (‰)	Weight (μg)
50-51cm	1337-1349	0.557	-2.278	22
50-51cm	1337-1349	0.976	-1.974	28
50-51cm	1337-1349	0.641	-2.406	30
50-51cm	1337-1349	0.924	-1.247	20
50-51cm	1337-1349	0.659	-2.187	20
50-51cm	1337-1349	0.927	-1.645	16
50-51cm	1337-1349	0.708	-2.100	23
50-51cm	1337-1349	0.501	-2.944	28
50-51cm	1337-1349	0.702	-1.827	16
50-51cm	1337-1349	0.825	-2.061	19
50-51cm	1337-1349	0.768	-2.848	18
50-51cm	1337-1349	0.329	-1.654	13
50-51cm	1337-1349	0.908	-2.200	32
50-51cm	1337-1349	0.588	-2.274	31
50-51cm	1337-1349	0.859	-1.900	21
50-51cm	1337-1349	0.563	-2.050	21
50-51cm	1337-1349	0.813	-2.133	21
50-51cm	1337-1349	0.988	-1.714	17
50-51cm	1337-1349	0.684	-2.085	25
50-51cm	1337-1349	0.848	-1.974	18
50-51cm	1337-1349	0.799	-2.315	29
50-51cm	1337-1349	0.546	-2.203	24
50-51cm	1337-1349	0.807	-1.940	25
50-51cm	1337-1349	0.803	-2.049	26
50-51cm	1337-1349	0.826	-2.331	30
50-51cm	1337-1349	0.854	-1.862	43
50-51cm	1337-1349	0.799	-2.235	21
50-51cm	1337-1349	0.716	-2.299	25
50-51cm	1337-1349	1.039	-1.714	21
50-51cm	1337-1349	0.952	-1.757	24
50-51cm	1337-1349	0.742	-2.274	26
50-51cm	1337-1349	0.636	-2.297	24
50-51cm	1337-1349	0.756	-1.572	18
50-51cm	1337-1349	0.383	-2.746	23

Depth in sediment core	Time slice	$\delta^{13}C$ (‰)	$\delta^{18}O$ (‰)	Weight (µg)
50-51cm	1337-1349	1.060	-1.506	24
50-51cm	1337-1349	-0.524	-2.007	18
50-51cm	1337-1349	0.981	-1.619	19
50-51cm	1337-1349	0.750	-2.560	28
50-51cm	1337-1349	0.675	-2.301	16
50-51cm	1337-1349	0.751	-2.393	25
50-51cm	1337-1349	0.756	-2.131	31
50-51cm	1337-1349	0.807	-2.067	28
50-51cm	1337-1349	0.732	-2.295	13
50-51cm	1337-1349	0.930	-2.583	30
50-51cm	1337-1349	0.688	-2.505	22
50-51cm	1337-1349	0.747	-2.556	34
50-51cm	1337-1349	0.868	-2.314	15
50-51cm	1337-1349	0.975	-1.541	20
50-51cm	1337-1349	0.837	-2.590	28
50-51cm	1337-1349	0.761	-2.508	30
54-55cm	1290-1302	NaN	-1.779	25
54-55cm	1290-1302	NaN	-2.128	22
54-55cm	1290-1302	NaN	-1.380	38
54-55cm	1290-1302	NaN	-2.473	20
54-55cm	1290-1302	NaN	-1.378	22
54-55cm	1290-1302	NaN	-1.816	21
54-55cm	1290-1302	NaN	-2.226	27
54-55cm	1290-1302	NaN	-2.478	33
54-55cm	1290-1302	NaN	-2.688	20
54-55cm	1290-1302	NaN	-1.513	23
54-55cm	1290-1302	NaN	-2.158	14
54-55cm	1290-1302	NaN	-2.411	20
54-55cm	1290-1302	0.599	-2.387	27
54-55cm	1290-1302	0.678	-2.204	25
54-55cm	1290-1302	0.673	-2.239	21
54-55cm	1290-1302	0.979	-1.467	27
54-55cm	1290-1302	0.627	-2.532	48
54-55cm	1290-1302	0.782	-2.103	23

Depth in sediment core	Time slice	δ^{13}C (‰)	δ^{18}O (‰)	Weight (µg)
54-55cm	1290-1302	0.930	-2.177	37
54-55cm	1290-1302	0.525	-2.085	23
54-55cm	1290-1302	0.654	-2.648	19
54-55cm	1290-1302	0.539	-2.379	30
54-55cm	1290-1302	1.035	-2.141	40
54-55cm	1290-1302	0.666	-2.047	29
54-55cm	1290-1302	0.859	-1.819	16
54-55cm	1290-1302	0.922	-1.412	16
54-55cm	1290-1302	0.543	-2.116	18
54-55cm	1290-1302	1.019	-2.051	17
54-55cm	1290-1302	0.883	-1.836	23
54-55cm	1290-1302	0.635	-1.350	12
54-55cm	1290-1302	0.734	-1.857	23
54-55cm	1290-1302	0.651	-1.892	21
54-55cm	1290-1302	0.352	-2.648	30
54-55cm	1290-1302	0.672	-2.218	26
54-55cm	1290-1302	0.717	-1.914	16
54-55cm	1290-1302	0.852	-2.315	31
54-55cm	1290-1302	0.835	-2.451	16
54-55cm	1290-1302	0.788	-1.816	22
54-55cm	1290-1302	0.766	-2.337	19
54-55cm	1290-1302	0.751	-1.928	24
54-55cm	1290-1302	0.806	-1.655	19
54-55cm	1290-1302	1.007	-1.772	15
54-55cm	1290-1302	0.559	-2.612	29
54-55cm	1290-1302	0.927	-1.306	17
54-55cm	1290-1302	1.122	-1.360	19
54-55cm	1290-1302	0.641	-0.893	26
54-55cm	1290-1302	0.729	-1.951	28
54-55cm	1290-1302	0.768	-2.288	36
54-55cm	1290-1302	0.875	-1.707	38
54-55cm	1290-1302	0.672	-1.867	15
54-55cm	1290-1302	0.723	-2.146	23
54-55cm	1290-1302	0.506	-2.432	28

Depth in sediment core	Time slice	$\delta^{13}C$ (‰)	$\delta^{18}O$ (‰)	Weight (µg)
54-55cm	1290-1302	0.422	-2.635	18
54-55cm	1290-1302	0.996	-1.845	39
54-55cm	1290-1302	0.663	-2.056	23
54-55cm	1290-1302	0.910	-1.736	21
54-55cm	1290-1302	1.073	-2.158	23
54-55cm	1290-1302	0.657	-2.286	23
54-55cm	1290-1302	0.730	-2.363	32
54-55cm	1290-1302	0.418	-2.710	25
58-60cm	1240-1265	0.764	-2.081	34
58-60cm	1240-1265	0.761	-2.106	47
58-60cm	1240-1265	0.907	-2.123	34
58-60cm	1240-1265	0.873	-1.358	44
58-60cm	1240-1265	0.909	-1.732	27
58-60cm	1240-1265	0.682	-2.269	32
58-60cm	1240-1265	0.679	-2.130	34
58-60cm	1240-1265	0.768	-2.053	22
58-60cm	1240-1265	0.793	-2.137	31
58-60cm	1240-1265	1.181	-1.067	42
58-60cm	1240-1265	0.931	-2.154	26
58-60cm	1240-1265	0.913	-1.948	52
58-60cm	1240-1265	0.962	-1.689	19
58-60cm	1240-1265	0.699	-2.545	28
58-60cm	1240-1265	0.950	-1.410	19
58-60cm	1240-1265	0.908	-1.966	45
58-60cm	1240-1265	1.040	-2.213	29
58-60cm	1240-1265	0.746	-2.120	21
58-60cm	1240-1265	0.603	-2.096	18
58-60cm	1240-1265	0.994	-1.991	19
58-60cm	1240-1265	0.749	-2.063	17
58-60cm	1240-1265	0.856	-2.098	18
58-60cm	1240-1265	0.834	-1.925	25
58-60cm	1240-1265	0.959	-2.038	26
58-60cm	1240-1265	0.511	-2.023	18
58-60cm	1240-1265	0.824	-1.283	15

Depth in sediment core	Time slice	δ^{13}C (‰)	δ^{18}O (‰)	Weight (µg)
58-60cm	1240-1265	0.826	-1.982	19
58-60cm	1240-1265	0.705	-2.358	14
58-60cm	1240-1265	0.896	-2.160	35
58-60cm	1240-1265	0.493	-2.666	18
58-60cm	1240-1265	1.060	-1.007	18
58-60cm	1240-1265	0.803	-2.099	18
58-60cm	1240-1265	0.801	-1.316	16
58-60cm	1240-1265	0.695	-2.538	25
58-60cm	1240-1265	0.938	-2.336	24
58-60cm	1240-1265	0.972	-1.191	19
58-60cm	1240-1265	0.745	-1.650	31
58-60cm	1240-1265	0.933	-2.108	29
58-60cm	1240-1265	0.730	-2.488	18
58-60cm	1240-1265	0.876	-1.480	20
58-60cm	1240-1265	0.705	-2.140	27
58-60cm	1240-1265	1.097	-2.138	42
58-60cm	1240-1265	0.918	-2.151	25
58-60cm	1240-1265	1.041	-1.510	23
58-60cm	1240-1265	0.883	-2.023	25
58-60cm	1240-1265	0.788	-1.807	26
58-60cm	1240-1265	0.810	-2.194	24
58-60cm	1240-1265	0.795	-2.190	31
58-60cm	1240-1265	0.973	-1.657	26
58-60cm	1240-1265	0.799	-2.017	22
58-60cm	1240-1265	0.879	-1.937	20
58-60cm	1240-1265	0.824	-1.736	22
58-60cm	1240-1265	0.804	-2.246	16
58-60cm	1240-1265	0.721	-2.005	20
58-60cm	1240-1265	1.046	-1.350	21
58-60cm	1240-1265	0.921	-2.060	22
58-60cm	1240-1265	0.687	-2.424	15
58-60cm	1240-1265	0.691	-2.548	26
58-60cm	1240-1265	0.870	-2.022	23
58-60cm	1240-1265	0.964	-2.291	32

Depth in sediment core	Time slice	$\delta^{13}C$ (‰)	$\delta^{18}O$ (‰)	Weight (μg)
58-60cm	1240-1265	0.499	-1.813	17
58-60cm	1240-1265	0.826	-1.496	11
58-60cm	1240-1265	0.933	-1.621	12
58-60cm	1240-1265	0.913	-1.974	16
58-60cm	1240-1265	1.027	-1.596	18
58-60cm	1240-1265	0.789	-2.083	21
58-60cm	1240-1265	0.606	-1.556	15
58-60cm	1240-1265	0.021	-1.946	17
58-60cm	1240-1265	0.884	-1.935	17
58-60cm	1240-1265	0.068	-2.272	15
58-60cm	1240-1265	1.011	-0.974	19
58-60cm	1240-1265	0.688	-1.847	15
58-60cm	1240-1265	0.719	-2.128	17
58-60cm	1240-1265	0.990	-1.787	14
58-60cm	1240-1265	0.918	-1.248	20
58-60cm	1240-1265	0.729	-1.817	10
58-60cm	1240-1265	1.212	-1.384	13
58-60cm	1240-1265	1.022	-0.881	16
58-60cm	1240-1265	0.778	-1.838	15
65-67cm	1139-1165	0.998	-2.264	46
65-67cm	1139-1165	1.205	-2.106	49
65-67cm	1139-1165	0.991	-2.047	37
65-67cm	1139-1165	1.198	-1.650	31
65-67cm	1139-1165	0.944	-2.152	32
65-67cm	1139-1165	0.874	-2.064	22
65-67cm	1139-1165	0.534	-2.611	32
65-67cm	1139-1165	0.482	-2.236	24
65-67cm	1139-1165	1.081	-2.095	46
65-67cm	1139-1165	0.757	-2.230	24
65-67cm	1139-1165	1.089	-1.575	21
65-67cm	1139-1165	0.891	-1.713	14
65-67cm	1139-1165	0.804	-2.418	32
65-67cm	1139-1165	0.868	-1.802	18
65-67cm	1139-1165	0.736	-2.065	26

Depth in sediment core	Time slice	δ^{13}C (‰)	δ^{18}O (‰)	Weight (μg)
65-67cm	1139-1165	0.777	-2.584	35
65-67cm	1139-1165	0.875	-1.576	37
65-67cm	1139-1165	0.489	-2.233	23
65-67cm	1139-1165	0.927	-2.083	32
65-67cm	1139-1165	0.916	-2.032	34
65-67cm	1139-1165	0.507	-2.439	27
65-67cm	1139-1165	0.796	-2.353	20
65-67cm	1139-1165	0.873	-1.939	29
65-67cm	1139-1165	0.516	-2.443	28
65-67cm	1139-1165	1.075	-1.819	31
65-67cm	1139-1165	0.258	-2.182	26
65-67cm	1139-1165	0.290	-1.648	27
65-67cm	1139-1165	1.463	-1.493	25
65-67cm	1139-1165	1.465	-2.048	17
65-67cm	1139-1165	0.215	-2.131	20
65-67cm	1139-1165	0.503	-2.140	26
65-67cm	1139-1165	0.807	-1.957	55
65-67cm	1139-1165	-0.230	-1.935	39
65-67cm	1139-1165	0.323	-2.274	22
65-67cm	1139-1165	0.832	-1.974	29
65-67cm	1139-1165	0.849	-1.815	21
65-67cm	1139-1165	0.753	-2.368	40
65-67cm	1139-1165	0.967	-1.852	31
65-67cm	1139-1165	0.717	-1.971	31
65-67cm	1139-1165	0.965	-1.751	27
65-67cm	1139-1165	0.817	-1.917	26
65-67cm	1139-1165	1.049	-2.086	34
65-67cm	1139-1165	0.812	-2.004	22
65-67cm	1139-1165	0.580	-2.918	15
65-67cm	1139-1165	0.745	-2.059	20
65-67cm	1139-1165	0.738	-2.356	22
65-67cm	1139-1165	0.950	-2.374	33
65-67cm	1139-1165	0.729	-1.750	19
65-67cm	1139-1165	1.013	-1.368	19

Depth in sediment core	Time slice	δ^{13}C (‰)	δ^{18}O (‰)	Weight (μg)
65-67cm	1139-1165	0.868	-1.615	22
65-67cm	1139-1165	0.883	-1.691	25
65-67cm	1139-1165	0.972	-1.972	34
65-67cm	1139-1165	0.884	-1.853	16
65-67cm	1139-1165	0.401	-1.940	19
65-67cm	1139-1165	1.012	-1.247	28
65-67cm	1139-1165	0.804	-1.820	22
65-67cm	1139-1165	0.531	-2.265	29
65-67cm	1139-1165	1.093	-1.195	25
65-67cm	1139-1165	0.641	-1.949	18
65-67cm	1139-1165	1.005	-1.218	24
65-67cm	1139-1165	0.968	-1.438	19
65-67cm	1139-1165	0.848	-1.757	20
65-67cm	1139-1165	0.491	-2.745	20
65-67cm	1139-1165	1.042	-1.921	23
65-67cm	1139-1165	1.053	-2.115	45
65-67cm	1139-1165	0.623	-1.985	21
65-67cm	1139-1165	0.458	-2.051	14
65-67cm	1139-1165	0.459	-1.664	18
65-67cm	1139-1165	0.855	-2.415	22
65-67cm	1139-1165	0.689	-2.059	21
65-67cm	1139-1165	1.063	-1.541	18
65-67cm	1139-1165	0.927	-2.132	17
65-67cm	1139-1165	0.727	-2.076	17
65-67cm	1139-1165	0.776	-1.427	19
65-67cm	1139-1165	0.954	-2.729	14
65-67cm	1139-1165	1.060	-1.520	21
65-67cm	1139-1165	0.714	-2.196	21
65-67cm	1139-1165	0.761	-2.449	19
65-67cm	1139-1165	0.699	-1.890	21
65-67cm	1139-1165	0.573	-1.940	20
65-67cm	1139-1165	0.744	-2.056	13
65-67cm	1139-1165	1.267	-0.881	16
65-67cm	1139-1165	0.899	-1.524	21

Depth in sediment core	Time slice	δ^{13}C (‰)	δ^{18}O (‰)	Weight (µg)
65-67cm	1139-1165	0.777	-1.804	16
65-67cm	1139-1165	0.602	-1.917	12
65-67cm	1139-1165	0.714	-2.001	16
65-67cm	1139-1165	0.939	-1.941	23
65-67cm	1139-1165	0.883	-1.943	29
71-73cm	1060-1087	1.052	-2.089	32
71-73cm	1060-1087	0.872	-2.153	39
71-73cm	1060-1087	0.967	-2.036	43
71-73cm	1060-1087	0.666	-2.157	18
71-73cm	1060-1087	0.773	-2.126	35
71-73cm	1060-1087	0.641	-1.711	23
71-73cm	1060-1087	0.959	-1.989	24
71-73cm	1060-1087	0.920	-2.319	28
71-73cm	1060-1087	1.096	-1.402	53
71-73cm	1060-1087	0.753	-2.385	22
71-73cm	1060-1087	0.935	-1.932	27
71-73cm	1060-1087	0.825	-2.090	19
71-73cm	1060-1087	0.770	-2.151	14
71-73cm	1060-1087	0.524	-2.410	24
71-73cm	1060-1087	0.828	-2.326	44
71-73cm	1060-1087	0.721	-2.457	24
71-73cm	1060-1087	0.892	-2.142	36
71-73cm	1060-1087	1.141	-1.777	27
71-73cm	1060-1087	0.724	-2.249	28
71-73cm	1060-1087	0.954	-1.948	25
71-73cm	1060-1087	0.861	-2.118	24
71-73cm	1060-1087	0.930	-2.139	25
71-73cm	1060-1087	0.953	-2.179	24
71-73cm	1060-1087	0.644	-2.555	21
71-73cm	1060-1087	0.742	-2.099	30
71-73cm	1060-1087	1.042	-1.093	15
71-73cm	1060-1087	0.778	-1.692	13
71-73cm	1060-1087	0.517	-2.516	23
71-73cm	1060-1087	0.979	-1.680	13

Depth in sediment core	Time slice	δ^{13}C (‰)	δ^{18}O (‰)	Weight (µg)
71-73cm	1060-1087	0.962	-2.502	18
71-73cm	1060-1087	0.944	-1.883	34
71-73cm	1060-1087	0.708	-2.446	29
71-73cm	1060-1087	0.877	-1.989	22
71-73cm	1060-1087	0.578	-2.033	12
71-73cm	1060-1087	0.841	-2.236	39
71-73cm	1060-1087	1.039	-1.557	18
71-73cm	1060-1087	1.154	-1.573	17
71-73cm	1060-1087	0.940	-1.821	29
71-73cm	1060-1087	0.567	-2.389	21
71-73cm	1060-1087	0.555	-2.233	30
71-73cm	1060-1087	0.977	-1.723	24
71-73cm	1060-1087	0.739	-1.973	24
71-73cm	1060-1087	0.607	-2.338	28
71-73cm	1060-1087	0.700	-1.667	22
71-73cm	1060-1087	0.579	-1.903	27
71-73cm	1060-1087	0.822	-2.132	24
71-73cm	1060-1087	0.779	-2.033	30
71-73cm	1060-1087	0.735	-1.948	21
71-73cm	1060-1087	0.825	-1.837	23
71-73cm	1060-1087	0.905	-2.082	25
71-73cm	1060-1087	0.980	-1.196	19
71-73cm	1060-1087	0.629	-2.111	17
71-73cm	1060-1087	1.079	-1.333	19
71-73cm	1060-1087	0.839	-1.526	18
71-73cm	1060-1087	0.963	-1.842	19
71-73cm	1060-1087	0.499	-2.403	25
71-73cm	1060-1087	0.829	-1.451	14
71-73cm	1060-1087	0.590	-2.166	18
71-73cm	1060-1087	0.747	-1.750	16
71-73cm	1060-1087	1.098	-1.848	18
71-73cm	1060-1087	0.557	-2.094	13
71-73cm	1060-1087	0.728	-2.111	35
71-73cm	1060-1087	0.436	-2.245	15

Depth in sediment core	Time slice	δ¹³C (‰)	δ¹⁸O (‰)	Weight (μg)
71-73cm	1060-1087	0.637	-1.491	16
71-73cm	1060-1087	0.843	-1.658	13
71-73cm	1060-1087	0.864	-2.265	15
71-73cm	1060-1087	0.777	-2.564	22
83-85cm	895-923	0.386	-2.792	24
83-85cm	895-923	1.101	-1.798	21
83-85cm	895-923	0.856	-2.279	38
83-85cm	895-923	0.673	-2.625	21
83-85cm	895-923	0.843	-0.642	40
83-85cm	895-923	0.733	-2.262	28
83-85cm	895-923	0.762	-2.355	31
83-85cm	895-923	0.786	-2.478	24
83-85cm	895-923	0.725	-2.004	25
83-85cm	895-923	1.083	-1.800	40
83-85cm	895-923	0.926	-1.689	16
83-85cm	895-923	0.830	-1.802	39
83-85cm	895-923	0.768	-2.448	19
83-85cm	895-923	0.427	-2.658	21
83-85cm	895-923	0.674	-2.003	13
83-85cm	895-923	0.983	-2.047	26
83-85cm	895-923	0.575	-2.345	19
83-85cm	895-923	0.963	-1.701	26
83-85cm	895-923	0.845	-1.461	22
83-85cm	895-923	0.937	-1.936	32
83-85cm	895-923	0.823	-1.679	42
83-85cm	895-923	0.955	-1.821	21
83-85cm	895-923	0.981	-2.288	15
83-85cm	895-923	0.799	-2.123	19
83-85cm	895-923	0.921	-1.294	15
83-85cm	895-923	0.803	-1.738	22
83-85cm	895-923	0.595	-2.092	16
83-85cm	895-923	0.911	-2.009	22
83-85cm	895-923	0.830	-1.906	24
83-85cm	895-923	0.943	-2.364	28

Depth in sediment core	Time slice	δ13C (‰)	δ18O (‰)	Weight (µg)
83-85cm	895-923	0.636	-2.280	32
83-85cm	895-923	0.829	-1.320	22
83-85cm	895-923	0.662	-2.264	22
83-85cm	895-923	0.806	-2.600	22
83-85cm	895-923	0.771	-2.298	27
83-85cm	895-923	1.006	-1.693	27
83-85cm	895-923	0.791	-2.234	24
83-85cm	895-923	0.779	-1.967	22
83-85cm	895-923	0.815	-2.101	20
83-85cm	895-923	0.815	-2.318	22
83-85cm	895-923	0.586	-1.735	11
83-85cm	895-923	0.726	-2.390	26
83-85cm	895-923	0.763	-1.950	20
83-85cm	895-923	0.746	-2.284	28
83-85cm	895-923	0.566	-2.088	33
83-85cm	895-923	0.910	-2.059	27
83-85cm	895-923	0.683	-2.638	31
83-85cm	895-923	0.642	-2.717	28
83-85cm	895-923	0.683	-2.168	20